Dynamics and stability of thin liquid films

R. V. Craster*

Department of Mathematics, Imperial College London, South Kensington Campus, London SW7 2AZ, United Kingdom

O. K. Matar†

Department of Chemical Engineering, Imperial College London, South Kensington Campus, London SW7 2AZ, United Kingdom

(Published 5 August 2009)

The dynamics and stability of thin liquid films have fascinated scientists over many decades: the observations of regular wave patterns in film flows down a windowpane or along guttering, the patterning of dewetting droplets, and the fingering of viscous flows down a slope are all examples that are familiar in daily life. Thin film flows occur over a wide range of length scales and are central to numerous areas of engineering, geophysics, and biophysics; these include nanofluidics and microfluidics, coating flows, intensive processing, lava flows, dynamics of continental ice sheets, tear-film rupture, and surfactant replacement therapy. These flows have attracted considerable attention in the literature, which have resulted in many significant developments in experimental, analytical, and numerical research in this area. These include advances in understanding dewetting, thermocapillary- and surfactant-driven films, falling films and films flowing over structured, compliant, and rapidly rotating substrates, and evaporating films as well as those manipulated via use of electric fields to produce nanoscale patterns. These developments are reviewed in this paper and open problems and exciting research avenues in this thriving area of fluid mechanics are also highlighted.

DOI: 10.1103/RevModPhys.81.1131 PACS number(s): 68.15.+e, 47.85.Dh, 47.55.nb

CONTENTS

I. Introduction 1131
II. Formulation 1135
A. Governing equations 1135
B. Scaling 1137
C. Negligible inertia: Lubrication theory 1138
1. Two-layer systems 1139
2. Single-layer systems 1140
D. Significant inertia: Integral theory 1142
III. Films Driven by Body Forces 1143
A. Flows driven by gravity 1143
1. Negligible inertia 1143
2. Significant inertia 1146
B. Flows driven by centrifugal forces 1150
C. Electrified films 1152
IV. Films Driven by Thermal Effects 1155
A. Uniform heating and evaporating films 1155
1. Modeling of thin films with evaporation 1156
2. Experimental and numerical studies 1157
B. Climbing films 1161
C. Flow patterning 1163
D. Flow with solidification and thermally varying viscosity 1164
V. Films Driven by Intermolecular Forces 1165
A. Fundamental considerations 1165
B. Free energy of interaction 1166
C. Experiments 1167
D. Modeling and simulations 1169
E. Contact line dynamics 1173
VI. Surfactant Driven Flows 1174
A. Monolayer spreading 1175
B. Surfactant-induced fingering 1177
C. Spreading at high concentrations 1179
VII. Effect of Bounding Wall 1180
A. Flow over topography 1180
B. Flow over flexible and compliant support 1182
C. Flow down vertical fibers 1183
D. Flow over porous media 1184
VIII. Concluding Remarks 1185
Acknowledgments 1186
Appendix A: Letter to the "The Engineer" (1884) 1186
Appendix B: Algebraic Detail 1186
Appendix C: Lubrication Theory for One-Sided Evaporation Models 1187
References 1189

*Present address: Department of Mathematical and Statistical Sciences, University of Alberta, Edmonton, Canada. craster@ualberta.ca
†o.matar@imperial.ac.uk

I. INTRODUCTION

The flows of thin fluid films dominate our daily lives; even something as trivial as the blink of an eye involves motion over a thin corneal fluid film. It is initially surprising that the same mathematical philosophy can be used to model flows on different length scales such as the corneal fluid film in the eye and, at the other extreme, large scale lava or continental ice sheet flows. Thin fluid films can generate a host of intriguing and

fascinating behaviors including complex dynamics featuring the formation of regular or chaotic structures, periodic waves, shocks and fronts, and "fingering" phenomena; this pattern formation has attracted many physicists, mathematicians, and engineers toward the field of thin films.

Importantly the modern and emerging areas of microfluidics and nanofluidics naturally call upon techniques associated with thin fluid films. Thus the entire area is currently thriving with new discoveries and applications occurring almost daily. Almost every issue of journals in the fields of physics, applied mathematics, and engineering will contain at least one article featuring thin films. In parallel with technologically important applications, the techniques available to tackle the nonlinear equations that arise have dramatically improved. These involve approaches based on asymptotic expansions and perturbation theory complemented by accurate and efficient numerical schemes capable of reproducing experiments often both quantitatively as well as qualitatively.

Flows of thin fluid layers spreading on solid surfaces have a distinguished history having been studied since the days of Reynolds, who was among the first to examine lubrication flows (Reynolds, 1886). Careful experiments by Beauchamp Towers in 1883 and 1884 prompted Reynolds to create what we now call "lubrication theory," which, subsequently, has been widely used to study thin film flows. This early interplay between theorists and experimentalists has remained a vital theme in the development of the subject with many instances of modeling advances motivated by careful experimentation. It is interesting to note that the great successes of lubrication theory and the technological advances that it would create were not foreseen at that time and indeed were partially dismissed. In fact, the whole approach did not meet with a universal welcome: the short letter to the editor of "The Engineer," February 1884 (see Appendix A), gives one a flavor of the time; little did that letter writer know to what ends that experiment and the ensuing theory would be put.

A flavor of the range of applications for which thin film flows are of importance can be gleaned from the many targeted reviews in which they feature. Notable applications and reviews are for complex coating flows, where a thin film adheres to a moving substrate (Weinstein and Ruschak, 2004), in engineering applications such as distillation units, condensers and heat exchangers, microfluidics as covered by Stone *et al.* (2004) and Squires and Quake (2005), and microelectromechanical devices, as well as nanotechnological settings (Eijkel and van den Berg, 2005). Other important applications of thin film theories are in geophysical settings, for instance, in gravity currents (Huppert, 2006), mud, granular and debris flows, snow avalanches (Ancey, 2007), ice sheet models (Baral *et al.*, 2001), and lava flows (Griffiths, 2000). Biological and biophysical scenarios, for instance, in lung airways and linings (Grotberg, 1994, 2001), in flexible tubes (Grotberg and Jensen, 2004), tear-film flows (Shyy *et al.*, 2001), and bioadhesion (Gallez and Coakley, 1996) also abound with thin films. There is also considerable mathematical interest in the analysis of thin film equations themselves as discussed by Myers (1998). Then, of course, there are connections with the area of wettability and the spreading of fluid over substrates by de Gennes (1985) and more recently by Bonn *et al.* (2008).

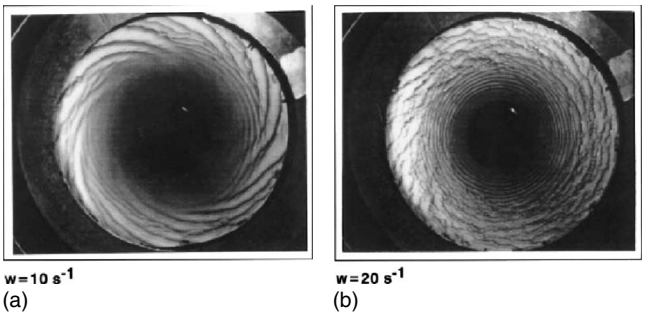

FIG. 1. Wave formation in thin film flows over spinning disks. The left panel shows well-defined regular spiral waves, which, at higher rotation rates, break down into an assembly of wavelets, as shown in the right panel. From Aoune and Ramshaw, 1999.

Over the past two decades, work has focused primarily on the dynamics of films driven to flow by various forces such as gravity, centrifugation, capillarity, thermocapillarity, and intermolecular forces over smooth or structured and impermeable or porous surfaces possibly in the presence of evaporation or condensation. These studies which have included flowing liquid sheets and flows involving so-called "moving contact lines" use modeling, asymptotic methods, numerical simulations, and direct experimentation to elucidate the variety of traveling-wave, rupture, dewetting, and fingering instabilities that the film can exhibit in these situations. The effect of having localized heating and chemically heterogeneous substrates to manipulate and control the flow of the film and to overcome limitations in the pattern length scale, which are set by instabilities inherent to the flow, has also been studied.

Much of the material up to the mid-1990s was reviewed by Oron *et al.* (1997); since then, progress in thin film research has been rapid. In the present review, we look back at the most prominent developments in the thin film area since the work of Oron *et al.* (1997). We delineate our review into how the films are driven and we structure our discussion accordingly. Films subjected to body forces such as centrifugation and gravity often exhibit interesting dynamics. In these cases, which are reviewed in Sec. III, film destabilization is often dramatic and may, in certain instances, be inertially driven. In Fig. 1, one sees that the flow of thin films over rapidly rotating disks at high rotational speeds is accompanied by the formation of large-amplitude waves. These waves are essentially axisymmetric near the disk inlet but become unstable to azimuthal disturbances with increasing radial distance, leading to the formation of a region of apparently disordered ripples further downstream. The large-amplitude waves engender an intense mixing envi-

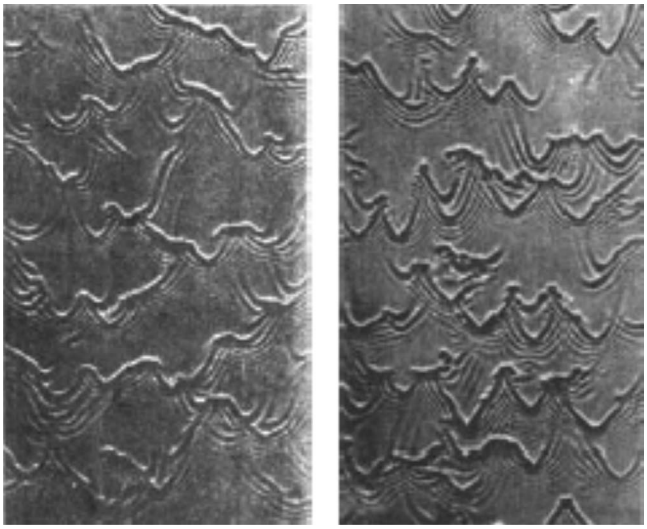

FIG. 2. Experiments of a water-ethanol mixture flowing down an inclined plate with increasing inertial influence; the Reynolds numbers are 16 and 45 in the left and right panels, respectively. These results demonstrate the development of noise-driven large-amplitude three-dimensional waves in falling films. From Alekseenko *et al.*, 1994.

ronment on the surface of the disk. This has technological implications and has been exploited by Matar *et al.* (2006) for a class of novel chemical reactors. Related to this is the commonly observed "windscreen flow," which involves a thin film flowing down an incline at moderate Reynolds number, as shown in Fig. 2. Inertia is, once again, important here and experiments demonstrate strongly coherent structures developing during the flow and ultimately three-dimensional waves. Despite the highly complex flow structures, recent advances and improvements in both theoretical and numerical techniques now allow one to capture this complex behavior within the context of a thin film model (Scheid *et al.*, 2006).

Inertia, however, is not necessary in order to create patterns and interesting dynamics. In fact, thin film instabilities occur even in regimes where inertia is irrelevant. These may be driven by body forces, which may be electrostatic in nature, for instance, and may feature multilayers as shown in Fig. 3. Here pattern formation occurs in a polymeric bilayer sandwiched between two electrodes and subjected to a voltage difference. The interface separating the two immiscible layers is susceptible to a linear electrohydrodynamic instability which leads to the creation of ridges in the nonlinear regime. The size of the remarkably periodic structures obtained is controllable and is in the range of 100 nm; this has applications in the manufacturing of semiconductors and microelectronics (Rockford *et al.*, 1999; Schaffer *et al.*, 2000, 2001; Lin *et al.*, 2001; Morariu *et al.*, 2003).

Interesting thin film dynamics are also brought about by surface forces, wherein surface tension and forces arising due to its variations play a key role. An example of this is the motion of a film driven by thermocapillarity: as surface tension is temperature dependent one

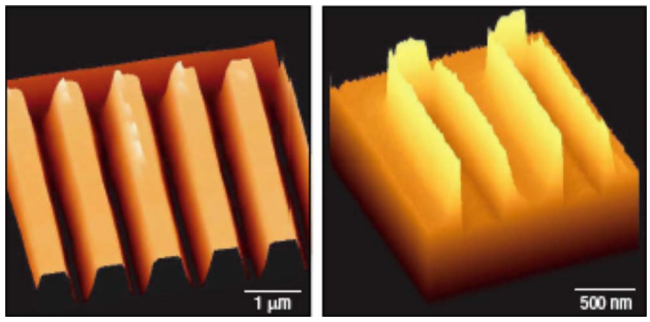

FIG. 3. (Color online) Electrohydrodynamically induced pattern formation in a polystyrene/polylmethylmethacrylate system using a topographically structured electrode showing an atomic force microscopy image of five replicated lines and a scanning electron microscopy image of the PMMA structure left behind after the polystyrene phase has been removed using cyclohexane. From Morariu *et al.*, 2003.

finds that thermal gradients drive flow. In certain cases, such films are driven to climb, by differential heating, against the action of gravity and exhibit the formation of "Lax" and undercompressive shocks (Münch and Bertozzi, 1999; Schneemilch and Cazabat, 2000a), as shown in Fig. 4. In cases wherein the thermocapillary-driven interfacial stress greatly exceeds gravitational forces, the shock located at the advancing contact line is vulnerable to perturbations in the spanwise direction that grow to form fingerlike structures, also shown in Fig. 4. The emergence of a detailed understanding of these shock mechanisms and finger development provides a good illustration of the positive effects that interaction between experimentalists and theorists can have. We review this topic in Sec. IV.

Despite the presence of small inertial contributions, even very thin films are vulnerable to a wide range of instabilities and exhibit rich and interesting dynamics and pattern formation; these cases will be reviewed in Sec. V. As shown in Fig. 5, sufficiently thin films bounded from below by a solid substrate of relatively low wettability undergo a dewetting instability (Becker *et al.*, 2003). At film thicknesses of order 1000 Å, long-range intermolecular forces become operative and drive film rupture that is stabilized at length scales of order 10–100 Å by short-range repulsive forces. This leads to the development of the pattern shown in Fig. 5 consisting of "holes" and discrete droplets connected by ultrathin films in which a balance exists between the short- and long-range forces. Careful numerical simulations by Becker *et al.* (2003) generated patterning that gives both qualitative and quantitative agreement.

A degree of complexity arises due to the presence of chemicals in the liquid layers. A paradigm is provided by the spreading of surface-active agents, "surfactants," present either as contaminants or by design as additives, on thin liquid films. In these cases, the driving "force" for motion and the concentration gradients evolve and are strongly coupled to the flow field through the dependence of the surface tension on the level of contamination. These flows are also accompanied by complex pat-

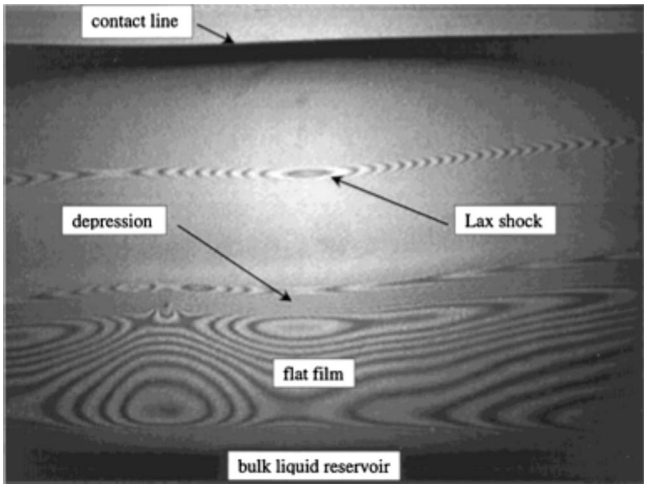

(a)

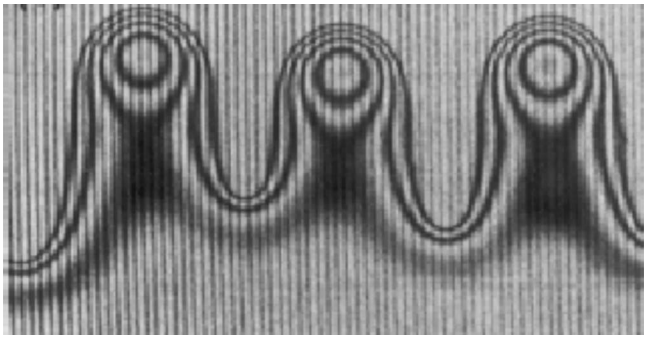

(b)

FIG. 4. Pattern formation in thermally driven thin climbing films. Top: An experimental image of the developing double shock structure showing a rising film driven by a thermal gradient. The leading "shock" is located at the leading contact line and, behind it, a Lax shock is developing. From Schneemilch and Cazabat, 2000a. Bottom: An image from the experiments using PDMS showing a fingering instability at the rising capillary ridge. The film is of the order of a micron thick and the rings represent interference patterns, utilized to give the film height; the peaks in thickness at the finger tips are also notable. From Cazabat *et al.*, 1992.

tern formation. Over the past decade, such flows have become of interest in connection with biomedical applications such as surfactant replacement therapy as a method of treatment for prematurely born neonates suffering from respiratory distress syndrome (Grotberg, 1994). Surfactant concentration gradients give rise to surface tension gradients and, in turn, to Marangoni stresses (Edwards *et al.*, 1991), which drive the formation of fingering structures. Examples of these patterns are shown in Fig. 6 depicting the phenomena that accompany the spreading of drops of surfactant solution ($C_{12}E_{10}$ in this case) of different concentrations emplaced on clean thin films. The characteristics of the fingering phenomena depend critically on the thickness of the film upon which the drop is deposited and on whether the concentration of the surfactant solution is above or below the critical micelle value. Recent modeling provides qualitative trends in line with the observed patterns and unmasks the mechanism for fingering (Edmonstone, Craster, and Matar, 2006); this is covered in Sec. VI.

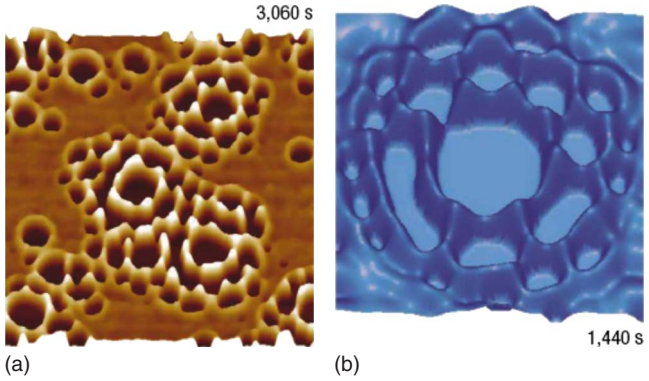

FIG. 5. (Color online) Dewetting of ultrathin films: AFM image of holes in a 4.9 nm polystyrene film (left) and the result of a numerical simulation of a dewetting film (right); the maximal height is 12 nm above the hole ground. From Becker *et al.*, 2003.

The depictions of the complex dynamics presented in Figs. 1–6 cover complex interfacial waves, patterning, dewetting, and fingering and give one a flavor of the range of possible behaviors. The presence of the deformable interface that bounds the film (and which, in cases involving multilayers, separates several layers of immiscible fluids) complicates the direct modeling of interfacial flows since the solution of the equations governing the flow must also include the precise location of the interface. Fortunately, as we shall see in the following section, it is possible to exploit disparities in the length scales arising naturally in thin film flows: the lat-

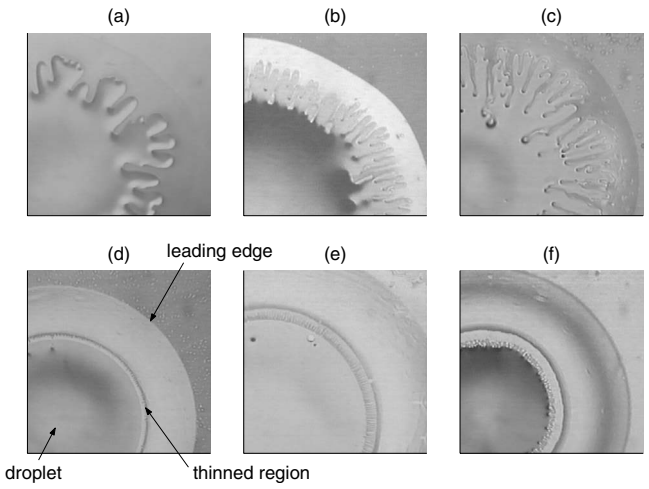

FIG. 6. Experimental photographs of surfactant-induced spreading using $C_{12}E_{10}$. The film thickness is held fixed at approximately 120 nm and the surfactant concentrations are 0.1, 0.25, 0.5, 1.5, 5, and 10 cmc in panels (a)–(f), respectively. Here cmc stands for the critical micelle concentration as discussed in Sec. VI.C. The thinned region, which straddles the surfactant leading edge and the droplet region is shown in (d). From Cachile, Schneemilch, *et al.*, 2002, and Hamraoui *et al.*, 2004.

eral length scales are much larger than the vertical ones giving rise to small aspect ratios that provide the small parameters for perturbation expansions. This, in turn, forms the basis of lubrication theory, which has been used extensively in the modeling of thin film flows. Lubrication-based theories involve the reduction in the Navier-Stokes equations through a rational asymptotic approach to more tractable yet highly nonlinear partial differential equations, still capable of capturing the dominant physics. Although a majority of work over the past decades has focused on the analysis of a single evolution equation, in recent years the field has moved toward the study of thin film flows governed by a system of coupled evolution equations for the film thickness and other scalar fields.

As mentioned above, we take our motivation from the examples shown in Figs. 1–6 and construct our review on the basis of the driving forces. In Sec. II, we provide a brief overview of the formulation of typical evolution equations and a discussion of scalings. In Sec. III, we turn to flows that are driven by body forces in the presence and absence of inertia. These involve both the dynamic wave motion of Figs. 1 and 2 and the patterning of Fig. 3. Body forces can be complemented, or replaced, by driving forces due to surface effects, be they at the fluid interface, surface tension, or at the substrate, and wettability effects, as reviewed in Secs. IV and V, respectively. Section VI covers surfactant-driven flows, while Sec. VII covers studies that have investigated the effect of the bounding walls' properties, such as topography, porosity, and flexibility, on thin film dynamics. Section VIII provides concluding remarks and a look at future work in thin film research.

The present work will not contain a review of moving contact lines; this topic and associated extensive body of literature will be the subject of another review by Bonn *et al.* (2009). Issues to do with the necessary relief of singularities at moving contact lines, such as the use of "slip" models (Münch and Wagner, 1999; Fetzer *et al.*, 2005; Blossey *et al.*, 2006) and precursor layers, for instance, will be discussed as they arise within the context of model formulation and instabilities in flows down inclined planes and in differentially heated films (Spaid and Homsy, 1996; Kondic and Diez, 2001). Dewetting of films is related to the presence of contact lines, however, the review in Sec. V will deal with situations in which the dynamics are driven by antagonistic forces so that dewetting fronts leave behind an ultrathin film rather than a bare substrate. Other topics that will not receive an in-depth review here are flows involving viscoelastic fluids (Spaid and Homsy, 1996; Herminghaus *et al.*, 1998; Zhang *et al.*, 2002, 2003a; Blossey *et al.*, 2006) viscoplastic media (Balmforth *et al.*, 2006), related thixotropic flows (Huynh *et al.*, 2005), and recent work on particle-laden thin films (Zhou *et al.*, 2005), films consisting of binary mixtures (Geoghegan and Krausch, 2003; Clarke, 2004, 2005) or thin films overlain by wrinkled skins (Huang and Suo, 2002b), complex materials such as liquid crystals (Ben Amar and Cummings, 2001; Schlagowski *et al.*, 2002; Cummings, 2004; Poulard and Cazabat, 2005; Carou *et al.*, 2006, 2007), and gels (Daniels *et al.*, 2005). We shall return to these topics when discussing future research directions in Sec. VIII.

II. FORMULATION

The dynamics of a flowing liquid film are potentially difficult to model. (Below we use the terms "liquid" and "fluid" interchangeably even though the review deals with liquids only and not gases.) In principle, one has to track the interfacial position while simultaneously solving the full governing fluid equations and any other relevant equations to do with, say, electrostatic forces, temperature, or chemical concentration. This is arduous with numerical schemes and unnecessary provided the flow falls into the class of problems treatable using thin film, lubrication-based models. The essential idea of these models is to "filter out" the explicit dependence on the depth coordinate and yet distill all essential physics into an evolution equation for the interfacial position coupled to temperature, chemical, or other fields. To illustrate the application of lubrication theory, we consider a canonical example: flow downslope.

Many of the most up-to-date models involve bilayer systems potentially coupled to evolving interfacial fields. With this in mind, we provide a concise description of the methodologies underlying the formulation for a system comprising two, superposed thin liquid layers. The relevant governing equations and boundary conditions presented below allow for the modeling of thin film dynamics taking into account a wide range of effects. This section provides, therefore, an exposition of the mathematical foundations underpinning the remainder of the review, which generalizes the analogous derivation by Oron *et al.* (1997).

We restrict ourselves to the derivation of relatively simple models in this section, which serve as illustrative examples. More complicated models, involving effects related to phase changes, electrostatic fields, and surfactant, for instance, are dealt with "locally" in each section where these effects appear, with appropriate cross referencing to the evolution equations derived in this section.

A. Governing equations

As shown in Fig. 7, the fluid bilayer is bounded from below by a solid substrate that may be potentially flexible, rough, and permeable and from above by a free surface; the mean position of this substrate is inclined at an angle θ to the horizontal. An essentially inviscid gas overlies the upper free surface of the bilayer. The fluids considered are incompressible but may be potentially non-Newtonian materials with a finite yield stress (although we make references below to "liquid-liquid" and "gas-liquid" interfaces and not consider non-Newtonian effects). The upper (lower) layer is characterized by a characteristic viscosity μ_1 (μ_2) and density ρ_1 (ρ_2), and the gas-liquid interface and liquid-liquid interface are endowed with interfacial tensions σ_1 and σ_2, respectively. We note that both σ_1 and σ_2 can depend on the

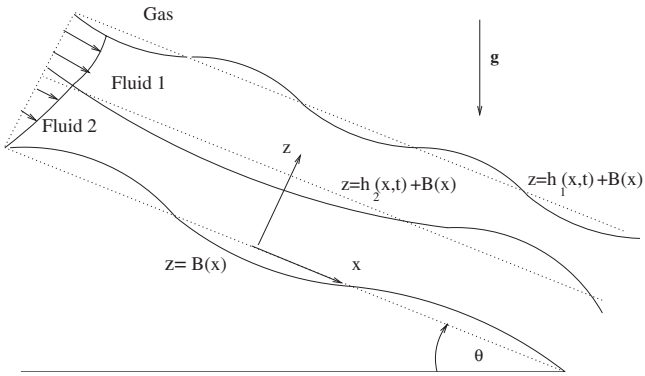

FIG. 7. A schematic of bilayer flow down an incline. The dotted lines represent the locations of the unperturbed interfaces.

interfacial concentration of surfactants, if present, and/or temperature through equations of state. As a result, the thin film dynamics will be coupled to a surfactant transport equation and/or an energy equation. The formulation discussed below will account for the presence of surfactant in preparation for the surfactant-induced effects that will be considered in detail in Sec. VI; thermal effects will be reviewed in Sec. IV.

The two-dimensional dynamics of the bilayer are modeled using a rectangular coordinate system (x,z), where x and z denote the downslope and normal coordinates, as shown in Fig. 7, respectively. The solid substrate is located at $z=B(x)$, the liquid-liquid interface is at $z=h_2(x,t)+B(x)$, and the gas-liquid interface is located at $z=h_1(x,t)+B(x)$, where $B(x)$ is a function describing the topography of the solid substrate. The undisturbed thickness of the lower layer is H_2.

The hydrodynamics of the bilayer are governed by the equations of momentum and mass conservation, which are expressed by

$$\rho_i(\mathbf{u}_{it}+\mathbf{u}_i\cdot\nabla\mathbf{u}_i)=-\rho_i\mathbf{g}-\nabla(p_i+\phi_i)+\nabla\cdot\mathbf{T}_i, \tag{1}$$

$$\nabla\cdot\mathbf{u}_i=0 \quad (i=1,2), \tag{2}$$

as shown in many texts on fluid mechanics (Batchelor, 1967; Bird *et al.*, 1987). There is no summation implied by the repeated indices either here, or later, in this paper. We assume the fluids to be incompressible as most thin film applications are in this limit. The 1 and 2 designate quantities associated with the upper and lower fluid layers, respectively. We will use 0 to designate a quantity associated with the overlying gas. The t subscript, and later, the x and z subscripts represent partial differentiation with respect to time and x and z, respectively, unless stated otherwise.

In these equations, ρ_i denote the (constant) densities of the two fluids and $\mathbf{g}$ is the gravitational acceleration vector; $\mathbf{u}_i=(u_i,0,w_i)$ $(i=1,2)$ are the two-dimensional velocity fields, wherein u_i and w_i denote their downslope and normal components, respectively; p_i represent the fluid pressures; ϕ_i are conjoining pressure functions, which take the form of energy per unit volume terms in the momentum conservation equations to account for the presence of intermolecular interactions between the various interfaces; and $\mathbf{T}_i$ is the stress tensor

$$\mathbf{T}_i=\boldsymbol{\tau}_i+\mathbf{M}_i,$$

where $\boldsymbol{\tau}_i$ is the deviatoric part of the total fluid stress tensor, which is related to the rate of strain tensor $\mathcal{E}_i=(\nabla\mathbf{u}_i+\nabla\mathbf{u}_i^T)/2$ through a constitutive relation, $\boldsymbol{\tau}_i=\boldsymbol{\tau}_i(\mathcal{E}_i)$. $\mathbf{M}_i$ are stress tensors related to an externally applied body force, which in the present review will be that due an electric field; hence the $\mathbf{M}_i$ are defined in Sec. III.C as Maxwell stress tensors (Saville, 1997).

Solutions of Eqs. (1) and (2) must be obtained subject to the following boundary conditions. At the lower boundary, $z=B(x)$, we have the following conditions for the case of a rigid, yet potentially permeable, solid support:

$$\mathbf{u}_2\cdot\mathbf{t}_w-b\mathbf{n}_w\cdot\nabla\mathbf{u}_2=0, \quad \mathbf{u}_2\cdot\mathbf{n}_w=W, \tag{3}$$

where $\mathbf{n}_w$ and $\mathbf{t}_w$ denote the outward pointing normal and tangential vectors orientated relative to the solid substrate. Here the first condition represents a Navier slip model (Dussan V and Davis, 1974; Greenspan, 1978), which accounts for the possibility of slip along the substrate wherein b is the slip coefficient. In the current context, the use of slip models or, alternatively, postulating the existence of a so-called "precursor" layer (de Gennes, 1985) (due, for instance, to vapor condensation or the action of intermolecular forces) is a device to relieve the singularity that arises at a moving contact line. These issues will receive limited attention in the review (see, for instance, Sec. V.E) since an up-to-date and comprehensive discussion has been provided by Bonn *et al.* (2009). W is the average speed in the normal direction to the substrate of the flow in the potentially permeable solid beneath $z=B(x)$. Note that the no-slip and no-penetration conditions, $u_2=w_2=0$, for a smooth flat impermeable substrate are recovered by setting $b=W=0$ and $B(x)=0$.

At each interface, $z=h_i(x,t)+B(x)$, we have the kinematic condition

$$\frac{D}{Dt}[z-(h_i+B)]=0, \tag{4}$$

where D/Dt represents a material derivative. The following stress conditions are taken at interface i:

$$j_{ie}[\mathbf{u}_e]_i+([p]_i\mathbf{I}-[\mathbf{T}]_i)\cdot\mathbf{n}_i=\kappa_i\sigma_i\mathbf{n}_i-\nabla_s\sigma_i, \quad i=1,2. \tag{5}$$

These equations describe the traction at each interface and by taking the dot product with the normal or tangential direction gives the normal and shear stress balances, respectively, at each interface. Interfacial quantities with subscript 1 (2) are taken to be at the gas-liquid (liquid-liquid) interfaces. The notation $[\ ]_i$ corresponds to a jump in a quantity across interface i (e.g., $[\mathbf{q}]_2=\mathbf{q}_2-\mathbf{q}_1$, where $\mathbf{q}$ is an arbitrary vector quantity). In Eq. (5), j_{ie} is the mass flux normal to the interface and for evaporation or condensation we would also require coupling to an energy equation [see Eq. (C2) of Appendix C (Burelbach *et al.*, 1988)]. The terms involving the surface

tension σ_i are readily interpreted. The first term on the left-hand side of Eq. (5) $\kappa_i\sigma_i\mathbf{n}_i$ is the surface tension force acting in the normal direction due to the curvature κ_i. The surface tension along the interface can, of course, be variable, and the surface stress generated by such variations appears within the equation as $\nabla_s\sigma_i$. The surface gradient operator is $\nabla_s=(\mathbf{I}-\mathbf{n}_i\mathbf{n}_i)\cdot\nabla$ in which $\mathbf{I}$ is the identity tensor, and this operator denotes differentiation along the interface. The term $[\mathbf{u}_e]_1=(\mathbf{u}_1-\mathbf{u}_{s1})-(\mathbf{u}_0-\mathbf{u}_{s1})$ represents differences between the relative velocities at the gas-liquid interface and $[\mathbf{u}_e]_2=(\mathbf{u}_2-\mathbf{u}_{s2})-(\mathbf{u}_1-\mathbf{u}_{s2})$ is the analogous term for the liquid-liquid interface; here $\mathbf{u}_{s1}$ and $\mathbf{u}_{s2}$ denote the velocities of the gas-liquid and liquid-liquid interfaces, respectively. Thus the velocities are not, in general, continuous across the interface due, for instance, to evaporation or condensation, which will be considered in Sec. IV.A. The outward pointing unit normal and the tangent are given by $\mathbf{n}_i=(-[h_i+B]_x,1)/(1+[h_i+B]_x^2)^{1/2}$ and $\mathbf{t}_i=(1,[h_i+B]_x)/(1+[h_i+B]_x^2)^{1/2}$, respectively, and the total curvature is expressed by $\kappa_i=-\nabla_s\cdot\mathbf{n}_i$.

As mentioned above, the surface and interfacial tensions of liquids depend on temperature, and this is important in Sec. IV and/or the concentration of surfactant at the interface. In this section, we consider the interfacial concentrations of surface active species at the relevant interface Γ_i $(i=1,2)$, which satisfy the following transport equations:

$$\Gamma_{it}+\nabla_s\cdot(\mathbf{u}_{is}\Gamma_i)+(\mathbf{u}_i\cdot\mathbf{n}_i)\Gamma_i(\nabla_s\cdot\mathbf{n}_i)=\mathcal{D}_i\nabla_s^2\Gamma_i+J_i, \quad (6)$$

with $i=1,2$. Here $\mathbf{u}_{is}=(\mathbf{I}-\mathbf{n}_i\mathbf{n}_i)\cdot\mathbf{u}_i$ is the velocity along interface i, $\mathcal{D}_i$ denotes the surface diffusion coefficients, and J_i are "sorptive" fluxes, which describe adsorption and desorption at or from the interface i. A derivation of this equation has been provided by Stone (1990) and some recent clarification of this derivation was provided by Wong *et al.* (1996), Cermelli *et al.* (2005), and Pereira *et al.* (2007). In particular, the time derivative in Eq. (6) should be interpreted as that which follows the interface in a direction normal to it. Equation (6) is a classical advection-diffusion equation in which the third term on its left-hand side $(\mathbf{u}_{is}\cdot\mathbf{n}_i)\Gamma_i(\nabla_s\cdot\mathbf{n}_i)$ accounts for transport associated with the stretching of the interface. As shown below, in the case of thin films, this term does not enter the problem at leading order. A cursory impression is that Eq. (6) is passively enslaved to the hydrodynamics. However, the surfactant concentration Γ_i is not decoupled from the flow field and its influence is felt through the surface tension σ_i, which is a function of Γ_i, and thus affects the interfacial shear of the fluid layer through the surface tension gradient term $\nabla_s\sigma_i$ in Eq. (5).

Several equations of state $\sigma_i(\Gamma_i)$ are used in the literature: the nonlinear equation of state by Sheludko (1967) or those of Frumkin and Langmuir, as detailed by Edwards *et al.* (1991). In practice, many modeling studies, for simplicity, adopt a dilute assumption with the surface tension being linearly dependent on surfactant concentration (Jensen and Grotberg, 1992; Warner *et al.*, 2004a).

B. Scaling

To progress it is essential to condense the equations by identifying nondimensional groupings. It is also essential to quantify the long-thin nature of the flow. Often in experiments, for instance, those of Fig. 6, natural length scales will present themselves: the droplet being of the order of millimeters across and the film being micrometers thick. These then give a characteristic length scale $\mathcal{L}$ along the film which is much greater than the characteristic thickness $\mathcal{H}$. The absolute scale of the flow itself is immaterial: instead of the spreading surfactant droplet we could have chosen the example of the spreading lava dome at Mt. St. Helens which ca. 1980 had a length of the order of 300 m and a height of 30 m. Although not so disparate as the surfactant droplet, the discrepancy of scales still allows one to introduce a small parameter ϵ as the aspect ratio $\epsilon\equiv\mathcal{H}/\mathcal{L}$. Since this is small we can use this knowledge to identify those terms that vary slowly across and along the fluid layer and thus can be discarded. This then gives a quantifiable and legitimate way of reducing the equations to a simpler form; it also then becomes clear when the theory will breakdown.

If no obvious length scales appear in the problem (e.g., in a case in which the dynamics of an initially uniform film are considered) then one can use the wavelength of typical interfacial disturbances to define $\mathcal{L}$. The lubrication-based theories wherein the wavelength is large relative to the thickness lead to the generation of so-called "long-wave" models; it is useful to remember that this is the origin of that phrase and that the predictions of these models should be treated with caution for short waves.

We render x and z, h dimensionless using the characteristic length scale $\mathcal{L}$ and height scale $\mathcal{H}=H_2$, respectively,

$$x=\mathcal{L}\tilde{x}, \quad (z,h_i)=\mathcal{H}(\tilde{z},\tilde{h}_i), \quad (7)$$

where the tilde denotes dimensionless quantities. These scales are used, together with a typical velocity scale $\mathcal{U}$, which emerges from the analysis and depends on the nature of the flow. We will demonstrate how this is done in Sec. II.C.2; for now it remains undetermined,

$$u_i=\mathcal{U}\tilde{U}_i, \quad (w_i,W_i)=\epsilon\mathcal{U}(\tilde{w}_i,\tilde{W}_i). \quad (8)$$

This follows from balancing terms in the mass conservation equations $u_{ix}+w_{iz}=0$ $(i=1,2)$. From the velocity scale, a typical time scale also emerges: $t=(\mathcal{L}/\mathcal{U})\tilde{t}$.

The pressure and stresses must also be nondimensionalized and we scale the pressure on P,

$$(p_i,\phi_i)=P(\tilde{p}_i,\tilde{\phi}_i), \quad (9)$$

where P may reflect a balance between the pressure gradient and viscous shear $P=\mu_2\mathcal{U}\mathcal{L}/\mathcal{H}^2$, which is appropriate in situations wherein inertia is negligible. For flows involving significant inertial contributions, the scale $P=\rho_2\mathcal{U}^2$ is more relevant, as discussed in Sec. II.D. In Eqs. (13) and (14), we therefore leave the pressure scaling as

P temporarily. The dimensionless stresses are given by

$$(\boldsymbol{\tau}_i, \mathbf{M}_i) = (\mu_2 \mathcal{U}/\mathcal{H})(\tilde{\boldsymbol{\tau}}_i, \tilde{M}_i).$$

Similarly one must nondimensionalize any auxiliary or interfacial equations. In order to nondimensionalize the surfactant transport equation, given in Eq. (6), the natural characteristic quantity is the concentration Γ_m, which represents the interfacial concentration of surface active species at saturation, for which the interfacial tensions attain their (constant) minimal values σ_{im} $(i=1,2)$; the spreading coefficients $S_i \equiv \sigma_{i0} - \sigma_{im}$ denote the difference between the maximal and minimal values of the interfacial tensions σ_{i0}, and σ_{im}. Thus the surface tensions and concentrations are scaled on these characteristic spreading pressures S_i and concentrations, Γ_m, respectively,

$$\sigma_i = \sigma_{im} + S_i \tilde{\sigma}_i, \quad \Gamma_i = \Gamma_m \tilde{\Gamma}_i, \tag{10}$$

$\tilde{\sigma}_i \equiv \tilde{\sigma}_i(\tilde{\Gamma}_i)$. There are also the mass and surfactant fluxes for which the natural scalings are

$$j_{ie} = (\mu_2/\mathcal{H})\tilde{j}_i, \quad J_i = (\Gamma_m \mathcal{U}/\mathcal{L})\tilde{J}_i. \tag{11}$$

In cases where evaporation or condensation effects are important, discussed in Sec. IV and Appendixes B and C, the mass flux will feature quite prominently. One then nondimensionalizes j_{ie} using thermal properties, defined in Appendix C: μ_2 in Eq. (11) is replaced by $\lambda_{\text{th}}\Delta T/\text{La}$; here λ_{th}, ΔT, and La denote the film thermal conductivity, an appropriate temperature difference, and the latent heat of vaporization, respectively.

These scalings and nondimensionalizations must then be substituted into the mass and momentum conservation equations to yield the following dimensionless equations (after suppressing the tilde of the flow variables which can now be discarded):

$$u_{ix} + w_{iz} = 0, \tag{12}$$

$$\epsilon \frac{\rho_i}{\rho_2} \text{Re}(u_{it} + u_i u_{ix} + w_i u_{iz}) = \frac{\rho_i}{\rho_2}\mathcal{G} - \left(\frac{P\mathcal{H}^2}{\mathcal{L}\mu_2\mathcal{U}}\right)(p_i + \phi_i)_x + \epsilon\tau_{ixx,x} + \tau_{izx,z}, \tag{13}$$

$$\epsilon^3 \frac{\rho_i}{\rho_2} \text{Re}(w_{it} + u_i w_{ix} + w_i w_{iz}) = -\epsilon\frac{\rho_i}{\rho_2}\mathcal{G}\cot(\theta) - \left(\frac{P\mathcal{H}^2}{\mathcal{L}\mu_2\mathcal{U}}\right)(p_i + \phi_i)_z + \epsilon^2\tau_{ixz,x} + \epsilon\tau_{izz,z}, \tag{14}$$

with $i=1,2$. Here τ_{ixx}, τ_{ixz}, τ_{izx}, and τ_{izz} denote the components of the tensors $\boldsymbol{\tau}_i$ $(i=1,2)$. Two fundamental nondimensional groupings emerge: $\text{Re} \equiv \rho_2 \mathcal{U}\mathcal{H}/\mu_2$ is the Reynolds number and $\mathcal{G} \equiv \rho_2 g \mathcal{H}^2 \sin(\theta)/\mu_2\mathcal{U}$ is a dimensionless parameter which reflects the relative significance of gravitational to viscous forces (its product with the Reynolds number produces a "Galileo" number). Note that we have implicitly made all assumptions associated with the "leaky dielectric" model (Saville, 1997) and assumed further that the dielectric constants in both fluids are constant. As a result of these assumptions, the electric field effects enter the problem in the interfacial conditions; this is discussed again in Sec. III.C. As a result, the components of the tensors $\mathbf{M}_i$ do not appear in Eqs. (13) and (14).

The dimensionless boundary conditions at $z = \mathcal{B}(x) \equiv B(x)/\mathcal{H}$ [Eq. (3)], to leading order in ϵ, are

$$u_2 - \beta u_{2z} = 0, \quad w_2 = W, \tag{15}$$

where $\beta \equiv b/\mathcal{H}$. The dimensionless kinematic boundary condition at each interface $z = h_i(x,t) + \mathcal{B}(x)$, from Eq. (4), is given by

$$h_{it} + u_{is}(h_i + \mathcal{B})_x = w_{is}, \tag{16}$$

where (u_{is}, w_{is}) is the interfacial velocity at interface i. The advent of mass loss from an interface due to, say, evaporation, as in Appendix C [see Eq. (C9)], results in an additional term in the kinematic condition involving the mass flux j_{ie}.

The dimensionless tangential and normal components of the stress condition at the interfaces are found by taking the dot product of Eq. (5) with $\mathbf{t}_i$ and $\mathbf{n}_i$, respectively; the exact expressions are rather cumbersome and have therefore been relegated to Appendix B. In Eqs. (B1) and (B2), two nondimensional groups appear: a Marangoni number $\mathcal{M}_i \equiv S_i\mathcal{H}/\mu_2\mathcal{U}\mathcal{L}$, representing the relative magnitude of surface-tension-gradient-driven Marangoni stresses to viscous drag, and an inverse capillary number $\mathcal{C}_i \equiv \mu_2\mathcal{U}/\sigma_{im}$, representing a dimensionless measure of viscous to capillary forces. Note that in the absence of surface tension gradients (for, say, zero thermal and/or surfactant concentration gradients), $\sigma_{i0} = \sigma_{im} = \sigma_i$, then $S_i = \mathcal{M}_i = 0$ and no Marangoni stresses are present. In this limiting case, $\mathcal{C}_i \equiv \mu_2\mathcal{U}/\sigma_{i0}$.

The dimensionless transport equations for the surfactant interfacial concentrations Γ_i $(i=1,2)$, when nondimensionalized also yield a dimensionless group, $\text{Pe}_i \equiv \mathcal{U}\mathcal{L}/\mathcal{D}_i$, which denotes a Péclet number that reflects the relative significance of convective to diffusive transport. These equations are lengthy and have also been relegated to Appendix B. Next, we show how the small value of ϵ can be exploited in order to derive models for the interfacial dynamics using appropriate perturbation theory.

C. Negligible inertia: Lubrication theory

Here we focus on situations wherein inertia does not play a crucial role. The key parameter $\epsilon \equiv \mathcal{H}/\mathcal{L}$, the film aspect ratio, is often referred to as the "lubrication parameter" and is taken asymptotically small so as to form the basis of perturbation expansions. We employ this lubrication theory to derive the reduced set of equations encapsulating the dominant physics. We take advantage of the small parameter $\epsilon \ll 1$ and expand the variables in powers of ϵ as follows,

$$u_i = u_{i0} + \epsilon u_{i1} + \cdots \quad (i=1,2), \tag{17}$$

and similarly for w_i, p_i, ϕ_i, $\boldsymbol{\tau}_i$, etc. It is therefore implicit in the lubrication approximation that topographic variations and free surface slopes are of order ϵ, although this can be relaxed and we return to this in Sec. VII.A. It is worth noting that in several places within this review, notably in Fig. 3, one sees dramatic and sharp changes in the free surface profile or in the base when discussing topographic changes with sharp steps as in Sec. VII. Several computations using lubrication theory also show sharp height changes such as the shock formation in Sec. VI. These features may appear to violate the small-slope assumption implicit in lubrication theory but this may not be the case when the solutions are viewed in dimensional coordinates. Additionally, comparisons between the predictions of the lubrication equations and those of the Stokes flow equations and experimental data (Mazouchi and Homsy, 2001; Gaskell *et al.*, 2004) show that lubrication theory is in error by 15% in the most extreme case when the fluid film is as thick as the sharp step topography over which the fluid is moving.

Assuming that the Reynolds number Re is $O(1)$, at most, then the inertial terms enter the problem at $O(\epsilon)$ and so can be discarded. However, in Secs. III.A.2 and III.B, we consider thin films falling under gravity and flowing over spinning disks in which inertia becomes important. In those cases, a combination of boundary-layer theory and integral methods are used to derive evolution equations to describe the flow. We outline that approach in Sec. II.D.

To leading order in ϵ, the governing equations are expressed by (following the suppression of the 0 subscripts)

$$u_{ix} + w_{iz} = 0, \quad i=1,2, \tag{18}$$

$$\frac{\rho_i}{\rho_2}\mathcal{G} - (p_i + \phi_i)_x + \tau_{izx,z} = 0,$$

$$\epsilon\frac{\rho_i}{\rho_2}\mathcal{G}\cot(\theta) + (p_i + \phi_i)_z = 0. \tag{19}$$

A number of research articles begin from this point or even with these equations in dimensional form, presupposing that the reader is aware of the assumptions and balances that lead to them. The dimensionless stress boundary conditions at $z=h_i(x,t)+\mathcal{B}(x)$ [Eqs. (B1) and (B2)] simplify as a result of the perturbation expansion and, at leading order, are given by

$$j_{ie}[u_e]_i - [\tau_{xz}]_i - [M_{xz}]_i = -\mathcal{M}_i(\sigma_{ix} + [h_i + \mathcal{B}]_x\sigma_{iz}). \tag{20}$$

It is important to emphasize that σ_{iz} is evaluated at the interfaces and so, as it appears later, it will not reintroduce explicit z dependence into the evolution equations. Also the normal stress jump across the interfaces is given by

$$[p]_i = -\left(\epsilon^2\mathcal{M}_i\sigma_i + \frac{\epsilon^3}{\mathcal{C}_i}\right)(h_i + \mathcal{B})_{xx} - \epsilon^2 j_{ie}([w]_i - (h_i + \mathcal{B})_x[u]_i), \quad i=1,2. \tag{21}$$

It might appear completely inconsistent to retain terms premultiplied by $\epsilon\mathcal{G}\cot(\theta), \epsilon^2\mathcal{M}_i, \epsilon^3/\mathcal{C}_i$ in equations claimed to be valid at $O(1)$. The $\epsilon^2 j_{ie}$ term in Eq. (21) also looks incongruous but needs to be retained as evaporative terms enter through this term. Similarly, the magnitude of $\mathcal{G}$, $\mathcal{M}$, and $\mathcal{C}$ may be such that these factors are $O(1)$ and it is therefore important to retain associated terms at this stage; depending on the nature of the flow, the appropriate decision can then be made as to whether or not to discard these terms.

The surfactant transport equation [Eq. (B3)] also simplifies and at leading order is given by

$$\Gamma_{it} + (u_{is}\Gamma_i)_x = \frac{1}{\mathrm{Pe}_i}\Gamma_{ixx} + J_i, \quad i=1,2. \tag{22}$$

The conditions at $z=\mathcal{B}(x)$ and the kinematic boundary conditions at $z=h_i+\mathcal{B}(x)$ remain unchanged from Eqs. (15) and (16). Next, we generate the evolution equations for the case of a bilayer. We then demonstrate how a variety of evolution equations used in the literature to model thin film flow can be obtained from the bilayer equations as limiting cases.

1. Two-layer systems

We assume the bilayer to be Newtonian, and we restrict the derivation to cases wherein electrostatic and phase change effects are absent $\mathbf{M}_i = j_{ie} = 0$, and to impermeable substrates $W=0$. Several derivations of the bilayer evolution equations are in the literature, the most relevant being that of Danov, Paunov, Alleburn, *et al.* (1998) who treated a bilayer evaporative system and those by Bandyopadhyay *et al.* (2005), Fisher and Golovin (2005), and Pototsky *et al.* (2005) who included effects of long- and short-range intermolecular forces.

The Newtonian constitutive relation leads to

$$\boldsymbol{\tau}_i = m_i\begin{pmatrix} 2\epsilon u_{ix} & u_{iz} + \epsilon^2 w_{ix} \\ u_{iz} + \epsilon^2 w_{ix} & 2\epsilon w_{iz} \end{pmatrix},$$

and so to leading order

$$\tau_{ixz} = \tau_{izx} = m_i u_{iz} + O(\epsilon^2), \quad i=1,2, \tag{23}$$

where $(m_1, m_2) \equiv (\mu_1/\mu_2, 1)$.

Integration of the second equation in Eq. (19) and application of the normal stress boundary conditions at $z=h_i+\mathcal{B}$ $(i=1,2)$ yield the following expression for the pressure in fluid 1:

$$p_1 + \phi_1 = \epsilon\frac{\rho_1}{\rho_2}\mathcal{G}\cot(\theta)(h_1 + \mathcal{B} - z) - \left(\epsilon^2\mathcal{M}_1\sigma_1 + \frac{\epsilon^3}{\mathcal{C}_1}\right) \times (h_1 + \mathcal{B})_{xx} + \phi_1|_{z=h_1+\mathcal{B}}, \tag{24}$$

together with a similar expression for p_2,

$$p_2+\phi_2=\epsilon\mathcal{G}\cot(\theta)(h_2+\mathcal{B}-z)+\epsilon\frac{\rho_1}{\rho_2}\mathcal{G}\cot(\theta)(h_1-h_2)-\left(\epsilon^2\mathcal{M}_1\sigma_1+\frac{\epsilon^3}{\mathcal{C}_1}\right)(h_1+\mathcal{B})_{xx}-\left(\epsilon^2\mathcal{M}_2\sigma_2+\frac{\epsilon^3}{\mathcal{C}_2}\right)(h_2+\mathcal{B})_{xx}+\phi_2|_{z=h_2+\mathcal{B}}. \tag{25}$$

The fluid pressure comprises hydrostatic terms, which are proportional to $\mathcal{G}$ and capillary terms arising from interfacial curvature proportional to $(h_i+\mathcal{B})_{xx}$. The pressure in the gas has been set to zero without loss of generality.

The downslope components of the velocity field in fluids 1 and 2, u_1 and u_2, are obtained via integration of the first equation in Eq. (19). Here the Newtonian constitutive relation and the tangential stress conditions at $z=h_i+\mathcal{B}$ are required as are the conditions at $z=\mathcal{B}$, given by Eqs. (23), (20), and (15). The expressions for u_1 and u_2 thus obtained are lengthy and can be found in Appendix B. Finally, integration of the continuity equations $u_{ix}+w_{iz}=0$ for fluids 1 and 2 between $h_2+\mathcal{B}$ and $h_1+\mathcal{B}$ and $\mathcal{B}$ and $h_2+\mathcal{B}$, respectively, and application of continuity of velocity and the kinematic boundary conditions [Eqs. (16)] at $z=h_i+\mathcal{B}$ yield the bilayer evolution equations,

$$h_{1t}+Q_{1x}+Q_{2x}=0,\quad h_{2t}+Q_{2x}=0. \tag{26}$$

Here Q_1 and Q_2 represent the volumetric flow rates per unit width in fluids 1 and 2, respectively,

$$\frac{Q_1}{h_1-h_2}=\left[(\beta+h_2)(h_1-h_2)+\frac{(h_1-h_2)^2}{3m_1}\right]\times([p_1+\phi_1]_x-n_1\mathcal{G})-\tfrac{1}{2}h_2(2\beta+h_2)\times([p_2+\phi_2]_x-\mathcal{G})+\frac{1}{2m_1}(2m_1(h_2+\beta)+h_1-h_2)\mathcal{M}_1(\sigma_{1x}+[h_1+\mathcal{B}]_x\sigma_{1z})+(\beta+h_2)\mathcal{M}_2(\sigma_{2x}+[h_2+\mathcal{B}]_x\sigma_{2z}), \tag{27}$$

$$Q_2=\int_{\mathcal{B}}^{h_2+\mathcal{B}}u_2dz=-\tfrac{1}{3}h_2^2(3\beta+h_2)([p_2+\phi_2]_x-\mathcal{G})+\tfrac{1}{2}h_2(2\beta+h_2)\times\left[\mathcal{M}_1(\sigma_{1x}+[h_1+\mathcal{B}]_x\sigma_{1z})+\mathcal{M}_2(\sigma_{2x}+[h_2+\mathcal{B}]_x\sigma_{2z})-(h_1-h_2)\times\left([p_1+\phi_1]_x-\frac{\rho_1}{\rho_2}\mathcal{G}\right)\right]. \tag{28}$$

Evaluation of u_1 and u_2, given by Eqs. (B4) and (B5), at the relevant interfaces yields u_{1s} and u_{2s}, which, upon substitution into Eq. (22), yields evolution equations for Γ_i that are fully coupled to Eq. (26). In Eqs. (27) and (28), the functions $\phi_{1,2}$ are $\phi_1(h_1,h_2)$ and $\phi_2(h_1,h_2)$ and represent conjoining pressures at the gas-liquid and liquid-liquid interfaces, respectively, and will be discussed in detail in Sec. V.

The relevant physics contained in the full Navier-Stokes equations and interfacial and wall boundary conditions, for thin fluid films, are now contained in Eqs. (26)–(28), which are highly nonlinear, fourth-order, coupled partial differential equations for h_1 and h_2. Solution of these equations yields the leading order dynamics and accounts for gravity, capillarity, Marangoni stresses (due to solutal capillarity and thermocapillarity), intermolecular forces, viscosity and density stratification, wall topography, and slip.

2. Single-layer systems

A number of evolution equations in the literature can now be obtained from Eq. (26). By taking appropriate limits, we show how this can be done resulting in equations that describe the dynamics of single thin films in a variety of different settings. We also discuss how the velocity scale $\mathcal{U}$ is deduced using dominant balances between the relevant forces.

In order to obtain an evolution equation for a single thin film, one takes the limit $h_2\to h_1$ and all subscripted fluid 1 parameters and variables are set to zero, i.e., $Q_1\to 0$. By dropping the subscript on all remaining parameters and variables so that $h_2\equiv h, \mu_2\equiv\mu$, etc., the following equation for h is obtained:

$$h_t+\left[\frac{h}{6}(3\mathcal{M}(2\beta+h)(\sigma_x+[h+\mathcal{B}]_x\sigma_z)-2h(3\beta+h)([p+\phi]_x-\mathcal{G}))\right]_x=0. \tag{29}$$

The bracketed term encapsulates the relevant physics: the Marangoni stresses are all encompassed in the term multiplied by $\mathcal{M}$, with surface tension gradients driving changes in h; the final term involving $\mathcal{G}$ gives the gravitational driving term while the pressure p is given by

$$p=\epsilon\mathcal{G}\cot(\theta)(h+\mathcal{B}-z)-\left(\epsilon^2\mathcal{M}\sigma+\frac{\epsilon^3}{\mathcal{C}}\right)(h+\mathcal{B})_{xx}. \tag{30}$$

The terms on the right-hand side of Eq. (30) represent hydrostatic pressure, linear in z, and the restoring capillary force due to surface curvature. The conjoining pressure term ϕ in Eq. (29) due to intermolecular forces will be described further in Sec. V.

Notably, the capillary terms involve high derivatives in h and this complicates analysis and the numerical solution of Eq. (29) which, although markedly simpler than the full Navier-Stokes equations, is a highly nonlinear partial differential equation containing fourth-order derivatives of h. It is also worth noting that evolution equations such as Eq. (29) can be recast in an energy formulation (Mitlin, 1993) with

$$h_t = \left[h^3 \frac{\partial}{\partial x} \frac{\delta F}{\delta h} \right]_x,$$

where F is the free energy of the film, given as an integral over x, and the term $\delta F/\delta h$ being its functional derivative. This representation is extensively used by Pototsky *et al.* (2005) for two-layer systems.

Once the one-dimensional equations have been deduced, it is straightforward to repeat the analysis with the transverse (cross-slope) direction y added in; alternatively, one can recognize that all partial derivatives with respect to x are replaced by $\nabla = (\partial_x, \partial_y)$ unless a term is being driven by gravity, say, purely in the x direction and $\mathcal{B}(x) \to \mathcal{B}(x,y)$, etc. In either case, Eq. (29) can be recast in the following form:

$$h_t + \frac{\mathcal{G}}{3}[h^2(3\beta + h)]_x + \nabla \cdot \left[\frac{h}{6}(3\mathcal{M}(2\beta + h)[\nabla\sigma + \sigma_z \nabla (h + \mathcal{B})] - 2h(3\beta + h) \nabla (p + \phi)) \right] = 0, \tag{31}$$

in which p is given by

$$p = \epsilon\mathcal{G} \cot(\theta)(h + \mathcal{B} - z) - \left(\epsilon^2 \mathcal{M}\sigma + \frac{\epsilon^3}{\mathcal{C}} \right) \nabla^2 (h + \mathcal{B}). \tag{32}$$

Equations (31) and (32) represent the starting point for many analyses involving a single Newtonian fluid layer in the literature and includes the effects of gravity, capillarity, solutal capillarity and thermocapillarity, short- and long-range intermolecular forces, slip, and substrate topography.

At this point, we note that the velocity scale is determined by the dominant balance that exists between the driving and retarding forces, which depends on the situation at hand. There are three cases that are particularly pertinent for this review: gravitationally-, surface-tension-gradient-, and capillary-dominated flows, each with their own characteristic velocity scale.

Gravitationally-dominated flows. Here $\mathcal{G}$ in Eq. (31) is set to unity, which yields the velocity scale $\mathcal{U} = \mathcal{U}_g \equiv \rho g \mathcal{H}^2 \sin(\theta)/\mu$, reflecting a dominant physical balance between gravity and viscous drag; as a result, Eq. (31) becomes

$$h_t + \frac{1}{3}[h^2(3\beta + h)]_x - \nabla \cdot \left[\frac{h^2}{3}(3\beta + h) \nabla (p + \phi) \right] = 0, \tag{33}$$

with $p = \epsilon \cot(\theta)(h + \mathcal{B} - z) - (\epsilon^3/\mathcal{C}_g)\nabla^2(h + \mathcal{B})$ (ignoring Marangoni forces so that $\mathcal{M} = 0$ and $\sigma = \sigma_0$) and $\mathcal{C}_g \equiv \rho g \mathcal{H}^2 \sin(\theta)/\sigma_0$, which is a Bond number reflecting the relative significance of gravitational to surface tension forces. This set of scalings is most relevant to Secs. III.A and VII.

Surface-tension-gradient-dominated flows. Marangoni effects dominate and so $\mathcal{M}$ is set to unity giving $\mathcal{U} = \mathcal{U}_m \equiv S\mathcal{H}/\mu\mathcal{L}$, reflecting a physical balance between Marangoni stresses and viscous drag; here $S = \sigma_0 - \sigma_m$, the maximal difference in surface tension that exists in the problem. The velocity scaling is most relevant to the flows discussed in Secs. IV and VI. Equation (31) now becomes

$$h_t + \frac{\mathcal{G}_m}{3}[h^2(3\beta + h)]_x + \nabla \cdot \left[\frac{h}{6}(3(2\beta + h)[\nabla\sigma + \sigma_z \nabla (h + \mathcal{B})] - 2h(3\beta + h) \nabla (p + \phi)) \right] = 0, \tag{34}$$

in which $p = \epsilon\mathcal{G}_m \cot(\theta)(h + \mathcal{B} - z) - \epsilon^2(\sigma + \sigma_m/S)\nabla^2(h + \mathcal{B})$, where $\mathcal{G}_m \equiv \rho g \mathcal{H}\mathcal{L} \sin(\theta)/S$. In Secs. IV and VI and Appendix C, we will use $\mathcal{C}_m$ where $\epsilon^3/\mathcal{C}_m = \epsilon^2\sigma_m/S$. Note that the effects of surface tension variations on capillarity, the final term in p, are often neglected but those of mean surface tension are kept (as $\sigma_m/\mathcal{S} \gg |\sigma|$ in practice), so that $p = \epsilon\mathcal{G}_m \cot(\theta)(h + \mathcal{B} - z) - \epsilon^2(\sigma_m/S)\nabla^2(h + \mathcal{B})$ (Jensen and Grotberg, 1992).

The surface tension σ depends on temperature and/or the concentration of surface active species present in the film through equations of state. In the former case, an additional energy transport equation must be solved subject to appropriate boundary conditions; this will be considered in Sec. IV. In the latter case, Eq. (34) is coupled to an evolution equation for the surfactant interfacial concentration. The surface velocity $u_s = u(z = h)$ is required,

$$u_s = (h - \mathcal{B} + \beta)\sigma_x + \tfrac{1}{2}(\mathcal{B}^2 - h(2\beta + h))([p + \phi]_x - \mathcal{G}_m). \tag{35}$$

Using this, and generalizing to two dimensions, yields the following transport equation for Γ:

$$\Gamma_t + \nabla \cdot \left[\Gamma \left((h - \mathcal{B} + \beta) \nabla \sigma + \frac{1}{2}(\mathcal{B}^2 - h(2\beta + h)) \nabla (p + \phi) \right) \right] - \frac{\mathcal{G}_m}{2}[\Gamma(\mathcal{B}^2 - h(2\beta + h))]_x = \frac{1}{\mathrm{Pe}} \nabla^2 \Gamma + J. \tag{36}$$

For weak surfactant solubility J, which is a flux of surfactant to the interface from the fluid layer, is zero. The case of soluble surfactants will be considered in Sec. VI.

Capillary-dominated flows. In the absence of surface tension gradients, the Marangoni number is zero $\mathcal{M} = 0$, and $\mathcal{U}$ is obtained by setting $\epsilon^3/\mathcal{C} = \epsilon^3\sigma/\mu\mathcal{U}$ to unity: $\mathcal{U} = \mathcal{U}_c \equiv \sigma\mathcal{H}^3/\mu\mathcal{L}^3$, reflecting the dominant physical balance between capillary and viscous forces, relevant to small-scale flows such as those in Sec. V. Here σ and μ denote the constant gas-liquid surface tension and the viscosity of the liquid. Now, Eq. (31) becomes

$$h_t + \frac{\mathcal{G}_c}{3}[h^2(3\beta + h)]_x - \nabla \cdot \left[\frac{h^2}{3}(3\beta + h) \nabla (p + \phi) \right] = 0, \tag{37}$$

with $p = \epsilon\mathcal{G}_c \cot(\theta)(h + \mathcal{B} - z) - \nabla^2(h + \mathcal{B})$ in which $\mathcal{G}_c \equiv \rho g \mathcal{H}^2 \sin(\theta)/\epsilon^3\sigma$ corresponds to a modified Bond number, equal to $\mathcal{C}_g/\epsilon^3$, which was defined above.

TABLE I. Typical values of physical quantities taken from two vastly differing applications: the flow of lava domes and the spreading of thin films containing surfactants. The data are from a variety of sources detailed in Balmforth *et al.* (2000) and Craster and Matar (2000) and one can obtain slip length estimates from Fetzer and Jacobs (2007) of 400–600 nm.

Parameter	Viscosity (Pa s)	Density (kg/m^3)	Spreading pressure	Diffusivity	Height scale	Length scale	Aspect ratio
Silicic lava	10^9	2600			160 m	400 m	0.4
Surfactant spreading	10^{-2}–10^2	1000	10 dyn/cm	10^{-5} cm^2/s	10^{-4} cm	10^{-2} cm	0.01

For illustrative purposes, typical material values for the flow of lava domes and surfactant spreading on a horizontal flat substrate are given in Table I and the resulting dimensionless groupings are in Table II. From these tables, one gets an idea of the typical size and importance of the different physical processes in these flows. The effect of hydrostatics in surfactant-driven spreading case is clearly minimal, as is that of inertia, justifying the omission of inertial effects in the theory developed in this section. Surfactant diffusion and capillary effects are also small and a discussion of the implications of this is presented in Sec. VI.

D. Significant inertia: Integral theory

We have thus far omitted inertia which, according to Table II, is clearly negligible in many applications. However, there are other situations where inertia plays a significant role, such as falling films and flows over spinning disks reviewed in Secs. III.A.2 and III.B, examples of which are shown in Figs. 1 and 2. There are a few nuances versus the inertialess theory which we illustrate here and demonstrate how integral theory and the von Kármán–Pohlhausen approximation can be used in conjunction to derive evolution equations that can describe the dynamics.

We focus on a single Newtonian layer (and drop all distinguishing subscripts), falling under the action of gravity as an example of such a system, in the absence of surface tension gradients, phase changes, electrostatic and intermolecular forces, and slip. Substrate topography is accounted for but the solid is assumed to be impermeable; this is reflected by

$$j = \mathbf{M} = \phi = \beta = W = \mathcal{M} = 0. \tag{38}$$

We directly use the scalings of Sec. II.B and Eqs. (12)–(14). The rapid inertial flows are primarily gravity driven and so, as in the gravitationally driven flows of Sec. II.C.2, we set the velocity scale through $\mathcal{G}=1$ hence $\mathcal{U}=\rho g\mathcal{H}^2\sin(\theta)/\mu$. The first change from the inertialess case is that the pressure scaling employed in Sec. II.C is inappropriate in the presence of appreciable inertia and it is replaced by $P=\rho\mathcal{U}^2$; this reflects a balance between pressure gradients and inertial forces. This change in the pressure scaling leads to the following rescaling: $p=\epsilon \mathrm{Re}\hat{p}$; as a result Eqs. (12)–(14) become the following boundary layerlike equations:

$$u_x + w_z = 0, \tag{39}$$

$$\epsilon\,\mathrm{Re}(u_t + uu_x + wu_z) = 1 - \epsilon\,\mathrm{Re}\,\hat{p}_x + u_{zz} + O(\epsilon^2), \tag{40}$$

$$\epsilon^3\,\mathrm{Re}(w_t + uw_x + ww_z) = -\epsilon\cot(\theta) - \epsilon\,\mathrm{Re}\,\hat{p}_z + O(\epsilon^2). \tag{41}$$

At this stage, one recalls that the Reynolds number is actually large so a scaled Reynolds number $\widehat{\mathrm{Re}}$ is introduced as $\widehat{\mathrm{Re}}=\epsilon\mathrm{Re}$. The leading order momentum equations are now

$$\widehat{\mathrm{Re}}(u_t + uu_x + wu_z) = 1 - \widehat{\mathrm{Re}}\,\hat{p}_x + u_{zz} + O(\epsilon^2), \tag{42}$$

$$\widehat{\mathrm{Re}}\,\hat{p}_z + \epsilon\cot(\theta) = O(\epsilon^2). \tag{43}$$

Notably, these are not easily integrated up and the procedure followed in Sec. II.C fails.

The boundary conditions follow from Eqs. (16), (20), and (21),

$$h_t + u(h+\mathcal{B})_x = w, \quad u_z = O(\epsilon^2),$$

$$\widehat{\mathrm{Re}}\,\hat{p} = -\frac{1}{\hat{\mathcal{C}}}(h+\mathcal{B})_{xx} + O(\epsilon^2) \quad \text{at } z = h+\mathcal{B}. \tag{44}$$

Here we have set $\mathcal{C}=\epsilon^3\hat{\mathcal{C}}$ to allow capillarity to play a role at leading order. Equation (39) and the conditions at $z=\mathcal{B}$, $u=w=0$, remain unchanged.

TABLE II. Order of magnitude estimates for the dimensionless parameters relevant to the spreading of surfactants on thin films based on the values listed in Table I.

	ϵ	Re	$\epsilon\mathcal{G}_m\cot(\theta)$	Pe	$\epsilon^3/\mathcal{C}_m$
Form	$\mathcal{H}/\mathcal{L}$	$\rho\mathcal{U}\mathcal{H}/\mu$	$\rho g\mathcal{H}^2/S$	$\mathcal{U}\mathcal{L}/D$	$\epsilon^2\sigma_m/S$
Estimate	10^{-2}	10^{-9}–10^{-1}	10^{-6}	1–10^6	10^{-4}–10^{-2}

Integration of Eq. (43) and application of the normal stress balance [Eq. (44)] yield

$$\hat{p} = \frac{\epsilon}{\widehat{\mathrm{Re}}}\cot(\theta)(h+\mathcal{B}-z) - \frac{1}{\widehat{\mathrm{Re}}\,\hat{\mathcal{C}}}(h+\mathcal{B})_{xx}, \tag{45}$$

which is a rescaled version of Eq. (24).

Integration of Eqs. (39) and (42) between $z=\mathcal{B}$ and $z=h+\mathcal{B}$ yields the following equation after making use of the kinematic boundary condition:

$$\widehat{\mathrm{Re}}\left[\left(\int_{\mathcal{B}}^{h+\mathcal{B}} u\,dz\right)_t + \left(\int_{\mathcal{B}}^{h+\mathcal{B}} u^2\,dz\right)_x\right] = h - \widehat{\mathrm{Re}}\int_{\mathcal{B}}^{h+\mathcal{B}} \hat{p}_x\,dz + u_z\big|_{\mathcal{B}}^{h+\mathcal{B}}. \tag{46}$$

One progresses by adopting a von Kármán–Pohlhausen approach, which postulates a closure relation for u. In the simplest case, a semiparabolic relation for the dependence of u on z is assumed, which satisfies the interfacial and wall boundary conditions (Shkadov, 1967). As we discuss in Sec. III.A.2, weighted residual methods represent a refinement of this approach. Here we use the following closure for u, which satisfies no slip at $z=\mathcal{B}$ and the tangential stress condition at $z=h+\mathcal{B}$,

$$u = -\frac{3Q}{2h^3}[z^2 - 2(h+\mathcal{B})z + \mathcal{B}(\mathcal{B}+2h)], \tag{47}$$

where $Q=\int_{\mathcal{B}}^{h+\mathcal{B}} u\,dz$ is the film volumetric flow rate. Substitution of Eq. (47) into Eq. (46) yields the following coupled pair of evolution equations for h and Q:

$$h_t + Q_x = 0,$$

$$\widehat{\mathrm{Re}}\left(Q_t + \frac{6}{5}\left[\frac{Q^2}{h}\right]_x\right) = h - \frac{3Q}{h^2} - \epsilon\cot(\theta)h(h+\mathcal{B})_x + \frac{h}{\hat{\mathcal{C}}}(h+\mathcal{B})_{xxx}. \tag{48}$$

Note that by taking the limit $\widehat{\mathrm{Re}}\to 0$ and setting $\hat{\mathcal{C}} = \epsilon^3/\mathcal{C}_g = 1/\mathcal{G}_c$, one recovers

$$Q = \frac{h^3}{3}\left(1 - \epsilon^2\cot(\theta)(h+\mathcal{B})_x + \frac{1}{\mathcal{G}_c}(h+\mathcal{B})_{xxx}\right), \tag{49}$$

and so one rederives Eq. (33) for gravity-driven thin films with negligible inertia. The approach outlined in this section was used by Shkadov (1967) in order to model falling film dynamics on smooth substrates ($\mathcal{B}=0$) and will be discussed further in Sec. III.A.2.

III. FILMS DRIVEN BY BODY FORCES

In this section, we review the developments in the study of thin films driven by body forces, such as gravity, centrifugation, and electric fields.

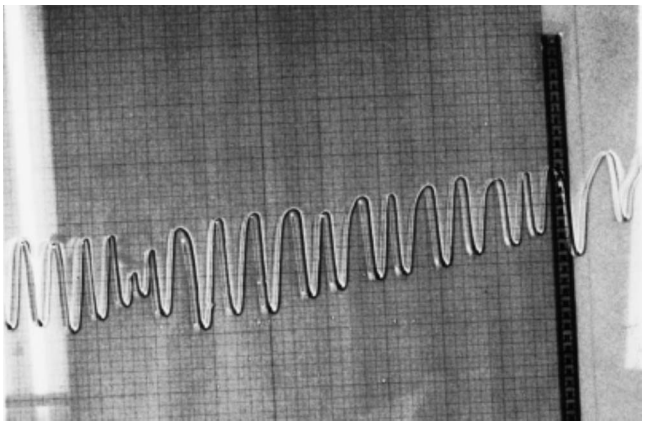

FIG. 8. The developing triangular shape of the leading edge of fluid (20Cst silicone oil) flowing down an incline. From Hocking *et al.*, 1999.

A. Flows driven by gravity

Here we consider thin films driven by gravitational forces, focusing first on negligible inertial contributions; falling film flows, in which significant inertial contributions are present, are reviewed next.

1. Negligible inertia

We consider situations where a film is driven by body forces at relatively small speeds, that is, in the absence of inertial contributions. Importantly, the cases considered in this section feature moving contact lines, whereas those reviewed in Sec. III.A.2, in which inertial effects are significant, will not.

The flow of a thin film down an inclined plane has received considerable attention. Here the contact line is unstable to transverse perturbations that develop into fingers or rivulets. As shown by Huppert (1982a) the shape of the rivulets can be of a triangular sawtooth shape or can be straight-sided constant-width fingertype rivulets. The velocity at the roots of the fingers is different for the sawtooth and fingerlike rivulets with the latter being stationary for finite volume release of fluid and the former gradually moving downstream. The transition from sawtooth to finger rivulets is a result of the angle of inclination of the plate being increased as shown experimentally by Johnson *et al.* (1999), theoretically and numerically (Bertozzi and Brenner, 1997; Münch and Wagner, 1999; Diez and Kondic, 2001; Kondic and Diez, 2001); typical triangular sawtooth fingers are shown developing in Fig. 8. There have been several detailed experimental studies on this fingering instability (Huppert, 1982a; Silvi and Dussan V, 1985; De Bruyn, 1992; Jerrett and De Bruyn, 1992; Hocking *et al.*, 1999) for fixed volume experiments and for constant flux (Johnson *et al.*, 1999) in this latter case, the finger roots always move suggesting that surface coverage is unaffected by the finger type.

The experiments by Hocking *et al.* (1999) focused on whether the fingers are triangular or straight edged and on how the time exponents of the finger tips and roots

compare to theory ignoring surface tension. They concluded that they are not inconsistent with the similarity solutions of Huppert (1982a). Notably, the finger type is also affected by the wettability and prewetting of the substrate (Veretennikov *et al.*, 1998). Related experiments involving the spin coating of drops on solid substrates have been performed by Melo *et al.* (1989), Frayse and Homsy (1994), and Spaid and Homsy (1997) for both Newtonian and non-Newtonian fluids. In the case of these spin-coated drops, the driving force is no longer gravity and it is replaced by centrifugal forces that play an analogous role; the effect of viscoelasticity is to have a stabilizing influence (Spaid and Homsy, 1997).

There have also been numerous theoretical investigations of the problem (Troian, Herbolzheimer, *et al.*, 1989; López *et al.*, 1996, 1997; Spaid and Homsy, 1996; Bertozzi and Brenner, 1997), which have focused on an analysis of Eq. (33) with $\phi=\mathcal{B}=0$; the singularity at the moving contact line is relieved either by assuming the existence of a precursor layer ahead of the moving contact line (Troian, Wu, and Safran, 1989) and/or by adopting a slip model (Spaid and Homsy, 1996), who compare the two approaches quantitatively when the precursor thickness and their slip parameter are equal. A linear stability analysis (Troian, Herbolzheimer, *et al.*, 1989) for flow down a vertical plane or down an incline (Bertozzi and Brenner, 1997) provides a band of unstable modes with a predicted wavelength for maximal growth, the "most dangerous mode," which agrees well with experimental observations and shows that this wavelength is approximately three times the width of the capillary ridge. This analysis also shows that short wavelengths are stabilized by capillarity, and decreasing the inclination angle shifts the most dangerous mode to longer wavelengths and decreases its growth rate. Spaid and Homsy (1996) also showed that the stability characteristics of the flow are weakly dependent on whether a precursor layer or a slip model is used. More recent analysis (Thiele and Knobloch, 2003) has investigated the stability of a fluid ridge moving down an inclined plane: the rear of the ridge recedes and that also induces an instability (Samid-Merzel *et al.*, 1998). Thiele and Knobloch (2003) investigated how this instability interacts with that at the front and their mutual dependence upon angle and the Rayleigh instability observed for a fluid ridge on a horizontal substrate.

One major step forward in thin film modeling is that two-dimensional computations of the evolution equations are now reliable and simulations of the fingering instability have been undertaken by many researchers (Schwartz, 1989; Eres *et al.*, 1999; Moyle *et al.*, 1999; Diez and Kondic, 2001; Kondic and Diez, 2001). Moreover, these are compared with the observed experimental patterns qualitatively reproducing trends (Eres *et al.*, 1999; Diez and Kondic, 2001) and furthermore allowing quantitative comparisons (Diez and Kondic, 2001). In particular, these studies demonstrate the importance of inclination upon finger shape (Kondic and Diez, 2001); see Fig. 9.

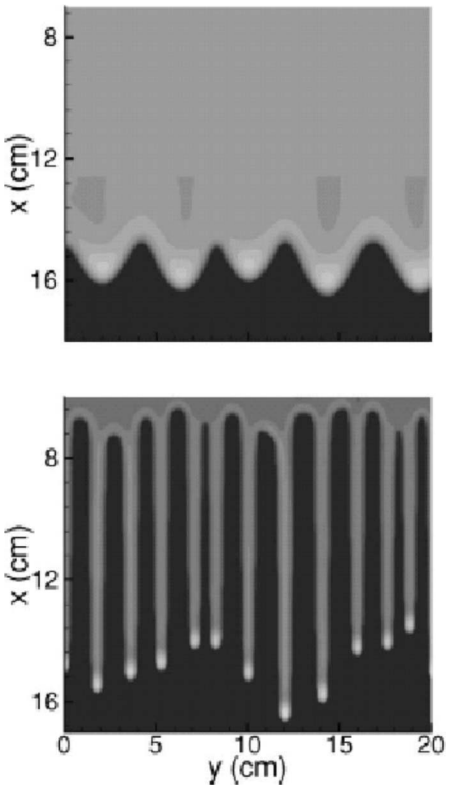

FIG. 9. Numerical solutions for the film thickness for flow down an inclined plane, showing the effect of decreasing the inclination angles from 90° to 13.9° in the left and right panels, respectively, plotted when the fluid traveled the same distance downslope. Quantitative comparisons of the calculated finger widths and wavelength with the experiments of Johnson *et al.* (1999) are provided in Kondic and Diez (2001); for the right-hand panel the widths are 3.2 ± 0.2 and 3.0 ± 0.3 cm, respectively, with similar agreement for the other cases they considered. From Kondic and Diez, 2001.

As pointed out by Spaid and Homsy (1996) through an energy analysis, small-amplitude perturbations in height at the capillary ridge grow as thicker regions experience less viscous drag relative to neighboring thinner regions and thus travel faster under the action of the body force; this mechanism leads to instability and finger formation. For small inclination angles, Bertozzi and Brenner (1997) [see also Ye and Chang (1999)] argued that linear stability theory is inadequate to explain the fingering observed (De Bruyn, 1992) and that these are brought about by transient growth[1] of perturbations at the contact line, which acts as an amplifier of initially infinitesimal disturbances. At larger inclination angles, a study of the nonlinear instability through a weakly nonlinear expansion (Kalliadasis, 2000) leads to a

[1]So-called "transient growth" (Trefethen *et al.*, 1993; Schmid and Henningson, 2001) describes the growth of perturabations on relatively short time scales due to the non-normality of the operators governing the evolution of linear disturbances; this may mask the response from an eigenvalue analysis, which dominates at long times.

Kuramoto-Sivashinsky style equation that gives a sawtooth pattern.

A more recent study by Grigoriev (2005) investigated carefully the relationship between transient growth and conventional linear theory and concludes that some of the discrepancies observed are due to the exact definition of transient growth and the form the perturbation takes; broadly speaking, the conclusion is that linear theory yields a good indication of the stability of the nonlinear system.

The foregoing focused on the time evolution of the fingering of a planar front of fluid flowing down a plane; other downslope flows, however, are of interest such as the flow of a single rivulet or the flow from a source on an incline. In the latter case, one envisages a flow with an edge, separating dry and wet regions. Here fluid issues from a point source and spreads outward, eventually reaching a stationary profile. This steady state is approachable with thin layer theory (Smith, 1973) where one assumes that the variations in the downslope direction x are much smaller than those in the y direction so that $\partial_x \ll \partial_y$. The edge of the flow is then defined by $y = \pm y_M(x)$. This example illustrates that one advantage of the evolution equations is that they can then be further approximated or approached themselves in further asymptotic limits. Equation (33) with $\mathcal{B}, \beta$ zero and $\theta \sim \epsilon$, i.e., a shallow incline, then becomes the much simpler time-independent equation,

$$(h^3)_x + \left(h^3 \left[\frac{\epsilon^3}{\mathcal{C}_g} h_{yy} - h \right]_y \right)_y = 0, \tag{50}$$

to be solved subject to the constraint that

$$\int_{-y_M}^{y_M} h^3 dy = C, \tag{51}$$

where C is a constant; this constraint follows from assuming the flux to be constant. In the absence of surface tension, Smith (1973) used similarity variables to show that width of the rivulet increases as $x^{3/7}$; these scalings are compared with experiments (Smith, 1973) and agree with numerical simulations (Schwartz and Michaelides, 1988). More recently, generalizations of this analysis have been pursued with surface tension-dominated flow (Duffy and Moffatt, 1997), for which the powers change to 3/13 and −1/13 for the width and height, respectively, in the case of a source. Subsequent studies by Wilson *et al.* (2001, 2002) also allow for surface shear to drive the flow, account for the effect of a (constant) contact angle, and consider a slender dry patch draining under gravity all of which are relevant to realistic flows. This is an interesting limit that deserves scrutiny.

A very closely related issue is that of a steady thin draining rivulet, with prescribed constant volume flux, and of constant but unknown width. If the cross section is thin then lubrication theory can be applied and the shape of the rivulet deduced (Allen and Biggin, 1974; Duffy and Moffatt, 1995). This is relevant not only to flow down a flat plane but to flows around cylinders and along slowly varying topographies (Wilson and Duffy 1998); other related work involves modifications due to thermal effects on viscosity (Duffy and Wilson, 2003; Wilson and Duffy, 2003) and to the wettability of the substrate (Wilson and Duffy, 2005a) which, interestingly, alters the results if perfectly wetting. The stability of a flowing rivulet is also of interest (Young and Davis, 1987; Wilson and Duffy, 2005b) and current attention has been moving toward the even more difficult question of how inertia, capillary, and hysteretic effects due to wetting govern its meandering form as the flow rate increases (Kim *et al.*, 2004; Mertens *et al.*, 2005; Le Grand-Piteira *et al.*, 2006).

Moving on from the work of Smith (1973) and Huppert (1982b), Lister (1992) considered the time dependent behavior of extrusions from a point source (line sources were also considered) placed upon a slope, whose flux varies as t^{α_f}, and this includes the release of a fixed volume of material. In the absence of surface tension, the film evolution equation [Eq. (33)] becomes

$$h_t = -(h^3)_x + (h^3 h_x)_x + (h^3 h_y)_y \tag{52}$$

[absorbing the factor of 3 into the time and setting $\epsilon = \tan(\theta)$]. This is valid provided the Bond number $\mathcal{G} \gg 1$ and capillarity is negligible. To fix on a specific problem, one can define how the volume of fluid varies and then Eq. (52) is solved subject to the constraint

$$\int_A h dx dy = Q t^{\alpha_f} \tag{53}$$

for a point source issuing fluid such that the volume increases as t^{α_f} and the area covered by fluid is A. This formulation ignores the precise detail of the vent. Notably one can employ similarity variables, i.e., for long times set $\xi = x t^{-\lambda}$, $\eta = y t^{-\mu}$, $h = \phi(\xi, \eta) t^{\gamma}$, thus the downslope length, the width, and the height scale as t^{λ}, t^{μ}, and t^{γ}, respectively (the exponents μ, λ, and γ are constants to be determined). This approach of adopting similarity variables is very powerful and commonplace in the study of evolution equations. Inserting these into the evolution equation (52) and constraint (53) leads to

$$\gamma\phi - \lambda\xi\phi_\xi - \mu\eta\phi_\eta = t^{1+2\gamma-\lambda}(\phi^3)_\xi + t^{1+3\gamma-2\lambda}(\phi^3\phi_\xi)_\xi + t^{1+3\gamma-2\mu}(\phi^3\phi_\eta)_\eta, \tag{54}$$

with

$$\int_A \phi d\xi d\eta = Q \tag{55}$$

if $\lambda + \mu + \gamma = \alpha_f$. One can now balance terms within the equations to deduce how the downslope length, width, and height vary with time; one can also utilize these variables within numerical schemes. Initially, the flow is axisymmetric and the downslope component of gravity plays no role, so it is very similar to flow on a horizontal plane. The last two terms on the right-hand side of the equation balance with that on the left-hand side so that $\mu = \lambda$ and $2\lambda = 1 + 3\gamma$. At long times, however, the first term on the right-hand side of Eq. (54) term grows until the dominant balance is now between the first and third

TABLE III. The power-law scalings expected from the similarity solutions (Lister, 1992), for constant mass flux extrusions ($\alpha_f=1$) and fixed volume droplets ($\alpha_f=0$), for the downslope length $X_{\max}$, the upslope length $X_{\min}$, the half-width Y_s, and the maximal height h_m.

Regime	Downslope length $X_{\max}$	Half-width, Y_s	Maximal height h_m
Early times ($\alpha_f=1$)	$t^{1/2}$	$t^{1/2}$	t^0
Late times ($\alpha_f=1$)	$t^{7/9}$	$t^{1/3}$	$t^{-1/9}$
Early times ($\alpha_f=0$)	$t^{1/8}$	$t^{1/8}$	$t^{-1/4}$
Late times ($\alpha_f=0$)	$t^{1/3}$	t^0	$t^{-1/3}$

right-hand side terms so that $\lambda=1+2\gamma$, $2\mu=1+3\gamma$. The crossover between these two regimes can also be predicted using these similarity scalings which is a powerful check on their application to, experiments or to interpreting field observations in geophysics. A summary of these scalings for $\alpha_f=1$, i.e., a constant mass flux, and $\alpha_f=0$, i.e., a fixed volume release is shown in Table III; the general scalings and further details are in Lister (1992) and generalizations to power law and other fluids in Balmforth *et al.* (2002). If one simply wants the scaling exponents, rather than reducing the evolution equations to simpler form, then one can balance forces as in Griffiths and Fink (1993); see also Sec. IV.D.

More recent work has involved extending these Newtonian results to viscoplastic extrusions thereby providing models of mud flows and silicic lava domes (Blake, 1990; Griffiths, 2000; Balmforth *et al.*, 2002, 2006), and to nonisothermal extrusions as models of lava flows (Fink and Griffiths, 1990, 1998; Balmforth *et al.*, 2004); this is described later in Sec. IV.D for which these scalings then are altered. In any event, scaling analyses like this are commonly used to extract useful practical information from thin layer equations; in this case, one can use them to "diagnose" whether a particular fluid is acting in a "Newtonian way" and to estimate areas of coverage versus time for lava flows and, of course, as a nontrivial check on numerical schemes.

We now ignore the contact line, and the transverse direction y is suppressed, and consider bilayer or multilayer flows down an incline, as in Fig. 7. The flow is relevant to various coating flows (Weinstein and Ruschak, 2004) and to geophysical flows where the superposed layers can model rock glaciers (Loewenherz and Lawrence, 1989). These flows are unstable even at zero Reynolds number. In the absence of any thin layer approximation, the stability of a bilayer interface, the viscous counterpart of the Kelvin-Helmholtz problem, has been considered by Hooper and Boyd (1983), Hinch (1984), and more recently by Charru and Hinch (2000). In the latter article, a detailed explanation of the long-wave instability is presented together with an explanation for the "thin layer effect," often seen in multilayer flows for which the flow is stable if the thinner layer is the less viscous and unstable otherwise. The instability occurs as there is now an additional degree of freedom associated with the motions of the interfaces within the fluid layered system. For thin layer flows, early work by Loewenhertz *et al.* (1989), Chen (1993), and Kilakhandler and Silvashinsky (1997) showed that a bilayer system is indeed unstable, as is the three layer system (Weinstein, 1999), and nonlinear solutions in the Newtonian and non-Newtonian systems confirm the bilayer scenario (Balmforth *et al.*, 2003). A review of the multilayer instability has been provided by Pozrikidis (2004) and more recently by Jiang, Helenbrook, and Lin (2005); Jiang and Lin (2005) elucidated the mechanism for the instability for bilayer and three layer systems (Jiang, Helenbrook, Lin, and Weinstein, 2005). Interestingly the growth rates of the instabilities can be orders of magnitude larger than those of the bilayer system and a careful study of the various terms shows that interfacial and Reynolds stresses drive the instability and theory compares reasonably with experiments. Incorporating surfactants (Frenkel and Halpern, 2002; Halpern and Frenkel, 2003; Gao and Lu, 2007) is also possible and, even in the absence of gravity, surfactants cause destabilization.

2. Significant inertia

Here we review the work on falling films as examples of thin gravitationally driven films with significant inertia. Falling films (Chang, 1994; Chang and Demekhin, 2002) have received considerable attention since the early studies of Kapitza (1948) and Kapitza and Kapitza (1949), who carried out experimental work on fluid films in tubes. This early work demonstrated the wide range of behavior and rich wave dynamics that can be exhibited by the flows of these films. So-called "natural" waves are driven by disturbances originating from noise at the inlet, which grow in the downstream direction. With increasing wave amplitude, nonlinearities lead to growth saturation, deviations from a sinusoidal shape, and deceleration to an essentially constant wave speed. Typically, two types of waves are observed with rather distinct shapes: one type corresponds to waves of short wavelength, of nearly sinusoidal shape and wide peaks; the other corresponds to pulselike solitary structures with tall widely separated narrow peaks preceded by small-amplitude capillary waves. These waves belong to the so-called γ_1 and γ_2 wave "families" (Chang *et al.*, 1993). The γ_2 waves travel on a thin film whose average thickness is smaller than that of a fully developed flat waveless film, commonly referred to in the falling film literature as the Nusselt film or thickness. These two-dimensional waves undergo transitions to three-dimensional structures, whose rate depends on the film Reynolds number Re.

More recent experimental work on falling films has been reported by Alekseenko *et al.* (1994) [see also Alekseenko *et al.* (1985)] and by Liu and Gollub (1993, 1994), Lui *et al.* (1995), Nosoko *et al.* (1996), Vlachogiannis and Bontozoglou (2001), Park and Nosoko (2003), Argyriadi *et al.* (2004), and Nosoko and Miyara (2004). Alekseenko *et al.* (1985), Liu *et al.* (1993, 1995), and

Nosoko *et al.* (1996). [see also Yoshimura *et al.* (1996) on mass transfer enhancement by wavy falling films] demonstrated that the application of periodic inlet forcing of constant frequency can control the structure of the waves downstream: high-frequency forcing results in slower waves with wide crests, while low-frequency forcing leads to the formation of large-amplitude solitary waves, corresponding to the wave types mentioned above. Vlachogiannis and Bontozoglou (2001) and Argyriadi *et al.* (2004) presented evidence to show that the breakup of regular wave trains due to the formation of waves on flat films separating two waves is not due to an inherent instability but to the development of pulses from a depressed region that originates from the tail of a large wave. All these studies provided measurements of wave speeds and wavelengths as a function of Re, which are of tremendous value in achieving fundamental understanding of these complex flows.

Liu *et al.* (1995) also showed the existence of secondary instabilities following the initial bifurcation from a flat film steady state; these instabilities are responsible for transitions from two- to three-dimensional wave patterns. Examples of such transitions include the formation of a so-called "herringbone" pattern from two-dimensional waves due to a subharmonic instability and a "synchronous" three-dimensional mode arising from a side-band instability; these correspond to situations wherein spanwise deformations of adjacent waves are out of phase and in phase, respectively. Park and Nosoko (2003) showed that the rate of spanwise variations in two-dimensional waves is slow at low Re and saturates at Re approximately near 40. Above this value, two-dimensional waves are unstable to three-dimensional disturbances through a mechanism that these authors attribute to a capillary instability. Nosoko and Miyara (2004) carried out similar work and investigated in detail the spatiotemporal evolution of the waves from inception near the inlet to the appearance of three-dimensional structures downstream, demonstrating differences between "natural" and "forced" waves in terms of wave shape and kinematics.

Modeling studies of thin falling films were conducted by Yih (1955, 1963) and Benjamin (1957) who performed linear stability analyses of the following base state:

$$h = h_o, \quad u(z) = \frac{\rho g \sin(\theta)}{\mu}\left(h_o z - \frac{z^2}{2}\right),$$

$$p(z) = \rho g \cos(\theta)(h_o - z). \tag{56}$$

Equation (56) is derived from $\mu u_{zz} = \rho g \sin(\theta)$ and $p_z = -\rho g \cos(\theta)$, with $(u_z, p) = (0,0)$ at $z = h_o$ and $u = 0$ at $z = 0$. These equations correspond to a falling film of uniform thickness h_o whose motion is driven by the streamwise gravitational component and retarded by gravity; the pressure is purely hydrostatic (with the pressure of the overlying gas set to zero without loss of generality) and surface tension effects are neglected. Their results indicated that this base state is unstable to long-wavelength disturbances. Benney (1966) extended the analysis of falling films into the nonlinear regime by deriving an evolution equation for the film thickness, which accounts for inertia, hydrostatic pressure, capillary, and viscous effects,

$$h_t + \frac{2}{3}(h^3)_x + \epsilon\left(\frac{16\,\mathrm{Re}}{15}h^6 h_x - \frac{2}{3}\cot(\theta)h^3 h_x + \frac{1}{3\tilde{\mathcal{C}}}h^3 h_{xxx}\right)_x = 0. \tag{57}$$

Here $\tilde{\mathcal{C}} = \mathcal{C}/\epsilon^2$, where $\mathcal{C}$ is the capillary number defined in Sec. II.B. Inspection of Eq. (57) reveals that the leading order terms simply give rise to wave steepening. The inclusion of inertia at order ϵ, however, leads to unstable flow which is mitigated by the hydrostatic pressure and capillary terms.

The dynamics of falling films in the nonlinear regime have also been studied by a number of researchers who have built on the approach adopted by Benney (Lin, 1969; Gjevik, 1970; Roskes, 1970; Atherton and Homsy, 1976; Pumir *et al.*, 1983; Nakaya, 1989; Joo and Davis, 1992; Oron and Gottlieb, 2004; Saprykin *et al.*, 2005). These studies involve the derivation of a single evolution equation for the interfacial position, in which the velocity is, essentially, enslaved to the film thickness. However, due to the fact that inertial contributions arise to order ϵ in Eq. (57), the single-equation approach to modeling falling films at moderate to large Reynolds numbers is ultimately doomed (Pumir *et al.*, 1983; Joo *et al.*, 1991; Rosenau and Oron, 1992; Ruyer-Quil and Manneville, 1998, 2000; Ooshida, 1999; Scheid, Ruyer-Quil, Thiele, *et al.*, 2005; Scheid *et al.*, 2006) invariably leading to finite-time "blowup" of solutions. Furthermore, a comparison of the linear stability characteristics of the Benney equation with those of the linearized Navier-Stokes equations and the Orr-Sommerfeld equation revealed poor agreement; this deteriorates rapidly with increasing Reynolds number. Thus, the Benney equation cannot be used for modeling thin films flows, at moderate or high Reynolds numbers, accurately in practically relevant settings.

It is possible to further reduce Eq. (57) in order to obtain a weakly nonlinear evolution equation for h, which following suitable rescalings reads

$$h_t + hh_x + h_{xx} + h_{xxxx} = 0. \tag{58}$$

This is known as the Kuramoto-Sivashinsky equation and has been derived (and rederived) by a number of researchers (Homsy, 1974; Nepomnyashchy, 1974; Kuramoto and Tsuzuki, 1975, 1976; Sivashinsky 1977) in different physical situations. These include falling films and annular flows (Sivashinsky and Michelson, 1980; Shlang and Sivashinsky, 1982; Hooper and Grimshaw, 1985; Papageorgiou *et al.*, 1990; Coward *et al.*, 1995; Tseluiko and Papageorgiou, 2006), which arise in chemical engineering applications, flame propagation and combustion (Sivashinsky, 1977), plasma physics (Cohen *et al.*, 1976), and the propagation of concentration waves (Kuramoto and Tsuzuki, 1975, 1976; Kuramoto, 1978).

Equation (58) looks deceptively simple. This apparent simplicity, however, masks truly complex behavior, which manifests itself via the appearance of periodic, quasiperiodic and chaotic solutions that remain bounded, as shown by a large number of analytical (Goodman, 1994; Jolly *et al.*, 2000); and computational studies (Sivashinsky and Michelson, 1980; Hyman and Nikolaenko, 1986; Kevrekidis *et al.*, 1990; Demekhin *et al.*, 1991; Papageorgiou and Smyrlis, 1991; Smyrlis and Papageorgiou, 1991, 1996); solutions for coupled Kuramoto-Sivashinsky equation in multilayers have also been obtained (Kliakhandler, 1999). Within the context of transition to chaos, computational work (Papageorgiou and Smyrlis, 1991; Smyrlis and Papageorgiou, 1991, 1996) has shown that this occurs through period doubling through a Feigenbaum-type scenario.

The discrepancies between the predictions of the Benney equation and those of the Orr-Sommerfeld equation could be alleviated by accounting for the neglected second-order streamwise dissipative term (Panga and Balakotaiah, 2003); this approach, however, does not remedy the blow-up issue. A method that employs a Padé approximant-type approach (Ooshida, 1999) seems to cure this issue but yields poor agreement with the speeds and amplitudes of solitary waves. This method was then applied to the development of an evolution equation for the flow rate (Panga *et al.*, 2005) which must be solved along with an equation for the film thickness that arises from integration of the continuity equation. This is a marked improvement over the single equation model and highlights the importance of having another degree of freedom in addition to the film thickness, such as the flow rate, when attempting to model falling film dynamics for Reynolds numbers far above the critical value Re_c for which the film first becomes unstable.

Methods that alleviate the blow-up problem with the Benney equation involve direct numerical simulations of the Navier-Stokes free-surface problem (Nagasaki and Hijikata, 1989; Salamon *et al.*, 1994; Ramaswamy *et al.*, 1996; Malamataris *et al.*, 2002; Argyriadi *et al.*, 2004; Nosoko and Miyara, 2004) or the numerical solution of the boundary-layer equations (Chang *et al.*, 1993, 1994, 1996; Chang, 1994); Fig. 10 shows an example of this approach. Other methods are those based on an approach that combines boundary-layer theory with the Kármán-Pohlhausen averaging method (Kapitza, 1948; Shkadov, 1967); here the pressure is due to capillarity. These methods, whose application was briefly outlined in Sec. II.D, require closure relations for the film velocity distribution and lead to the derivation of coupled equations for the film thickness and volumetric flow rate. Shkadov (1967) used a semiparabolic velocity profile, which satisfies no slip and zero stress at the solid wall and gas-liquid interface, respectively, to derive

$$h_t + q_x = 0,$$

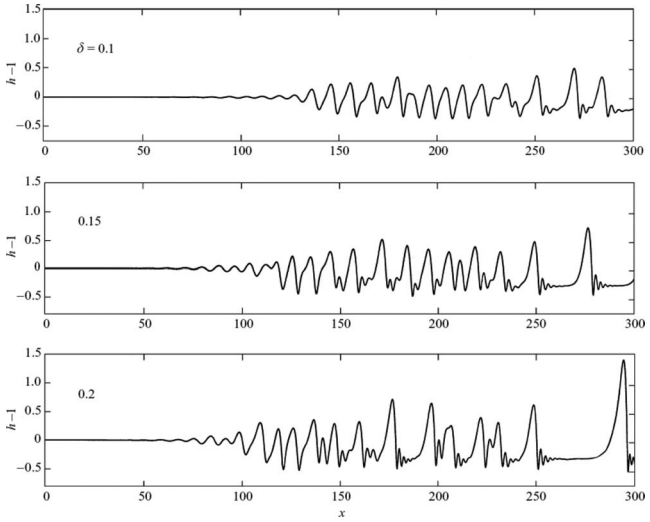

FIG. 10. Numerical simulations of noise-driven wave dynamics on a falling film obtained via the solution of the boundary-layer equations with pressure due to capillarity. The inertial effects become progressively stronger with increasing δ, where $\delta \equiv (\rho H_c^{11} g^4/\sigma)^{1/3}/45\nu^2$ as in Eq. (59). From Chang *et al.*, 2002.

$$q_t + \frac{6}{5}\left(\frac{q^2}{h}\right)_x = \frac{1}{5\delta}\left(h(h_{xxx}+1) - \frac{q}{h^2}\right). \tag{59}$$

Here q denotes the film volumetric flow rate and the parameter $\delta \equiv (\rho H_c^{11} g^4/\sigma)^{1/3}/45\nu^2$, in which H_c corresponds to the film thickness in the absence of waves (also known as the Nusselt solution), was introduced by Shkadov (1977). Equations (59) represent an example of two-field or two degrees of freedom models, where the velocity or the flow rate are not simply enslaved to the film thickness. Note that Eq. (59) can be obtained from Eq. (48) via the following transformations:

$$Q \to \left(\frac{3^7 5^9 \delta^9}{\hat{\mathcal{C}}^3 \widehat{\mathrm{Re}}^9}\right)^{1/11} q, \quad h \to \left(\frac{3^6 5^3 \delta^3}{\hat{\mathcal{C}} \widehat{\mathrm{Re}}^3}\right)^{1/11} h,$$

$$t \to \left(\frac{3\,\widehat{\mathrm{Re}}^5}{5^5 \hat{\mathcal{C}}^2 \delta^5}\right)^{1/11} t, \quad x \to \left(\frac{3^2 5 \delta}{\hat{\mathcal{C}}^4 \widehat{\mathrm{Re}}}\right)^{1/11} x. \tag{60}$$

Equations such as the ones given in Eq. (59) are highly nonlinear partial differential equations and exhibit multiple steady solutions for the same set of parameter values, which complicates comparisons between the modeling predictions and experimental data. That is, for fixed flow rate and liquid physical properties, several smooth sets of traveling-wave families of solutions can exist for a given wave frequency, characterized by different maximal film thickness or velocity. Shkadov (1967) and Bunov *et al.* (1984) calculated the first two wave families for falling films, while Sisoev and Shkadov (1999) succeeded in constructing waves belonging to all falling film wave families. Extensive numerical experiments (Sisoev and Shkadov, 1997a, 1997b) have demonstrated the emergence of attracting wave regimes, the so-called "dominating waves," which are realized independently of initial conditions. These waves, which have the great-

est wave velocity and largest peak height for a given set of system parameters, provided a natural point of comparison between theory and experiment. Indeed, the agreement with the predictions of the Shkadov model and the experiments of Alekseenko *et al.* (1994) was found to be relatively good particularly for the case of relatively fast-moving waves in terms of wave speed and amplitude [see, for instance, Fig. 22(b) in Shkadov and Sisoev (2004)]. The comparisons required the experimental observations to be parametrized by at least two parameters such as the wave velocity and wavelength.

The Shkadov equations also exhibit discrepancies with the Orr-Sommerfeld predictions. These can be eliminated by applying the method of weighted residuals (Ruyer-Quil and Manneville, 1998, 2000; Scheid *et al.*, 2006), which results in a modification of the evolution equation for q. Numerical solutions of the two-dimensional versions of these equations were carried out by Scheid *et al.* (2006) on doubly periodic domains and yield predictions of the three-dimensional spatiotemporal evolution of a film flowing down an incline (see Fig. 12). In order to account for the fact that the film thins beneath the waves due to its acceleration (see the third panel of Fig. 10), computations were conducted for average thickness less than the Nusselt value; this is apparently necessary in order to ensure good correspondence between the numerical solutions and experimental observations. Numerical solutions were obtained starting from small-amplitude white noise imposed on two-dimensional waves that resemble the herringbone and synchronous structures observed by Liu *et al.* (1995) for the relatively slow γ_1 waves at low wall inclinations; the agreement with the experimental data is qualitative and, in certain cases, also quantitative (see, for instance, Fig. 15 in Scheid *et al.*, 2006). Their results also indicate that direct computation of the synchronous mode is sensitive to initial conditions, depending on the balance between two-dimensional oscillatory modes and three-dimensional modes; they also demonstrate that the inclusion of second order dissipation terms, normally neglected by models based on long-wave and integral theory, is essential in order to capture experimental observations.

The simulations of Scheid *et al.* (2006) also yielded qualitative agreement with the experimental results of Park and Nosoko (2003) for γ_2 waves. For Re less than approximately 40, spanwise disturbances imposed at the inlet decay rapidly, while an increase in Re to 40 and above leads to the development of three-dimensional waves that exhibit remarkably rounded fronts. Increasing Re further to $\mathrm{Re} \approx 60$ gives rise to the "horseshoe" shaped structures shown in Fig. 11, which are in very good qualitative agreement with experimental observations (Scheid *et al.*, 2006); similar structures were also observed by Alekseenko *et al.* (2005). Similar agreement was also found with the noise-driven natural waves studied experimentally by Alekseenko *et al.* (1994).

Films falling down curved supports, such as fibers, for instance, have also been examined. This flow has an important distinguishing feature: the azimuthal curvature

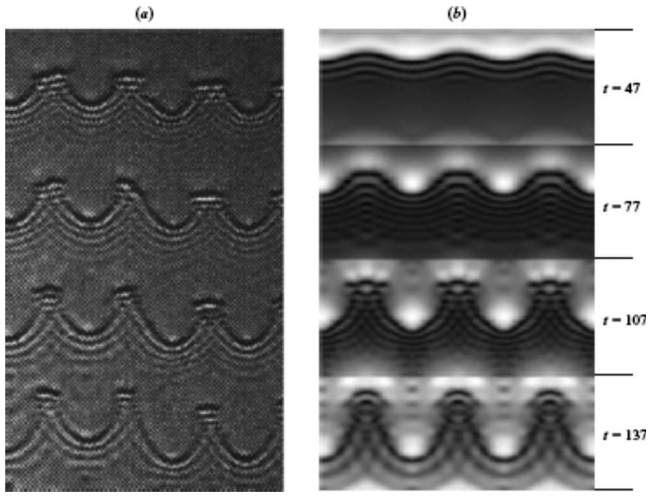

FIG. 11. Comparison of experimentally observed "horseshoe" structures reproduced. From Park and Nosoko, 2003. (a) With computations (Scheid *et al.*, 2006) and (b) showing the evolution of wave structure with time, at moderate Reynolds number ($\mathrm{Re}=59.3$), for a flow down an incline. The lowest panel in (b) should be compared with the experiments in (a). From Scheid *et al.*, 2006.

of the interface can, for sufficiently large film thickness to cylinder radius ratio, give rise to a Rayleigh instability, which, in the case of jets or threads, can lead to breakup (Eggers, 1997). Surface tension can therefore play both a stabilizing and, crucially, a destabilizing role due to the axial and azimuthal film curvatures, respectively. Trifonov (1992) used a von Kármán–Pohlhausen averaging method, similar to that employed to derive the Shkadov equations, with a velocity profile that comprised parabolic and logarithmic terms for closure; these reflect gravitational forcing and the importance of cylindrical geometry with increasing film thickness to cylinder radius ratios. This work has recently been revisited (Sisoev *et al.*, 2006; Ruyer-Quil *et al.*, 2008) and reformulated as an extension of the falling film problem. Sisoev *et al.* (2006) showed through a bifurcation analysis and time dependent numerical simulations that the solutions resemble those obtained in the falling film case at low thickness to radius ratios; these solutions become more beadlike for relatively large ratios. Flows down fibers will be revisited in Sec. VII.C.

Falling films in the presence of chemical reactions have also been studied using the long-wave method and approaches leading to coupled h and q evolution equations (Trevelyan *et al.*, 2002; Trevelyan and Kalliadasis, 2004a, 2004b); these studies accounted for the heat released (absorbed) by exothermic (endothermic) reactions and the associated Marangoni effects arising from the resultant interfacial heating (cooling). Several studies have also considered the effect of wall heating and evaporation on the falling film dynamics. Joo *et al.* (1991) examined the flow of uniformly heated falling films in the presence of evaporation as well as attractive van der Waals forces using a long-wave approach. More recently, Miladinova and Lebon (2005) modeled the dy-

namics of a thin evaporating falling film on uniformly and nonuniformly heated solid substrates also using long-wave theory. Their solutions revealed the influence of evaporation and thermocapillarity on the film dynamics leading to the formation of multihumped waves; in the presence of nonuniform heating leads to large deformations in the film and enhancement of the heat transfer rates.

Investigations at relatively large flow rates, where long-wave models are no longer valid, have also been conducted. Kalliadasis *et al.* (2003a) applied the weighted residual method to study falling films bounded by uniformly heated walls. A linear test function was used for the temperature in order to derive a model comprising evolution equations for the film thickness, volumetric flow rate, and interfacial temperature. This model was, in fact, derived by Kalliadasis *et al.* (2003b) as part of their modeling of the experiments carried out by Kabov *et al.* on locally heated falling films (Kabov, 1998; Kabov *et al.*, 2000). Kalliadasis *et al.* (2003b) showed that a steady state is established due to competition between gravity and Marangoni stresses (due to local heating), which is unstable to spanwise perturbations. This analysis yielded predictions for a critical Marangoni number for the onset of fingering and for finger wavelengths (as a function of the thermal Péclet number), which were of the same order of magnitude as experimental observations; the instability was enhanced at small Péclet numbers. Detailed quantitative comparisons with experiments, however, were complicated by the fact that a constant temperature boundary condition was specified at the wall in the model, whereas a constant wall heat flux was maintained in the experiments; even if a constant heat flux condition had been used in the model, the heat transfer coefficient at the wall remained an unknown quantity (Kalliadasis *et al.*, 2003b).

The models of Kalliadasis *et al.* (2003a, 2003b) were extended to include effects of viscous dissipation in both the momentum and energy equations, which arise at second order (Ruyer-Quil *et al.*, 2005; Scheid, Ruyer-Quil, Kalliadasis, *et al.*, 2005) so that they can predict critical conditions in agreement with the Orr-Sommerfeld equation. Heated falling films were also examined recently by Trevelyan *et al.* (2007) who used a heat flux condition at the liquid-solid interface, as opposed to the constant temperature condition at this interface employed previously (Ruyer-Quil *et al.*, 2005; Scheid, Ruyer-Quil, Kalliadasis *et al.*, 2005). The condition imposed by Trevelyan *et al.* (2007) included contributions from the heat flux provided by the heater placed in the wall and that associated with heat losses from the solid-gas interface; the latter is characterized by a heat transfer coefficient. As a further refinement, the test functions employed by these authors in their weighted residual method satisfied all boundary conditions; in the previous work, this was done as part of the averaging process through the boundary terms. Using both bifurcation theory and time dependent numerical simulations Trevelyan *et al.* (2007) showed the existence of solitary waves exhibiting "negative humps" for certain parameter values only when heat flux conditions are imposed; this is in contrast to the typical (positively humped) waves observed in isothermal films, shown in Fig. 10.

Closely related to the falling film literature is that of roll waves which are readily observed in guttering after heavy rainfall. These waves which visually appear to be hydraulic jumps traveling with the flow are no longer influenced by capillarity and an adjustment of the analysis in Sec. II.D leads to coupled evolution equations. These are commonly called a "St-Venant model," which is another application of the von Kármán–Pohlhausen approach and is developed using the depth-averaged velocity $\bar{u}(x,t)$, so $q=h\bar{u}$ in Sec. II.D, and mass conservation is $h_t+(h\bar{u})_x=0$. One then has to decide on an appropriate closure for the velocity field u. Popular choices are a semiparabolic profile for laminar flows as in Sec. II.D or plug flow for turbulent regimes. In the latter case, a typical St-Venant model is expressed by

$$\bar{u}_t+\bar{u}\bar{u}_x+Gh_x=1-\bar{u}^2/h^2+(\nu/h)\bar{u}_{xx}, \tag{61}$$

where G is a dimensionless group that incorporates *ad hoc* basal drag. The models often include artificial viscosity to avoid shock formation (Needham and Merkin, 1984), which leads to the $\bar{u}_{xx}$ term (Chang *et al.*, 2000; Balmforth and Mandre, 2004). The strongly coupled and highly nonlinear equations give rise to interesting coarsening dynamics and the models have been compared with experiments both qualitatively and quantitatively by Chang *et al.* (2000). Roll waves are also observed on related thin-film flows such as in multiphase fluids (Engelund and Wan, 1984; Huang and Garcia, 1998; Woods *et al.*, 2000), mudflow (Balmforth and Liu, 2004), and even in granular layers (Forterre and Pouliquen, 2003).

B. Flows driven by centrifugal forces

Here we review the work on thin films driven by centrifugation. We consider flows over rapidly rotating disks as examples of flows with significant inertial contributions. "Spin-coating" flows, which involve a fixed quantity of liquid with time-dependent average flow properties (Lawrence, 1990; Reisfeld *et al.*, 1991; Dandapat and Ray, 1994; Spaid and Homsy, 1996; McKinley *et al.*, 1999; Kitamura *et al.*, 2002; Usha *et al.*, 2005), will not be reviewed here.

The flow of a thin film over a rapidly rotating disk is accompanied by the formation of large amplitude waves, just like films falling under the action of gravity discussed in the previous section. Interest in this flow has experienced a recent resurgence due to the fact that they can be exploited for engineering and commercial applications: the film thickness can be made quite thin at high disk rotational speeds and the waves give rise to an intense mixing environment. These features lead to very high rates of heat and mass transfer that have led to the recent construction and use of so-called "spinning disk reactors" (SDRs), which are compact devices based on the flow of thin films over spinning disks used for the manufacturing of fine chemicals and pharmaceuticals

(Aoune and Ramshaw, 1999; Boodhoo *et al.*, 2004, 2006; Matar and Lawrence, 2006a). In fact, continuously operated SDRs have been used to perform fast gas-liquid reactions (Trippa *et al.*, 2002; Burns and Jachuck, 2005), crystallization (Trippa *et al.*, 2002), heterogeneous catalysis (Vicevic *et al.*, 2004) with high conversions and selectivities, and polymerization with narrow molecular weight distributions (Boodhoo *et al.*, 2006; Matar and Lawrence, 2006a).

The experimental work carried out in this area has identified different flow regimes depending on the flow rate: with increasing flow rate, a smooth film surface gives way to axisymmetric waves, with helical waves appearing at higher flow rates (Espig and Hoyle, 1965). Also, four distinct regions along the disk radius have been identified: a region near the disk inlet, a "first laminar-wave" region populated by axisymmetric waves, a "turbulent" region covered with disordered ripples, which is then followed by "second laminar-wave" region (Butuzov and Puhovoi, 1976; Rifert *et al.*, 1982; Thomas *et al.*, 1991). Woods (1995) used an optical technique to record detailed wave profiles along the disk and the emergence of three-dimensional flow structures from axisymmetric waves.

Due to the formation of waves, the time-averaged film thickness was found to be less than the waveless Nusselt value (Charwat *et al.*, 1972; Leneweit *et al.*, 1999); this is similar to the observations made for falling films in the previous section, particularly for the γ_2 waves (Chang and Demekhin, 2002). Burns *et al.* (2003) also carried out film thickness and film velocity measurements using an electrical conductivity technique and showed that inertial and viscous forces are important near the disk inlet and periphery, respectively. They also showed the establishment of an "injection" zone near the disk inlet in which the liquid experiences significant torque following its injection onto the surface of the disk; this is then followed by an "acceleration" zone in which the liquid is accelerated by centrifugation leading to an increase in radial velocity; this zone gives way to a "synchronization" region, which is dominated by viscous effects with a small angular slip velocity. The combination of the injection and acceleration zones was referred to as the "spin-up" zone by Burns *et al.* (2003) who demonstrated that its radial extent depends on liquid distributor diameter, flow rate, kinematic viscosity, and disk rotational speed.

The wave-induced enhancement in the rates of heat and mass transfer has given rise to a number of modeling studies. Steady axisymmetric waveless solutions have been obtained in the limit of large Ekman number $E \equiv \nu/\Omega H^2$, where ν, Ω, and H denote the kinematic viscosity, rotational speed, and a characteristic film thickness, respectively (Rauscher *et al.*, 1973; Shkadov, 1973; Woods, 1995). Steady solutions were also obtained for finite E (Dorfman, 1967; Miyasaka, 1974; Lepekhin *et al.*, 1981; Sisoev *et al.*, 1986; Shvets *et al.*, 1992) using boundary layer theory and the von Kármán–Pohlhausen method. Other studies have used lubrication theory to analyze the steady flow characteristics (Emslie *et al.*, 1958; Needham and Merkin, 1987).

Stability analyses of this flow also showed that axisymmetric perturbations are dominant and Coriolis forces are stabilizing in the long-wave and large E limits (Charwat *et al.*, 1972). The stability characteristics were also shown to approach those of falling films in the limit of large disk radii (Eliseev, 1983). The stability of locally uniform flow on the surface of the disk was examined using an Orr-Sommerfeld analysis for large E and axisymmetric disturbances (Sisoev and Shkadov, 1987), as well as for finite E and nonaxisymmetric perturbations (Sisoev and Shkadov, 1990). Needham and Merkin (1987) provided a criterion for instability using lubrication theory $Q\Omega^2/2\pi g\nu > 5/6$ in which Q is the volumetric flow rate in the large E limit but neglected surface tension effects; consequently, they could not predict a large wave-number cutoff. Woods (1995) who also used lubrication theory accounted for surface tension effects but not for Coriolis forces, which enter the problem at the same order as other inertial terms and are therefore negligible in the lubrication approximation (Myers and Charpin, 2001).

In order to account for the presence of interfacial waves, Sisoev *et al.* (2003a, 2003b), Matar, Sisoev, and Lawrence (2004), Matar, Lawrence, and Sisoev (2005), and Matar and Lawrence (2006a) extended the work of Shkadov (1967, 1973). This work mirrors that in Sec. II.D and employs boundary-layer theory together with the von Kármán–Pohlhausen approximation, which requires a closure relation for the film velocity profile; typically, a semiparabolic radial velocity profile is adopted which satisfies the no-slip and no-penetration conditions at the underlying solid wall and continuity of stress at the gas-liquid interface. This approach, which, as shown in Sec. III.A.2, has been successfully used to model falling films, gives rise to strongly coupled evolution equations for the film thickness and volumetric flow rate. In the case of flow over a spinning disk, this approach yields three evolution equations (Matar, Lawrence, and Sisoev, 2005),

$$h_t + \frac{1}{r} f_r = 0,$$

$$f_t + \frac{6}{5}\left(\frac{f^2}{rh}\right)_r - \frac{155}{126}\frac{g^2}{r^2 h} = \lambda^2 hr\left[\frac{1}{r}(rh_r)_r\right]_r - 3\frac{f}{h^2} + r^2 h + 2g,$$

$$g_t + \frac{17}{14}\frac{1}{r}\left(\frac{fg}{h}\right)_r = -\frac{5g}{2h^2} - 2f. \tag{62}$$

Here $f = r\int_0^h u\,dz$ is the radial volumetric flow rate and $g = r\int_0^h v\,dz$ denotes the angular momentum in which u and v are the radial and azimuthal components of the velocity field, respectively; the parameter $\lambda \equiv (\sigma/\rho)^{1/2}(2\pi/Q)(\nu/\Omega)^{3/4}$ is a modified Weber number. These equations, which account for inertial, centrifugal, Coriolis, capillary, and viscous forces, are very similar to

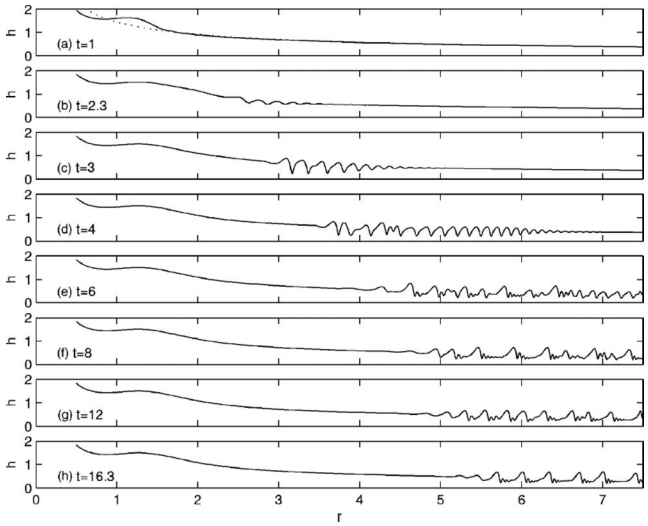

FIG. 12. Spatiotemporal evolution of surface waves in thin film flows over a spinning disk. The panels depict the development of small-amplitude waves at early times (a)–(c) into large-amplitude nonlinear waves (h); evidence of wave interaction and coalescence is shown in (d)–(g). The initial condition for the simulation giving rise to these results is shown as a dotted line in (a). From Matar, Lawrence, and Sisoev, 2005.

those derived by Sisoev *et al.* (2003b) and Matar, Sisoev, and Lawrence (2004) except for rescalings.

Sisoev *et al.* (2003a) showed through a linear stability analysis that Coriolis forces stabilize long-wave disturbances. They also demonstrated the fact that Eq. (62) exhibits multiple solutions for fixed parameters in a similar manner to Eq. (59) describing falling film dynamics, as discussed in Sec. III.A.2. They used continuation techniques to determine families of axisymmetric, periodic, or so-called "regular" waves. Using the concept of "dominating waves" (Sisoev and Shkadov, 1997a, 1997b, 1999; Shkadov and Sisoev, 2004) to circumvent difficulties associated with solution multiplicity, Sisoev *et al.* (2003a) carried out detailed comparisons with the experimental data of Woods (1995) with excellent quantitative agreement, as shown by Sisoev *et al.* (2003a). Matar *et al.* conducted numerical simulations of the flow on a spinning disk and showed the development of interfacial waves, which, through coarsening driven by wave interactions, become large-amplitude long regular waves that are separated by flat film regions (see bottom panel of Fig. 12) (Matar, Sisoev, and Lawrence, 2004; Matar, Lawrence, and Sisoev, 2005); these waves bear strong resemblance to those observed in falling films (Chang and Demekhin, 2002).

Models for the mass transfer of chemicals absorbed at the gas-liquid interface have also been derived (Matar, Lawrence, and Sisoev, 2005; Sisoev *et al.*, 2005) and these solutions, which are in reasonably good agreement with the experimental measurements of Aoune and Ramshaw (1999) in terms of spatially averaged mass transfer rates (see, for instance, Fig. 16 of Matar, Lawrence, and Sisoev, 2005), highlight the effect of the nonlinear wave dynamics on the mass transfer. Results by Sisoev *et al.* (2005) indicated that the potentially substantial intensification of the mass transfer rates over those associated with the waveless flow regime depends strongly on the structure of the dominating waves which, for a given set of "global" parameters, such as the flow rate and physical properties, depends on the wave frequency. They also demonstrated that the mechanism for intensification is dependent on the degree of deformation of the diffusion boundary layer beneath the gas-liquid interface by the waves that accompany the flow. These results further suggest that the intensification may be maximized using frequency forcing at the inlet to select appropriate wave regimes for given global parameters.

More recently, these studies have been extended to show that Marangoni stresses brought about by the presence of insoluble surfactant retard the flow by rigidifying the interface leading to wave suppression (Matar and Lawrence, 2006a). Also, externally applied electric fields have been shown to promote the formation of even more complex wave dynamics than can be obtained in the absence of electric fields; this is accompanied by sustained wave formation and an associated increase in process intensification (Matar and Lawrence, 2006b).

C. Electrified films

The interaction of an externally applied electric field with a thin liquid film can give rise to interesting flow instabilities and pattern formation. As shown below, these instabilities can be exploited in practical engineering applications. We review studies which feature thin liquid films in the presence and absence of inertia. Examples of the former involve examining the behavior of falling films at moderate flow rates; examples of the latter involve patterning of thin single and multilayers at the microscale and nanoscale. Note that despite the fact that this topic is reviewed under "films driven by body forces," the starting point for all of the modeling cases discussed below is the so-called "leaky dielectric" model (Saville, 1997) in which electric forces enter the problem in the interfacial boundary conditions, i.e., as surface effects.

The framework developed in Sec. II is used to derive an evolution equation for the interface separating two incompressible Newtonian fluids, sandwiched between two horizontal, smooth, rigid, and impermeable electrodes subjected to a solenoidal and irrotational electric field. We neglect inertia and effects related to gravity, surface tension gradients, phase changes, and intermolecular forces and set $\theta=\mathcal{G}=\mathcal{B}=j_{ie}=\phi_i=\mathcal{M}_i=0$ $(i=1,2)$ in Secs. II.A–II.C. In this example, the extra stress tensor $\mathbf{M}_i$ is now of vital importance as it corresponds to the Maxwell stresses exerted by the electric field. The upper and lower electrodes are located at $z=h_1\equiv\alpha$ $(=\text{const})$ and $z=0$, respectively; the liquid-liquid interface is located at $h_2\equiv h(x,t)$, as in Fig. 7, but horizontal and with the upper interface fixed to be constant.

The electric field strengths, $\mathbf{E}_i$ $(i=1,2)$, satisfy $\nabla\cdot\mathbf{E}_i=0, \nabla\times\mathbf{E}_i=0$ in the electrostatic limit and so potentials

in each fluid ψ_i are conveniently introduced as $\mathbf{E}_i = -\nabla\psi_i$ so that

$$\nabla^2\psi_i = 0, \quad i = 1,2. \tag{63}$$

The tensors $\mathbf{M}_i$ in Sec. II.A correspond to the Maxwell stress tensors and are identified explicitly as

$$\mathbf{M}_i = \varepsilon_0\varepsilon_i\left(\mathbf{E}_i\mathbf{E}_i - \frac{|\mathbf{E}_i|^2}{2}\mathbf{I}\right), \tag{64}$$

in which ε_0 and ε_i denote the permittivity of free space and the dielectric constant for fluid i. Allowing for an interfacial charge density q to be present at the interface leads to boundary conditions for the electric equations,

$$\psi_2 = \psi_0 \quad \text{at } z = 0, \tag{65}$$

$$\varepsilon_0(\varepsilon_2\mathbf{E}_2 - \varepsilon_1\mathbf{E}_1)\cdot\mathbf{n}_1 = -q,$$

$$\mathbf{E}_1\cdot\mathbf{t}_1 = \mathbf{E}_2\cdot\mathbf{t}_2 \quad \text{at } z = h(x,t), \tag{66}$$

$$\psi_1 = 0 \quad \text{at } z = \alpha, \tag{67}$$

where ψ_0 is the mean potential at the bottom electrode. Importantly, as q is the interfacial charge density at $z = h(x,t)$ it can evolve and so satisfies a transport equation, nicely described in a related context (Mestel, 1994), which is naturally similar to the surfactant transport equation of Eq. (6),

$$q_t + \mathbf{u}_s\cdot\nabla_s q - (\mathbf{u}_s\cdot\mathbf{n}_1)q\nabla_s\cdot\mathbf{n}_1 = (k_2\mathbf{E}_2 - k_1\mathbf{E}_1)\cdot\mathbf{n}_1. \tag{68}$$

Here k_i denote the electrical conductivity of fluid i and we have taken all the assumptions underlying the leaky-dielectric model to be valid (Saville, 1997).

Introduction of the same scaling as in Sec. II.B along with $\psi_i = \psi_0\tilde{\psi}_i$ $(i=1,2)$, $\mathbf{E}_i = (\psi_0/\mathcal{H})\tilde{\mathbf{E}}_i$, and $q = (\varepsilon_0\psi_0/\mathcal{H})\tilde{q}_1$ into Eqs. (63)–(68) yields the following in the lubrication approximation:

$$\psi_{izz} = 0, \quad i = 1,2, \tag{69}$$

which satisfies $\psi_1 = 0$ and $\psi_2 = 1$ at $z = \alpha$ and $z = 0$, respectively, and

$$\psi_1 = \psi_2, \quad q = -(\varepsilon_1\psi_{1z} - \varepsilon_2\psi_{2z}) \tag{70}$$

at $z = h(x,t)$. Continuity of the normal and tangential stress at $z = h(x,t)$ requires that

$$p_1 - p_2 + \frac{\varepsilon_2}{2}\psi_{2z}^2 - \frac{\varepsilon_1}{2}\psi_{1z}^2 = h_{xx}, \tag{71}$$

$$\frac{\mu_1}{\mu_2}u_{1z} - u_{2z} = q(\psi_{1x} + \psi_{1z}h_x), \tag{72}$$

and q satisfies

$$q_t + (u_1|_h q)_x = K_1\psi_{1z} - K_2\psi_{2z} \quad \text{at } z = h(x,t), \tag{73}$$

where $K_i \equiv \mathcal{L}k_i/\mathcal{U}\varepsilon_0$ $(i=1,2)$ are the ratios of the charge relaxation to flow time scales. The velocity scale is chosen so that electric field effects are dominant, the pressure and Maxwell stresses balance in Eq. (71), with $\mathcal{U} = \varepsilon_0\psi_0^2/\mu_2\mathcal{L}$ and $\mathcal{L} = (\sigma\mathcal{H}^3/\varepsilon_0\psi_0^2)^{1/2}$; here σ the surface tension, is assumed to be independent of the electric field.

The hydrodynamics are governed by

$$u_{ix} + w_{iz} = 0, \quad -p_{1x} + m_1u_{1zz} = 0, \quad -p_{2x} + u_{2zz} = 0, \tag{74}$$

with $p_{iz} = 0$ $(i=1,2)$, these follow from Eqs. (18), (19), and (23) of Sec. II.C; no-slip and no-penetration conditions, $u_i = w_i = 0$, are applied at $z = 0$ and $z = \alpha$. There is a further nuance; due to the confinement, u_1 and u_2 must also satisfy the following constraint (Craster and Matar, 2005):

$$\int_\alpha^h u_1 dz = \int_0^h u_2 dz. \tag{75}$$

This comes from integrating the continuity equation in fluids 1 and 2 over the depth, making use of the Leibnitz rule and demanding continuity of the normal and tangential velocity components at the interface.

Solution of Eqs. (69) and (74) subject to the above boundary conditions leads to explicit solutions for ψ_i, u_i, w_i, and p_i in terms of h and q. Using the kinematic boundary condition [Eq. (22)] evolution equations for h and q can be derived after some lengthy algebra,

$$h_t + \left[c_1\frac{h^2}{2}\right]_x = 0, \quad q_t + [c_2q(h-\alpha)]_x = K_1c_3 - K_2c_4, \tag{76}$$

where $c_i = c_i(h,q;\varepsilon_1,\varepsilon_2,\lambda)$; these are rather cumbersome and will not be reproduced here as they have been given by Shankar and Sharma (2004) and Craster and Matar (2005). One can now use these evolution equations that incorporate the essential dominant physics, and Eq. (76) has been used to study the instabilities shown in Fig. 3 and drop manipulation using electric fields (Yeo *et al.*, 2007).

It is also possible to derive an evolution equation for the case of a single layer either overlying or overhanging a solid horizontal substrate, which corresponds to a grounded infinitely long electrode. One can also incorporate inertial effects as in Sec. II.D. Consider a film sandwiched between this electrode and another sufficiently far from the position of the interface such that, at infinity, the electric field lines are normal to the interface and its strength approaches a constant value $\mathbf{E}_0$. This would coincide with Fig. 7 at $\theta = 0$, $h_2 \to 0$, and $h_1 \equiv h$. The film is either between $0 \leqslant z \leqslant h$ or $-h \leqslant z \leqslant 0$ corresponding to the overlying and overhanging cases, respectively; the other electrode would be at infinity from the interface $z = h(x,t)$. Tseluiko and Papageorgiou (2006, 2007) considered such situations and solved Laplace's equation for the potential in the gas phase with appropriate boundary conditions at infinity and at the interface; when coupled to the hydrodynamics governed by lubrication theory, the following equation for h is obtained (Tseluiko and Papageorgiou, 2007):

$$h_t + \tfrac{1}{3}[h^3(h_{xxx} - \mathcal{G}_e h_x + 2\mathrm{We}\bar{H}_t[h_{xx}])]_x = 0, \tag{77}$$

where $\mathcal{G}_e = \rho g \mathcal{H}^3/\epsilon_0\psi_0^2$ and $\mathcal{G}_e > 0$ ($\mathcal{G}_e < 0$) for overlying (overhanging) films. An "electric" Weber number $\mathrm{We} = (\epsilon_0\psi_0^2/\sigma\mathcal{H})^{1/2}$ also arises which provides a measure of electrical to fluid pressures and premultiplies an operator $\bar{H}_t$; this corresponds to a Hilbert transform, which is an integral involving h, over all x and a crucial point here is that the electric stresses enter the problem as a nonlocal contribution.

For a thin film an important consideration is its stability. The effect of electric fields on fluid-fluid interfacial stability has been well studied since the early work of Taylor and McEwan (1965) and Melcher and Smith (1969). Related recent applications have included utilizing an electrokinetic instability as a micromixer (Oddy *et al.*, 2001) or considering how electrical charges could be used with surfactants to create patterning (Warner *et al.*, 2003a). A review by Saville (1997) summarizes the effect of electric fields in engendering electrohydrodynamic instabilities in systems featuring fluid-fluid interfaces. The majority of the work described therein involves situations where gravity is important and a critical voltage is required to destabilize disturbances of intermediate wave number; long and short wavelength disturbances are stabilized by gravity and capillarity, respectively. These studies have focused primarily on determining the dependence of the critical voltage on whether they are "perfect" or "leaky" dielectrics, which is whether or not there exists the possibility of free charge conduction and charge accumulation and lateral transport on the interface. It was shown by Melcher and Smith (1969) that the presence of even the slightest amount of surface charge is sufficient to destabilize the interface at significantly lower voltages than in systems of perfectly dielectric fluids.

Recent interest has been generated by the wish to manipulate films and droplets on a small scale. Kim *et al.* (1992, 1994), Bankoff *et al.* (1994), Bankoff *et al.* (2002), and Griffing *et al.* (2006) indicated the possibility that thin films on electrostatic film radiators in space could be controlled using electric fields. Kim *et al.* (1992) derived evolution equations for low and moderate Reynolds numbers, which describe the film dynamics of a perfect dielectric material in the presence of electric effects. In the low Reynolds number case, this equation is similar to the Benney equation (57) and includes a term related to Maxwell stresses. Solutions of these equations suggest that the Maxwell stresses reduce the pressure at the gas-liquid interface sufficiently so as to substantially reduce the rate of fluid leakage from holes which may develop in cooling equipment used in space applications.

Equations of the Benney type were also derived by Gonzalez and Castellanos (1996) to model the dynamics of a film falling down a grounded inclined electrode with the other electrode at infinity. The equation they derived contains a nonlocal term, which owes its existence to the electric contributions. Similar equations were also derived by Tilley *et al.* (2001) and Papageorgiou and Vanden-Broeck (2004a, 2004b) in the case of electrified thin, planar, and free liquid sheets; here the nonlocal electrostatic term takes the form of a Hilbert transform. Gonzalez and Castellanos (1996) showed, through a linear stability analysis and a subsequent weakly nonlinear analysis, that the electrically induced transition to instability is via a supercritical bifurcation at a critical value of the electric field strength; this is done at small Reynolds numbers for which the evolution equation reduces to a generalized Kuramoto-Sivashinsky equation. This equation, expressed by

$$h_t + hh_x \pm h_{xx} + h_{xxxx} + \gamma\bar{H}_t[h_{xxx}] = 0, \tag{78}$$

was studied numerically by Tseluiko and Papageorgiou (2006). Here γ is proportional to an electric Weber number We and multiplies a Hilbert transform operator in which h is a scaled interfacial amplitude; the plus sign premultiplying the h_{xx} term is taken in situations wherein the critical Reynolds number, required to render the flow down an inclined plane unstable in the absence of an electric field, is exceeded. With $\mathrm{We} \to 0$, Eq. (78) reduces to the Kuramoto-Sivashinsky equation [Eq. (58)].

Tseluiko and Papageorgiou (2006) cataloged the various types of behavior exhibited by Eq. (78) as a function of γ and the dimensionless size of the system; these included the formation of spatially nonuniform as well as time-periodic traveling waves and chaotic dynamics. In particular, they showed that for sufficiently large values of the electric Weber number electric stresses can give rise to chaotic solutions at Reynolds numbers for which the film is linearly stable in the absence of an electric field. Thus the influence of an electric field could have an impact upon issues such as mixing which is enhanced by the presence of surface deformations and waves. In any event, electrically driven thin films with inertia are of interest and much remains to be discovered.

Another topic of interest is in generating well-defined and controllable patterns at small scales and in the absence of inertia. Contrasts in electric properties, such as dielectric constants and conductivities, are also found to give rise to electrohydrodynamic interfacial instabilities that manifest themselves via the formation of columnar structures in two-layer immiscible systems (Dong *et al.*, 2001). In the presence of shear, however, Bankoff *et al.* (2002) and Griffing *et al.* (2006) demonstrated that the disturbance amplitude saturates in the nonlinear regime. These electrohydrodynamic instabilities have also been used in order to form well-controlled patterns at the microscale and nanoscale. This is exemplified by Schaffer *et al.* (2000, 2001), Lin *et al.* (2001), and Morariu *et al.* (2003) who demonstrated the appearance of columnar structures in an initially flat polymer-air or polymer-polymer interface, as shown in Fig. 3. In these experiments, the initial film thickness is in the range of 100–1000 nm and the pattern wavelength is of order 100 nm. Lin *et al.* (2002) performed an experimental study of electrohydrodynamically induced patterns in air-polystyrene (PS)-polymethylmethacrylate (PMMA)

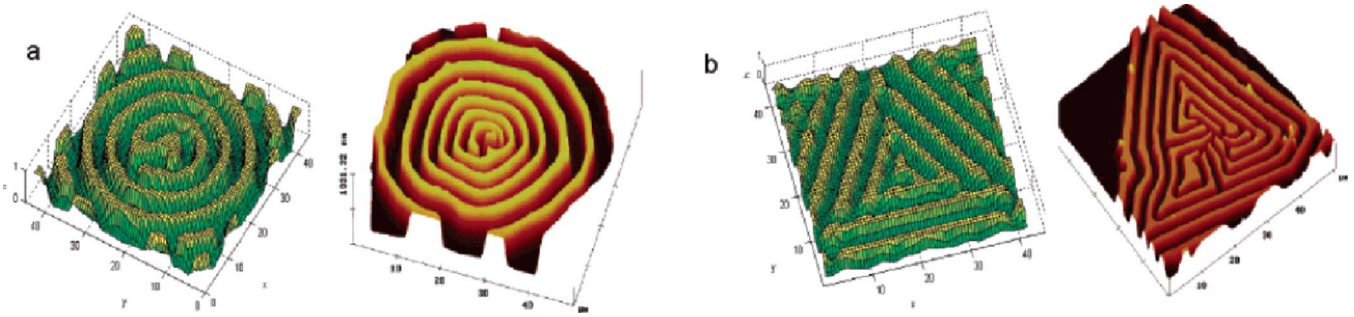

FIG. 13. (Color online) Electrohydrodynamically induced patterns in thin films of polymer melts under patterned masks: concentric rings, triangular, hexagonal, and square arrays. The right and left figures correspond to experimental observations (Chen *et al.*, 2005) and the results of numerical simulations, respectively. From Wu *et al.*, 2005.

thin films; these were confined between two electrodes across which a voltage is applied. They demonstrated that for sufficiently low voltages the PS phase dewets the underlying PMMA phase. For larger voltages, the formation of columns, which span from the PMMA phase to the upper electrode, was observed.

The linear stability characteristics of thin films of perfect dielectric (Herminghaus, 1999; Lin *et al.*, 2001; Schaffer *et al.*, 2001) and leaky-dielectric liquids (Pease and Russel, 2002; Shankar and Sharma, 2004; Craster and Matar, 2005), were examined in a number of studies. Herminghaus (1999) showed that the pattern wavelength is proportional to $h_0^{-3/2}$, where h_0 is the thickness of the dielectric film which underlies a conducting fluid of much larger thickness. Schaffer *et al.* (2001) used the lubrication approximation to determine the dependence of the fastest growing linear mode on system parameters for a polymer-air interface. Lin *et al.* (2001) conducted an experimental study using optical and atomic force microscopy and modeling work to study the dependence of pattern wavelength on the viscosity ratio in two-layer polymeric systems. Their modeling study predicts the wavelength to be independent of the viscosity ratio. The linear stability analyses of Pease and Russel (2002) and Shankar and Sharma (2004) and the numerical simulations of Craster and Matar (2005) of single-layer and two-layer leaky-dielectric films carried out using lubrication theory (as developed earlier in this section) showed that the presence of conductivity exerts a destabilizing influence. These studies also showed that, in contrast to perfect dielectric films, in the case of leaky dielectrics variation in the viscosity ratio has a significant effect on the pattern wavelength.

Weakly nonlinear analyses and two-dimensional numerical simulations have elucidated the interfacial evolution and the role of the initial thickness ratio on the observed three-dimensional patterns (Merkt *et al.*, 2005; Verma *et al.*, 2005; Wu *et al.*, 2005). These simulations have also yielded much insight into the design of the patterned "masks," which are used to induce pattern formation, so as to maximize the area of highly ordered patterns (Wu *et al.*, 2005). In Fig. 13, numerical and experimental patterns are compared and show strong qualitative similarities.

Electric fields have also recently been used in the manipulation and actuation of small liquid volumes, which are of interest in the area of microfluidics and the development of "lab-on-a-chip" type of devices (Prins *et al.*, 2001; Mugele and Baret, 2005). So-called "drop surgery" is an example of this and involves the splitting or translation of drops (Pollack *et al.*, 2002; Cho *et al.*, 2003) with fine precision at the microscale and nanoscale; simulations of drop surgery have been carried out recently by Yeo *et al.* (2007) using lubrication theory. There are also interesting effects when the wettability is altered by the electric field leading to a ratchetlike fluid motion (John and Thiele, 2007) and this joint electrical and dewetting flow connects with Sec. V.

IV. FILMS DRIVEN BY THERMAL EFFECTS

In this section, we review the work on thin films driven by surface stresses due to thermocapillarity and discuss the instabilities associated with these flows. We also review the work on films in the presence of phase changes such as evaporation or condensation.

A. Uniform heating and evaporating films

Evaporatively driven interfacial flows have a long and distinguished history going back to the work of Thomson (1855) and Marangoni (1865) after whom the driving forces due to surface tension gradients are now named. Oron *et al.* (1997) summarized the work carried out on thin films in the presence of evaporation and condensation processes until the mid-1990s and provided a clear exposition of the relevant equations that describe these systems in the limit where the vapor phase dynamics are neglected. In Sec. IV.A.1, we review more recent work that extends these so-called "one-sided" models to account for the dynamics in the vapor phase (Sultan *et al.*, 2004, 2005). We then summarized in Sec. IV.A.2 the work done on uniformly heated films with no phase changes and evaporatively driven thin films since the review of Oron *et al.* (1997).

1. Modeling of thin films with evaporation

The theory underlying the development of long-scale models for evaporative thin films has been reviewed by Oron *et al.* (1997) [see also Burelbach *et al.* (1988) for a comprehensive exposition of the derivation of the relevant equations]. The assumption that the ratios of the gas density, viscosity, and thermal conductivity and their liquid counterparts are very small, results in considerable simplification and in the formulation of so-called one-sided models (Burelbach *et al.*, 1988; Shklyaev and Fried, 2007). A brief derivation of these models is provided in Appendix C, giving an evolution equation for a single surfactant-free layer of fluid on a horizonal rigid and impermeable substrate bounded from above by an inviscid gas,

$$h_t = -\frac{E_n}{h+\mathcal{K}} + \left[\frac{h^3}{3}\left(-\frac{\epsilon^3}{\mathcal{C}_m}h_{xx} + \frac{\mathcal{R}}{(h+\mathcal{K})^2}\right)_x - \frac{\mathcal{K}}{2}\frac{M_{\rm th}h^2h_x}{(h+\mathcal{K})^2}\right]_x. \tag{79}$$

This equation is discussed further in Appendix C and is closely related to Eq. (34). Notably, the first term of the right-hand side corresponds to height changes caused by mass loss, while the term involving $\mathcal{R}$ corresponds to vapor "recoil." The final term is related to the presence of surface tension gradients that arise due to interfacial temperature variations, which can be determined explicitly in terms of h (see Appendix C). In this equation,

$$E_n \equiv \frac{\mathcal{L}\lambda_{\rm th}(T_0-T_\infty)}{\rho\mathcal{U}_m\mathcal{H}^2{\rm La}}, \quad \mathcal{K} \equiv \frac{\lambda_{\rm th}}{j_0\mathcal{H}{\rm La}},$$

$$\mathcal{R} \equiv \frac{1}{\mu\rho_g\mathcal{L}\mathcal{U}_m}\left[\lambda_{\rm th}\left(\frac{T_0-T_\infty}{\rm La}\right)\right]^2,$$

$$M_{\rm th} = -\frac{(T_0-T_\infty)}{(\sigma_0-\sigma_m)}\frac{d\sigma}{dT} \tag{80}$$

are dimensionless groups that correspond to an evaporation number E_n, a measure of the departure from equilibrium $\mathcal{K}$, and a vapor recoil number $\mathcal{R}$ giving a measure of the importance of the pressure imparted by vapor thrust on the interface. There is also a group $M_{\rm th}$ that relates the coefficient of the linear equation of state to the maximal temperature and surface tension changes; notably it is positive for most fluids. In Eq. (80), j_0 is a parameter in the constitutive equation for the evaporative flux j_e; T_0 and T_∞ denote the temperatures of the solid substrate and at saturation, respectively; and σ_0 and σ_m represent the surface tensions at these temperatures, respectively. The characteristic velocity is $\mathcal{U}_m \equiv S\mathcal{H}/\mu\mathcal{L}$, where in $S \equiv \sigma_0-\sigma_m$ is the maximal surface tension difference in the problem. The dimensional linear equation of state used in Appendix C to generate Eq. (79) is $\sigma=\sigma_\infty+d\sigma/dT(T_s-T_\infty)$, where $d\sigma/dT$ is the (constant) surface tension variation with temperature. Typical parameter values for the physical quantities and dimensionless groups appearing in Eqs. (79) and (80) can be found in Burelbach *et al.* (1988).

Motivated by the observation that some evaporative processes are diffusion limited and so the vapor phase is relevant, recently the one-sided formulation has been extended to account for the influence of the vapor phase in so-called "two-sided" models (Sultan *et al.*, 2004, 2005). If $J_0\mathcal{H}/\rho D_g \ll 1$, where J_0 is a characteristic evaporation rate, D_g is the vapor diffusion coefficient, $\mathcal{H}$ and ρ denote a characteristic film thickness and density, respectively, then diffusion in this phase is assumed to be quasistatic. Consequently, the vapor density ρ_g is obtained via solution of Laplace's equation

$$\nabla^2\rho_g = 0, \tag{81}$$

subject to the following boundary conditions:

$$\rho_{gz} \sim -\frac{J_0}{D_g} \quad \text{as } z\to\infty,$$

$$j_e = -D_g\mathbf{n}\cdot\nabla\rho_g = v_{\rm th}(\rho_{g,{\rm eq}}(T_s)-\rho_g) \quad \text{at } z=h. \tag{82}$$

Here T_s is the interfacial temperature and $v_{\rm th}$ is a velocity scale that depends on the interfacial temperature, vapor molecular weight, and the accommodation coefficient (Sultan *et al.*, 2005). This a parameter-rich problem and sample values of all parameters are listed in Sultan *et al.* (2005) for water, nonane, octane, heptane, and hexane and for water and ethanol in Burelbach *et al.* (1988) together with estimates of the magnitudes of the nondimensional groups. The density of the vapor in equilibrium with the liquid phase $\rho_{g,{\rm eq}}$ is given by a linear equation of state $\rho_{g,{\rm eq}}(T)=\rho_{g,{\rm eq}}(T_0)+\frac{d\rho_{g,{\rm eq}}}{(T-T_0)}dT$, where T_0 is the substrate temperature. The first condition in Eq. (82) specifies the density gradient far from the interface, while the interfacial condition reflects the continuity of the normal evaporative flux and the vapor mass flux, which is related to the departure from equilibrium at the interface.

The temperature is governed by the same equations and boundary conditions as in the one-sided model, whose derivation is summarized in Appendix C. Expressing the dimensional solution for the temperature in Eq. (C10) in terms of j_e, we obtain $T_s-T_0=-{\rm La}j_eh/\lambda_{\rm th}={\rm La}D_g(\mathbf{n}\cdot\nabla\rho_g)_{|_h}h/\lambda_{\rm th}$, which can be used to re-express the density equation of state; this is then used to recast the interfacial condition in Eq. (82) as follows:

$$-D_g\left(1+v_{\rm th}\frac{d\rho_{g,{\rm eq}}}{dT}\frac{\rm La}{\lambda_{\rm th}}h\right)\mathbf{n}\cdot\nabla\rho_g = v_{\rm th}[\rho_{g,{\rm eq}}(T_0)-\rho_g], \tag{83}$$

where La is the latent heat of vaporization.

In order to render Eqs. (81)–(83) dimensionless, one needs to introduce separate characteristic horizontal and vertical length scales in the regions $0\le z\le h$ and $z>h$. In the former region, $x=\mathcal{L}\tilde{x}$ and $z=\mathcal{H}\tilde{z}$, which are lubrication-type scalings, and, in the latter, $(x,z)=\mathcal{H}(\tilde{x},\tilde{z})$; the vapor density is scaled as $\rho_g=(J_0/D_g)\tilde{\rho_g}$ and the following transformation is introduced: $\tilde{\rho_g}=\hat{\rho_g}$

$+\tilde{\rho}_{g,\mathrm{eq}}(T=1)$. These scalings result in the following dimensionless Laplace equation for the vapor density (after suppressing the tildes):

$$\hat{\rho}_{gxx} + \hat{\rho}_{gzz} = 0, \tag{84}$$

and the following boundary conditions:

$$\hat{\rho}_{gz} \sim -1 \quad \text{as } z \to \infty,$$

$$j_e(1 + \chi h) = -\mathrm{Pe}_{\mathrm{th}}\hat{\rho}_g \quad \text{at } z = h. \tag{85}$$

Here $\mathrm{Pe}_{\mathrm{th}} \equiv v_{\mathrm{th}}\mathcal{H}/D_g$ is a Péclet number that characterizes the importance of diffusion in the vapor phase and the need to have a two-sided model, and $\chi \equiv \mathcal{H}v_{\mathrm{th}}(d\rho_{g,\mathrm{eq}}/dT)\mathrm{La}/\lambda_{\mathrm{th}}$ is a dimensionless measure of thermal expansion.

Equation (79) can be recast in terms of j_e, as shown in Appendix C,

$$h_t = -E_n j_e + \left[\frac{h^3}{3}\left(-\frac{\epsilon^3}{\mathcal{C}_m}h_{xx} + \mathcal{R}j_e^2\right)_x - M_{\mathrm{th}}\frac{h^2}{2}(hj_e)_x\right]_x. \tag{86}$$

In this case, it is not possible to write down a closed form formula for j_e; this has to be obtained numerically via solution of Eq. (84) subject to Eq. (85). Note that the one-sided model equations can be recovered by letting $\hat{\rho}_g \to \hat{\rho}_g \mathrm{Pe}_{\mathrm{th}}/\chi$ and taking the limit $\mathrm{Pe}_{\mathrm{th}} \to 0$; this then yields $j_e = 1/(h+\mathcal{K})$ and $\hat{\rho}_g = \mathrm{const}$.

In the absence of evaporation or condensation, that is, with $E_n = \mathcal{R} = 0$, it is still possible to have thermocapillary forces through a cooling boundary condition at the gas-liquid interface, usually Newton cooling is assumed,

$$-\lambda_{\mathrm{th}}\nabla T \cdot \mathbf{n} = a_{\mathrm{th}}(T - T_\infty), \tag{87}$$

where a_{th} is a heat transfer coefficient; the dimensionless version of this equation is

$$T_z = -B_{\mathrm{th}}T, \tag{88}$$

where $B_{\mathrm{th}} = a_{\mathrm{th}}\mathcal{H}/\lambda_{\mathrm{th}}$ is an interfacial Biot number. The remaining equations and boundary conditions for the hydrodynamics, the temperature field, and the temperature dependence of the surface tension remain unaltered from those presented in Appendix C. The temperature T is then given by

$$T = \frac{1 + B_{\mathrm{th}}(h - z)}{1 + B_{\mathrm{th}}h}, \tag{89}$$

which yields

$$h_t + \left[\frac{\epsilon^3}{\mathcal{C}_m}\frac{h^3}{3}h_{xxx} + \frac{B_{\mathrm{th}}}{2}\frac{M_{\mathrm{th}}h^2h_x}{(1 + B_{\mathrm{th}}h)^2}\right]_x = 0 \tag{90}$$

using the same procedure as outlined in Appendix C. Note that the second term on the left-hand side of Eq. (90) is structurally similar to the fourth term on the right hand side of Eq. (79); they both owe their existence to the presence of thermocapillary, Marangoni stresses.

For $B_{\mathrm{th}} \ll 1$, with $T_{zz} = 0$ as in Eq. (C7), $T = \mathrm{const}$, and, in the presence of a spatially varying basal temperature, $T_b(x)$, $T = T_b(x)$. From the shear stress boundary condition at $z = h$ in Eq. (C8), $u_z = \sigma_x = -M_{\mathrm{th}}T_{bx} \equiv \tau_{\mathrm{th}}$, whence $u = \tau_{\mathrm{th}}z - (z^2/2 - zh)h_{xxx}\epsilon^3/\mathcal{C}_m$. Using the kinematic boundary condition, the following evolution equation for h can be obtained:

$$h_t + \left[\frac{\epsilon^3}{3\mathcal{C}_m}h^3h_{xxx} + \tau_{\mathrm{th}}\frac{h^2}{2}\right]_x = 0. \tag{91}$$

Normally, the imposed basal temperature is assumed linear in x and so τ_{th} is constant. Equation (91) will be discussed later within the context of "climbing films" in Sec. IV.B.

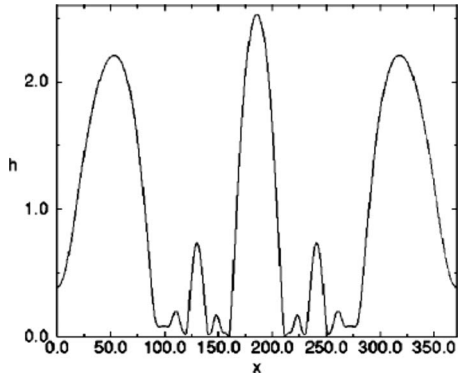

FIG. 14. The film interface at rupture for a uniformly heated film, showing the secondary droplet formation in the thinned regions. This was computed using a long-wave evolution equation [Eq. (90) with an additional gravity term] and is virtually indistinguishable from a finite element calculation in Krishnamoorthy *et al.* (1995). From Oron, 2000a.

2. Experimental and numerical studies

For thin films with a free surface and uniform heating from below, a long-wave Marangoni instability emerges. As noted by Oron (2000a), the film must be sufficiently thin in order that buoyancy effects are not dominant. Experiments by VanHook *et al.* (1995, 1997) on heated silicone oil layers of thicknesses 70–270 μm demonstrate, at the very lowest thicknesses, that a long-wave instability occurs with a dry spot forming and that for these very thin layers this replaces the usual short-wave convective instability; these two competing instabilities have been discussed by Golovin *et al.* (1994). Initially, one-dimensional numerical modeling using either boundary integral formulations for the full Stokes equations (Boos and Thess, 1999) or thin-layer evolution equations in two dimensions (Oron, 2000a) was performed. The work by Oron (2000a) utilizes a two-dimensional version of Eq. (90) with an additional gravity term that is retained in the pressure as in Eq. (34). Both studies found no steady state and that thinning followed by rupture occurs via a sequence of fingering events leading to the emergence of secondary drops, as shown in Fig. 14. It is worth noting that earlier work by Krishnamoorthy *et al.* (1995) compares long-wave theory with finite element solutions of the full Navier-Stokes equations for this problem; the two numerical schemes deliver quantitative agreement except very close to rup-

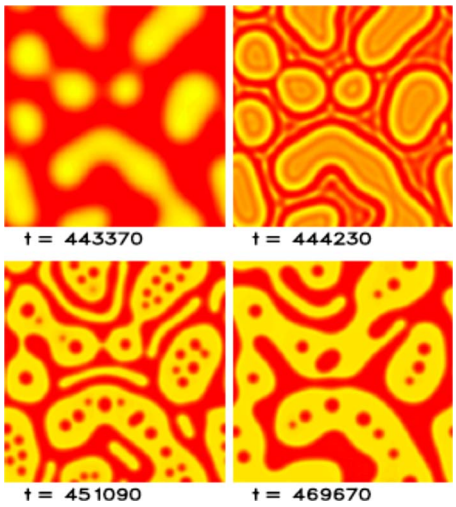

FIG. 15. (Color online) Two-dimensional computations for a uniformly heated thin film. In this long-time simulation, the lighter and darker areas represent thin and thick or droplet regions, respectively. These computations are complementary to those shown in Fig. 17 and demonstrate the development of small droplets forming within the larger holes. From Bestehorn *et al.*, 2003.

ture. Both schemes demonstrate the formation of secondary droplets and thus, as noted by Oron (2000a), this is not an artifact of thin-layer, or long-wave, theory. Once rupture occurs and a dry spot forms, within a numerical scheme it must necessarily halt unless a conjoining pressure containing a repulsive term is introduced [ϕ in Eq. (34)] into the two-dimensional version of Eq. (90); this leads to stabilization of the thin film at thicknesses of the orders of tens of nanometers. Recently, Bestehorn *et al.* (2003) used exactly this approach allowing the long time evolution of the instability to be followed. A host of different instabilities occur leading to holes, drop, or labyrinthine mazes depending on the parameters, as shown in Fig. 15.

Nonuniform heating as considered by Yeo *et al.* (2003) complicates matters by driving a thermocapillary flow with a thinned region upstream and a thickened region downstream of the applied thermal gradient. The thinned region becomes unstable to a streamwise rupturing instability and near the rupture point a cascade of fingering structures and secondary droplet formation is seen, which is similar to the phenomena observed in the computations of Boos and Thess (1999) and Oron (2000a).

The studies reviewed above have all involved a single thin film. Multilayer flows allow for even more interesting and diverse behavior. Kats-Demyanets *et al.* (1997) and Nepomnyashchy and Simanovskii (1997) considered linear stability for the long-wave limit in a horizontal trilayer system albeit enclosed by rigid walls from above and below. This system has two internal free interfaces and so additional long-wave instabilities are identified. Kliakhandler *et al.* (1998) took the analysis one step further into the weakly nonlinear regime and showed that, when one fluid layer is thin relative to the others, this instability is governed by a Cahn-Hilliard equation modified by coupling to a linear equation. It is therefore worth noting that even the uniformly heated thin fluid layer exhibits rich and interesting dynamics.

Some of the studies featuring evaporating films have been motivated by "the coffee ring" left by an evaporating drop of coffee (Deegan *et al.*, 2000), the explanation of which is that the hydrodynamics generated by evaporation lead to preferential particulate concentrations at the edge. Many authors have also considered evaporative effects coupled to other effects such as those associated with substrate wettability. As one might naturally expect, evaporation causes the fluid film to thin until eventually dewetting phenomena occur and some overlap with Sec. V occurs.

The dewetting dynamics and formation of "holes" in an evaporating thin film of low wettability were experimentally investigated by Thiele *et al.* (1998) who observed the "heterogeneous nucleation" of holes for relatively "thick" films, which give way to "spinodal dewetting" (see Secs. V.C and V.D for a discussion of these mechanisms) once the mean film thickness has been reduced to approximately 10 nm by evaporation; destabilizing polar interactions were shown to be responsible for this mode of dewetting. Sharma (1998) also studied thin evaporating-condensing films and presented a theory showing that the local evaporation-condensation rates are strong functions of the local film curvature and conjoining pressure. He also demonstrated that the dewetting of thin evaporating water films on partially wettable solid substrates is driven by hydrophobic attraction and mitigated by van der Waals interactions. Increasing the relative significance of the hydrophobic attraction destabilizes the film at increasingly larger thicknesses, leading to an overall decrease in the number density of the holes formed.

Complementary to these studies is that of Padmakar *et al.* (1999) who performed time-dependent simulations of the thin film behavior by obtaining numerical solutions of an evolution equation [a reduced form of Eq. (79)] for the interfacial position derived using lubrication theory. This equation accounted for capillarity, evaporation, conjoining pressure, and viscous drag. Their numerical results confirmed previous findings (Sharma, 1998) and also showed that the evaporation rate has a profound influence on the length scale of the patterns accompanying the film dynamics.

Oron and Bankoff (1999) also studied evaporating films in the presence of intermolecular forces using an evolution equation, essentially Eq. (79) enhanced with a conjoining pressure term, and showed that, in the absence of evaporation, static liquid ridges emerged connected by very thin films; these resulted from a balance of the long-range attractive and short-range repulsive intermolecular forces. In the presence of evaporation, the ridges flattened and eventually disappeared.

Kargupta *et al.* (2001) examined the pattern formation accompanying the dewetting of evaporating films on homogeneous and chemically heterogeneous substrates using time-dependent numerical simulations. Their nu-

merical solutions of the thin film lubrication equation showed that the rate of dewetting and the number of holes formed in the film increase substantially with evaporation rate on homogeneous substrates. In the case of chemically heterogeneous substrates, a combination of the evaporation rate and gradients of the interaction potential controls the dewetting dynamics and hole size distribution. Lyushnin *et al.* (2002) studied an instability that accompanies the growth of dry regions in evaporating thin films of polar liquids on chemically heterogeneous solid substrates. The instability manifests itself in the form of fingering patterns between thin dry regions and thick wet ones. The numerical study accounted for the effect of varying the evaporation rate, polar forces, and the substrate chemical heterogeneity.

Fluids, such as paints, for instance, can also be composed of volatile and nonvolatile components, and the relative concentrations are important in chemical drying processes. In this case, gradients in the chemical concentration lead to surface tension variations. In order to elucidate the mechanics of paint drying, Eres *et al.* (1999) used lubrication theory to study the three-dimensional dynamics of an evaporating thin film of a multicomponent fluid. The "paint" is taken to be composed of a "solvent" and a "resin," which correspond to the volatile and nonvolatile components, respectively. The model of Eres *et al.* (1999) accounts for gravity, capillarity, and thermal Marangoni effects, as well as evaporation, and for the dependence of the diffusion coefficient, film viscosity, and evaporation rate on the resin concentration. Thus there are now two coupled evolution equations, one for the height and another for the soluble chemical. This then results in a system akin to the surfactant chemical equations [Eqs. (117) and (119)], to be discussed in Sec. VI, complemented by evaporation. Their numerical simulations demonstrate the profound effect of Marangoni stresses, which are brought about by the evaporation-induced compositional changes.

Pattern formation in evaporating thin films of mixtures of volatile fluids, such as alcohols, has also been studied of which the so-called "tears of wine" are an example (Thomson, 1855); see Fig. 16. Here evaporation causes the alcohol concentration (surface tension) in the thin film above the meniscus to decrease (increase) driving a Marangoni flow that draws the wine upward into a thickened rim that ultimately becomes unstable due to gravity and falls back toward the meniscus as a "tear." These have been examined by Fanton and Cazabat (1998) and Hosoi and Bush (2001). The latter authors developed a thin film equation using lubrication theory capable of reproducing the ridgelike features shown in Fig. 16.

The evaporation of droplets has attracted much interest. As the fluid evaporates the droplet is either pinned (Deegan *et al.*, 2000) due to a rough substrate or recedes on a wetting substrate (Cachile, Benichou, *et al.*, 2002). In the latter case, provided the evaporation is limited by diffusion of vapor in the air the droplet radius $R(t)$ scales as $\sqrt{t_{\mathrm{end}}-t}$, where t_{end} is the time the droplet vanishes.

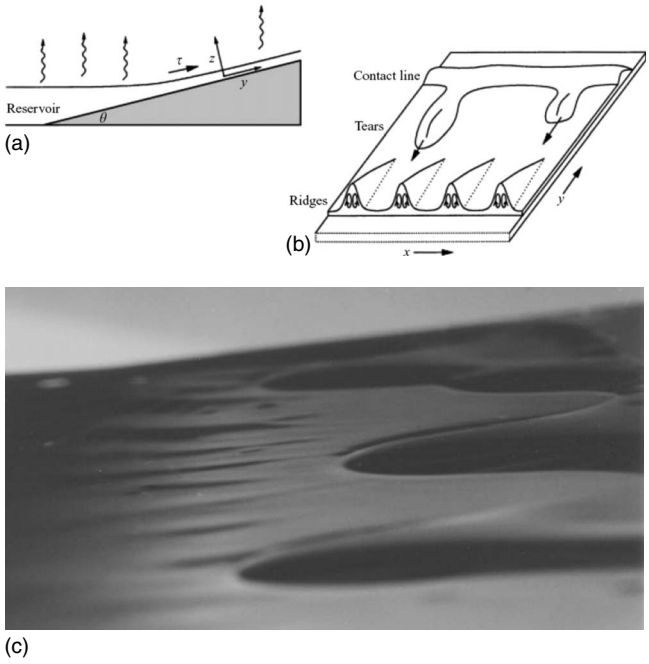

FIG. 16. The formation of tears and ridges in thin evaporating climbing films of a methanol and water mixture. Schematic of the flow (a) and of the tears and ridges (b); (c) a photograph showing descending tears (right in photo) and ridge-formation upstream. From Hosoi and Bush, 2001, and courtesy of John Bush and Anette Hosoi, MIT.

This follows from simple scaling arguments (Deegan *et al.*, 1997; Shahidzadeh-Bonn *et al.*, 2006), provided thermal and Marangoni effects are negligible the majority of the evaporation occurs at the edge: $dV/dt \propto -2\pi R$, where the volume $V \propto R^2 h$, and further assuming that the contact angle is constant so $h/R \sim$ const leads to the scale above. This is reliant upon the thermal- and Marangoni-related assumptions mentioned above but is nonetheless accurate for many fluids (Cachile, Benichou, and Cazabat, 2002). Interestingly, for water the exponent changes from 1/2 to about 0.6 (Shahidzadeh-Bonn *et al.*, 2006) which is hypothesized to be due to water vapor being lighter than air and thus convection becomes important.

Evaporating droplets also demonstrate interesting both instabilities at the contact lines (Rendon *et al.*, 1992; Poulard *et al.*, 2003; Gotkis *et al.*, 2006) and, for volatile liquids, instabilities occur in the bulk (Hegseth *et al.*, 1996; Kavehpour *et al.*, 2002) driven by Marangoni forces. In the experiments of Poulard *et al.* (2003) (see also Benichou *et al.*, 2003) the dynamics were found to be controlled by the film properties and fluid volatility. The presence of contact line instabilities and nonmonotonic receding contact angle behavior was also demonstrated; an example of this is shown in Fig. 17. The behavior at the contact line is further accentuated if the substrate dissolves [Gonuguntla and Sharma (2004) who considered a solvent droplet] and its dissolution is a function of the solvent concentration; there is a delicate interplay between dissolution and evaporation leading to intricate patterning near the contact line.

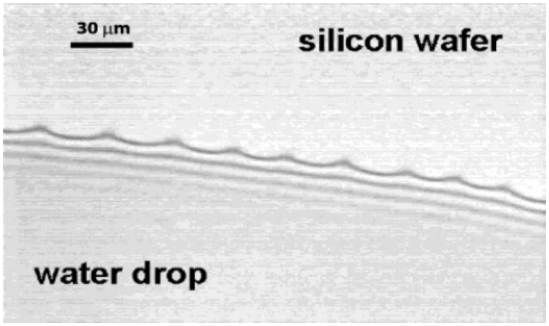

FIG. 17. The formation of festoonlike patterns at the contact line of an evaporating water droplet. From Poulard *et al.*, 2003.

In terms of theory, the diffusion-limited model allows for analogy with electrostatics (Deegan *et al.*, 2000; Cachile, Benichou, *et al.*, 2002) that gives the mass flux explicitly. The one-sided theory (Burelbach *et al.*, 1988), where the vapor plays virtually no role, has also been used to investigate the evaporation of droplets (Anderson and Davis, 1995), assuming that the contact angle is only affected weakly by evaporation. More recently, Ajaev (2005b) used a conjoining pressure in the mass flux to create a stable adsorbed film on the substrate ahead of the droplet. Numerical solutions of this model were found to be consistent with experimental observations of pattern formation in thin film drying. The model of Ajaev (2005b) is also discussed in Appendix C. Bestehorn and Merkt (2006) studied numerically the interplay between evaporation and the Rayleigh-Taylor instability in a thin liquid film on the underside of a solid substrate. In the presence of evaporation, Bestehorn and Merkt (2006) demonstrated the development of long-wave hexagonal patterns (see Fig. 18), which replace coarsening to large drops in the absence of evaporation.

A number of studies have also considered the effect of surface-active additives on the behavior of evaporating-condensing thin films. For instance, Danov, Alleborn, *et al.* (1998) used lubrication theory to study the dynamics of evaporating films in the presence of surfactants, interfacial viscosity, solutal and thermal Marangoni effects, as well as disjoining pressure. They carried out a linear stability analysis which revealed the competition that exists between the various destabilizing mechanisms. Paunov *et al.* (1998) extended this work to examine the stability of an evaporating two-layer surfactant-laden system in the nonlinear regime. Their numerical results revealed that the film exhibits both solutal and thermal Marangoni instabilities and that sufficiently large surfactant concentrations stabilize waves of intermediate and high wave numbers. These results also showed that the difference between estimates of the film rupture time based on the predictions of linear and nonlinear theories decreases with increasing surfactant concentration. Drying techniques, which are based on the deposition of surface-active vapor on wet wafers, have been developed in the semiconductors and microelectronics industry (Marra and Huethorst, 1991). These processes have also been modeled by Matar and Craster (2001) using lubrication theory, who demonstrated that the ultrathin film left behind during the drying process depends strongly on the nonlinearity of the surfactant equation of state and the rate of its desorption from the interface to the bulk.

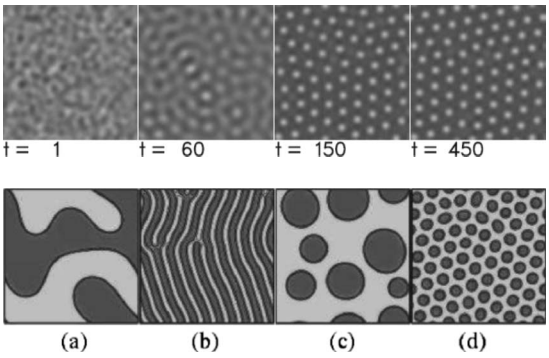

FIG. 18. Dynamics of a thin liquid film on the underside of a horizontal wall heated from below (or cooled from above): Rayleigh-Taylor-driven rupture stabilized by evaporation. Top: The formation of hexagonal stationary structures. Bottom: "Mazes" and coarsening drops are calculated in the absence of evaporation, shown in (a) and (c), and stripes and hexagons are shown in (b) and (d) with evaporation From Bestehorn and Merkt, 2006.

Hu and Larson (2005a 2005b) carried out a numerical study of an evaporating droplet resting on a solid support with a pinned contact line; the finite element method was used to solve the Stokes flow equations, coupled with Laplace equations for the thermal field within the droplet and the vapor concentration above the droplet in the slow evaporation limit. This study revealed good agreement with the predictions of lubrication theory at low capillary and Reynolds numbers. In the presence of Marangoni stresses, similarly good agreement was demonstrated; in this case, the lubrication solution was found to be accurate for relatively large contact angles (as high as 40°) [see Fig. 5 of Hu and Larson (2005b)]. The recent work by Sultan *et al.* (2005), reviewed in Sec. IV.A.1, has been aimed at developing two-sided models that connect the diffusion-limited and one-sided models. Their equations in the diffusion-controlled limit are parametrized by capillary and Marangoni numbers and linear stability results indicate that Marangoni stresses are destabilizing while capillarity and evaporation are stabilizing.

A number of studies have also been devoted to examining how evaporation of thin films and slender droplets can be utilized in self-assembly of particles and the development of surface patterning; for particulate flows this is akin to the coffee ring problem of Deegan (2000) and Deegan *et al.* (2000). Govor, Reiter, Bauer, and Parisi (2004), Govor, Reiter, Parisi, and Bauer (2004), and Govor *et al.* (2005) reported the formation of micrometer-sized rings of nanoparticles in thin evaporating films of binary mixtures of nitrocellulose in amyl acetate and hexadecylamine in hexane. Phase separation of the mixture into a bilayer is followed by dewetting of the hexadecylamine-rich top layer into droplets.

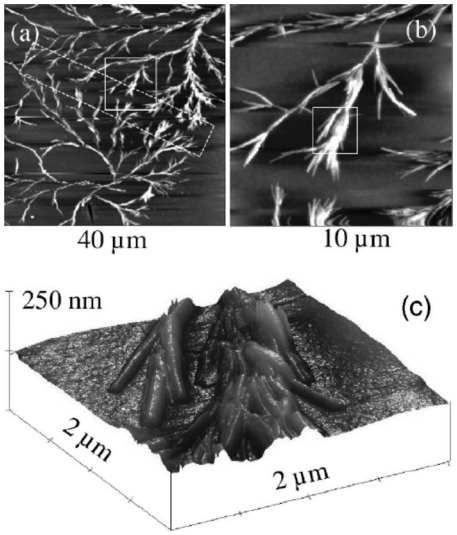

FIG. 19. Results of atomic force microscopy measurements showing the formation of treelike structures during the evaporation of polyisobutylmethacrylate and nitrocellulose bilayers in (a). (b) A magnified image of the box in (a). (c) A three-dimensional image of a branch highlighted in (b). From Govor *et al.*, 2006.

Evaporation-induced retraction of the three-phase contact line drives the self-assembly of the nanoparticles located there to form rings. More recently, Govor *et al.* (2006) also demonstrated the formation of treelike structures during the evaporation of the solvent, such as the ones shown in Fig. 19. Other primarily experimental groups (Weh, 1999, 2005; Weh and Venthur, 2004; Bormashenko *et al.*, 2005a 2005b) have also been exploring the formation of surface patterning driven by evaporation and this is an area that requires modeling.

Motivated by the results of O'Hara and Gelbart (1998), who observed the formation of annular rings of particles during the dewetting of particles-laden thin films, Warner *et al.* (2003b) used lubrication theory to model the evolution of an evaporating ultrathin film containing potentially surface-active nanoparticles (a combination of the modeling of this section and of Sec. VI.A); the film was considered sufficiently thin so as to undergo "spinodal dewetting." The results of Warner *et al.* (2003a) demonstrated the evolution of an initially uniform distribution of particles into bands or rings; the dependence of the pattern spacing on the initial packing concentration, evaporation rate, particle surface activity, and the nature of the intermolecular forces present was elucidated. Thus patterning and self-emplacement of nanoparticles can be approached by these theories. There has also been work by Rabani *et al.* (2003) that reproduces many patterns seen experimentally using Monte Carlo simulations, valid when the fluid film is extremely thin and the hydrodynamics play less of a role. Here one topic of interest is how one could incorporate this into a lubrication-style analysis for thicker films.

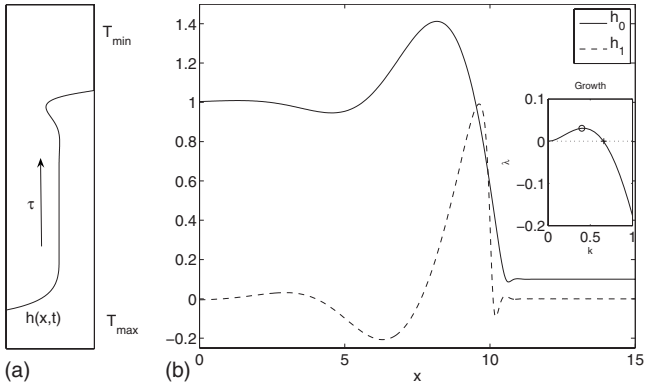

FIG. 20. The height profiles for a climbing film. (a) Schematic of a thin film climbing against gravity under the action of Marangoni stress τ; this is induced by a temperature gradient imposed along the underlying substrate. (b) The base state, a traveling wave solution (solid line), is vulnerable to transverse perturbations (dashed line) that localize near the contact line. A typical dispersion curve, depicting the dependence of the growth rate λ on the disturbance wave number k is also shown as an inset in (b), which demonstrates the existence of a linear instability for a range of k values. The "most dangerous mode," having maximal growth rate and wave number k_m and the "cutoff" mode, with $\lambda=0$ are highlighted by a circle and a cross, respectively. A precursor layer thickness $h_p=0.1$ was used to generate these results.

B. Climbing films

The surface tension of the majority of fluids is a decreasing function of temperature. Thus, it is possible to induce a film to climb out of a reservoir and spread along a vertical or inclined solid wall via the imposition of a temperature gradient. This gives rise to a surface tension gradient and thermocapillary-driven Marangoni stresses, which induce flow from the warm low surface tension region near the reservoir to the cooler regions of higher surface tension up the wall. This relatively simple flow, shown in Fig. 20, has generated considerable interest. Early experiments by Ludviksson and Lightfoot (1971) showed that fluid is drawn out of the reservoir and at its leading edge, a capillary ridge is seen. This ridge is also vulnerable to finger formation in a similar way to the gravity-driven case described in Sec. III.A.1 (Troian, Wu, and Safran, 1989; Cazabat *et al.*, 1990, 1992; Brzoska *et al.*, 1992; Carles and Cazabat, 1993). As the film thickens and gravity, which, in this case counteracts the Marangoni-driven upward flow becomes more important; later experiments (Bertozzi *et al.*, 1998; Schneemilch and Cazabat, 2000a, 2000b) showed that the capillary ridge widens into an undercompressive shock.

As indicated in Sec. IV.A, for sufficiently thin fluid layers and small Biot numbers the surface temperature can be taken to be equal to that of the substrate. For the case of a linear dependence of the surface tension on temperature and a basal temperature linear in the streamwise direction x, the surface shear stress reduces to a constant τ_{th}. This is modeled by Eq. (91), which

following the introduction of the rescalings $x \to \epsilon/(\mathcal{C}_m \tau_{\rm th})^{1/3} x$ and $t \to \epsilon/(\mathcal{C}_m \tau_{\rm th}^4)^{1/3} t$, and a generalization to account for the transverse direction, reduces to

$$h_t + \tfrac{1}{2}(h^2)_x + \tfrac{1}{3}\nabla \cdot (h^3 \nabla \nabla^2 h) = 0. \tag{92}$$

Note that as the constant temperature gradient is solely in the x direction, the Marangoni term involves a derivative in x only. Modeling proceeds as in the gravitationally driven case by considering the linear stability of the ridge (Kataoka and Troian, 1997) and via numerical simulations of Eq. (92) (Eres *et al.*, 2000). The contact line singularity is relieved by postulating the presence of a precursor layer, of thickness h_p, ahead of the contact line (Kataoka and Troian, 1997) and that the upstream condition is $h=1$. A traveling wave solution of the base state is then obtained via numerical solution of the following equation (Moriarty *et al.*, 1991; Kataoka and Troian, 1997):

$$\frac{2h^3}{3} h_{\xi\xi\xi} + h^2 + h_p - (h_p + 1)h = 0, \tag{93}$$

where $\xi = x - ct$, and now $h(x,t) \equiv h(\xi)$, in which $c = (1 + h_p)/2$ is the traveling wave speed that depends on the precursor film thickness h_p. The solutions obtained are subject to $h \to 1$ as $\xi \to -\infty$ and $h \to h_p$ as $\xi \to \infty$. A useful review of the treatment of the ordinary differential equations that arise in this type of analysis has been provided by Tuck and Schwartz (1990).

The base state $h_0(\xi) \equiv h(\xi)$ from Eq. (93) is now perturbed in the transverse direction and its linear stability is investigated using normal modes by substituting $h(x,y,t) = h_0(\xi) + h_1(\xi)\exp(iky + \lambda t)$ into the nonlinear two-dimensional evolution equation [Eq. (92)] and linearizing. Here k and λ correspond to the (real) disturbance wave number and (complex) growth rate, respectively, and h_1 satisfies the following ordinary differential eigenvalue equation:

$$\lambda h_1 = \frac{1}{2}(h_p + 1)h_{1\xi} - (h_0 h_1)_\xi - \frac{1}{3}[3h_0^2 h_1 h_{0\xi\xi\xi} + h_0^3(h_{1\xi\xi\xi} - k^2 h_{1\xi})]_\xi + \frac{k^2}{3}(h_0^3[h_{1\xi\xi} - k^2 h_1]) \tag{94}$$

with $(h_1, h_{1x}) \to 0$ as $\xi \to \pm\infty$. A typical base state profile, an eigenfunction h_1 for $k=0$, and a dispersion curve showing $\lambda(k; h_p = 0.1)$ are depicted in Fig. 20. The growth rate $\lambda \geqslant 0$ for $0 \leqslant k \leqslant k_c$, indicating the presence of a linear instability, with well-defined cutoff wave number k_c and a most dangerous mode with wave number k_m, which maximizes the growth rate. Provided the perturbation to the flow is small, linear theory predicts that this is the mode observed in experiments. The disturbances are localized at the capillary ridge; varying the wave number k gives very minor changes in the form of the eigenfunction and its location.

The dimensionless precursor layer h_p is relatively large in Fig. 20; decreasing it steepens the front and increases the height of the capillary ridge, which also leads to an increase in the maximal growth rate (Kataoka and Troian, 1997). The physical mechanism for the observed instability is similar to that at work in the gravity-driven case (see Sec. III.A): locally thick regions flow faster than those which are relatively thinner since they feel less drag induced by the wall. These initially small perturbations are amplified and lead to finger formation for sufficiently small values of h_p; streamwise capillarity provides the mechanism for high-wave number cutoff.

We now consider situations in which thermocapillarity, which drives the film to climb up the plate, is opposed by gravity. The generalization of Eq. (92) to this case is

$$h_t + \left(\frac{h^2}{2} - \frac{h^3}{3}\right)_x + \nabla \cdot \left(\frac{h^3}{3}(\nabla \nabla^2 h - \mathcal{G} \nabla h)\right) = 0. \tag{95}$$

Equation (95) follows from Eq. (34) after omitting conjoining pressure, topography, and slip and rescaling x, y, and t to remove the parameters; a concise derivation has been given in Haskett *et al.* (2005). Equation (95) also involves an additional $(h^3/3)_x$ term, which is the gravitational term premultiplied by $\mathcal{G}_m$ in Eq. (34). Note there is a sign change as the x axis is, for this problem, conventionally taken to be orientated up the incline, that is, in the direction of the Marangoni driving with gravity acting in opposition. In Eq. (95) we have included a term multiplied by $\mathcal{G}$ [proportional to $\epsilon \mathcal{G}_m \cot(\theta)$]. This term is only required for the nearly horizontal flows considered by Münch and Wagner (1999), and Münch and Evans (2005) when $\theta \sim O(\epsilon)$ and $\mathcal{G}$ becomes order 1, and it is otherwise $O(\epsilon)$ and thus usually omitted.

Early experiments by Ludviksson and Lightfoot (1971) demonstrated that fluid can be drawn up the inclined substrate by the temperature gradient and the front is often unstable and fingering occurs, but intriguingly the contact line can also be surprisingly stable. Interest in this flow was reignited when several authors (Fanton *et al.*, 1996; Bertozzi *et al.*, 1998; Schneemilch and Cazabat, 2000a, 2000b) also demonstrated that these contact line instabilities were suppressed in some cases. For very thin films, they observed the single traveling wave shown in Fig. 20 and the contact line is unstable and fingers eventually form. But as the thickness of the film increases by increasing, say, the thermal gradient, the contact line becomes stable, and the capillary bump widens over time (Bertozzi *et al.*, 1998), and it also propagates more slowly than the steady prediction. One no longer observes a steady solution, but an unsteady one that consists of a leading and a trailing shock that propagate at different speeds, which then separate over time. As also shown by Bertozzi *et al.* (1998, 2001), the leading undercompressive shock is stable to transverse perturbations, which could be useful when uniform coating is required. The trailing Lax (compressive) shock is, however, unstable albeit with a longer wavelength than that found when the Lax shock, for very thin films, is the leading shock. It is also possible to incorporate conjoining pressure effects to mimic the effect of van der Waals forces, Sec. V into this analysis (Golovin *et al.*, 2001), and their effect is stabilizing.

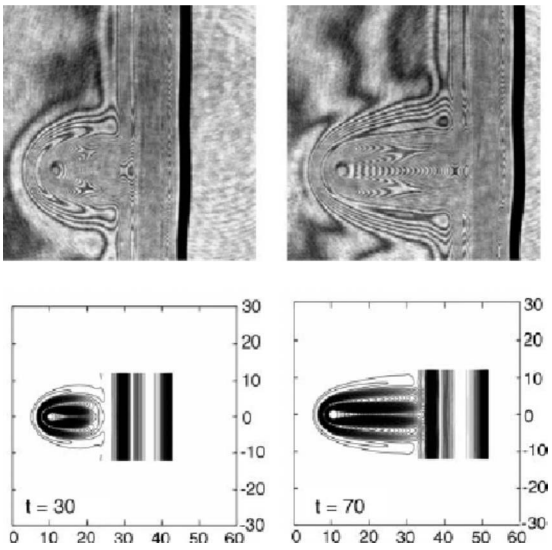

FIG. 21. Comparison of the experimentally observed height with a perturbation traveling into a trailing compressive shock (top panels) with the results of a numerical simulation (bottom panels), showing remarkable resemblance between theory and experiment. From Bowen *et al.*, 2005.

The term "shock wave" comes from an interpretation in the absence of the higher order derivatives (Bertozzi *et al.*, 1999) when the equations are hyperbolic

$$h_t + [f(h)]_x = 0, \quad f(h) = \frac{h^2}{2} - \frac{h^3}{3}, \tag{96}$$

and the shock structure can be explicitly extracted: it is a clear physical example of a nonclassical undercompressive shock which might otherwise be thought of as a mathematical abstraction. A good summary of the difference between compressive and undercompressive shocks in the context of this problem has been given by Bowen *et al.* (2005). They have absorbed the factors of 1/2 and 1/3 into the nondimensional groups at the outset, but for consistency with earlier sections we have not done so.

Careful experiments by Schneemilch and Cazabat (2000a) confirmed the theory, at least qualitatively, and further theoretical work (Bertozzi and Shearer, 2000; Münch, 2000; Münch and Evans, 2005; Evans and Münch, 2006) expands its range further by, for instance, coupling the advancing fronts to the behavior at the meniscus (Evans and Münch, 2006) and discussing how the threshold thickness is determined whereby the double-shock structure forms (Levy and Shearer, 2005). It is also often the case that the heat source is localized in space rather than just being perfectly linear, nonetheless the theory can be adjusted. Small oscillations in the meniscus can affect the behavior of the propagating thin film and localized heating can be used to isolate the meniscus region (Haskett *et al.*, 2005). Similarly one might be interested in how a perturbation to the stable leading shock affects the trailing one and in fully two-dimensional simulations, this has been undertaken by Bowen *et al.* (2005). In Fig. 21, from Bowen *et al.* (2005), we show a comparison of their simulations with experiment demonstrating remarkable resemblance between the two. In the experiments, the perturbation is generated precisely using a laser to create a local heat source and this is then mimicked in the numerics with a Gaussian source. The agreement shown in Fig. 21 is typical of the capability of modern numerical simulations to qualitatively reproduce experimental observations. Other recent work (Münch, 2003; Sur *et al.*, 2003) showed that the single compressive shock and the separating shocks are also complemented by other shock structures for a draining film competing with gravity.

C. Flow patterning

Accurate, efficient, and reliable manipulation of small volumes of liquid is of tremendous importance to numerous micromechanical and microfluidic devices. These involve the transport of fluids in channels driven by a variety of mechanisms, which include electrowetting, electro-osmosis, electrohydrodynamic pumping, and thermocapillary pumping. The presence of a fingering instability at the contact lines of thin films, either flowing down an inclined plane or climbing under the action of thermocapillarity, which leads to patterns of well-defined wavelengths, can potentially be exploited for channeling small volumes of fluid. The presence of contamination and surface defects, however, can give rise to large variations in the pattern wavelength. In the case of spreading over homogeneous substrates, the precise location along the thickened front from which the fingers emerge is not reproducible. In order to counteract these difficulties, Kataoka and Troian (1999) allowed a thermally driven climbing film to flow over a patterned silicon wafer, which had regularly spaced stripes of bared and coated SiO_2. The combination of this periodic surface energy pattern, which corresponds to alternating regions of high and low wettabilities, was shown to be highly effective in channeling the flow; it was also shown to be robust to the presence of contamination and surface irregularities (Kataoka and Troian, 1999; Darhuber *et al.*, 2000).

An important issue is related to the minimal width of a stripe in the substrate pattern, which can give rise to reproducible channeling. The experiments of Kataoka and Troian (1999) showed that, above a critical value of the stripe width, the channel spacing corresponds to the substrate pattern rather than the wavelength predicted by linear theory (see Fig. 22). Numerical simulations of this system were also carried out (Kondic and Diez, 2002), using an evolution equation similar to Eq. (33) with a spatially varying conjoining pressure to mimic the contrast between the high- and low-wettability regions on the substrate. The experimental results of Kataoka and Troian (1999) and the numerical predictions of Kondic and Diez (2002) (an example of these is depicted in Fig. 23) showed that the critical width of the wettable stripes is fixed by the marginal stability wavelength, as predicted by the linear stability analysis.

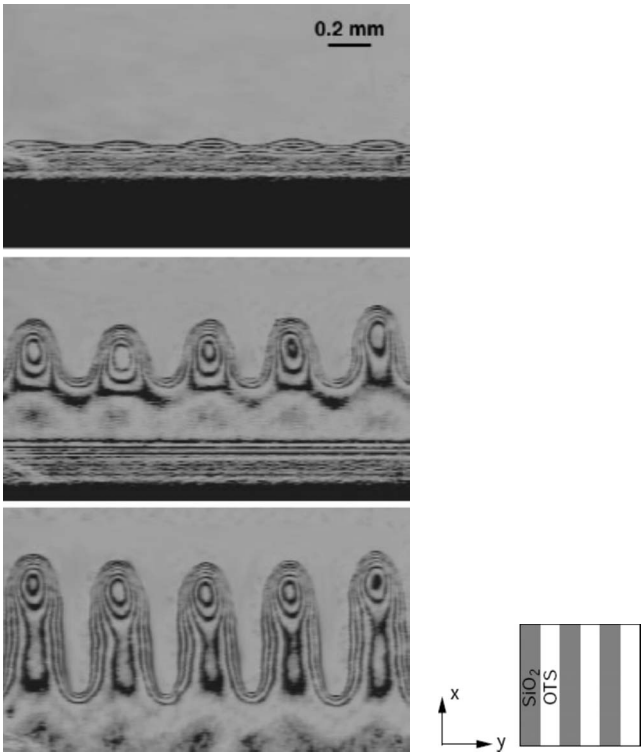

FIG. 22. Interferograms of thin silicone-oil films (left) climbing over silicon wafers patterned with alternating stripes of OTS and SiO_2 (right). From Kataoka and Troian, 1999.

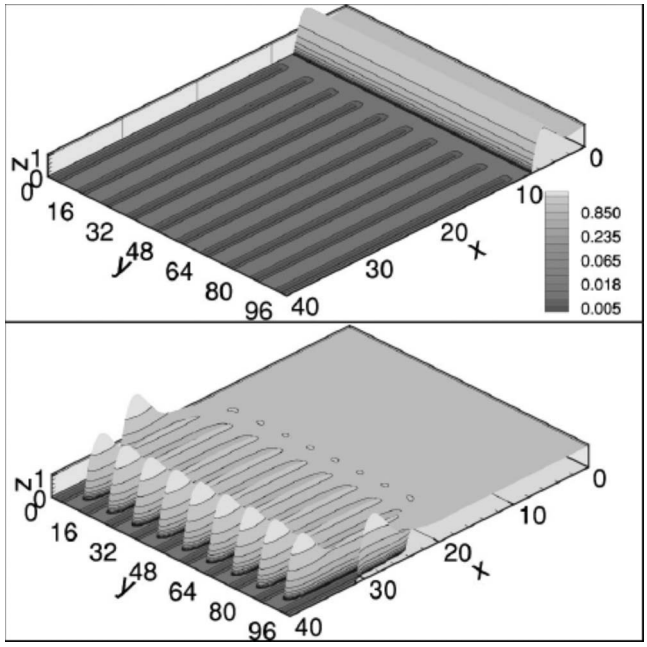

FIG. 23. Numerical simulations of thin films spreading over patterned substrates. Top: Initial conditions. Bottom: Fully developed fingering patterns. From Kondic and Diez, 2002.

D. Flow with solidification and thermally varying viscosity

Many spreading scenarios involve fluids whose properties depend strongly on temperature. Indeed, a common-day experience, spreading honey on hot toast, is that heating a fluid decreases the viscosity significantly. This is also observed in a number of settings that range from lava flows (Griffiths, 2000), solid-state mantle plume heads (Bercovici and Lin, 1996), glaciers (Hutter, 1983), and ice sheets (Baral *et al.*, 2001) in geological settings to the flow of molten films in chemical engineering (Braun *et al.*, 1995) and nuclear coolants (Dinh *et al.*, 2000). Ice is included here as temperature (pressure and water content) affects the viscosity and so in geophysical applications a fully coupled thermal-hydrodynamic problem must be solved (Greve, 1997).

In order to model such situations, the mass and momentum conservation equations must then be solved in conjunction with an energy conservation equation [Eq. (C3)] for the temperature. The viscous heating term is commonly ignored as the nondimensional group that characterizes its importance, and the Brinkman number defined as $\mu\mathcal{L}\mathcal{U}/\mathcal{H}^2\rho C_{sp}\Delta T$, is very small; here C_{sp} is the specific heat capacity of the fluid and ΔT is the typical temperature change from ambient. For lava and experimental flows typical values are $O(10^{-4})$ and have been given by Balmforth and Craster (2000) together with material properties. Solutions are obtained subject to Eq. (87) at $z=h$ and a condition on the temperature and/or its gradient at $z=0$. For fluids such as lavas, for instance, radiative cooling is more appropriate and the right-hand side of Eq. (87) is replaced by $a_{th}(T^4-T_\infty^4)$ or $a_{th}(T-T_\infty)^{4/3}$ (Griffiths and Fink, 1997; Balmforth and Craster, 2000); here T_∞ represents the ambient temperature. The temperature is coupled to the flow through the viscosity whose dependence on the temperature is given by

$$\mu(T) = \mu_* e^{-\tilde{G}(T-T_\infty)}, \tag{97}$$

where μ_* is the viscosity evaluated at the ambient temperature T_∞ and $\tilde{G}$ are prescribed constants. Such exponential forms for the temperature dependence are commonly used for lavas (Shaw, 1969; McBirney and Murase, 1984; Pinkerton and Norton, 1995) and their laboratory analogs (Fink and Griffiths, 1990; Stasiuk *et al.*, 1993); they are also used for ice sheets (Hutter, 1983). These relations are often justified theoretically because the Arrhenius reaction rate has exponential form in the Frank-Kamenetskii approximation.

In the case of rapid vertical conduction, the dynamics are described by coupled evolution equations for the thickness and the vertically isothermal temperature (Bercovici and Lin, 1996; Balmforth and Craster, 2000; King *et al.*, 2000). The procedure used to derive these equations is similar to that which will be described in Sec. VI.A in the case of rapid vertical diffusion of surfactant molecules across a thin film. There is thus a similarity with Eqs. (117) and (119) with bulk concentration replaced by temperature: both correspond to diffusing and advecting fields and are treated identically in the lubrication limit. Several features such as the formation of fingers or lobes at the edge of a cooling spreading droplet of hot fluid [often observed in the field and in

experiments (Griffiths and Fink, 1997)] can be interpreted using this model: locally thinner areas cool faster and thus have higher viscosities and advance less rapidly; conversely, thicker areas remain hotter and less viscous.

The flow of metals and many lavas, however, is characterized by large thermal Péclet numbers, the development of thermal boundary layers, and the formation of a highly viscous "skin" near the free surface; the approach discussed above leading to the development of a "reduced" model is therefore inappropriate in this case. In order to model this situation, the von Kármán–Pohlhausen approach has been used for the temperature field by Balmforth *et al.* (2004). Typical isotherms for an evolving fluid dome (an extrusion of hot fluid from a vent) showed that in the rapid conduction limit, the flow becomes vertically isothermal and the reduced model works well. However, in the opposite limit, the dependence of the temperature on the vertical direction becomes pronounced and cool fluid is gradually advected along the surface, accumulates at the edge, and is eventually over-ridden.

Another approach involves balancing various driving and restraining forces to deduce similarity scalings (Griffiths and Fink, 1993; Stasiuk *et al.*, 1993; Lister and Kerr, 1994). If one considers an axisymmetric dome of hot fluid supplied from a vent at a constant rate, then one set of variables of interest (nondimensional ones are used here for convenience) is the radius $R(t)$ and maximal height $h_{\max}(t)$. These can be estimated as follows. For a constant-flux extrusion, the radius and height are connected by $h_{\max}R^2 \sim t$; moreover, radial pressure gradients $p_r = h_r \sim h_{\max}/R$ drive expansion and must be balanced by fluid stresses. On equating the volume-averaged driving force $\int\int p_r r dr dz \sim R h_{\max}^2$ with the volume average of the dominant resistive stress, one can then extract the scaling exponent of the power law that characterizes the temporal behavior of the maximum dome height and radius. For instance, if the fluid is all at the eruption temperature and the viscosity is fixed then the radial velocity $u \sim R/t$ and $\tau_{rz} = u_z \sim R/h_{\max}t$ and the resistive stress $\int\int \partial_z \tau_{rz} r dr dz \sim R^3/h_{\max}t$. The dimensional scaling results obtained in this way can be found by Griffiths and Fink (1993) who showed that the power-law exponents for R and $h_{\max}$ depend strongly on the nature of the retarding mechanism. These exponents are expected to vary during the course of the flow as the dominant physics changes to promote one resistive stress over the others. The simple method outlined above can be used to great effect in generating theoretically power-law scalings that signify the balance between certain driving and retarding forces; these scalings can be used to provide qualitative explanations of experimental data and will be utilized again in Sec. VI.A.

Thin film flow in the presence of solidification has not received much attention presumably due to the associated complication of rigid crust formation, possible fracturing, and buckling; these require a level of modeling that has not been developed fully. However, there have been attempts to perform numerical simulations (Bunk, 1999) and derive similarity solutions for basal solidification (Bunk and King, 2003). There is also interest in ice accretion and solidification with respect to aircraft icing and evolution equations, as extensions of Eq. (37), have been developed with that application in mind (Myers *et al.*, 2002) incorporating accretion, solidification, and general topography. Also Zadražil *et al.* (2006) performed numerical simulations and presented experimental data for solidifying droplets atop a porous medium; this work is for small droplets for which capillarity is important. Nonetheless much of the complicated physics behind surface cooling creating a surface skin remains to be incorporated within the lubrication model. It is worth noting that chemically inert and constant thickness skins have been incorporated via nonlinear skin models into providing surface boundary conditions for skins (Sridhar *et al.*, 2001; Huang and Suo, 2002a, 2002b) leading to surface patterning and morphology but await coupling to thermal or other fields.

V. FILMS DRIVEN BY INTERMOLECULAR FORCES

In this section, we focus on thin films driven by intermolecular forces; a seminal review by de Gennes (1985) provides a detailed background to this area. A considerable amount of progress has been made since then and since the last major review by Oron *et al.* (1997) with a number of theoretical, numerical, and experimental studies focusing on the rupture and subsequent dewetting of ultrathin single films and bilayers. We begin by reviewing preliminary fundamental concepts and, for completeness and where appropriate, provide a link back to classical results despite the fact that they may have been reviewed by Oron *et al.* (1997).

A. Fundamental considerations

In situations whereby the local film thickness achieves values in the range of 1000 Å or lower, intermolecular forces become operative (de Gennes, 1985; Sharma and Ruckenstein, 1986; Israelachvili, 1992; Reiter, 1992; Sharma and Jameel, 1993; Elbaum and Lipson, 1994; Stange *et al.*, 1997) and often have a dramatic influence on the dynamics. If the underlying support corresponds to a low-energy solid substrate, which is only partially wetted by the fluid, or if the film contains low-surface energy particles, then intermolecular forces play a destabilizing role, amplifying perturbations, which may lead to film rupture in finite time, followed by dewetting. These processes are manifested via the appearance of holes and discrete droplets in the initially uniform coating, connected by ultrathin films, as shown in Fig. 5 (Becker *et al.*, 2003).

Coating nonuniformities in the automotive industry can lead to surface "mottling" and oxidization, wear, or corrosion (Viens *et al.*, 1996). In gravure printing and photofinishing applications, film deformations may lead to rupture, which is undesirable, leading to so-called "reticulation" (Schwartz and Roy, 2001). Recently, however, pattern formation in thin liquid films resting on homo-

geneous and heterogeneous solid substrates has emerged as a potentially positive effect and has received considerable attention (Jacobs, Herminghaus, and Mecke, 1998; Sferrazza *et al.*, 1998; Reiter *et al.*, 1999; Konnur *et al.*, 2000; Seemann *et al.*, 2001a, 2005; Kargupta and Sharma, 2002; Neto *et al.*, 2003; Reiter, 2003; Kalliadasis and Thiele, 2007) as a method which can be used for the templating films in microelectronics. Understanding thin film stability in the presence of complex intermolecular interactions is vital to both model and control and, in some cases, prevents pattern formation phenomena in thin films.

B. Free energy of interaction

In order to describe additive interactions between molecules and flat surfaces, one performs a triple integration provided the separation between a molecule and the surface is much larger than a molecular diameter. For purely attractive pair potentials of the form $\varphi(r) = -C/r^n$, where C and r denote the interaction strength and the separation distance between two molecules, respectively, the net energy of interaction for a molecule with a distance r from a surface is $\Phi(r)_{ms} = 2\pi C\rho/(n-2)(n-3)r^{n-3}$; here ρ is the number density of the molecules in the solid and the dependence on r has been modified as a result of the triple integration. Similarly, the energy of interaction between two surfaces is $\Phi(r)_{ss} = 2\pi C\rho^2/(n-2)(n-3)(n-4)r^{n-4}$ (Israelachvili, 1992). Unretarded Lifshitz–van der Waals (LW) induced dipole-dipole interactions between molecules, due to polarization fluctuations, scale as r^{-6}, and in the presence of retardation effects, which become effective for distances exceeding 100 nm, these interactions scale as r^{-7}. In the former cases, for two planar surfaces, the interaction energy per unit area is described by

$$\Phi(r) = -A/12\pi r^2. \tag{98}$$

Here $A = \pi^2\rho_1\rho_2 C$ is the Hamaker constant where ρ_1 and ρ_2 correspond to the number densities of the surfaces. The values of A are in the range of 10^{-20}–10^{-19} J (Israelachvili, 1992) and can be determined from dielectric constants of the interacting media. The van der Waals interactions are relatively long range and can be significant over distances of order 100 nm since $\Phi(r) \sim r^{-2}$. If $A > 0$ then energy is gained by decreasing the separation of the two surfaces r and vice versa.

The effective excess free energy of per unit area $\Phi(h)$ dictates the possibility of dewetting in thin films, where we have replaced r by h, which corresponds to the distance between the interacting "surfaces," the gas-liquid and liquid-solid interfaces. Following Seemann *et al.* (2001a), if the global minimum of $\Phi(h)$ is at a finite value of h, $h_{\min}$, where $h_{\min}$ represents the equilibrium film thickness then dewetting will occur; this is readily satisfied for curves 2 and 3 in Fig. 24 but not for curve 1. Provided the second derivative of $\Phi(h)$, often referred to as the "spinodal parameter," is negative $\Phi_{hh} < 0$, then an initial perturbation of wave number k can undergo

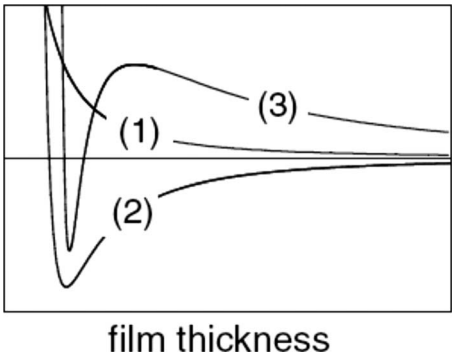

FIG. 24. Schematic of $\Phi(h)$ where 1, 2, and 3 represent Φ for which the films are stable, unstable, and metastable, respectively (see text). From Seemann *et al.*, 2001a.

exponential growth, with a growth rate that depends on k, and a most dangerous mode associated with an intermediate value of k, k_{m}, for which the growth rate is maximized. This mode dominates the initial stages of the ensuing pattern formation before nonlinearities become significant. This mechanism has been termed "spinodal" dewetting due to its similarity to spinodal decomposition of mixtures, an analogy identified and explored by Mitlin (1993), which occurs when the second derivative of the free energy with respect to composition becomes negative (Cahn, 1965; Vrij, 1966; Vrij and Overbeek, 1968; Brochard-Wyart and Daillant, 1990; Mitlin, 1993).

For metastable films, characterized by curve 3 in Fig. 24, $\Phi_{hh} < 0$ for a sufficiently small film thickness but for larger film thickness $\Phi_{hh} > 0$. For these thicker films, dewetting can also arise, which, in this case, occurs through the nucleation of holes in the film due to the presence of so-called "defects." This, in turn, may be brought about by the presence of substrate heterogeneities that may occur either accidentally, via chemical patterning of the substrate, or from the presence of dust particles on the surface of the liquid. This is due to local gradients in chemical potential or wettability and is often referred to as "heterogeneous nucleation" (Mitlin, 1993, 1994). If the value of h is such that the sign of Φ_{hh} is close to being reversed, the dewetting mechanism is termed homogeneous nucleation; in this case, energy barriers for dewetting are overcome via thermal fluctuations (Blossey, 1995). Both thicker and thinner films that dewet could undergo a long wave instability (Becker *et al.*, 2003), the difference is that in the thicker film dewetting by nucleation occurs first. An informative discussion of these issues and of stable, unstable, and metastable states, which is slightly different from that advanced in Seemann *et al.* (2001a), has been given by Thiele (2003). It is arguable that assigning terms such as "metastable" to a specific form of the disjoining pressure could be misleading. One could, for instance, consider whether, for a particular disjoining pressure, a film of a certain thickness is linearly stable, unstable, or metastable. An informative review of this topic and of the experimental issues has been given by Jacobs *et al.* (2008).

The free energies of interaction per unit area discussed so far have featured a long-range apolar component only. However, short-range repulsion forces are also present and act over distances typically equal to 10 nm. These forces may be due to electrostatic interactions (de Gennes, 1985; Teletzke *et al.*, 1988; Israelachvili, 1992) arising from the overlap of diffuse electric double layers, which form near interfaces involving polar fluids (Derjaguin and Landau, 1941; Verwey and Overbeck, 1948). The free energy per unit volume $\phi=\Phi_h$, given by Sharma and Jameel (1993),

$$\phi = \frac{A}{6\pi h^3} - \frac{S^P}{l}\exp\left[\delta_l\left(1-\frac{h}{h_{\min}}\right)\right], \tag{99}$$

is also known as the "conjoining" pressure (the "disjoining" pressure is $\Pi=-\phi$) and enters the evolution equations of Sec. II, where $h_{\min}$ and l denote an equilibrium distance due to short-range repulsion and a correlation length, respectively; note that $\phi(h_{\min})=0$ and typically $h_{\min}\sim 1.58$ Å and $l\sim 0.6$ nm so that $\delta_l \equiv h_{\min}/l \ll 1$. In the presence of long-range forces only, that is, with $S^P=0$, an initially uniform film is unstable (stable) if $A>0$ ($A<0$).

The function ϕ comprises long-range apolar LW and short-range polar (P) forces, represented by the first and second terms on the right-hand side of Eq. (99), respectively. In Eq. (99) $A=-12\pi h_{\min}^2 S^{\mathrm{LW}}$ and S^{LW} and S^{P} denote the LW and P components of the spreading coefficient, $S=S^{\mathrm{LW}}+S^{\mathrm{P}}$. Here $S=\sigma_s-(\sigma_{ls}+\sigma)$ with S^{LW} and S^{P} defined with the same functional dependence on the surface tensions except that each σ acquires superscripts of LW and P, respectively. The surface tensions of the gas-liquid, liquid-solid, and gas-solid interfaces are σ, σ_{ls}, and σ_s and have been decomposed into their LW and P components. Note that the LW components of the interfacial tensions can be evaluated using the Good-Girifalco-Fowkes combining rule (Good and Girifalco, 1960) while the P components can be determined from "acid-base" interactions obtained from contact angle measurements (van Oss *et al.*, 1987; Janczuk *et al.*, 1989). The second term in Eq. (99) demonstrates that the polar component of the excess free energy per unit volume decays exponentially in space (Sharma, 1993).

Polar forces can be considered negligible provided the film and at least one of the bounding media are apolar (Sharma, 1993). In this case, the following expression for ϕ is used (Mitlin, 1995; Seemann *et al.*, 2001a):

$$\phi = \frac{A}{6\pi h_{\min}^n}\left[\left(\frac{h_{\min}}{h}\right)^n - \left(\frac{h_{\min}}{h}\right)^m\right], \tag{100}$$

where $m>n>1$ and the second term represents short-range Born repulsion, with $(n,m)=(3,9)$, ϕ corresponds to a so-called 6-12 Lennard-Jones potential (Mitlin, 1993, 1994). If both Born and electrostatic repulsion forces are operative then a combination of Eqs. (99) and (100) can be used (Mitlin, 1995). As will be discussed in Sec. V.D, the inclusion of repulsion forces in ϕ is necessary in order to simulate dewetting dynamics past the stage where the film ruptures. We shall return to Eq. (100) in Sec. V.E to show how this equation can be used in the simulation of films involving contact lines.

An alternative form for the disjoining pressure was recently proposed by Pismen and Pomeau (2000). This approach was derived starting from the generalized equations for hydrodynamics for nonequilibrium systems comprising diffuse interfaces (Anderson *et al.*, 1998); the density is treated as an additional dynamic "phase" variable. A contact line was considered and the interaction between the gas-liquid and liquid-solid interfaces was determined. The form of the disjoining pressure obtained recovers that in the sharp interface limit (Pismen, 2001, 2002); this form also does not give rise to singularities as $h\to 0$ since the disjoining pressure exhibits a minimum with h ensuring that the solid substrate is recovered by a precursor layer. In the context of moving contact lines, this diffuse interface approach has been reviewed by Bonn *et al.* (2008).

C. Experiments

A large number of dewetting experiments have made use of polystyrene films, which are weakly volatile, nonpolar, and inert chemically. Thin layers of polystyrene dissolved in suitable solvent (e.g., toluene) are deposited on a solid substrate (e.g., silicon wafers or cleaved mica sheets) using spin or dip coating. Evaporation of the solvent leads to the formation of a layer of polystyrene at a temperature below the glass transition value T_g. The thickness of this glassy polymer layer can range from several nanometers to micrometers and the wettability of the substrate can be altered by silanation. Ellipsometry and atomic force microscopy (AFM) are used to measure the film thickness and its topography (Seemann *et al.*, 2005). Upon heating the layers above T_g, the dewetting commences. This process starts due to film rupture and hole formation, which is followed by hole widening and coalescence. This is then followed by breakup of the ridges separating holes into drops via a Rayleigh instability.

Distinguishing between nucleation-driven and spinodally driven ruptures is often done by measuring the average hole wavelength. However, this is rather difficult particularly for relatively thick films for which spinodal growth rates are slow (they vary as h^{-5} as will be shown in Sec. V.D); the invariable presence of chemical heterogeneities which lead to local gradients in Φ also complicates matters (Herminghaus *et al.*, 1998; Jacobs, Herminghaus, and Mecke, 1998; Konnur *et al.*, 2000). So-called "Minkowski functionals" are used in order to determine the statistics of the distribution of holes particularly in situations wherein radial correlation functions or Fourier transforms cannot be used to demonstrate correlations between the location of the holes (Jacobs *et al.*, 2000). The existence of these spatial correlations is a signature of spinodal dewetting scenarios; their absence is often indicative of dewetting driven by heterogeneous nucleation (Reiter, 1992, 1993; Jacobs, Herminghaus, and Mecke, 1998; Jacobs *et al.*, 2000) although the origin of the nucleated holes remains some-

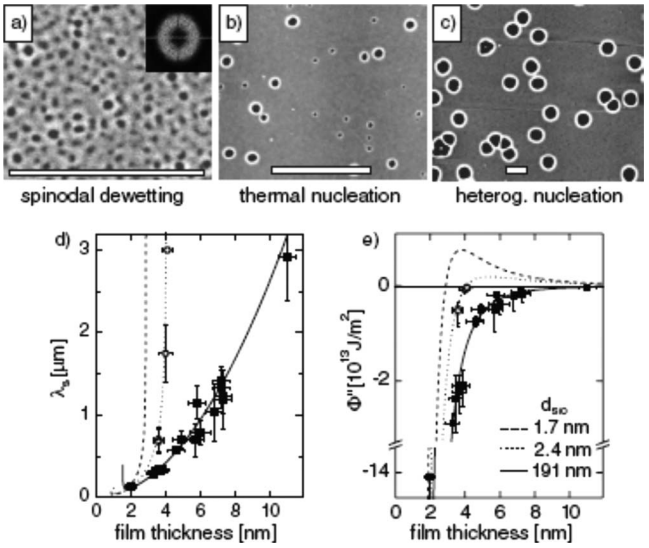

FIG. 25. Atomic force microscopy images of dewetting patterns in polystyrene (molecular weight 2.05 kg/kmol) films of initially uniform thickness h on silicon wafers covered with layer of silicon oxide d. In (a)–(b) and (c), $(h,d)=(3.9,191)$, (4.1,2.4), and (6.6,1.7) nm, and the patterns observed are representative of spinodal dewetting, homogeneous thermal nucleation, and heterogeneous nucleation, respectively. In each panel, the bar indicates 5 μm and the elevation ranges from 0 to 20 nm represented by black and white regions, respectively. (d) The dependence on h of the pattern wavelength predicted for a spinodally driven dewetting process λ_s for two different silicon oxide thicknesses: 2.4 nm (open circles) and 191 nm (filled squares). (e) Reconstructed Φ_{hh} as a function of h for various d values using Eq. (101). From Seemann *et al.*, 2001a.

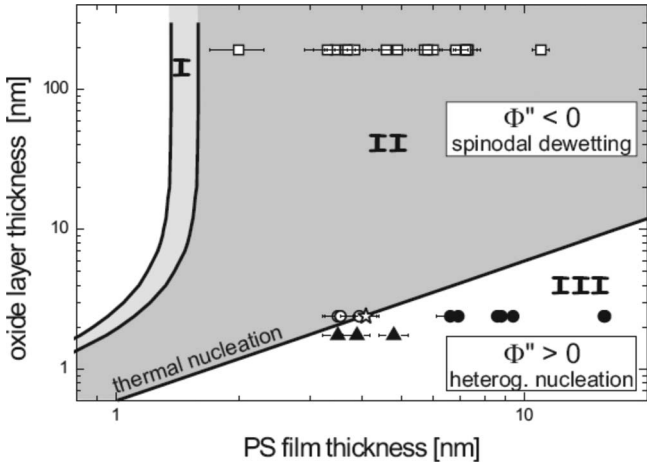

FIG. 26. Stability diagram showing the regions in the space of the polystyrene film thickness and the thickness of the underlying silicon oxide layer where spinodal, thermal nucleation, and heterogeneous nucleation-driven dewetting occurs. From Seemann *et al.*, 2001b.

what unclear (Seemann *et al.*, 2005). Thus Minkowski functionals can be used to distinguish between the mechanisms underlying dewetting.

Experiments involving polystyrene films on silicon wafers covered with silicon oxide of known thickness d have been carried out in order to study spinodal and nucleation-driven dewetting. Variation in d over a typical range of 0–200 nm (Seemann *et al.*, 2005) allows the alteration of Φ: increasing d leads to negative values of the long-range component of Φ at sufficiently small thicknesses (less than 10 nm). Figure 25 (Seemann *et al.*, 2001a, 2005) shows the dependence of dewetting patterns observed using AFM on the value of d. Also shown in this figure are variations in λ_s and Φ_{hh} with h plotted parametrically as a function of h where λ_s is given by (Vrij, 1966; Ruckenstein and Jain, 1974)

$$\lambda_s = (-8\pi^2\sigma/\Phi_{hh})^{1/2}. \tag{101}$$

This formula illustrates the fact that $\lambda_s > 0$ if and only if $\Phi_{hh} < 0$ and that $\lambda_s \to \infty$ as $\Phi_{hh} \to 0$. Furthermore, knowledge of σ and direct measurement of λ_s for varying h allow one to determine Φ_{hh}, which, in turn, can be used to construct $\Phi(h)$. This is done by first using the Hamaker constant as a fitting parameter, then by fixing the value of $\Phi(h_{\min})$ through the use of $\Phi(h_{\min}) = \sigma[1 - \cos(\theta)]$, where θ is the macroscopic angle (which should not be confused with the angle of inclination to the horizontal in Sec. II) subtended at the contact line by the film (Frumkin, 1938); this is followed by fixing the location of $\Phi(h_{\min})$ via measurement of $h_{\min}$ directly using, for instance, x-ray reflectivity (Seemann *et al.*, 2001a, 2001b, 2005).

Inspection of panels (a)–(c) of Fig. 25 reveals that the patterns observed are subtly different: for relatively small h and large d, the patterns are characterized by a reasonably well-defined wavelength, as demonstrated by panel (a) [and the filled squares in panel (d)]; for the case of relatively large h and small d shown in (c), there appears to be no such wavelength and virtually no correlations between the locations of the holes, which, in this case, result from nucleation events (Jacobs, Herminghaus, and Mecke, 1998). It is possible to construct a diagram describing the stability of the film and the type of patterns one observes as a function of d and h (Seemann *et al.*, 2001b); an example of such a diagram is shown in Fig. 26.

The holes become deeper via expulsion of the material beneath a depression and its accumulation into "rims" or capillary "ridges"; these correspond to the white regions in Fig. 25(c). During retraction of the rim, the majority of the energy dissipation occurs at the contact line between the film and the underlying substrate. Depending on the nature of the material, whether a simple Newtonian fluid or a non-Newtonian polymer melt, the behavior at the contact line will be different and this impacts the variation in the hole radius R with time (Brochard-Wyart *et al.*, 1987, 1992, 1994; Redon *et al.*, 1994). For relatively thick films for which the film thickness greatly exceeds the slip length viscous dissipation dominates and $R \sim t$; in the opposite case, slip dominates resulting in $R \sim t^{2/3}$ (Brochard-Wyart *et al.*, 1994). Expressions for $R(t)$ have been developed (Jacobs, Seemann, *et al.*, 1998; Neto and Jacobs, 2004) that combine

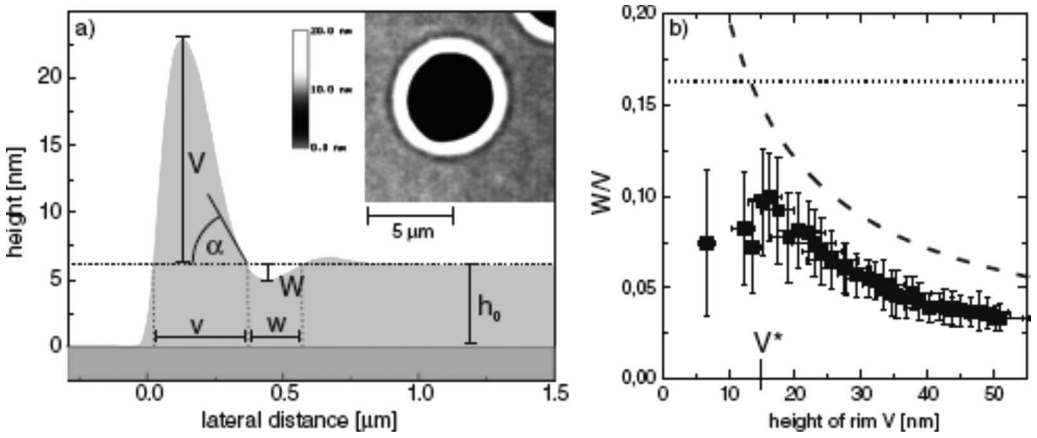

FIG. 27. Radial cross section of a hole (a) scanned via AFM (see inset) for a 6.6 nm thick polystyrene (PS) film on a 191 nm silicon oxide layer resting on a silicon wafer. (b) The ratio of the depression depth W to the rim height V as a function of V for a 11 nm thick PS film on a similar substrate to that in (a). Here the dots represent experimental data, while the dotted and dashed lines represent the predictions of lubrication theory at early and late times (Herminghaus *et al.*, 2001, 2003) respectively. From Seemann *et al.*, 2005.

both mechanisms, which appear to capture the dynamics throughout the lifetime of a hole. Specifically, at early times $R \sim t^{2/3}$ and at later times $R \sim t$.

AFM measurements also show that during hole growth and rim retraction the contact angle remains essentially constant with time as well as temperature. A typical AFM scan of a hole is shown in Fig. 27, which exhibits the salient features: the interfacial slope is high near the contact line and comparatively lower upstream of the rim. The degree of asymmetry seen in Fig. 27 becomes accentuated with polymer chain length. For short chains, the hole profile is oscillatory in space and exhibits a "trough" upstream of the rim, as shown in Fig. 27(a) (Ghatak *et al.*, 1999; Seemann *et al.*, 2001a). More recent work has examined the influence of the film rheology on the interfacial shape (Jacobs, Herminghaus, and Mecke, 1998; Reiter, 2001; Seemann *et al.*, 2001a; Herminghaus *et al.*, 2002) which has demonstrated that the shape of dewetting fronts can be influenced by elastic effects.

In certain cases, the rim shown in Fig. 27 can be vulnerable to azimuthal or transverse disturbances and undergoes a fingering instability, which leads to a more efficient dewetting process (Brochard-Wyart and Redon, 1992; Reiter, 1992; Sharma and Reiter, 1996; Xie *et al.*, 1998; Sharma and Khanna, 1999; Ghatak *et al.*, 2000; Reiter and Sharma, 2001). The fingers may eventually pinch off into droplets an example of which is provided in Fig. 28 (Reiter and Sharma, 2001). In the experiments of Reiter and Sharma (2001), films of polydimethylsiloxane (PDMS) dewetting over silicon wafers coated with grafted polymer brushes of end-functionalized PDMS molecules exhibited fingering; in contrast, PDMS films on adsorbed PDMS layers exhibited stable dewetting fronts. Furthermore, whereas the velocity of the mean position of the dewetting fronts was essentially constant on adsorbed layers, in the case of dewetting on grafted PDMS layers, this velocity decreased with time during the early stages of the dewetting process before achieving an approximately constant value. For the grafted PDMS layers, the slip length was estimated to be approximately 10 μm whereas in the adsorbed PDMS layer case it was negligibly small, which illustrates the important role of slip as a key "ingredient" for the fingering observed in dewetting (Reiter and Sharma, 2001). The fingering phenomena, the spatially oscillatory nature of the hole profile, and the need to simulate the collective three-dimensional dewetting dynamics provided challenging problems for theorists. A review of modeling and simulations studies in this area is provided next.

D. Modeling and simulations

Numerical simulations of rupture and dewetting processes have been carried out using lubrication theory by including ϕ as an extra pressure or energy per unit volume in the momentum conservation equations, as demonstrated in Sec. II. By setting $\mathcal{G}=\mathcal{B}=0$, $\mathcal{U}=\epsilon A/6\pi\mu\mathcal{H}^2$, $\mathcal{L}=\mathcal{H}^2/(A/6\pi\sigma)^{1/2}$, and scaling ϕ on $A/6\pi\mathcal{H}^3$, the evolution equation (37) then becomes

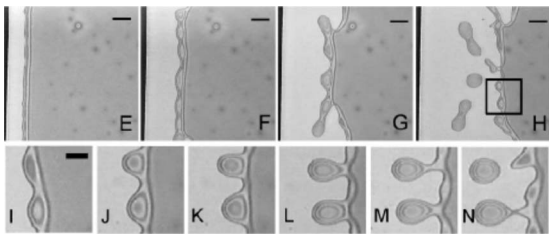

FIG. 28. A sequence of optical micrographs showing the onset and evolution of a fingering instability during the retraction of a 50 nm PDMS film on a silicon wafer coated with a grafted PDMS layer of 6 nm thickness. The area shown in I–N corresponds to the box depicted in H. The bar length corresponds to 10 μm in I–N and 25 μm in E–H. From Reiter and Sharma, 2001.

$$h_t - \nabla \cdot \left[\frac{h^2}{3}(3\beta + h)\, \nabla\, (p + \phi) \right] = 0, \tag{102}$$

with $p = -\nabla^2 h$ in which ϕ is given by either Eq. (99) or (100) whose dimensionless versions are given by

$$\phi = \frac{1}{h^3} - \mathcal{S} \exp\left[\delta_l \left(1 - \frac{h}{h_{\min}} \right) \right], \tag{103}$$

$$\phi = \frac{1}{h_{\min}^n} \left[\left(\frac{h_{\min}}{h} \right)^n - \left(\frac{h_{\min}}{h} \right)^m \right], \tag{104}$$

where $\mathcal{S} \equiv (S^P/l)/(\Lambda/6\pi\mathcal{H}^2)$. Note that $\mathcal{L}/\mathcal{U} = \sigma\mu\mathcal{H}^5/(\Lambda/6\pi)^2$, which shows that the time scales for dewetting process scale as $\mathcal{H}^5$, as mentioned in Sec. V.C and that pattern length scales vary as $\mathcal{H}^2$. This dependence of the spatial and temporal scales on the film thickness is typical of situations wherein $\Phi_{hh} < 0$ (see curve 2 in Fig. 24) and spinodal dewetting is prevalent (Sharma, 2003; Thiele, 2003).

Equation (102) has been used to investigate rupture by employing Eq. (104) in the absence of short-range repulsion in Cartesian coordinates (Ruckenstein and Jain, 1974; Williams and Davis, 1982; Sharma and Ruckenstein, 1986) and axisymmetry (Witelski and Bernoff, 1999; Zhang and Lister, 1999; Vaynblat *et al.*, 2001) and with surfactant (Jensen and Grotberg, 1992; Lin *et al.*, 2000; Warner *et al.*, 2002). These studies have shown that van der Waals forces grow under depressions, driving fluid away from these regions, which strengthens these forces further and drives a rupture instability. The work of Zhang and Lister (1999) demonstrated that rupture occurs in a self-similar manner, with the scaling $h \sim (t - t_r)^{-1/5}$, where t_r is the rupture time, by balancing van der Waals and capillary forces; this scaling holds even with the presence of surfactant (Warner *et al.*, 2002) as the height and surfactant equations locally decouple close to rupture.

In order to simulate dewetting dynamics using Eq. (102), however, Eq. (103) or (104) with short-range repulsion has been used; this provides the necessary stabilization against rupture that may bring about nonphysical singularities as $h \to 0$. Studies based on the numerical solution of these equations in one dimension, starting from initially pseudorandom small-amplitude perturbations, for parameter values where spinodal dewetting is expected to dominate, have yielded detailed information about the short- and long-time dynamics of dewetting. The agreement with the predictions of linear theory in terms of preferred wavelengths and time scales is also very good [see, for instance, Sharma (1993, 2003); Sharma and Jameel (1993); Ghatak *et al.* (1999), and references therein]. These one-dimensional studies were extended to account for the interplay between dewetting and evaporation-condensation effects (Oron and Bankoff, 1999, 2001) and time-dependent substrate wettability (Suman and Kumar, 2006) using an equation similar to Eq. (79), in which ϕ [with Eq. (104) and $(n,m) = (3,4)$] was added to the pressure.

Thiele *et al.* (2001) using Eq. (103) showed that the existence of parameter ranges within the spinodal regime for which nucleation is the dominant mechanism for dewetting; here the dependence on the initial finite-amplitude disturbances is significant. In the spinodal regime, however, the early-time dewetting dynamics are dominated by the fastest growing linear mode. These findings are important since they demonstrate that spinodal dewetting is not always dominant for linearly unstable film thickness ranges and provide an explanation of the results of Jacobs, Herminghaus, and Mecke (1998) who observed nucleation-driven patterns when spinodal dewetting was expected. Glasner and Witelski (2003) studied the process by which morphological changes are engendered in thin films as a result of dewetting and the "coarsening" process by which droplets connected by ultrathin films move on very long time scales. This was done via reduction in Eq. (102) [with ϕ given by Eq. (104) and $(n,m) = (3,4)$] to a system of ordinary differential equations for the locations and pressures of N droplets. This work showed that $N \sim t^{-2/5}$, which provides a scaling law for the droplet number and an indication of the rate of coarsening in dewetting processes.

Lubrication theory has also been used to investigate some of the features discussed in the previous section such as the spatially oscillatory interfacial profile, the fingering phenomena, and the effects of slip and viscoelasticity on the dynamics. Lubrication-based models have been developed for significant slip (Kargupta *et al.*, 2004; Münch *et al.*, 2005), which comprise two coupled evolution equations, one for h and another for the streamwise velocity component u_o, which, in this limit, is independent of the vertical coordinate (the so-called "plug flow" limit),

$$h_t + (u_0 h)_x = 0,$$

$$\mathrm{Re}(u_{0t} + u_0 u_{0x}) = \frac{4}{h}(h_0 u_{0x})_x + (h_{xx} - \phi)_x - \frac{u_0}{\beta h}. \tag{105}$$

In the limit, $\beta \to \infty$, Eq. (105) reduces to those used to study "free" films (films of one fluid sandwiched between layers of other fluids) (Erneux and Davis, 1993). It is also straightforward to show that Eq. (105) also reduces to Eq. (102) as $\beta \to 0$ (Münch *et al.*, 2005), the latter being appropriate in situations wherein the effects of slip are relatively weak but non-negligible. Models for intermediate slips have also been derived using lubrication theory (King and Bowen, 2001; Fetzer *et al.*, 2005; Münch and Wagner, 2005; Münch *et al.*, 2005). The use of linear stability theory, matched asymptotic expansions and numerical techniques in these models provided an explanation of the fingering phenomena (Münch and Wagner, 2005; King *et al.*, 2006) and the change in the interfacial profile of a hole from a damped oscillation [see Fig. 27(b)] to monotonic decay from the rim toward the unperturbed film by increasing the slip length (Fetzer *et al.*, 2005; Münch *et al.*, 2005); the latter feature had been attributed to elastic effects (Herminghaus *et al.*, 2002, 2003; Saulnier *et al.*, 2002; Shenoy and Sharma,

2002). The location of the dewetting front was found to vary in time as t in the weak- and strong-slip limits and as $t^{2/3}$ in the intermediate-slip limit (Münch *et al.*, 2005). Furthermore, increasing the relative significance of slip in these Newtonian models leads to more asymmetric rim profiles (Münch *et al.*, 2005), which had also been attributed to the presence of viscoelasticity. Blossey *et al.* (2006) showed further that in the weak- and strong-slip limits linear viscoelastic effects do not affect rupture and that strong slip influences the preferred pattern wavelength λ_s. This calls into question the use of Eq. (101) for the reconstruction of $\Phi(h)$ via measurement of λ_s in the presence of strong slip.

The one-dimensional lubrication models have been extended to account for two-layer systems as in the evolution equations (26) of Sec. II. In the absence of short-range repulsion, Danov, Paunov, Alleborn, *et al.* (1998), Danov, Paunov, Stoyanov, *et al.* (1998), and Paunov *et al.* (1998) first considered the stability of two-layer films to van der Waals–driven rupture in the presence of evaporation, thermocapillarity, and soluble surfactants. Their linear stability analysis showed that both unstable squeezing and bending linear modes (often referred to as "varicose" and "sinuous," or "zigzag" modes, respectively) exist; their numerical simulations demonstrated that varicose modes eventually lead to rupture for all but the thinnest films considered. More recent work examined the effect on the bilayer stability of having a highly viscous upper layer (Matar *et al.*, 2002) in one case and a non-Newtonian lower layer (Zhang *et al.*, 2003a) in another within the context of pulmonary flows and tear film rupture, respectively. The effect of confinement by an upper wall on the stability of an interface separating two thin immiscible layers sandwiched between two plates was also studied using the lubrication approximation by Joo and Hsieh (2000). They derived a single evolution equation for the interfacial position (and deal with the effect of confinement in a similar way to that outlined in Sec. III.C), accounting for van der Walls forces and thermocapillary effects. They demonstrated that rupture occurs in the thinner, less viscous, and hotter of the two confined layers.

To probe the nonlinear two-layer film dynamics, the presence of short-range repulsive forces was also added to the model equations (Fisher and Golovin, 2003; Pototsky *et al.*, 2004, 2005; Merkt *et al.*, 2005); these studies have also taken into account heating from above and below (Merkt *et al.*, 2005; Pototsky *et al.*, 2005), upper wall confinement (Merkt *et al.*, 2005), and the presence of surfactants (Fisher and Golovin, 2005). The equations underlying these models correspond to those derived in Sec. II [Eqs. (26)–(28)], with $\mathcal{G}=\mathcal{B}=0$ and the functions $\phi_1(h_1,h_2)$ and $\phi_2(h_1,h_2)$, the conjoining pressures at the gas-liquid and liquid-liquid interfaces, respectively, given by the following expressions:

$$\phi_1 = \frac{\mathcal{A}_{21g}}{(h_1-h_2)^3} + \frac{\mathcal{A}_{g12s}}{h_1^3} - \mathcal{S}_1 \exp\left(\frac{h_{\min}-(h_1-h_2)}{\ell_2}\right), \tag{106}$$

$$\phi_2 = \frac{\mathcal{A}_{12s}}{h_2^3} - \frac{\mathcal{A}_{21g}}{(h_1-h_2)^3} - \mathcal{S}_1 \exp\left(\frac{h_{\min}-h_2}{\ell_1}\right) + \mathcal{S}_2 \exp\left(\frac{h_{\min}-(h_1-h_2)}{\ell_2}\right). \tag{107}$$

These formulas represent generalizations of Eq. (103). Here $\mathcal{A}_{21g}$, $\mathcal{A}_{g12s}$, $\mathcal{A}_{12s}$, and $\mathcal{A}_{21g}$ are given by

$$\mathcal{A}_{21g} \equiv \frac{A_{21g}}{6\pi P\mathcal{H}^3}, \quad \mathcal{A}_{g12s} \equiv \frac{A_{g12s}}{6\pi P\mathcal{H}^3}, \quad \mathcal{A}_{12s} \equiv \frac{A_{12s}}{6\pi P\mathcal{H}^3}, \tag{108}$$

and denote dimensionless Hamaker constants that characterize the magnitude of the dispersive van der Waals interactions between the gas-liquid and liquid-liquid interfaces, the gas-liquid and liquid-solid interfaces, and the liquid-liquid and liquid-solid interfaces, respectively. The dimensional Hamaker constants can be related to the refractive indices of the media (Israelachvili, 1992; Pototsky *et al.*, 2005). Here $P=\mu\mathcal{U}\mathcal{L}/\mathcal{H}^2$ with $\mu=\mu_2$, $\mathcal{H}=H_2$, and $\mathcal{U}=\epsilon A_{21g}/6\pi\mu_2\mathcal{H}_2^2$ giving $P=A_{21g}/6\pi\mathcal{H}_2^3$. The parameters $\mathcal{S}_1$ and $\mathcal{S}_2$ are given by

$$\mathcal{S}_i \equiv S_i^P/P\mathcal{H}, \quad i=1,2, \tag{109}$$

where S_i^P characterize the short-range interactions between the liquid-liquid and liquid-solid and gas-liquid and liquid-liquid interfaces; $(\ell_0,\ell_1,\ell_2)\equiv(l_0,l_1,l_2)/\mathcal{H}$, where $(l_1,l_2)\sim 1-10$ nm are correlation lengths. Equations (106) and (107) can be generalized to include short-range interactions between the gas-liquid and liquid-solid interfaces.

The two-fluid studies have shown that systems comprising two layers are more unstable than an effective single-layer system with growth rates potentially dramatically increased (Pototsky *et al.*, 2004). As noted (Sec. III.A.2), multilayered systems often demonstrate enhanced growth of instabilities. Through a linear stability analysis, they have also demonstrated the existence of sinuous and varicose unstable modes, while the results of time-dependent numerical simulations indicate the richness of the dynamics. This is exemplified by switching between the two unstable modes in the nonlinear regime or coarsening in only one mode (Pototsky *et al.*, 2004, 2005; Merkt *et al.*, 2005); an example of such a transition is shown in Fig. 29. The main advances here correspond to re-expressing Eqs. (26)–(28) in terms of an energy functional, which, in the absence of surface tension gradients, is simply a Lyapunov functional that decays in time (Pototsky *et al.*, 2005). The re-expressed two-layer equations can be analyzed with tools from the theory of dynamical systems [e.g., continuation techniques (Doedel *et al.*, 1997)]. Within this framework, a periodic sequence of drops and flat films corresponds to periodic orbits and fixed points in phase space, respectively.

Other two-layer studies have included effects of soluble surfactants but neglected Born repulsion (Fisher and Golovin, 2005); the Hamaker constants in this case were also functions of the surfactant concentration. The

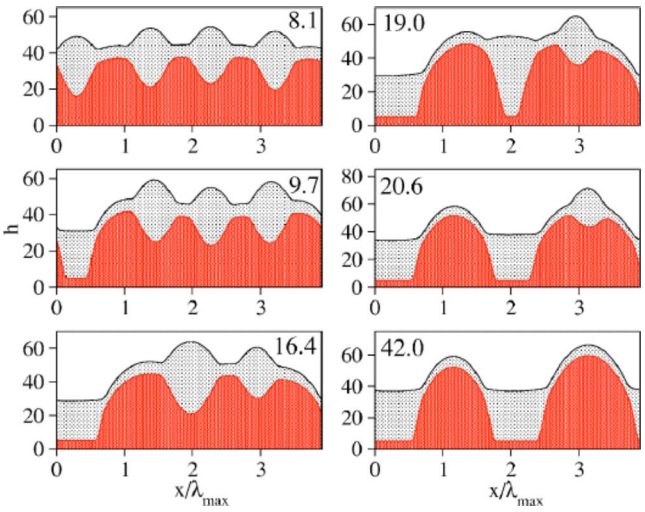

FIG. 29. (Color online) An example of numerical simulations of dewetting in a Si/PMMA/PS/air system, where λ_{max} corresponds to the preferred wavelength from linear theory. These images show a transition from a varicose to a sinuous (or zigzag) mode. From Pototsky *et al.*, 2005.

results of this work showed that rupture is preceded by an oscillatory (in time) instability and the development of standing or traveling waves. This instability is absent from surfactant-free single- and two-layer films and present in surfactant-laden single layers only if the dependence of the Hamaker constant on surfactant concentration is sufficiently strong.

In addition to the above one-dimensional investigations, there have been a large number of studies that reported the results of numerical simulations of the three-dimensional dewetting dynamics. Note that by "three dimensional" we mean that the solutions of Eq. (102) are obtained for $h=h(x,y,t)$: the z coordinate has been eliminated through the application of lubrication theory as outlined in Sec. II. In reviewing this work, it proves helpful to define a "critical" film thickness h_c such that $\Phi_{hh}(h_c)=0$; clearly, for initial thicknesses less (more) than h_c, one would expect to observe spinodal (nucleation) dewetting.

The results of numerical simulations have shown that the morphology of the patterns obtained in the nonlinear regime may be influenced strongly by the perturbation amplitude and wave number depending on the relative magnitude of the initial thickness to h_c. For initial thicknesses smaller than h_c, agreement with the predictions of linear theory in terms of hole density is good [see Sharma and Khanna (1998); Oron (2000b); Bestehorn and Neuffer (2001); Becker *et al.* (2003); Bestehorn *et al.* (2003); Sharma (2003), and references therein]. An example of situations where the initial thickness is well below h_c is illustrated in Fig. 30, which shows a comparison between AFM scans of dewetting PS films on oxidized silicon substrates and the results of numerical simulations of Eq. (102) [with ϕ given by Eq. (104) with $(n,m)=(3,9)$] (Becker *et al.*, 2003; Neto *et al.*, 2003). The agreement in terms of the predicted and measured pattern morphology and time scales is reasonably good. It can also be seen from Fig. 30(a) that the pattern of holes is correlated, which is a signature of spinodal dewetting.

As the initial film thickness approaches h_c from below, the sensitivity of the ensuing dynamics to the presence of defects increases. Thus, although the agreement with linear theory predictions remains favorable in terms of hole density, the patterns observed in both the experiments and simulations are reflective of a combination of spinodal and nucleation-driven dewetting. An example of this is shown in Fig. 31(a), wherein the evolution of a

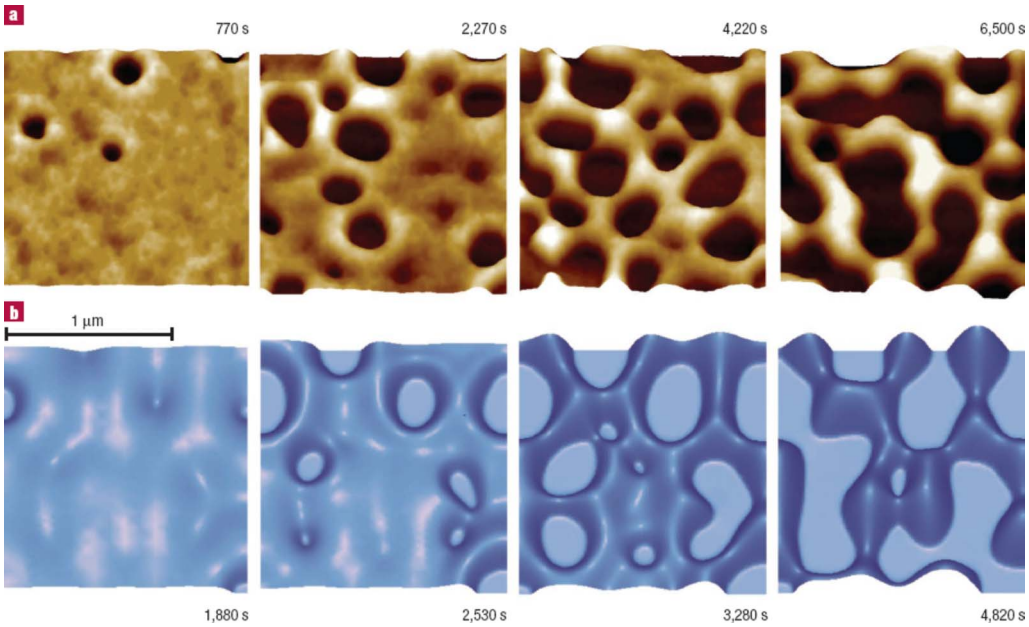

FIG. 30. (Color online) Comparison between experiments (a) and simulations (b) for a 3.9 nm PS film dewetting on oxidized silicon wafers. From Becker *et al.*, 2003.

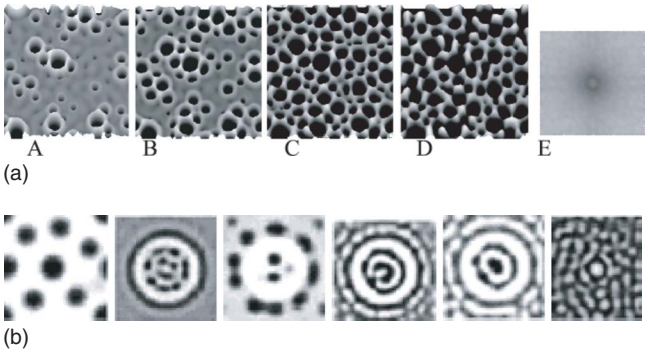

FIG. 31. (Color online) Simulations of dewetting in thin films via numerical solution of Eq. (102) starting from random small-amplitude perturbations. (a) An example of transition from a bimodal to a monomodal distribution of hole size in spinodal dewetting is shown in A–D; E is a Fourier transform of C. (b) Examples of patterns formed around heterogeneities (Kargupta *et al.*, 2000; Konnur *et al.*, 2000; Zope *et al.*, 2001). From Sharma, 2003.

dewetting instability in a 5.5 nm film (h_c=6.8 nm in this case) is simulated in a $10\lambda_s \times 10\lambda_s$ domain (Sharma, 2003). The Fourier transform of panel C of this figure, shown in E, reveals the isotropy of the patterns formed; furthermore, the number of holes in C is 93, which is in excellent agreement with 100, the value predicted from linear theory. The interface evolution, however, is accompanied by the formation of a small number of primary holes, followed by the development of secondary, "satellite" holes (Becker *et al.*, 2003; Neto *et al.*, 2003; Sharma, 2003) in the trough of the primary holes; this is then followed by the formation of other rows of satellite holes around the periphery of the primary one in a cascade of spinodal-driven events. This dewetting behavior is evident in panel B of Fig. 31(a) [Sharma (2003); see also the more recent work of Verma and Sharma (2007)] and in the work of Becker *et al.*, 2003 (see Fig. 5, which is from Fig. 2 of their paper). The coexistence of patterns in the spinodal regime, whose underlying mechanisms are different, has been predicted by Thiele *et al.* (2001). The results of the above studies indicate that the sensitivity of the simulated patterns observed to the initial conditions used in the simulations increases as the initial film thickness approaches h_c; precise knowledge of interfacial and substrate heterogeneities is required to obtain agreement between experiments and simulations in this case (Reiter 2003; Sharma, 2003).

For film thicknesses greater than h_c, the heterogeneous nucleation of a hole may be brought about by an interfacial or substrate defect (or a large-amplitude disturbance in a simulation). In this case, numerical work has shown that this mechanism becomes more dominant than the spinodal one on the basis of kinetics (Kargupta *et al.*, 2000; Konnur *et al.*, 2000; Zope *et al.*, 2001); it has also demonstrated that the time scales associated with the emergence of patterns in simulations exhibit greater sensitivity to the heterogeneity than do the length scales (Kargupta and Sharma, 2001, 2003; Thiele *et al.*, 2003). The presence of heterogeneities can have an organizing influence giving rise to a range of structures that exhibit local order; examples of these patterns are shown in Fig. 31(b). Chemical heterogeneities, which lead to gradients in the interaction potential Φ, can be exploited in the engineering of templated patterns in thin films at the microscale and nanoscale in the presence (Lenz and Kumar, 2007a) and absence (Karim *et al.*, 1998; Kargupta and Sharma, 2001, 2003; Thiele *et al.*, 2003) of an upper wall.

Three-dimensional simulations have also been carried out for two-layer systems (Pototsky *et al.*, 2006), extending the earlier studies of Merkt *et al.* (2005) and Pototsky *et al.* (2004, 2005). The results of these simulations, carried out for superposed layers of PS and PMMA sandwiched between air and a substrate of either silicon or silicon oxide, indicate that different transitions in the interfacial morphology are possible. For silicon substrates a transition occurs from drops to holes at the gas-liquid interface and vice versa in the case of silicon oxide.

Given the very small height scales of interest during dewetting, that is, of the order of nanometers, one could query whether stochastic effects due to thermal noise could become important. Recently, this has been probed by Davidovitch *et al.* (2005) and Grün *et al.* (2006) who generated Langevin lubrication equations. These are the standard lubrication models augmented by an extra driving stress fluctuation term (Mecke and Rauscher, 2005) due to the thermal activity. The solutions, when stochastic terms dominate over surface tension, then modify Tanner's law so that a droplet spreads as $t^{1/6}$ rather than $t^{1/10}$ (Davidovitch *et al.*, 2005). It is also shown that the dewetting process itself can be affected (Grün *et al.*, 2006) with coarsening occurring on the micrometer scale (Fetzer *et al.*, 2007) and thus it is potentially important in practice.

E. Contact line dynamics

We conclude this section by reviewing studies that have employed practical methods for dealing with thin film flows involving moving contact lines. We start off by recalling that perfect and partial wetting situations are characterized by spreading pressures S such that $S>0$ and $S<0$, respectively. In the latter case, a drop of water, say, partially wets a hydrophobic substrate and forms a well-defined equilibrium contact angle θ_e. From the Young-Laplace equation we have $S/\sigma+1=\cos(\theta_e)$ which, for droplets of small aspect ratio, that is $\theta_e \ll 1$, reduces to $S \sim -\theta_e^2\sigma/2$ and this, provided $S<0$, links S^{LW} and S^{P} such that the latter can be calculated (Sharma and Jameel, 1993).

The relation between ϕ and substrate wettability has been exploited in modeling thin film flows in the presence of contact lines using lubrication theory (Schwartz and Eley, 1998). This approach involves postulating the existence of a precursor layer of thickness $h_{\min}$, which is stabilized by the presence of antagonistic short- and

long-range intermolecular forces. Here the following form of ϕ has been used:

$$\phi = \frac{B}{h_{\min}^n}\left[\left(\frac{h_{\min}}{h}\right)^n - \left(\frac{h_{\min}}{h}\right)^m\right] \tag{110}$$

(Mitlin, 1994; Schwartz and Eley, 1998) whence the disjoining pressure is $\Pi = -\phi$. At equilibrium, one assumes that the droplet relaxes to a dimensionless equilibrium shape, given by $h = 1 - x^2$. The dimensionless slope at the edge of the drop $x = 1$ is therefore $h_x = -2$. The tangent of the apparent equilibrium contact angle $\tan(\theta_e)$ is equal to negative of the interfacial slope at the contact line $-h_x = 2$. In the lubrication approximation, θ_e is assumed to be small so that $\tan(\theta_e) \sim \theta_e \approx 2$, which, in dimensional terms, yields $\theta_e = 2\mathcal{H}/\mathcal{L}$; in this context, $\mathcal{H}$ and $\mathcal{L}$ correspond to the central height of the drop and its lateral extent at equilibrium, respectively.

Schwartz and Eley (1998) defined the energy per unit area to displace the interface from $h_{\min}$ to h_d as

$$E(h) = -\int_{h_{\min}}^{h_d} \Pi dh, \tag{111}$$

where h_d is the value of the thickness at a sufficiently large distance from the drop edge such that $h_{\min}/h_d \ll 1$. A horizontal force balance is then performed: the force (per unit length) components responsible for wetting are σ and $E(h_{\min})$; those pulling the drop toward its center, away from the "contact line" region are $\sigma\cos(\theta_e)$ and $E(h_d)$. In the lubrication limit where θ_e is small, this force balance permits the elimination of B in Eq. (110) (Schwartz and Eley, 1998),

$$\Pi = \frac{2(n-1)(m-1)}{(n-m)h_{\min}}\left[\left(\frac{h_{\min}}{h}\right)^n - \left(\frac{h_{\min}}{h}\right)^m\right]. \tag{112}$$

As a result, Π is characterized by $h_{\min}$, m, and n only.

This method obviates the need to explicitly track the edge of droplet and can be used to model the spreading and dewetting of drops on substrates whose wettability is either uniform or nonuniform (Schwartz and Eley, 1998; Schwartz *et al.*, 2005). Computations using this approach (Schwartz and Eley, 1998) recover Tanner's law (Tanner, 1979) and capture complex behavior characterized by hysteretic drop motion (which can arise despite the absence of contact angle hysteresis) (Schwartz, 1998) and "pearling" (Schwartz *et al.*, 2005). The idea is of quite general use and many computations attest to its accuracy and utility (Schwartz *et al.*, 2005; Zhao and Marshall, 2006). Generalizations to bilayers or evolving "lenses" (Matar and Craster, 2006), which are immiscible droplets of one fluid above a layer of another and to droplets in the presence of electric fields (Yeo *et al.*, 2007), have been carried out.

As noted by Schwartz and Eley (1998), the deficiency of this approach is that the choice of $h_{\min}$ clearly affects the spreading rates, although the computed values of these quantities are found to be inversely proportional to the logarithm of $h_{\min}$, in agreement with theoretical predictions (de Gennes, 1985). One can identify the actual $h_{\min}$ for a specific system from experiments and then use a realistic $h_{\min}$ in the numerical simulations. However, for three-dimensional simulations [i.e., when $h = h(x,y,t)$], a compromise is struck between computational efficiency and achieving agreement with experiments in terms of the spreading rates (Schwartz and Eley, 1998).

The work of Pismen and Pomeau (2000) also deserves attention within the context of moving contact lines. As mentioned in Sec. V.B, their approach, which is based on diffuse interface theory, yields an evolution equation for the film thickness within the lubrication approximation that is similar to Eq. (37) for relatively thick films [see also Pismen (2001)]. For films sufficiently thin for intermolecular forces to become operative, their equation contains a disjoining pressure term, which is free from singularities in the limit $h \to 0$; at steady state, the Young-Laplace equation is recovered. This approach can also account for effects of evaporation and condensation at the contact line (Pismen, 2001, 2002; Pismen and Pomeau, 2002). The review by Bonn *et al.* (2008) contains an in-depth discussion of the application of diffuse interface theory to the moving contact line problem.

VI. SURFACTANT DRIVEN FLOWS

Processes involving the spreading of surfactants on thin films are of importance to numerous industrial, biomedical, and daily life settings; these include coating flow technology, microfluidics, surfactant replacement therapy for neonates, film drainage in emulsions and foams, and drying of semiconductor wafers in microelectronics (Leenaars *et al.*, 1990; DeWitt *et al.*, 1994; Grotberg, 1994; Braun *et al.*, 1999; Matar and Craster, 2001; Afsar-Siddiqui *et al.*, 2003a). The spreading is driven by the presence of surfactant concentration gradients, which, due to the dependence of surface tension on surfactant concentration, give rise to surface tension gradients. These, in turn, give rise to Marangoni stresses (Edwards *et al.*, 1991), which drive rapid surfactant spreading in the direction of the uncontaminated (surfactant-free) liquid.

The fundamental difference between surfactant-driven flows and other stress-driven thin film flows such as those driven by thermal gradients discussed in Sec. IV.B is that in the latter case the surface stress resulting from the differential heating of the plate underlying the film is constant. In contrast, the surfactant concentration is strongly coupled to the film evolution: the surfactant molecules are advected along the surface, and, in the case of soluble surfactant, within the bulk. At sufficiently large concentrations, surfactants form "micellar aggregates," and, if volatile, evaporate or adsorb on the substrate rendering it chemically heterogeneous. This extra ingredient of dynamic coupling enriches the models considerably and leads to many interesting dynamics absent from the relatively simpler case of thermally driven films. We discuss later the latest developments in this area.

A. Monolayer spreading

We begin by considering the spreading of a monolayer of insoluble surfactant emplaced upon a pre-existing uncontaminated fluid film of constant depth; this fundamental problem was considered by Borgas and Grotberg (1988), Gaver and Grotberg (1990, 1992), Jensen and Grotberg (1992), Espinosa *et al.* (1993), and Jensen (1994). This work was carried out in connection with surfactant replacement therapy, used as a method of treatment for premature neonates suffering from respiratory distress syndrome (RDS), whose lungs cannot produce adequate quantities of pulmonary surfactant. As a result, RDS gives rise to lung collapse and oedema and is responsible for a large fatality rate in neonates (Grotberg, 1994; Grotberg and Gaver, 1996).

The spreading dynamics are described by a pair of coupled evolution equations for the film thickness and surfactant interfacial concentration derived using lubrication theory (Jensen and Grotberg, 1992; Warner *et al.*, 2004a),

$$h_t = -\nabla\cdot\left(\frac{\mathcal{C}_m}{3}h^3\nabla\nabla^2 h + \frac{1}{2}h^2\nabla\sigma\right), \tag{113}$$

$$\Gamma_t = \frac{\nabla^2\Gamma}{\mathrm{Pe}_s} - \nabla\cdot\left(\frac{\mathcal{C}_m}{2}h^2\Gamma\nabla\nabla^2 h + h\Gamma\nabla\sigma\right). \tag{114}$$

Equations (113) and (114) follow from Eqs. (34) and (36) for a smooth substrate and in the absence of gravitational and intermolecular forces, slip, and surfactant adsorption and desorption: $\mathcal{B}=\mathcal{G}_m=\phi=\beta=J=0$; here $\mathcal{C}_m=\epsilon^2\sigma_m/S$ corresponds to a capillary parameter. The surface tension σ is independent of z and related to the surfactant interfacial concentration Γ via an equation of state. The simplest such equation, suitable for dilute concentrations, is the dimensionless linear relation $\sigma=1-\Gamma$ (Jensen and Grotberg, 1992; Warner *et al.*, 2004a). Note that the dependence of σ on Γ enters the problem only through the surface-tension gradient or Marangoni term; it does not affect the capillary term.

In Table I, we provide estimates for the physical quantities, which are relevant to the surfactant spreading problem with biomedical applications. These estimates are used to determine order of magnitude estimates of the relevant dimensionless parameters, which are listed in Table II. Inspection of Table II reveals that, for biomedical applications in particular, the Bond number $\epsilon\mathcal{G}_m\cot(\theta)$ is sufficiently small so as to render gravitational effects negligible. Within the context of laboratory experiments, however, where the film thickness can be in the millimeter range, gravity can play an important role, leading to flow reversal that counteracts Marangoni-driven spreading (Gaver and Grotberg, 1990, 1992).

Inertial effects are typically negligible at all but the earliest times (Jensen and Grotberg, 1992), as characterized by the product of the film aspect ratio ϵ and the Reynolds numbers, which as shown in Table II are negligibly small. Péclet numbers for these types of flows are large, which reflects their convective nature. Nevertheless, diffusive effects are retained in the models since they are important over boundary layers in which the surfactant concentration undergoes rapid spatial variations; neglecting diffusive effects also gives rise to a singular perturbation problem since they are represented by the highest order concentration derivative in the problem. Similarly, capillary effects are retained despite the small value of the capillary parameter, which scales as ϵ^2. This parameter also multiplies the highest order derivative in the film thickness: discarding it will lead to a singular perturbation problem and its retention provides a physically justifiable regularization mechanism, which aids the computations.

These equations are solved starting from a film of initially uniform thickness $h(x,0)=1$ and a nonuniform distribution of surfactant concentration such as $\Gamma(x,0)=\exp(-\lambda_M x^2)$ or $\Gamma(x,0)=\frac{1}{2}(1+\tanh(\lambda_M[1-x]))$ with λ_M a constant, say, 100 (Gaver and Grotberg, 1990; Jensen and Grotberg, 1992; Warner *et al.*, 2004a). Numerical solutions are found using the method of lines and Gear's method in time subject to

$$(h_x, h_{xxx}, \Gamma_x)(0,t) = 0, \quad (h-1, h_{xxx}, \Gamma)(\mathcal{L}_c, t) = 0, \tag{115}$$

where $\mathcal{L}_c$ is the length of the computational domain. The results of a typical simulation in planar geometry starting from the above initial conditions are shown in Fig. 32. The spreading process follows a power law, whose exponent can be determined using a simple scaling analysis (cf. Sec. IV.D). For a finite mass of surfactant $M=\int_0^\infty\Gamma dx$, $\Gamma\sim M/L_s$, where L_s is the extent of the monolayer (or the position of the surfactant leading edge measured from the flow origin). From the height evolution equation, we obtain $h/t\sim h^2\Gamma/L_s^2$, hence, assuming that $h\sim 1$, $L_s\sim t^{1/3}$ in rectangular geometry. Indeed these scalings are in agreement with the numerical solutions shown in Fig. 32. It is straightforward to generalize this analysis to axisymmetry and to cases wherein $M\sim t^{\alpha_f}$: the surfactant leading edge $L_s\sim t^{(1+\alpha_f)/3}$ or, in cylindrical coordinates, $R_s\sim t^{(1+\alpha_f)/4}$ (Borgas and Grotberg, 1988; Espinosa, 1991; Jensen and Grotberg, 1992). It is also possible to extend this to multilayer configurations or to non-Newtonian fluids (Jensen, 1994; Craster and Matar, 2000).

In Fig. 32, it can be seen that the Marangoni-driven spreading process is accompanied by the formation of a sharp shocklike front away from the flow origin, in the direction of low surfactant concentration, with a severely thinned region upstream; the maximal thickness is almost twice the initial undisturbed height. The thinning, which occurs behind the front, takes place in order to balance the surface stress caused by the large surfactant concentration gradient in this region. Both the film thickness and surfactant concentration appear to vary linearly with distance apart from boundary-layer regions near the flow origin and the surfactant leading edge, in which the solutions satisfy the boundary conditions given by Eq. (115).

The regions away from the boundaries are dominated by Marangoni stresses with diffusion and capillarity be-

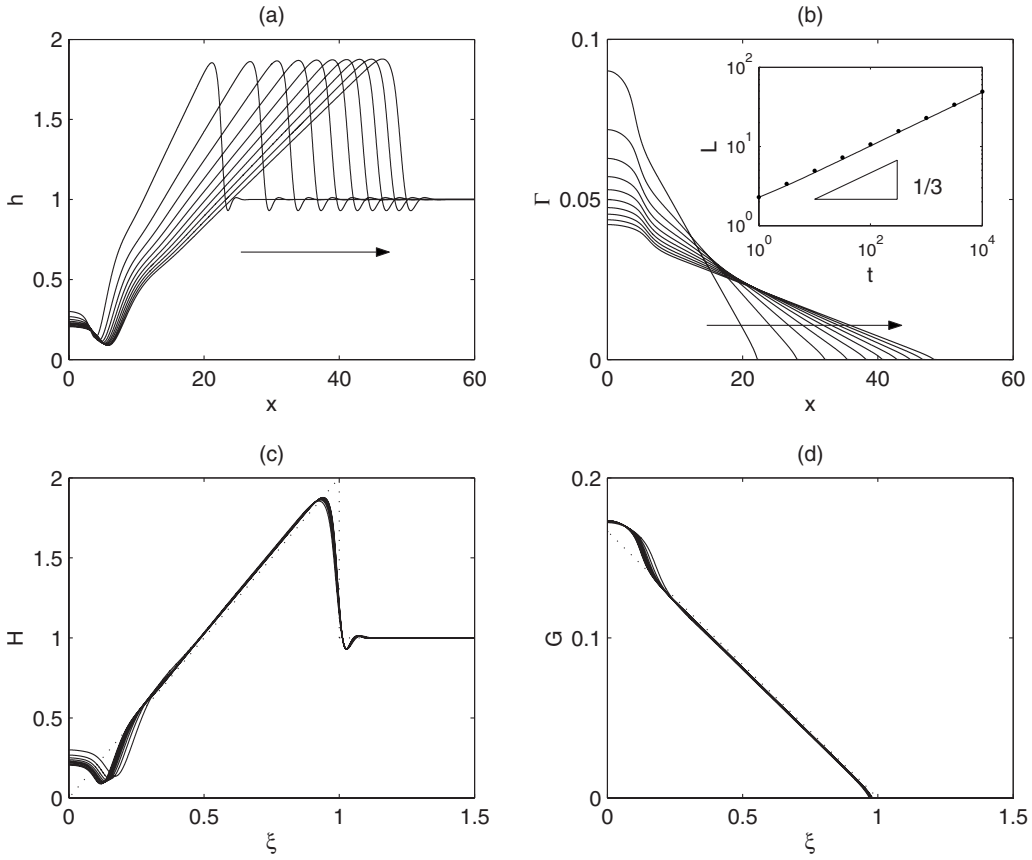

FIG. 32. Numerical simulation of monolayer spreading on thin films: (a) typical film thickness and (b) concentration evolution for $t=10^3-t=10^4$ in steps of 10^3; the arrows indicate the direction of increasing time. (c) and (d) The collapse of these solutions onto the similarity solutions (see text) shown by dotted lines. The inset to (b) shows the position of the surfactant leading edge versus time together with the similarity solution prediction (represented by dots) (Jensen and Grotberg, 1992).

ing asymptotically small. These regions can be described by similarity solutions, which, for the case of fixed surfactant mass, i.e. $\alpha_f=0$, are given by Jensen and Grotberg (1992):

$$h(x,t)=H(\xi)=2\xi, \quad \Gamma(x,t)=\xi_s^2\tfrac{1}{6}(1-\xi)t^{-1/3}, \qquad (116)$$

where $\xi=(x/\xi_s)t^{-1/3}$ and $\xi_s=12^{1/3}$ for $0<\xi<1$. The agreement between the numerical predictions and the similarity solutions is shown in Fig. 32; the position of the surfactant leading edge also emerges as $L_s=(12t)^{1/3}$ and this is shown in the inset in panel (a). The smoothing in the vicinity of the front and the thinning region is due to surface diffusion and capillary corrections; in the figure shown extreme values, $\mathrm{Pe}_s=10^6$ and $\mathcal{C}_m=10^{-3}$, were taken to show how closely the shock can be captured by numerics, lower values are taken in Jensen and Grotberg (1992), and the shock is then further smoothed. The similarity analysis has been extended to cover axisymmetry and situations involving time-dependent surfactant mass (Jensen and Grotberg, 1992) (here similarity solutions of the second kind have been found), surfactant spreading over power-law fluids and the closing of an axisymmetric surfactant-bare patch (Jensen, 1994), and spreading over Herschel-Bulkley bilayers (Craster and Matar, 2000).

Numerical solutions of Eqs. (113) and (114) have also shown that increasing the Péclet number and decreasing the capillary parameter lead to the formation of sharper fronts and more pronounced thinning upstream (Borgas and Grotberg, 1988; Gaver and Grotberg, 1990; Jensen and Grotberg, 1992; Grotberg, 1994; Afsar-Siddiqui *et al.*, 2003a). In fact, the Marangoni-driven thinning can be sufficiently severe that the film thickness local to the thinned region can reach thicknesses of order 1000 Å at which the intermolecular forces discussed in Sec. V become operative. Jensen and Grotberg (1992) showed that Marangoni stresses promote conditions for van der Waals forces to give rise to rupture in finite time. van der Waals–driven thinning then leads to the expulsion of liquid and surfactant from the thinned region, which creates Marangoni stresses that counteract the thinning process. This analysis was extended by Matar *et al.* (2002) to bilayer systems, where the top layer corresponds to a thin highly viscous "skin," which models the mucus layer that overlies the PCL in pulmonary airways. The effects of $\Gamma(x,0)$ and of using a nonlinear equation of state on the numerical solutions have been explored (Gaver and Grotberg, 1990; Afsar-Siddiqui *et al.*, 2003a).

Equations (113) and (114) have also been extended to account for the presence of an "endogenous" surfactant species, already present on the interface prior to the

deposition of an exogenous surfactant patch (Espinosa *et al.*, 1993; Grotberg *et al.*, 1995). In this case, the exogenous surfactant-driven front compresses the endogenous surfactant downstream, leading to an increase in its concentration. This drives a Marangoni flow, which opposes that due to the exogenous surfactant and, as a result, retards its spreading. This is a situation which may arise within the context of biomedical applications such as SRT if the interface has been contaminated by, for instance, a previous surfactant deposition.

The effects of surfactant solubility on the spreading process have also been studied (Halpern and Grotberg, 1992; Jensen and Grotberg, 1993; Jensen, 1994). Lubrication theory was used in conjunction with the rapid bulk diffusion assumption and cross-sectional averaging in order to derive the following system of evolution equations for the film thickness h, surfactant interfacial concentration Γ, and bulk concentration c,

$$h_t = -\nabla \cdot \left(\frac{\mathcal{C}_m}{3} h^3 \nabla \nabla^2 h + \frac{1}{2} h^2 \nabla \sigma \right), \tag{117}$$

$$\Gamma_t = \frac{\nabla^2 \Gamma}{\mathrm{Pe}_s} - \nabla \cdot \left(\frac{\mathcal{C}_m}{2} h^2 \Gamma \nabla \nabla^2 h + h\Gamma \nabla \sigma \right) + J, \tag{118}$$

$$c_t = \frac{1}{h\mathrm{Pe}_b} \nabla \cdot (h \nabla c) - \left(\frac{\mathcal{C}_m}{3} h^2 \nabla \nabla^2 h - \frac{h}{2} \nabla \sigma \right) \cdot \nabla c - \frac{\beta_s J}{h}. \tag{119}$$

The total mass of surfactant deposited is given by $M = \int_{-\infty}^{\infty} \int_0^{\infty} h c dx dy + \beta_s \int_{-\infty}^{\infty} \int_0^{\infty} \Gamma dx dy$. In Eqs. (118) and (119), $J = K_s(c - \Gamma)$ is the sorptive flux and β_s and K_s denote solubility and sorption kinetics parameters, respectively: $\beta_s \gg 1$ represents a weakly soluble surfactant and the spreading process is then described by Eqs. (113) and (114); $K_s \gg 1$ corresponds to the case of rapid sorption kinetics in which the interfacial and bulk concentrations come to equilibrium on a time scale of $O(1/K_s)$; Pe_b is a bulk Péclet number. Jensen and Grotberg (1993) showed through numerical solutions of Eqs. (117)–(119) that for highly soluble surfactants the maximal film thickness at the surfactant leading edge can exceed twice the undisturbed film height; in this case and local to the surfactant leading edge, the film resembles a narrow pulse rather than the front shown in Fig. 32.

Jensen *et al.* (1994) then used a similar model to that discussed above to examine the effect of surfactant-driven flow on the transport of a passive (such as a surface-inactive chemical, for instance) solute in the bulk of the film. This model has also been extended in order to obtain transit times for the delivery of surfactant to a pulmonary airway of a particular generation in the lung (Jensen *et al.*, 1993; Halpern *et al.*, 1998; Zhang *et al.*, 2003b). This involved accounting for the considerable dilution effects associated with the branching of the pulmonary airways in a typical lung (Weibel and Gomez, 1962). Zhang *et al.* (2003b) built on previous work (Halpern and Grotberg, 1992; Jensen and Grotberg, 1993; Jensen *et al.*, 1993; Jensen, 1994; Grotberg *et al.*, 1995; Halpern *et al.*, 1998; Espinosa and Kamm, 1999) and presented a model for the delivery of chemicals, such as gene vectors and drugs, to pulmonary airways, which uses exogenous surfactant as a vehicle. They studied the effects of pulmonary absorption rate, surfactant-chemical recombinant volume, surfactant dose, endogenous surfactant concentration, fluid viscosity, surfactant and chemical diffusivity, and lung ventilation rate on the distribution of the chemical along pulmonary airways for a given chemical dose. Their results suggest that the use of exogenous surfactant, which drives a Marangoni flow, can expedite the delivery of chemicals to the lung.

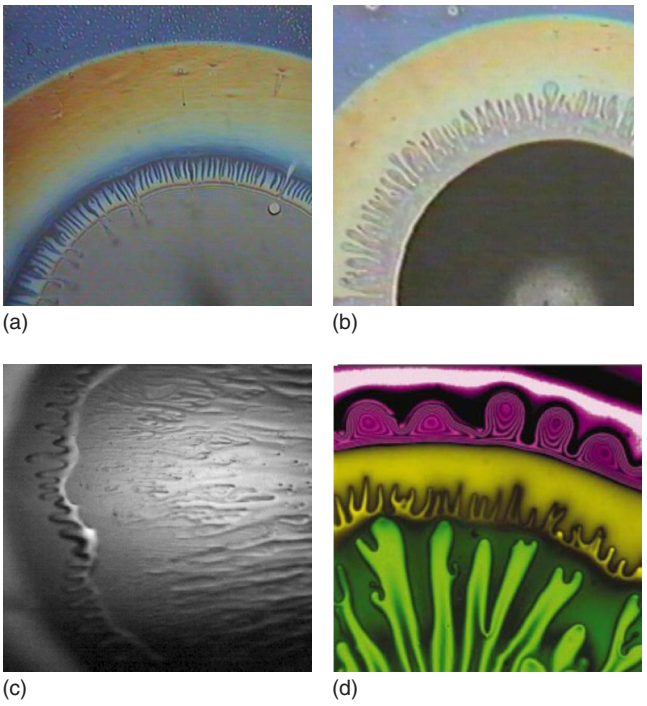

FIG. 33. (Color online) Examples of surfactant-induced fingering phenomena. (a) $C_{12}E_{10}$ at 1.5 cmc on a 120 nm film of ethyleneglycol (EG). (b) $C_{12}E_4$ at 1 cmc on a 120 nm EG film. From Hamraoui *et al.*, 2004. (c) 2.8 cmc SDS in a 4:1 glycerol/water suspension on an approximately 250 nm film. From Lee, Gee and Luckham, 2005). (d) SDS in glycerol spreading on a 1–10 μm film. From Darhuber and Troian, 2003.

B. Surfactant-induced fingering

A long-standing question has been the physical origin of the striking fingering mechanism that is observed when a surfactant-laden drop is placed atop a preexisting uncontaminated thin film; examples of such phenomena are shown in Figs. 6 and 33. Marmur and Lelah (1981) first observed the fingering phenomena and these have subsequently been studied (Troian, Wu, and Safran, 1989; Frank and Garoff, 1995; He and Ketterson, 1995; Bardon *et al.*, 1996; Cachile and Cazabat, 1999; Cachile *et al.*, 1999; Cachile, Benichou, *et al.*, 2002; Afsar-Siddiqui *et al.*, 2003a, 2003b, 2003c). Both the fluid within the droplet and that of the thin film are identical,

so these patterns are not simply a manifestation of the well-known viscous fingering instability (Saffman and Taylor, 1958), whereby a less viscous fluid displaces a more viscous one. Nevertheless, certain similarities exist between the surfactant-induced patterns and those driven by viscous fingering: adverse mobility gradients are present in both cases. In the former case, these are brought about by the spreading of a thicker more mobile surfactant-laden drop, which has potential for Marangoni-driven flow and feels the retarding effects of the underlying wall far less than the much thinner uncontaminated film downstream, and, in the latter, by the penetration of a more mobile (less viscous) fluid into a less mobile (more viscous) one.

As shown in Fig. 33(a), in certain experiments, the fingers are located in the thinned region downstream of the deposited surfactant-laden drop and upstream of the thickened advancing ridge; the structure of the film, which emerges during the spreading process of a monolayer (as opposed to a drop) in the absence of perturbations, which features the thinned region and the thickened ridge, was discussed above. In Fig. 33(b), however, the spreading occurs in the absence of a pronounced thinned region and the fingers appear to emanate directly from the relatively thick drop (the dark region in the panel). In Fig. 33(c), the spreading is accompanied by the formation of two fronts: a thickened region that exhibits rather ramified fingers is located between a thinned region, which itself shows evidence of fingering, and an advancing front (a ring of lighter shade of gray), barely discernible in the panel. Evidence of multifronts and fingering on different scales is also shown in Fig. 33(d). The results shown in Fig. 33 demonstrate the richness of the dynamics and the aesthetically appealing patterns, which accompany the surfactant-driven spreading of a drop. Naturally, these results generated much interest in isolating the mechanism responsible for the fingering phenomena.

The early work of Troian *et al.* (1990) represents the first attempt at achieving fundamental understanding of the mechanism underlying the fingering process. Through a linear stability analysis (in which they neglected film thickness perturbations but considered concentration disturbances) they exploited the similarities between the surfactant-driven and classical Saffman-Taylor fingering instabilities and identified Marangoni stresses as being responsible for the instability. Matar and Troian then examined the stability of a monolayer spreading on a thin film of initially uniform thickness (Matar and Troian, 1997, 1998, 1999a, 1999b) in the presence of Marangoni stresses, surface diffusion, capillarity, and van der Waals forces. They used linear stability and transient growth analyses, as well as direct numerical simulations of the fully nonlinear governing equations [Eqs. (113) and (114)] to show that sustained perturbation growth could only be obtained following the inclusion of van der Waals forces; this was also shown by Warner *et al.* (2002). In their absence, large initial transient growth was obtained, notably localized at the front rather than the thinned region, followed by decay. Fischer and Troian (2003) obtained sustained growth but only in the presence of surfactant "feeding" at the flow origin with a prescribed rate.

The majority of experimental observations, however, were recorded in situations where the fingering phenomena occurred on pre-existing films that are far too thick for van der Waals forces to be operative or are performed on hydrophilic substrates (Cachile and Cazabat, 1999; Cachile *et al.*, 1999; Cachile, Benichou, *et al.*, 2002). Furthermore, as shown by Afsar-Siddiqui *et al.* (2003b, 2003c), who studied the fingered spreading of AOT and SDS surfactant on water films resting on glass substrates, the average finger wavelength is proportional to $H_b^{2/3}$, where H_b is the undisturbed film thickness. From the evolution equations [Eqs. (113) and (114)] one can balance the Marangoni and capillary forces in the transverse direction, i.e., $h^2\Gamma_y \sim h^3 h_{yyy}$ and if the transverse length scale is that of a finger wavelength λ the thickness is H_b and Γ_y, locally constant, then $\lambda \sim H_b^{2/3}$. Thus, the observed scaling is consistent with a Marangoni-driven rather than a van der Waals–driven fingering instability; the latter would have given rise to a H_b^2 scaling.

The modeling studies of Matar and Troian (1997, 1998, 1999a, 1999b), Warner *et al.* (2002), and Fischer and Troian (2003), have two key limitations: the absence of a drop and the associated thickness disparity between the drop and underlying pre-existing film and the restriction to surfactant concentrations below the critical micelle concentration (CMC), above which surfactants form micellar aggregates. However, the experiments shown in Fig. 33 were carried out at concentrations above the CMC. Warner *et al.* (2004a) addressed the first of the above limitations for the case of insoluble surfactant present in dilute concentrations. They demonstrated through a linear stability analysis in the quasi-steady-state approximation a transient growth analysis, and full numerical simulations that the thickness disparity between the surfactant drop and the underlying thinner liquid film is a key ingredient for the appearance of the fingers which target the thickness minimum between the drop and the advancing front; this problem was also studied by Jensen and Naire (2006) using asymptotic methods. The results of Warner *et al.* (2004a) also showed that sustained growth is possible in the absence of van der Waals forces and surfactant feeding (see Fig. 34). Warner *et al.* (2004b) then extended their work to account for surfactant solubility, sorption kinetics, and bulk diffusion by assuming rapid vertical diffusion and employing the method of cross-sectional averaging previously used by Jensen and Grotberg (1993); a nonlinear equation of state was also used. Their results demonstrated that, for a given level of equation of state nonlinearity, increasing surfactant solubility destabilizes the spreading process except for very high solubility where Marangoni stresses are too weak to drive instability.

Warner *et al.* (2004a, 2004b) performed a decomposition of the disturbance "energy," which indicated that local height increases in the thinned region results in a local increase in surface velocity and in surfactant transport rate; this gives rise to a decrease in the surfactant

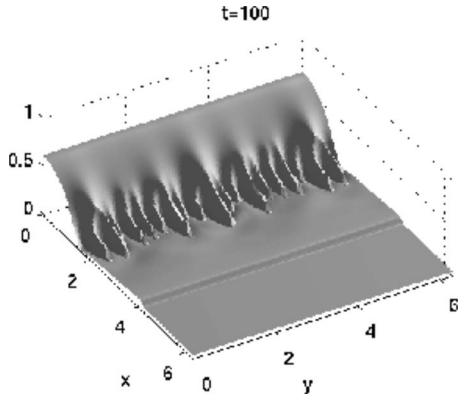

FIG. 34. Numerical simulations of surfactant-induced fingering instabilities for insoluble surfactant. A surface plot of the film thickness $h(x,y,t)$ showing the fingering patterns, generated with $\mathrm{Pe}_s=10^4$, $\mathcal{C}_m=10^{-4}$ after 100 time units starting from an initial localized height covered with surfactant and given a small initial perturbation. From Warner *et al.*, 2004a.

concentration, which coincides with locally elevated regions. This local concentration decrease drives Marangoni flow toward the elevation from adjoining depressed surfactant-rich regions, which amplifies the instability. The thicker regions then spread faster than the neighboring thinned ones and elongate to form fingerlike patterns.

More recently, Edmonstone, Craster, and Matar (2006), Edmonstone, Matar, and Craster (2006), and Edmonstone *et al.* (2004, 2005) further extended the work of Warner *et al.* (2004a, 2004b) to account for gravitational forcing in thin films flowing down an inclined plane with surfactant. They considered the flow of either a drop or a film with a constant flux at the flow origin. In both configurations, they found the presence of surfactant to be destabilizing and the perturbations, which assumed the shape of fingers, were found to localize downstream of the capillary ridge near the surfactant leading edge. Close inspection of the flow profiles revealed that the surfactant concentration is larger outside a finger. This gives rise to Marangoni-driven flow, which draws more fluid into protrusion and enhances finger formation. Edmonstone, Matar, and Craster (2006) also showed that surfactant solubility is destabilizing over an intermediate range of solubilities.

Even in the absence of fingering, flow down an incline with surfactant has several interesting features (Edmonstone *et al.*, 2004). In particular, a step of height approximately twice that of the precursor film forms ahead of the capillary ridge. Recent work (Levy and Shearer, 2006; Witelski *et al.*, 2006; Levy *et al.*, 2007) investigated this structure and extracted scaling results by moving to a traveling wave coordinate.

C. Spreading at high concentrations

Once the concentration exceeds a critical value, the CMC, it becomes energetically favorable for surfactant monomers to create micelles, as discussed in many colloid chemistry texts, i.e., Hunter (1991). Edmonstone, Craster, and Matar (2006) developed a model using lubrication theory to account for the possibility of micellar formation and breakup at concentrations above the CMC. This model also assumes rapid vertical diffusion of surfactant in the bulk of the film and accounts for capillarity, Marangoni stresses, surface and bulk diffusion, sorption kinetics, and solubility,

$$h_t = -\nabla\cdot\left(\frac{\mathcal{C}_m}{3}h^3\nabla\nabla^2 h+\frac{1}{2}h^2\nabla\sigma\right), \tag{120}$$

$$\Gamma_t = \frac{\nabla^2\Gamma}{\mathrm{Pe}_s}-\nabla\cdot\left(\frac{\mathcal{C}_m}{2}h^2\Gamma\nabla\nabla^2 h+h\Gamma\nabla\sigma\right) + K_s[Rc(1-\Gamma)-\Gamma], \tag{121}$$

$$c_t = \frac{1}{h\mathrm{Pe}_b}\nabla\cdot(h\nabla c)-\left(\frac{\mathcal{C}_m}{3}h^2\nabla\nabla^2 h+\frac{h}{2}\nabla\sigma\right)\cdot\nabla c - \frac{\beta_s}{h}K_s[Rc(1-\Gamma)-\Gamma]-K_b(c^n-m), \tag{122}$$

$$m_t = \frac{1}{h\mathrm{Pe}_m}\nabla\cdot(h\nabla m)-\left(\frac{\mathcal{C}_m}{3}h^2\nabla\nabla^2 h+\frac{h}{2}\nabla\sigma\right)\cdot\nabla m + K_b(c^n-m). \tag{123}$$

These equations correspond to Eqs. (117)–(119) augmented by an equation for the micelle concentration m. The total mass in the presence of micellar formation is given by $M=\int_{-\infty}^{\infty}\int_0^{\infty}h(c+m)dxdy+\beta_s\int_{-\infty}^{\infty}\int_0^{\infty}\Gamma dxdy$; here a nonlinear equation of state was used (Sheludko, 1967; Gaver and Grotberg, 1990, 1992; Jensen and Grotberg, 1992; Warner *et al.*, 2004b). In Eqs. (120)–(123), n represents the number of surfactant monomers that form a single micelle, Pe_m is a Péclet number for the micellar phase, and K_b and R provide dimensionless measures of the rate at which micelles are formed and of the propensity of the surfactant to form micelles; large R corresponds to a low propensity.

Edmonstone, Craster, and Matar (2006) showed that the micelles remain localized within the drop region and, with decreasing R, their concentration remains relatively high during the latter stages of the spreading; increasing R results in the rapid breakup of micelles, the formation of large Marangoni stresses that give rise to a thickened front and severely thinned regions that straddle the front and the drop, which remains as a cap at late times and advances slowly. Figure 35 shows the dependence of h on M and R. As can be seen, the spreading dynamics are accompanied by the formation of a "protuberance," which is absent for $M=1$, becomes prominent for $M=3$, but remains attached to the drop, and separates from the drop for $M=5$ to form an isolated "secondary" front.

Edmonstone, Craster, and Matar (2006) also showed through a transient growth analysis that the spreading process is least stable for intermediate values of M and large R. They attributed this to the fact that the protuberances that form for intermediate M have the largest

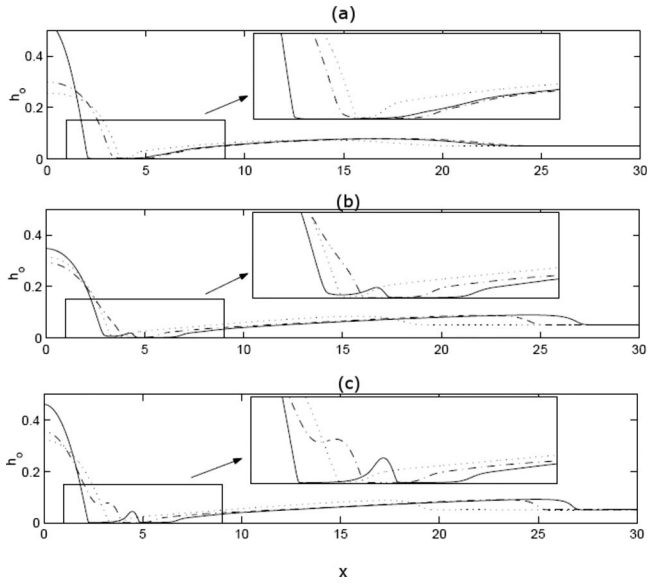

FIG. 35. The effect of varying M and R on the h profiles obtained via the solution of Eqs. (120)–(123) at $t=10^4$; $R=1,10,100$ in (a)–(c), respectively, and in each panel, $M=1,3,5$ are represented by dotted, dot-dashed, and solid lines, respectively. The main feature to note is the emergence of the small peak in the thinned region as M increases, which is unstable to a fingering instability, and can be seen in Figs. 37(c) and 37(d). From Edmonstone, Graster, and Matar, 2006.

adverse mobility gradients, which led to instability. It is interesting to note that these features have similar structure to the capillary ridges that accompany the flow of films down inclined planes (Troian, Herbolzheimer, *et al.*, 1989; Kondic, 2003; Edmonstone *et al.*, 2005) and thermally driven climbing films (Kataoka and Troian, 1997; Eres *et al.*, 2000). Their time-dependent numerical simulations of the two-dimensional and fully nonlinear evolution equations given by Eqs. (120)–(123) revealed that initially pseudorandom disturbances organize into coherent structures, which target the thinned region, protuberance, and secondary front for relatively low, intermediate, and large M, respectively. Associated with this (Fig. 36) are numerical results showing evidence of nonlinear phenomena such as tip splitting, coalescence, and shielding reminiscent of experimental observations.

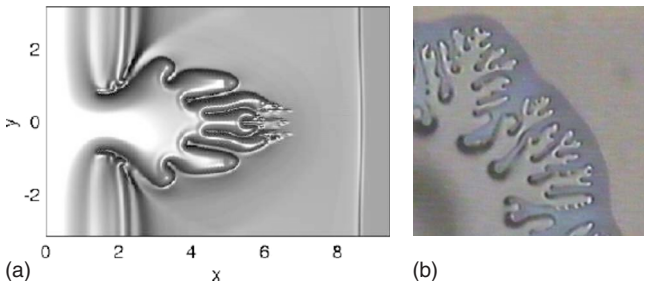

FIG. 36. (Color online) Surfactant-induced fingering: (a) Simulated tip splitting. From Edmonstone, Craster, and Matar, 2006. (b) Experimentally observed fingering. From Hamraoui *et al.*, 2004.

Several other situations involving Marangoni-driven flow of droplets due to surfactant concentration gradients have been studied recently. Examples of these have been provided by Nierop *et al.* (2006) who studied the spreading and recoil of lenses caused by interfacial chemical reactions that alter the spreading coefficient and Stocker and Bush (2007) who examined lens oscillation driven by evaporation. There are also related spreading droplet situations wherein the surfactant can adsorb on the underlying solid substrate and dynamically alter the wettability. This can render an originally hydrophilic substrate hydrophobic and thus an initially spreading droplet can finally retract in a process called "autophobing" (Afsar-Siddiqui *et al.*, 2004; Craster and Matar, 2007).

Related to the process of autophobing is that of reactive wetting, whereby a droplet causes a reaction on the substrate leading to a wettability gradient. Remarkably in such situations, self-propelled droplets can be observed (Bain *et al.*, 1994; Lee *et al.*, 2002; Sumino *et al.*, 2005) and modeled (John *et al.*, 2005) using an evolution equation. This equation is similar to Eq. (37), without any gravity, coupled with a reaction-diffusion equation for the chemical field that feeds into the conjoining pressure ϕ thereby altering the local wettability. Wettability gradients then drive the droplet motion. Similar effects occur for droplets driven by surface phase transitions, as shown by experimental (Lazar and Riegler, 2005) and theoretical (Yochelis and Pismen, 2005) approaches. The unifying theme of autophobing and self-propelled droplets is that the wettability of the substrate is dynamically affected by the droplet.

VII. EFFECT OF BOUNDING WALL

In this section, we review some of the work that has been carried out involving the effect of the bounding wall on the dynamics of thin films. The studies that will be considered are concerned with the effect of substrate topography, compliance, and geometry on the flow. We do not review other previous research involving, for instance, the effects of reactive and/or dissolving substrates [see, for instance, Warren *et al.* (1998), Hunter *et al.* (2002), Gonuguntla and Sharma (2004), and references therein] and wall oscillations (Or and Kelly, 1998; Matar, Kumar, and Graster, 2004) on film evolution.

A. Flow over topography

Here we consider the behavior of thin films over topographical features for which general evolution equations have been developed using coordinate systems based on the substrate (Roy *et al.*, 2002; Howell, 2003) as extensions of those in Sec. II.C. Formally, the equations of Sec. II.C implicitly assume that slopes of the free surface and substrate are small and that the topography enters through the gradient of the substrate curvature as a forcing term. Howell (2003) showed how to incorporate larger substrate curvatures into the evolution equa-

tions. We consider topographic variations that, at least formally, have small slopes and these extensions are not required.

Flows over varying topographies are of importance for the coating of patterned substrates in the manufacturing of microelectronics, optical, and magnetic devices using spin-coating techniques. The topographical features give rise to variations in the coating layer, such as capillary waves and ridges, which could potentially affect adversely the fabrication process and, ultimately, the quality of the final product (Stillwagon and Larson, 1988, 1990; Kalliadasis *et al.*, 2000).

In order to analyze the film leveling processes, Kalliadasis *et al.* (2000) used lubrication theory to study the flow of a thin film over a "trench," as an example of a topographical feature. This equation can be derived from Eq. (37) (with $\mathcal{G}_c=1$) by first considering one-dimensional situations at steady state with a flux at the left boundary $\mathcal{UH}$,

$$[h^3(1+(h+\mathcal{B})_{xxx})]_x = 0. \tag{124}$$

The $\mathcal{B}_{xxx}$ corresponds to an extra capillary pressure due to the topography. Here the flux $\mathcal{UH}$ may be due to the presence of gravity or centrifugation, for instance, and the function $\mathcal{B}(x)$ describes the shape of the trench:

$$\mathcal{B}(x) = D\left[1+\frac{1}{\pi}\left(\tan^{-1}\left(\frac{x-w}{\delta_b}\right)-\tan^{-1}\left(\frac{x}{\delta_b}\right)\right)\right],$$

where D, w, and δ_b represent the trench depth, width, and steepness, respectively; the trench may be viewed as the union of a "step-up" or a "step-down" feature. In this case, $\mathcal{H}$ is the film thickness away from the topographical feature and ϵ is the ratio of $\mathcal{H}$ to the width of the topographical feature.

A capillary ridge is formed just upstream of the stepdown (Kalliadasis *et al.*, 2000; Kalliadasis and Homsy, 2001) whose height increases with D and $1/\delta_b$; no such feature forms over a stepup. Moreover, this ridge is shown to be, perhaps surprisingly, linearly stable to transverse perturbations (Kalliadasis and Homsy, 2001) and studies using transient growth analysis (Trefethen *et al.*, 1993; Davis and Troian, 2005) and nonlinear computations (Bielarz and Kalliadasis, 2003) confirm this conclusion. An energy calculation (Kalliadasis and Homsy, 2001) suggests that the mechanism leading to stability is due to a pressure gradient from the topography (for long waves) and from surface tension (for short waves).

This work has been generalized to account for the delicate interplay between topographic variations, thermocapillary (Alekseev *et al.*, 2005; Kabova *et al.*, 2006; Gambaryan-Roisman and Stephan, 2007; Saprykin *et al.*, 2007), and electric fields effects (Tseluiko *et al.*, 2008). Extensions to two- (Lenz and Kumar, 2007b) and three-layer (Lenz and Kumar, 2007c) flows confined between two walls have also been carried out. The former work (Lenz and Kumar, 2007b) demonstrated that the height of the capillary ridge preceding a "stepdown" is maximized for an intermediate step size; this is absent in the single-layer case and is attributed to the pressure gradients in the upper layer. The latter work (Lenz and Kumar, 2007c) delineated the different modes of instability dominating the early stages of disturbance growth and its final stages as rupture is approached as a function of thickness, viscosity, and interfacial tension ratios.

Formally the lubrication approximation fails precisely at the sharp stepdown and must be replaced by the Stokes equations there; a variety of numerical studies (Mazouchi and Homsy, 2001; Gaskell *et al.*, 2004) confirmed that the results from the lubrication approximation are accurate, at least for small capillary numbers, and so the conclusions drawn from it can be trusted.

Apart from directly calculating the Stokes flow solution and comparing with a lubrication flow that formally fails at sharp or re-entrant corners, one could move to a new coordinate system in which the small-slope restriction is no longer present, although a coordinate singularity normally appears. For re-entrant corners, a hyperbolic coordinate system has been used to some effect by Stocker and Hosoi (2005) as has a seminumerical technique (Heil and White, 2002; Jensen *et al.*, 2004) for large humps using volume conservation and the full curvature.

The flow of a thin film over a periodically wavy wall also has a number of engineering applications, which include the design of heat exchangers and the use of highly corrugated surfaces, so-called "structured packings" (Valluri *et al.*, 2002), for enhanced mass transfer rates in distillation and absorption columns. These applications rely on the disruption of the flow by the wall corrugations. Determining the steady film thickness in these situations is far from simple due to potential competition between several length scales, corresponding to the lateral and vertical corrugation dimensions and any pertinent dynamic spatial scales (e.g., the Nusselt film thickness in falling films) (Wierschem *et al.*, 2002). Previous studies have detailed the occurrence of flow separation and vortices in flow down inclined sinusoidal walls at vanishingly small Reynolds numbers for a critical film thickness, which is a function of the wall waviness, inclination angle, and surface tension [see Wierschem *et al.* (2003), and references therein]; the presence of these vortices had been predicted by numerical simulations in the creeping flow limit (Pozrikidis, 1988). The film thickness is made more uniform by the presence of surfactants (Pozrikidis, 2003).

In the presence of inertia and in the range of Reynolds numbers of 10–100, resonance between the gas-liquid interface and the corrugated wall gives rise to static waves having the same wavelength as the substrate topography (Bontozoglou and Papapolymerou, 1997; Vlachogiannis and Bontozoglou, 2002). Similar observations were made for falling films down doubly and triply periodic structured packing surfaces by Valluri *et al.* (2005) via use of Eq. (48). Hydraulic jump formation was found to occur at relatively low inclination angles and strong waviness (Wierschem and Aksel, 2004a). Experiments (Vlachogiannis and Bontozoglou, 2002; Argyriadi *et al.*, 2006) and numerical work (Trifonov, 1998; Wierschem and Aksel, 2003, 2004b) showed that wall corru-

gations exert a stabilizing influence on the flow, delaying transition to instability to higher Reynolds numbers in comparison to flow over flat walls.

B. Flow over flexible and compliant support

The dewetting instabilities reviewed in Sec. V occur for thin films bounded from below by a rigid wall. Recent studies have attempted to exploit the strong deformations accompanying dewetting in order to engender pattern formation in layers of soft solids, e.g., polymers, gels, or elastomers (Bowden *et al.*, 1998; Martin *et al.*, 2000; Hosoi and Mahadevan, 2004; Kumar and Matar, 2004; Matar, Gkamis, and Kumar, 2005; Yoo and Lee, 2005; Bandyopadhyay *et al.*, 2008); this is in contrast to the two-layer dewetting work already reviewed in Sec. V.D, which featured thin viscous bilayers (Bandyopadhyay *et al.*, 2005; Pototsky *et al.*, 2006). Previous experimental (Bowden *et al.*, 1998; Yoo and Lee, 2005) and modeling studies (Huck *et al.*, 2000; Sridhar *et al.*, 2001; Cerda and Mahadevan, 2003; Huang, 2005) demonstrated interfacial "wrinkling" into stripes and labyrinths when a thin polymer film (less than 100 nm thick) is bounded from below by a relatively thick viscous film (more than 100 nm thick) resting on a rigid substrate. The possibility of creating patterns with controllable dimensions in polymeric films, and which can then be quenched, may be valuable in studying adhesion of cells and vesicles to surfaces in biological systems (de Souza and Gallez, 1998; Coakley *et al.*, 1999; de Souza *et al.*, 2001).

When the viscous film separating the polymeric layer from the rigid substrate is less than 100 nm in thickness, it becomes vulnerable to van der Waals–driven instabilities (Martin *et al.*, 2000). Hosoi and Mahadevan (2004) studied peeling, healing, and bursting of a thin elastic sheet on a viscous film, wherein van der Waals forces are operative. Kumar and Matar (2004) and Matar, Gkanis, and Kumar (2005) and Matar, Lawrence, and Sisoev (2005), studied dewetting of thin films near soft elastomers, described as a linear viscoelastic material using a linear stability analysis and numerical simulations of lubrication-based models. These models comprised evolution equations for the positions of the air-liquid and solid-liquid interfaces and account for the presence of van der Waals forces and short-range repulsion in the thin viscous film but not in the viscoelastic solid. Matar, Gkamis, and Kumar (2005) and Matar, Lawrence, and Sisoev (2005) showed the formation of fluid ridges on depressed solid regions, as depicted in Fig. 37. Recent work by Bandyopadhyay *et al.* (2008) has extended these studies to account for intermolecular forces in both the polymeric and viscous layers in configurations where the former is bounded from above by either a rigid wall or an inviscid gas.

The flow of thin films over flexible solid substrates and membranes has also been studied. Halpern and Grotberg (1992, 1993) [see also Grotberg and Jensen (2004)] derived evolution equations for the interfacial and wall positions and the surfactant surface concentration using

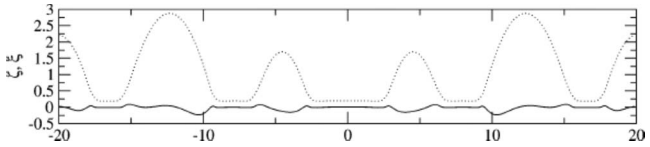

FIG. 37. Pattern formation in thin liquid films (dotted line) on a soft solid layer (solid lines); ξ and ζ represent the solid-liquid and air-liquid interfacial positions, respectively. From Matar, Gkamis, and Kumar, 2005.

lubrication theory. These equations, which can be considered to be extensions of Eqs. (113) and (114), were used to study the instabilities that arise in the thin films that line the inside of pulmonary airways and which lead to airway closure via liquid bridge formation and/or wall collapse. The airway walls were modeled as elastic circular tubes. Closure was found to occur beyond a critical film thickness which decreases with increasing surface tension and decreasing surfactant concentration.

Kumar and Matar (2004) showed that wall flexibility can affect significantly the rupture of surfactant-covered thin films. More recently, Matar and Kumar (2007) studied the stability of flow down a flexible plane inclined with angle θ to the horizontal. They used lubrication theory to derive the following coupled evolution equations for the film thickness, h, and wall deflection, η:

$$(h+\eta)_t = -\frac{\sin(\theta)}{3}[(h+\eta)^3]_x + \frac{1}{3}\nabla\cdot[(h+\eta)^3\nabla p],$$

$$\Sigma\eta_t = \mathcal{T}\nabla^2\eta - \nabla^2 h, \tag{125}$$

where $p=-\nabla^2 h$; here Σ and $\mathcal{T}$ provide dimensionless measures of the relative significance of wall damping and wall tension, respectively. If $\Sigma \gg 1$ and/or $\mathcal{T} \gg \infty$, that is, for large wall damping and/or wall tension, Eq. (125) reduces to Eq. (33) with $\beta=\mathcal{B}=0$, $\mathcal{U}=\rho g\mathcal{H}^2/\mu$, and $\mathcal{L}=(\sigma\mathcal{H}/\rho g)^{1/3}$.

The wall model used by Matar and Kumar (2007) is similar to that used by Halpern and Grotberg (1992) and Halpern and Grotberg (1993), which assumed the wall to be infinitely long, isotropic, impermeable, and sufficiently thin for the wall tension to be considered constant; bending stresses are neglected. Matar and Kumar (2007) showed decreasing the wall tension and damping leads to larger wall deformations and smaller thickness modulations. They also showed that the flow, which is already unstable in the rigid wall case, as discussed in Sec. III.A, is further destabilized by decreasing $\mathcal{T}$ and over an intermediate range of Σ. This work was recently extended to account for inertial effects by deriving extensions to the Benney, Kuramoto-Sivashinsky, and Shkadov equations [Eqs. (57)–(59)], to account for effects of wall flexibility (Matar *et al.*, 2007). The results of this study show that decreasing the relative magnitude of wall tension and/or damping promotes chaos and severe wall deformations in the weakly nonlinear and fully nonlinear regimes, respectively.

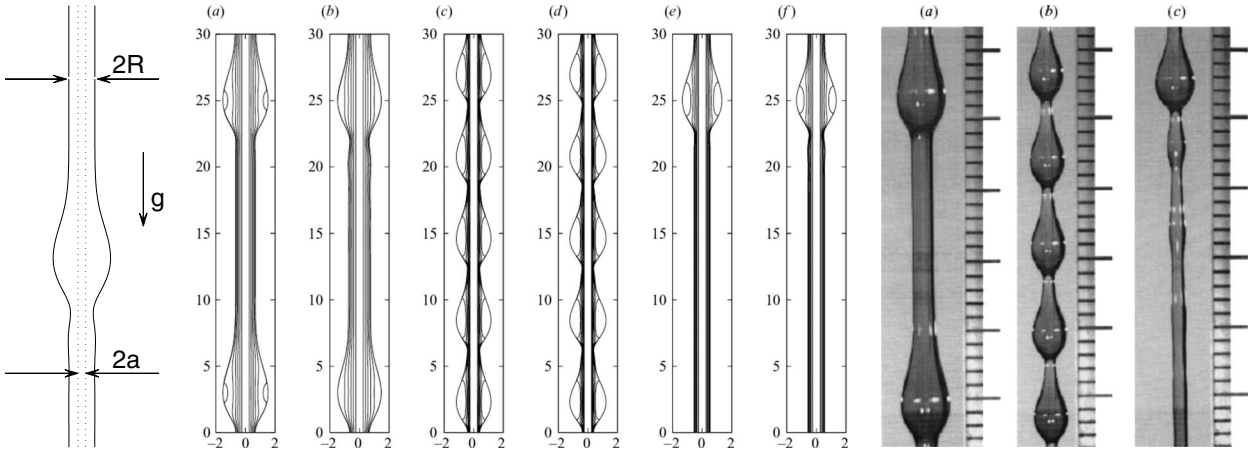

FIG. 38. The leftmost panel shows a schematic representation of the geometry for film flow down a vertical fiber. Here a and R represent the fiber radius and interfacial position, respectively. Comparison of modeling predictions and experimental observations of film flow down a vertical fiber. Left panels (a)–(f) show computed profiles and streamline. From Ruyer-Quil *et al.*, 2008. Right panels show profiles for the experimental regimes a–c. From Kliakhandler *et al.*, 2001. The results presented in (a), (c), and (e) were generated using a two-equation model based on the method of weighted residuals that includes second order dissipation, which is an extension of those considered in Sec. III.A.2; those in (b), (d), and (f) were obtained via solution of Eqs. (126) and (127).

C. Flow down vertical fibers

An extreme topographic variation is that of a cylinder and many real applications involve the coating of a thin fluid film along a cylindrical fiber; the geometry is shown in Fig. 38. We use this as an example to illustrate that the ideas and formulation presented earlier can be extended to other related situations, such as this one. The typical situation is that droplets emerge along the fluid film and it is of interest to characterize both their shape and speed. Flow down fibers often arise in the context of drawing fibers from reservoirs (Quéré, 1999) with and without surfactant (Shen *et al.*, 2002) and as an example of flows on the outside of cylinders. The presence of a mean flow field modifies the surface tension-driven flow that promotes film breakup (Eggers, 1997); this results in the formation of finite-amplitude interfacial waves (Quéré, 1990; De Ryck and Quér, 1996). A number of studies (Frenkel, 1992; Kalliadasis and Chang, 1994; Kerchman and Frenkel, 1994; Chang and Demekhin, 1999) have assumed the film thickness to be much smaller than the fiber radius. The notable point, physically, is that capillary forces depend both on the streamwise interfacial curvature, which is stabilizing, and on the azimuthal curvature, which is destabilizing. It is worth noting that despite the low inertial contributions in this case, this system exhibits rich dynamics, characterized by the formation of pulses and wave patterns.

When the film thickness is at least as large as the fiber radius, experiments by Kliakhandler *et al.* (2001) and Craster and Matar (2006) also revealed the richness of the dynamics and existence of several flow regimes. An equation for the interfacial position $R(x,t)$, as defined in Fig. 38, is derived using a somewhat similar approach to that followed in Sec. II. The equations of mass and momentum conservation in cylindrical coordinates and boundary conditions on the fiber surface and at the free surface [see Craster and Matar (2006), for details] are scaled using the following scalings: $r=R_0\tilde{r}$, $x=\mathcal{L}\tilde{x}$, $p=\rho g\mathcal{L}\tilde{p}$, $t=\mathcal{L}\tilde{t}/\mathcal{V}$, $w=\mathcal{V}\tilde{w}$, and $u=\epsilon\mathcal{V}\tilde{u}$, where $\mathcal{V}\equiv\rho R_0^2 g/\mu$ and $\mathcal{L}\equiv\gamma/\rho g R_0$. The scaling used here is similar in spirit to those adopted in the long-wave theories of viscous single and compound threads and jets (Eggers and Dupont, 1994; Papageorgiou, 1995a, 1995b; Eggers, 1997; Craster *et al.*, 2002; Craster and Matar, 2005). Craster and Matar (2006) assumed that the radius of the initially undisturbed fluid ring R_0 is much smaller than its characteristic, capillary length scale. Expanding variables in powers of $\epsilon\equiv R_0/\mathcal{L}$, solution of the Navier-Stokes equations and application of the boundary conditions, at leading order, yield the following evolution equation for the fluid interface position $R(x,t)$:

$$8(R^2)_t=\left(P_x\left[2R^2\left(\alpha_r^2-R^2+2R^2\log\frac{R}{\alpha_r}\right)-(\alpha_r^2-R^2)^2\right]\right)_x, \tag{126}$$

where $P_x=p_x-1$, in which the pressure p is given by

$$p=1/R-\epsilon^2 R_{xx}, \tag{127}$$

and $\alpha_r\equiv a/\mathcal{R}<1$ is the dimensionless ratio of the fiber radius to the initial fluid radius. The coordinate x is measured downward in the direction of flow. Inspection of Eq. (127) for the pressure reveals the competition between $1/R$ and R_{xx}, which are destabilizing (driving the formation of drops) and stabilizing, respectively. Their combined effect is to settle on a compromise whereby a droplet forms, which cannot pinch off due to the presence of the fiber. Equation (126) bears strong resemblance to Eq. (33) with h replaced by R, the pressure augmented by an azimuthal curvature term, and the simple nonlinearity of h^3 replaced by a cumbersome function of R [the square bracketed term in Eq. (126)]. Equation (126) has also been derived by Kliakhandler *et*

al. (2001) but without the ϵ^2 factor multiplying the S_{xx} term since $(r,x)=R_0(\tilde{r},\tilde{x})$ in Kliakhandler *et al.* (2001).

If we now consider $h=R-\alpha_r$ and assume it is small relative to the fiber radius so $h \ll \alpha_r$, then Eqs. (126) and (127) simplify to

$$\left(1+\frac{h}{\alpha_r}\right)h_t+\frac{1}{3}\left[h^3\left(1+\frac{h}{\alpha_r}\right)\left(1+\frac{h_x}{\alpha_r^2(1+h/\alpha_r)^2}+\epsilon^2 h_{xxx}\right)\right]_x=0, \tag{128}$$

which is related to the thin-layer model of Roy *et al.* (2002) deduced in the manner of Sec. II but using a general coordinate system for variable substrates. One can further simplify to the evolution equation derived by Frenkel (1992), used by Kalliadasis and Chang (1994) and others, by taking the limit $(1+h/\alpha_r)\to 1$ and $\alpha_r \to 1$,

$$h_t+\tfrac{1}{3}[h^3(1+h_x+\epsilon^2 h_{xxx})]_x=0. \tag{129}$$

This equation, with strong similarities to Eq. (33) where the restoring pressure due to gravity is supplanted by a restoring force due to the surface tension in the azimuthal direction, is equally valid on both the outside and inside of a cylinder of dimensionless radius α_r. This evolution equation also corresponds to that of Hammond (1983) describing the dynamics of a thin film on the inside of a cylinder, to within a rescaling, when the gravitational term is absent,

$$h_t+\tfrac{1}{3}[h^3(h_x+\epsilon^2 h_{xxx})]_x=0. \tag{130}$$

It is therefore interesting to note that there is a natural hierarchy of evolution equations descending from Eq. (126) to (130) that encompasses various sublimits.

The numerical solutions of Kliakhandler *et al.* (2001) and Craster and Matar (2006) can be compared with experiments; a set of experimental figures for varying flow rates are shown in Fig. 38 together with the results of some simulations (Ruyer-Quil *et al.*, 2008). Duprat *et al.* (2007) and Smolka *et al.* (2008) also considered the droplet formation and subsequent instability and expanded further on the experimental aspect. One can, of course, incorporate inertia as was carried out in Sec. III.A.2 on falling films and generate coupled model equations (Trifonov, 1992; Sisoev *et al.*, 2006), for the volumetric flow rate and interfacial position R using a combination of integral theory and a closure relation for the axial velocity component. Ruyer-Quil *et al.* (2008) employed the weighted residual approach, included second order dissipation, and compared the predictions of these extended equations with those of the simple single evolution equation [Eq. (126)] in terms of the speed and shapes of traveling waves. This comparison, which is shown in Fig. 38, reveals good agreement between the extended and simple models, and experimental data: for regime a, for instance, the experimentally observed drop speeds are 25 mm/s and the extended and simple models predict speeds of 22.4 and 24.7 mm/s, respectively. However, discrepancies emerge between the predictions of the extended models of Ruyer-Quil *et al.* (2008) and Eq. (126) in terms of predicting the spatiotemporal dynamics, the extended model being more accurate versus experiments.

D. Flow over porous media

The main focus of this review has been on flows over impermeable substrates; however, many applications such as the coating of textiles, spray painting, and ink-jet printing involve the spreading on porous substrates. There have been studies of droplet motion over porous media addressing several varied scenarios (Davis and Hocking, 1999a, 1999b), which use lubrication theory for a spreading droplet coupled to a permeable substrate modeled as an array of vertical pores of constant width and for a finite thickness layer as a porous medium. These studies provide details of the behavior near the contact line and time scales of the dynamics for limiting cases. Importantly, when using the lubrication scalings in the porous medium fluid flow takes place, to leading order, vertically within the medium (Acton *et al.*, 2001).

The pores are usually assumed long and thin, so the dimensional equations within the porous medium are (in rectangular geometry)

$$u_x+w_z=0, \quad p_z=-\rho g+\mu w_{xx}, \quad p_x=0, \tag{131}$$

with $w=0$ at $x=0$, $w_x=0$ at $x=b_p$, and a condition on the "saturation front" separating dry and wet solid: $p=-2\sigma/b_p$, where b_p is the pore half-width. Here we scale x, z, w, t, and p on b_p, l, $\mathcal{W}$, $l/\mathcal{W}$, and $\mu\mathcal{W}l/b_p^2$, respectively, where $\mathcal{W}$ is a characteristic velocity in the porous media and l is the pore length. The velocity component w is obtained in a straightforward manner from Eq. (131) and $W=(n/2)\int_0^2 w dx$, where n denotes the number of pores. Coupled evolution equations for the droplet height h and saturation front position h_p can then be derived (Alleborn and Raszillier, 2004),

$$h_t-\left[\frac{h^3}{3}(\mathcal{G}_c h-h_{xx}+\phi)_x\right]_x=W, \quad h_{pt}=-\frac{W}{\varphi}, \tag{132}$$

where φ is the porosity of the medium. Note that the evolution equation for h can be obtained using the procedure outlined in Sec. II to derive Eq. (37) but with $w=W\neq 0$ in Eq. (15) and $\mathcal{G}=\rho g\mathcal{L}^2/\sigma$ in which $\mathcal{L}=a_0$ is the initial drop width. Alleborn and Raszillier (2004) study involved the use of the disjoining pressure model to relieve the contact line singularity and they perform numerical simulations of droplet spreading. Aradian *et al.* (2000) who looked at the modifications to dewetting by the effect of porosity and Zadražil *et al.* (2006) considered extensions to solidifying droplets that can also simultaneously be imbibed by the underlying porous medium. Complementary to the theoretical literature there is also a range of primarily experimental work (Clarke *et al.*, 2002; Holman *et al.*, 2002; Starov, Kostvintsev, Sobolev, *et al.*, 2002) for isothermal contexts and for nonisothermal flows with solidification (Zadražil *et al.*, 2006).

VIII. CONCLUDING REMARKS

We have presented a review of the work carried out on thin films flows, focusing attention on the studies undertaken after the review by Oron *et al.* (1997). With regard to the theoretical-modeling developments, it is clear that lubrication theory has been used to elucidate a wide variety of flows in which films have small aspect ratios. These include flows involving single or multiple layers, driven by body and surface forces, potentially confined between rough or smooth, impermeable or porous, compliant or rigid walls, in the presence or absence of heat and mass transfer, phase changes, non-Newtonian rheology, and surface active contamination. In cases where inertia is important, methodologies combining boundary-layer theory and the use of Kármán-Pohlhausen approach have been used. The agreement between the modeling predictions, with and without inertia, and experimental measurements has been demonstrably favorable; examples of this include simulation of thin film flows down inclined planes, thermally driven climbing films, films undergoing dewetting, falling film flows, flows over spinning disks, and surfactant-driven flows.

Given the large volume of research conducted in this area since the time of Reynolds and Beauchamp-Towers, it is natural to ask the question: What next? What is currently exciting the community? The answers to these questions are, of course, somewhat subjective.

The area of falling films and spinning disks is active with new work on interactions between external forcing by, or coupling with, electrical and thermal fields as well as chemical reactions. Much work remains to be done here and the field is vibrant with new research by Tseluiko and Papageorgiou (2006) and Trevelyan *et al.* (2007) among others. Some of this recent progress is due, in no small part, to advances in numerical and analytical techniques (Scheid *et al.*, 2006). Future work is likely to focus on uncovering the mechanisms underlying the emergence of coherent structures in surface "turbulence" in falling films (Demekhin *et al.*, 2007a, 2007b). In the absence of inertia, templating is a vital aspect of modern nanoscience and the use of electric fields, demonstrated by the experiments of Morariu *et al.* (2003) and Chen *et al.* (2005) shown in Figs. 3 and 13 and simulations of Merkt *et al.* (2005), Wu *et al.* (2005), and Bandyopadhyay and Sharma (2007), provides an exciting avenue into producing patterns of precisely controlled dimensions.

Although a common process, evaporation is still relatively poorly understood. Anomalous exponents in retracting and evaporating water droplets have only recently been interpreted (Shahidzadeh-Bonn *et al.*, 2006) and in terms of theory there are new models being developed (Ajaev 2005b; Fried *et al.*, 2006; Shklvaev and Fried, 2007) to allow for more realistic mass and momentum exchange; the work of Pismen and Pomeau (2000) promises to account naturally for evaporative effects. There are interesting instabilities in evaporating droplets (Poulard *et al.*, 2003; Gotkis *et al.*, 2006) that require detailed mechanisms to be identified, and then there are the patterns left behind by evaporating droplets containing nanoparticles (Govor, Reiter, Parisi, and Bauer, 2004) and polymer solutions (Bormashenko *et al.*, 2005c). Recent progress has been made on the patterning of very thin uniform films (Rabani *et al.*, 2003) using diffusionlike discrete lattice models; the challenge now is to couple this with the evolving hydrodynamics.

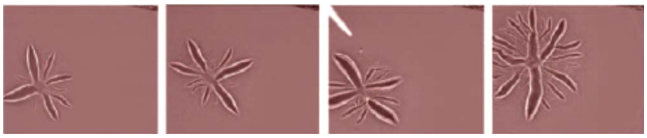

FIG. 39. (Color online) "Star bursts" in surfactant spreading over gels (reprinted with permission from Daniels *et al.*, 2005, copyright 2005, AIP).

Much interest currently is in the slippage of dewetting films atop substrates (Fetzer and Jacobs, 2007) and in the possibility or otherwise of instabilities at the rim (Reiter and Sharma, 2001) in which there has been recent progress theoretically (King *et al.*, 2006). The modeling associated with dewetting on chemically patterned, possibly topographically varying, substrates (Kargupta *et al.*, 2000; Geoghegan and Krausch, 2003), or the simultaneous dewetting and phase separation of binary mixtures (Clarke 2005), requires quantitative connections with experiments and much remains to be done here. Thin films consisting of binary mixtures and the resulting thermosolutal Marangoni instabilities that form are another topical area rich in both theory that is being developed by Podolny, Nepomnyashechy, and Oron (2007) and Podolny, Oron, and Nepomnyashchy (2007) and in observed experimental patterns (Zhang *et al.*, 2007). Nanoscale patterning of bilayers comprising thin soft solid and viscous films is also an active area strongly related to instabilities associated with dewetting (Hosoi and Mahadevan, 2004; Matar, Gkanis, and Kumar, 2005; Bandyopadhyay *et al.*, 2008).

Many interesting fundamental questions remain. It is still unclear how a water droplet "superspreads" on a hydrophobic substrate when laden with certain types of surfactant above the CMC (Nikolov *et al.*, 2002). Do micelles alter the intermolecular forces in the contact line region, thereby facilitating spreading? How does the contact angle of the spreading droplet depend on these effects? In other situations the substrate itself could play a significant role in the observed phenomena: Why is the spreading of surfactant-laden drops on the surface of gels accompanied by patterns resembling "star bursts" [see Fig. 39 showing results of the recent experimental work of Daniels *et al.* (2005) which is expanded upon further in Daniels *et al.* (2007)]? Do Marangoni stresses promote cracking of the gel? If so, then what is the nature of the coupling that leads to crack propagation? Other topical areas are connected with the fluid rheology: If this is no longer simply Newtonian then how do we account for complex rheology within the framework of lubrication theory as would be necessary in the case

of liquid-crystalline drops spreading on solid substrates (Poulard *et al.*, 2006) and thin films undergoing sol-gel transitions (Lee *et al.*, 2006)? In the latter case, the rheology is time dependent as a result of evaporation-induced self-assembly.

There are many open and interesting issues in geophysics related to thin film flows: debris, dense particulate, and avalanche flows (Ancey, 2007) present substantial challenges in their modeling using thin layer theories due to their rheology. Added to this are the possible thixotropic-ageing effects (Huynh *et al.*, 2005) that many real muds have and the hysteretic behavior that is associated with these effects. The thin film methodology is popular in dry granular flows (Forterre and Pouliquen, 2008) where, again, the rheology is only just beginning to be unraveled. Progress in these areas will continue to utilize the lubricationlike model, both with and without inertia, and it will play a large part in understanding these important flows.

Recently, the aggregation of nanoparticulates and their influence on the hydrodynamics of films has become of great interest. How do nanoparticles self-aggregate on the surface of drying droplets to create ordered monolayers (Bigioni *et al.*, 2006) and how is that coupled to the hydrodynamics? The creation of nanoparticles or surfactants via chemical reactions gives rise to Marangoni effects (Pereira *et al.*, 2007) which manifest themselves in recoiling or oscillating fluid lenses (van Nierop *et al.*, 2006; Stocker and Bush, 2007) and droplet motion driven by dynamically varying substrate wettability (John *et al.*, 2005; Yochelis and Pismen 2005); these systems are beginning to be understood.

For the biological questions associated with the mechanisms of cell motion, lubrication-based droplet models have recently been developed for both cell movement (Oliver *et al.*, 2005) and cell division (Schwartz *et al.*, 2004) and provide the beginnings of a new area in lubrication flows.

Thus we observe that, over 125 years after its discovery, research involving thin films and lubrication theory is still going strong and gaining momentum; moreover, its range of applications is widening year upon year. We look forward to the next few decades with anticipation for the new discoveries that will occur in this field.

ACKNOWLEDGMENTS

O.K.M. would like to thank E.S.M. and the late K.E.M. for their support. O.K.M. also acknowledges the support of the EPSRC through Grants No. EP/E056466/1, No. EP/F009194/1, and No. EP/E021468/1. We thank Tom Witelski for his reading of an earlier version of this work and the numerous useful comments made by a number of extremely helpful referees that have led to a considerably more thorough review. Finally, we thank Andrew Bernoff for giving us the idea for the review at a meeting which took place at the Institute for Pure and Applied Mathematics in Los Angeles, 2006.

APPENDIX A: LETTER TO THE "THE ENGINEER" (1884)

Here we reproduce extracts from a short letter to the editor of "The Engineer" February 1884, which has been referred to in Sec. I:

> "Sir, I have read with much attention and no small disappointment the article entitled "What is Friction?" which appeared in the last number of the Engineer. I anticipated that Mr Towers' researches would have had some practical value; but as far as I can see they might just as well never have been undertaken. To certain minds I have no doubt that it may prove valuable to know that friction between dry surfaces is not the same thing as friction between oiled surfaces; but to the great body of engineers the statement is simply useless. It is really a matter of no importance whatever that frictional coefficients vary with the speed, because the fact cannot be usefully applied. Again, we gain absolutely nothing of any value from the discovery, if such it be, that the use of an oil bath diminishes friction enormously. We cannot use oil baths, and the fact is therefore of no importance. It seems to be the fate of the Institution of Mechanical Engineers to always carry out investigations of no practical value to anyone. If Mr Towers had told us something about the relative values of different materials for bearings he would have done good service. So-called scientific research is rapidly becoming nothing but a method by which considerable incomes may be earned in finding out things of no earthly use to any mortal. The Institution of Mechanical Engineers ought to keep clear of this sort of thing and its money ought to be spent on inquiries likely to prove of practical value to its members. There is no lack of subjects for investigation." by T.C.H, Birmingham, 25th February 1884.

It is interesting to observe the valuable interplay between experiment theory and, of course, with the great advantage of hindsight to marvel at the short-sighted and narrow thinking evident in the letter: Mr Beauchamp Towers did thought-provoking experiments carefully and presented the material in a manner that motivated Osborne Reynolds to create and validate the theory upon which ultimately, some 125 years later, much of this review is based.

APPENDIX B: ALGEBRAIC DETAIL

This appendix contains expressions for interfacial conditions, transport equations, and velocity components, which are necessary for the derivation of the evolution equations in Sec. II and Appendix C. These expressions are too cumbersome to be included in the main text. The dimensionless tangential and normal stress conditions at $z=h_i+\mathcal{B}$ from Sec. II.B are

$$j_{ie}([u_e]_i+\epsilon^2(h_i+\mathcal{B})_x[w_e]_i)\Delta-\epsilon(h_i+\mathcal{B})_x([\tau_{zz}]_i-[\tau_{xx}]_i+[M_{zz}]_i-[M_{xx}]_i)+(2-\Delta^2)([\tau_{zx}]_i+[M_{zx}]_i)=[-\mathcal{M}_i(\sigma_{ix}+[h_i+\mathcal{B}]_x\sigma_{iz})]\Delta, \quad \text{(B1)}$$

$$\epsilon^2\Delta^2 j_{ie}([w_e]_i - [h_i+\mathcal{B}]_x[u_e]_i) + \Delta([p]_i\Delta^2 - \epsilon([\tau_{zz}]_i + [M_{zz}]_i) + 2\epsilon^2(h_i+\mathcal{B})_x([\tau_{zx}]_i + [M_{zx}]_i) + \epsilon(1-\Delta^2)([\tau_{xx}]_i + [M_{xx}]_i)) = -\left(\epsilon^2\mathcal{M}_i\sigma_i + \frac{\epsilon^3}{\mathcal{C}_i}\right)(h_i+\mathcal{B})_{xx}, \quad \text{(B2)}$$

where $\Delta \equiv (1+\epsilon^2[h_i+\mathcal{B}]_x^2)^{1/2}$ and σ depends on temperature and/or the interfacial concentration of any surfactants that may be present.

The surfactant transport equation is expressed by

$$\Gamma_{it} + \frac{1}{\Delta^2}\left(u_{is}\Gamma_{ix} + \epsilon^2 h_{ix}w_{is}\Gamma_{ix} + \epsilon^2\Gamma_i(w_{is} - u_{is}h_{ix})\frac{h_{ix}}{\Delta^2}\right) = \frac{1}{\mathrm{Pe}_i}\frac{[\Gamma_{ixx} - \epsilon^2\Gamma_{ix}(h_{ix}h_{ixx}/\Delta^2)]}{\Delta^2} + J_i. \quad \text{(B3)}$$

The expressions for u_1 and u_2 are

$$u_1 = \frac{\mathcal{M}_1}{m_1}[-\mathcal{B} + h_2(m_1-1) + \beta m_1 + z][\sigma_{1x} + (h_1 + \mathcal{B})_x\sigma_{1z}] + \mathcal{M}_2(\beta+h_2)[\sigma_{2x} + (h_2+\mathcal{B})_x\sigma_{2z}] - \frac{1}{2}h_2(2\beta+h_2)([p_2+\phi_2]_x - \mathcal{G}) + \frac{1}{2m_1}(\mathcal{B}^2 + h_2[2m_1(\beta+h_2) - h_2] + 2\mathcal{B}(h_1-z) + z^2 - 2h_1[h_2(m_1-1) + \beta m_1 + z]) \times([p_1+\phi_1]_x - n_1\mathcal{G}), \quad \text{(B4)}$$

$$u_2 = (z - \mathcal{B} + \beta)(\mathcal{M}_1[\sigma_{1x} + (h_1+\mathcal{B})_x\sigma_{1z}] + \mathcal{M}_2[\sigma_{2x} + (h_2+\mathcal{B})_x\sigma_{2z}]) + (h_1-h_2)(\mathcal{B}-\beta-z)([p_1+\phi_1]_x - n_1\mathcal{G}) + \frac{1}{2}[z^2 - 2z(\mathcal{B}+h_2) + 2h_2(\mathcal{B}-\beta) + \mathcal{B}^2] \times([p_2+\phi_2]_x - \mathcal{G}). \quad \text{(B5)}$$

APPENDIX C: LUBRICATION THEORY FOR ONE-SIDED EVAPORATION MODELS

Here we provide a derivation of the so-called one-sided models (Burelbach *et al.*, 1988) given in Sec. IV.A for a single thin film resting on an impermeable, rigid, and smooth substrate driven by evaporation or condensation. This is an important example showing the influence of the interfacial mass flux j_e introduced in Sec. II [Eqs. (5) and (11)]. We can employ the same formal transformations and take the same limits as in Sec. II.C.2 but for brevity we neglect slip, all body, and intermolecular forces, so that $(\beta, \mathcal{G}, \mathcal{B}, \mathbf{M}, \phi) \to 0$.

We consider finite mass fluxes associated with phase changes $j_e > 0$, where we have dropped any distinguishing decoration since only a single layer is considered; we do, however, use subscript g to designate quantities pertaining to the gas phase overlying the film. In order to model processes involving evaporation or condensation, the same framework as that used in Secs. II.A–II.C is employed here, but, due to temperature effects, the following additional (dimensional) equations and closure relations are required: an interfacial mass balance,

$$j_e = \rho(\mathbf{u} - \mathbf{u}_s)\cdot\mathbf{n} = \rho_g(\mathbf{u}_g - \mathbf{u}_s)\cdot\mathbf{n}, \quad \text{(C1)}$$

no slip at the interface $[\mathbf{u}]\cdot\mathbf{t} = 0$ and an interfacial energy balance (Delhaye, 1974),

$$j_e[\mathrm{La} + \tfrac{1}{2}|(\mathbf{u}-\mathbf{u}_s)\cdot\mathbf{n}|^2] + \lambda_{\mathrm{th}}\nabla T\cdot\mathbf{n} + 2\mu(\mathcal{E}\cdot\mathbf{n})\cdot(\mathbf{u}-\mathbf{u}_s) = \frac{j_e}{2}|(\mathbf{u}_g - \mathbf{u}_s)\cdot\mathbf{n}|^2 + \lambda_{\mathrm{th},g}\nabla T_g\cdot\mathbf{n} + 2\mu_g(\mathcal{E}_g\cdot\mathbf{n})\cdot(\mathbf{u}_g - \mathbf{u}_s), \quad \text{(C2)}$$

are required where $\mathbf{u}_s$ is the interfacial velocity, La is the latent heat of vaporization, and λ_{th} and $\lambda_{\mathrm{th},g}$ are the thermal conductivities of the liquid and gas phases, respectively. The remaining variables have already been defined in Sec. II.

The temperature T evolves as a result of convection, conduction, and evaporation or condensation and satisfies an advection-diffusion equation,

$$C_{\mathrm{sp}}(T_t + \mathbf{u}\cdot\nabla T) = \lambda_{\mathrm{th}}\nabla^2 T/\rho, \quad \text{(C3)}$$

where C_{sp} is the specific heat capacity of the fluid. For closure, the following equation of state relating temperature and mass flux at $z = h(x,t)$ is usually employed:

$$j_e = j_0(T_s - T_\infty), \quad \text{(C4)}$$

where T_s and T_∞ denote the interfacial and saturation temperatures, respectively, and j_0 is a parameter which depends on T_∞, the molecular weight and density of the vapor phase, and an "accommodation" coefficient (Plesset and Prosperetti, 1976; Burelbach *et al.*, 1988; Oron *et al.*, 1997). Recently, Ajaev (2005b) utilized an extension of Eq. (C4) augmented by a pressure jump in the mass flux based on thermodynamic considerations,

$$j_e = j_0(T_s - T_\infty) + C(p - p_g). \quad \text{(C5)}$$

The derivation and the precise form of the constant of proportionality C are given in Moosman and Homsy (1980). Fried *et al.* (2006) and Shklyaev and Fried (2007) augmented this evaporation model further incorporating a nonvolatile dissolved surfactant on the interface and suggested a more general replacement for the mass flux; they develop the one-sided model in the light of these new assumptions.

The temperature at $z = 0$ is set to $T = T_0$ to reflect the case of a highly conducting base. The dependence of the surface tension on the temperature is given by the linear equation of state $\sigma = \sigma_m + (d\sigma/dT)(T_s - T_\infty)$, where $d\sigma/dT < 0$ since, for most fluids, surface tension is a decreasing function of temperature; here σ_m denotes the surface tension at the saturation temperature T_∞.

The evaporative flux j_e, the temperature T, and the surface tension σ are then nondimensionalized,

$$j_e = \frac{\lambda_{\rm th}(T_0 - T_\infty)}{\mathcal{H}\mathrm{La}}\tilde{j}_e, \quad T = T_\infty + (T_0 - T_\infty)\tilde{T},$$

$$\sigma = \sigma_m + (\sigma_0 - \sigma_m)\tilde{\sigma}, \tag{C6}$$

where the tildes have been reintroduced to designate dimensionless quantities; the surface tension difference in the problem is then $S=\sigma_0-\sigma_m$. It should be noted that the scaling for j_e in Eq. (C6) is different from that in Eq. (11) (with $\mu_2 \to \mu$ since we are dealing with a single layer). The j_e in Eq. (11) can be recovered by multiplying that in Eq. (C6) by $\lambda_{\rm th}(T_0-T_\infty)/\mu\mathrm{La}$.

Substitution of the temperature scaling into Eq. (C3) yields an additional equation to Eqs. (12)–(14) applied for a single layer in the lubrication approximations,

$$u_x + w_z = 0, \quad p_x = u_{zz}, \quad p_z = 0, \quad T_{zz} = 0. \tag{C7}$$

In obtaining equation $T_{zz}=0$, we have implicitly assumed that the thermal Péclet number $\mathrm{Pe}_{\rm th} = \rho C_{\rm sp}\mathcal{U}/(\mathcal{L}\lambda_{\rm th})$ is small so that diffusion across the thin layer is rapid. Some discussion of the opposite limit in the context of temperature dependent flows is in Sec. IV.D. Substitution of the temperature and surface tension scalings in Eq. (C6) into the equation of state yields $\sigma = 1 - M_{\rm th}T$, where $M_{\rm th} = -[(T_0-T_\infty)/(\sigma_0-\sigma_m)]d\sigma/dT$; note that $M_{\rm th}>0$ for most fluids since $d\sigma/dT<0$.

Substitution of the scalings in Eqs. (7), (8), and (C6) into Eq. (C1) yields the following dimensionless relation:

$$\epsilon^2([w_e] - h_x[u_e]) = \frac{\lambda_{\rm th}(T_0 - T_\infty)}{\mathcal{U}\mathcal{L}\mathrm{La}\rho_g} j_{ie}.$$

Similarly, nondimensionalizing Eq. (C2) and assuming that the gas density, viscosity, and thermal conductivity are much smaller than their liquid counterparts, which is the essence of the one-sided model (Burelbach *et al.*, 1988), yield at $z=h$

$$j_e = -T_z.$$

Interfacial conditions are obtained by considering Eqs. (B1) and (B2). In these equations, j_e must be rescaled according to Eq. (C6); this yields the following at $z=h$ to leading order in ϵ after invoking the one-sided assumptions above,

$$u_z = \sigma_x + h_x\sigma_z, \quad p = -\epsilon^3 h_{xx}/\mathcal{C}_m + \mathcal{R}j_e^2, \tag{C8}$$

where

$$\mathcal{R} \equiv \frac{1}{\mu\rho_g\mathcal{L}\mathcal{U}_m}\left[\lambda_{\rm th}\left(\frac{T_0 - T_\infty}{\mathrm{La}}\right)\right]^2$$

is a vapor "recoil" number, characterizing the relative importance of the force on the interface due to vapor thrust; this is due to the fact that the density ratio $\rho_g/\rho \sim 10^{-3}$. Here it is important to note that, due to the no-slip condition at the interface, $[\mathbf{u}]\cdot\mathbf{t}=\mathbf{0}$, j_e does not appear in Eq. (D1). We have also set the Marangoni number $\mathcal{M}=1$, thereby fixing the velocity scale as $\mathcal{U}_m = S\mathcal{H}/\mu\mathcal{L}$, as in the discussion near Eq. (34). Also the effects of mean surface tension on capillarity, characterized by $\epsilon^3/\mathcal{C}_m = \epsilon^2\sigma_m/S$ in Eq. (D2), have been retained in the pressure; those due to surface tension variations, characterized by $\epsilon^2\sigma$ in Eq. (D2), have been neglected, as also discussed near Eq. (34).

Combination of the dimensionless Eq. (C1) with the kinematic boundary condition and nondimensionalization of Eq. (C4) yield the following equations at $z=h$:

$$E_n j_e + h_t + u_s h_x - w_s = 0, \quad \mathcal{K}j_e = T. \tag{C9}$$

Notably, there is now an extra term $E_n j_e$, reflecting the presence of an interfacial mass flux. Here $E_n \equiv \mathcal{L}\lambda_{\rm th}(T_0 - T_\infty)/\rho\mathcal{U}_m\mathcal{H}^2\mathrm{La}$ is an evaporation number and $\mathcal{K} \equiv \lambda_{\rm th}/j_0\mathcal{H}\mathrm{La}$ represents the departure from equilibrium conditions. At $z=0$, $T=1$, and $u=w=0$.

The temperature and evaporative flux follow from these equations

$$T = 1 - j_e z, \quad j_e = 1/(h + \mathcal{K}), \tag{C10}$$

and the leading order evolution equation then reads

$$h_t = -\frac{E_n}{h+\mathcal{K}} + \left[\frac{h^3}{3}\left(-\frac{\epsilon^3}{\mathcal{C}_m}h_{xx} + \frac{\mathcal{R}}{(h+\mathcal{K})^2}\right)_x - \frac{M_{\rm th}\mathcal{K}}{2}\frac{h^2 h_x}{(h+\mathcal{K})^2}\right]_x, \tag{C11}$$

which is also Eq. (79) in Sec. IV.A. This is an evolution equation, which is structurally similar to Eq. (34). The second and third terms on the right-hand side of Eq. (C11) are associated with evaporation or condensation and vapor recoil, respectively. The fourth term is associated with Marangoni stresses entering the problem through the surface tension dependence on temperature and the dependence of the latter on h. In deriving this equation, we have neglected implicitly the temperature dependence of the viscosity; the effects that such a dependence generate are discussed in Sec. IV.D.

Equation (C11) can be recast in terms of j_e as follows. From Eq. (C10), $T=1-j_e z$, so that the tangential stress condition at $z=h$ given by Eq. (C8) becomes $u_z = \sigma_x + h_x\sigma_z = -M_{\rm th}(hj_e)_x$; the normal stress condition in this case remains unaltered. Equation (79) then becomes

$$h_t = -E_n j_e + \left[\frac{h^3}{3}\left(-\frac{\epsilon^3}{\mathcal{C}_m}h_{xx} + \mathcal{R}j_e^2\right)_x - M_{\rm th}\frac{h^2}{2}(hj_e)_x\right]_x. \tag{C12}$$

This equation can be augmented by a conjoining pressure term $\phi(h)$ which allows evaporative dewetting patterning to be studied (Bestehorn, 2007) or droplet retraction to be followed (Ajaev, 2005a). An advantage of incorporating the pressure into the mass flux, as in Eq. (C5), is that it leads to an equilibrium film thickness, where the mass flux is zero $j_e=0$. Thus evaporation and van der Waals effects balance allowing for the experimentally observed microscopic adsorbed film on the substrate (DasGupta *et al.*, 1993).

REFERENCES

Acton, J. M., H. E. Huppert, and M. G. Worster, 2001, J. Fluid Mech. **440**, 359.

Afsar-Siddiqui, A. B., P. F. Luckham, and O. K. Matar, 2003a, Adv. Colloid Interface Sci. **106**, 183.

Afsar-Siddiqui, A. B., P. F. Luckham, and O. K. Matar, 2003b, Langmuir **19**, 696.

Afsar-Siddiqui, A. B., P. F. Luckham, and O. K. Matar, 2003c, Langmuir **19**, 703.

Afsar-Siddiqui, A. B., P. F. Luckham, and O. K. Matar, 2004, Langmuir **20**, 7575.

Ajaev, V. S., 2005a, Phys. Rev. E **72**, 031605.

Ajaev, V. S., 2005b, J. Fluid Mech. **528**, 279.

Alekseenko, S. V., V. A. Antipin, V. V. Guzanov, S. M. Kharlamov, and D. M. Markovich, 2005, Phys. Fluids **17**, 121704.

Alekseenko, S. V., V. E. Nakoryakov, and B. T. Pokusaev, 1985, AIChE J. **31**, 1446.

Alekseenko, S. V., V. E. Nakoryakov, and B. T. Pokusaev, 1994, *Wave Flow of Liquid Films* (Begel House, New York).

Alekseev, A., T. Gambaryan-Roisman, and P. Stephan, 2005, Phys. Fluids **17**, 062106.

Alleborn, N., and H. Raszillier, 2004, Chem. Eng. Sci. **59**, 2071.

Allen, R. F., and C. M. Biggin, 1974, Phys. Fluids **17**, 287.

Ancey, C., 2007, J. Non-Newtonian Fluid Mech. **142**, 4.

Anderson, D. M., and S. H. Davis, 1995, Phys. Fluids **7**, 248.

Anderson, D. M., G. B. McFadden, and A. A. Wheeler, 1998, Annu. Rev. Fluid Mech. **30**, 139.

Aoune, A., and C. Ramshaw, 1999, Int. J. Heat Mass Transfer **42**, 2543.

Aradian, A., E. Raphael, and P. G. De Gennes, 2000, Eur. Phys. J. E **2**, 367.

Argyriadi, K., K. Serifi, and V. Bontozoglou, 2004, Phys. Fluids **16**, 2457.

Argyriadi, K., M. Vlachogiannis, and V. Bontozoglou, 2006, Phys. Fluids **18**, 012102.

Atherton, R. W., and G. M. Homsy, 1976, Chem. Eng. Commun. **2**, 57.

Bain, C. D., G. D. Burnetthall, and R. R. Montgomerie, 1994, Nature (London) **372**, 414.

Balmforth, N. J., A. S. Burbidge, R. V. Craster, J. Salzig, and A. Shen, 2000, J. Fluid Mech. **403**, 37.

Balmforth, N. J., and R. V. Craster, 2000, J. Fluid Mech. **422**, 225.

Balmforth, N. J., R. V. Craster, A. C. Rust, and R. Sassi, 2006, J. Non-Newtonian Fluid Mech. **139**, 103.

Balmforth, N. J., R. V. Craster, and R. Sassi, 2002, J. Fluid Mech. **470**, 1.

Balmforth, N. J., R. V. Craster, and R. Sassi, 2004, J. Fluid Mech. **499**, 149.

Balmforth, N. J., R. V. Craster, and C. Toniolo, 2003, Phys. Fluids **15**, 3370.

Balmforth, N. J., and J. J. Liu, 2004, J. Fluid Mech. **519**, 33.

Balmforth, N. J., and S. Mandre, 2004, J. Fluid Mech. **514**, 1.

Bandyopadhyay, D., R. Gulabani, and A. Sharma, 2005, Ind. Eng. Chem. Res. **44**, 1259.

Bandyopadhyay, D., and A. Sharma, 2007, J. Colloid Interface Sci. **311**, 595.

Bandyopadhyay, D., A. Sharma, and V. Shankar, 2008, J. Chem. Phys. **128**, 154909.

Bankoff, S. G., E. Griffing, and R. Schluter, 2002, Ann. N.Y. Acad. Sci. **974**, 1.

Bankoff, S. G., M. J. Miksis, and H. K. R. Gwinner, 1994, Nucl. Eng. Des. **149**, 441.

Baral, D., K. Hutter, and R. Greve, 2001, Appl. Mech. Rev. **54**, 215.

Bardon, S., M. Cachile, A. M. Cazabat, X. Fanton, and S. Villette, 1996, Faraday Discuss. **104**, 307.

Batchelor, G. K., 1967, *An Introduction to Fluid Dynamics* (Cambridge University Press, Cambridge).

Becker, J., G. Grün, R. Seemann, H. Mantz, K. Jacobs, K. R. Mecke, and R. Blossey, 2003, Nature Mater. **2**, 59.

Ben Amar, M., and L. J. Cummings, 2001, Phys. Fluids **13**, 1160.

Benichou, O., M. Cachile, A. M. Cazabat, C. Poulard, M. P. Valignat, F. Vandenbrouck, and D. V. Effenterre, 2003, Adv. Colloid Interface Sci. **100**, 381.

Benjamin, T. B., 1957, J. Fluid Mech. **2**, 554.

Benney, D. J., 1966, J. Math. Phys. (Cambridge, Mass.) **45**, 150.

Bercovici, D., and J. Lin, 1996, J. Geophys. Res., [Solid Earth] **101**, 3291.

Bertozzi, A. L., and M. P. Brenner, 1997, Phys. Fluids **9**, 530.

Bertozzi, A. L., A. Münch, X. Fanton, and A. M. Cazabat, 1998, Phys. Rev. Lett. **81**, 5169.

Bertozzi, A. L., A. Münch, and M. Shearer, 1999, Physica D **134**, 431.

Bertozzi, A. L., A. Münch, M. Shearer, and K. Zumbrun, 2001, Eur. J. Appl. Math. **12**, 253.

Bertozzi, A. L., and M. Shearer, 2000, SIAM J. Math. Anal. **32**, 194.

Bestehorn, M., 2007, Eur. Phys. J. Spec. Top. **146**, 391.

Bestehorn, M., and D. Merkt, 2006, Phys. Rev. Lett. **97**, 127802.

Bestehorn, M., and K. Neuffer, 2001, Phys. Rev. Lett. **87**, 046101.

Bestehorn, M., A. Pototsky, and U. Thiele, 2003, Eur. Phys. J. B **33**, 457.

Bielarz, C., and S. Kalliadasis, 2003, Phys. Fluids **15**, 2512.

Bigioni, T. P., X. M. Lin, T. T. Nguyen, E. I. Corwin, T. A. Witten, and H. M. Jaeger, 2006, Nature Mater. **5**, 265.

Bird, R. B., A. R, C, and O. Hassager, 1987, *Dynamics of Polymeric Liquids* (Wiley, New York), Vol. 1.

Blake, S., 1990, in *IAVCEI Proceedings in Volcanology*, edited by J. H. Fink (Springer-Verlag, New York), Vol. 2, pp. 88–128.

Blossey, R., 1995, Int. J. Mod. Phys. B **9**, 3489.

Blossey, R., A. Münch, M. Rauscher, and B. Wagner, 2006, Eur. Phys. J. E **20**, 267.

Bonn, D., J. Eggers, J. Meunier, and E. Rolley, 2009, Rev. Mod. Phys. **81**, 739.

Bontozoglou, V., and G. Papapolymerou, 1997, Int. J. Multiphase Flow **23**, 69.

Boodhoo, K. V. K., W. A. E. Dunk, M. S. Jassim, and R. J. J. Jachuck, 2004, J. Appl. Polym. Sci. **91**, 2079.

Boodhoo, K. V. K., W. A. E. Dunk, M. Vicevic, R. J. J. Jachuck, V. Sage, D. J. MacQuarrie, and J. H. Clark, 2006, J. Appl. Polym. Sci. **101**, 8.

Boos, W., and A. Thess, 1999, Phys. Fluids **11**, 1484.

Borgas, M. S., and J. B. Grotberg, 1988, J. Fluid Mech. **193**, 151.

Bormashenko, E., R. Pogreb, O. Stanevsky, Y. Bormashenko, and O. Gendelman, 2005a, Mater. Lett. **59**, 3553.

Bormashenko, E., R. Pogreb, O. Stanevsky, Y. Bormashenko, T. Stein, and O. Gengelman, 2005b, Langmuir **21**, 9604.

Bormashenko, E., R. Pogreb, O. Stanevsky, Y. Bormashenko, S. Tamir, R. Cohen, M. Nunberg, V. Z. Gaisin, M. Gorelik, and O. V. Gendelman, 2005c, Mater. Lett. **59**, 2461.
Bowden, N., S. Brittain, A. G. Evans, J. W. Hutchinson, and G. M. Whitesides, 1998, Nature (London) **393**, 146.
Bowen, M., J. Sur, A. L. Bertozzi, and R. P. Behringer, 2005, Physica D **209**, 36.
Braun, R. J., B. T. Murray, W. J. Boettinger, and G. B. McFadden, 1995, Phys. Fluids **7**, 1797.
Braun, R. J., S. A. Snow, and U. C. Pernisz, 1999, J. Colloid Interface Sci. **219**, 225.
Brochard-Wyart, F., and J. Daillant, 1990, Can. J. Phys. **68**, 1084.
Brochard-Wyart, F., P. G. de Gennes, H. Hervet, and C. Redon, 1994, Langmuir **10**, 1566.
Brochard-Wyart, F., J.-M. di Meglio, and D. Quéré, 1987, C. R. Acad. Sci., Ser. II: Mec., Phys., Chim., Sci. Terre Univers **304**, 553.
Brochard-Wyart, F., and C. Redon, 1992, Langmuir **8**, 2324.
Brochard-Wyart, F., C. Redon, and C. Sykes, 1992, C. R. Acad. Sci., Ser. II: Mec., Phys., Chim., Sci. Terre Univers **314**, 19.
Brzoska, J. B., F. Brochard-Wyart, and F. Rondelez, 1992, Europhys. Lett. **19**, 97.
Bunk, M., 1999, *Spreading with basal solidification*, Ph.D. thesis, University of Karlsruhe, Germany.
Bunk, M. A., and J. R. King, 2003, ZAMP **83**, 820.
Bunov, A. V., E. A. Demekhin, and V. Y. Shkadov, 1984, J. Appl. Math. Mech. **48**, 495.
Burelbach, J. P., S. G. Bankoff, and S. H. Davis, 1988, J. Fluid Mech. **195**, 463.
Burns, J. R., and R. J. J. Jachuck, 2005, Int. J. Heat Mass Transfer **48**, 2540.
Burns, J. R., C. Ramshaw, and R. J. J. Jachuck, 2003, Chem. Eng. Sci. **58**, 2245.
Butuzov, A. I., and I. I. Puhovoi, 1976, J. Eng. Phys. **31**, 217.
Cachile, M., O. Benichou, and A. M. Cazabat, 2002, Langmuir **18**, 7985.
Cachile, M., O. Benichou, C. Poulard, and A. M. Cazabat, 2002, Langmuir **18**, 8070.
Cachile, M., and A. M. Cazabat, 1999, Langmuir **15**, 1515.
Cachile, M., A. M. Cazabat, S. Bardon, M. P. Valignat, and F. Vadenbrouck, 1999, Colloids Surf., A **159**, 47.
Cachile, M., M. Schneemilch, A. Hamraoui, and A. M. Cazabat, 2002, Adv. Colloid Interface Sci. **96**, 59.
Cahn, J. W., 1965, J. Chem. Phys. **42**, 93.
Carles, P., and A.-M. Cazabat, 1993, J. Colloid Interface Sci. **157**, 196.
Carou, J. Q., B. R. Duffy, N. J. Mottram, and S. K. Wilson, 2006, Phys. Fluids **18**, 027105.
Carou, J. Q., N. J. Mottram, S. K. Wilson, and B. R. Duffy, 2007, Liq. Cryst. **34**, 621.
Cazabat, A. M., F. Heslot, S. M. Troian, and P. Carles, 1990, Nature (London) **346**, 824.
Cazabat, A. M., F. Heslot, S. M. Troian, and P. Carles, 1992, Adv. Colloid Interface Sci. **39**, 61.
Cerda, E., and L. Mahadevan, 2003, Phys. Rev. Lett. **90**, 074302.
Cermelli, P., E. Fried, and M. E. Gurtin, 2005, J. Fluid Mech. **544**, 339.
Chang, H.-C., 1994, Annu. Rev. Fluid Mech. **26**, 103.
Chang, H.-C., M. Cheng, E. A. Demekhin, and D. I. Kopelevitch, 1994, J. Fluid Mech. **270**, 251.
Chang, H.-C., and E. A. Demekhin, 1999, J. Fluid Mech. **380**, 233.
Chang, H.-C., and E. A. Demekhin, 2002, *Complex Wave Dynamics on Thin Films* (Elsevier, Amsterdam).
Chang, H.-C., E. A. Demekhin, and E. Kalaidin, 1996, AIChE J. **42**, 1553.
Chang, H.-C., E. A. Demekhin, and E. Kalaidin, 2000, Phys. Fluids **12**, 2268.
Chang, H.-C., E. A. Demekhin, and D. I. Kopelevitch, 1993, J. Fluid Mech. **250**, 433.
Chang, H.-C., E. A. Demekhin, and S. S. Saprikin, 2002, J. Fluid Mech. **462**, 255.
Charru, F., and E. J. Hinch, 2000, J. Fluid Mech. **414**, 195.
Charwat, A. F., R. E. Kelly, and C. Gazley, 1972, J. Fluid Mech. **53**, 227.
Chen, K. P., 1993, Phys. Fluids A **5**, 3038.
Chen, L., L. Zhuang, P. Deshpande, and S. Y. Chou, 2005, Langmuir **21**, 818.
Cho, S. K., H. Moon, and C.-J. Kim, 2003, J. Microelectromech. Syst. **12**, 70.
Clarke, A., T. D. Blake, K. Carruthers, and A. Woodward, 2002, Langmuir **18**, 2980.
Clarke, N., 2004, Eur. Phys. J. E **14**, 207.
Clarke, N., 2005, Macromolecules **38**, 6775.
Coakley, W. T., D. Gallez, E. R. de Souza, and H. Gauci, 1999, Biophys. J. **77**, 817.
Cohen, B. I., J. A. Krommes, W. M. Tang, and M. N. Rosenbluth, 1976, Nucl. Fusion **16**, 971.
Coward, A. V., D. T. Papageorgiou, and Y. S. Smyrlis, 1995, ZAMP **46**, 1.
Craster, R. V., and O. K. Matar, 2000, J. Fluid Mech. **425**, 235.
Craster, R. V., and O. K. Matar, 2005, Phys. Fluids **17**, 032104.
Craster, R. V., and O. K. Matar, 2006, J. Fluid Mech. **553**, 85.
Craster, R. V., and O. K. Matar, 2007, Langmuir **23**, 2588.
Craster, R. V., O. K. Matar, and D. T. Papageorgiou, 2002, Phys. Fluids **14**, 1364.
Cummings, L. J., 2004, Eur. J. Appl. Math. **15**, 651.
Dandapat, B. S., and P. C. Ray, 1994, J. Phys. D **27**, 2041.
Daniels, K. E., S. Mukhopadhyay, and R. P. Behringer, 2005, Chaos **15**, 041107.
Daniels, K. E., S. Mukhopadhyay, P. J. Houseworth, and R. P. Behringer, 2007, Phys. Rev. Lett. **99**, 124501.
Danov, K. D., N. Alleborn, H. Raszillier, and F. Durst, 1998, Phys. Fluids **10**, 131.
Danov, K. D., V. N. Paunov, N. Alleborn, H. Raszillier, and F. Durst, 1998, Chem. Eng. Sci. **53**, 2809.
Danov, K. D., V. N. Paunov, S. D. Stoyanov, N. Alleborn, H. Raszillier, and F. Durst, 1998, Chem. Eng. Sci. **53**, 2823.
Darhuber, A. A., and S. M. Troian, 2003, Phys. Fluids **15**, 1295.
Darhuber, A. A., S. M. Troian, J. M. Davis, S. M. Miller, and S. Wagner, 2000, J. Appl. Phys. **88**, 5119.
DasGupta, S., J. A. Schonberg, I. Y. Kim, and P. C. Wayner, 1993, J. Colloid Interface Sci. **157**, 332.
Davidovitch, B., E. Moro, and H. A. Stone, 2005, Phys. Rev. Lett. **95**, 244505.
Davis, J. M., and S. M. Troian, 2005, Phys. Fluids **17**, 072103.
Davis, S. H., and L. M. Hocking, 1999a, Phys. Fluids **11**, 48.
Davis, S. H., and L. M. Hocking, 1999b, Phys. Fluids **12**, 1646.
De Bruyn, J. R., 1992, Phys. Rev. A **46**, R4500.
De Ryck, A., and D. Quéré, 1996, J. Fluid Mech. **311**, 219.
Deegan, R. D., 2000, Phys. Rev. E **61**, 475.
Deegan, R. D., O. Bakajin, T. F. Dupont, G. Huber, S. R. Nagel, and T. A. Witten, 1997, Nature (London) **389**, 827.
Deegan, R. D., O. Bakakin, T. F. Dupont, G. Huber, S. R.

Nagel, and T. A. Witten, 2000, Phys. Rev. E **62**, 756.
de Gennes, P. G., 1985, Rev. Mod. Phys. **57**, 827.
Delhaye, J. M., 1974, Int. J. Multiphase Flow **1**, 395.
Demekhin, E. A., E. N. Kalaidin, S. Kalliadasis, and S. Y. Vlaskin, 2007a, Phys. Fluids **19**, 114103.
Demekhin, E. A., E. N. Kalaidin, S. Kalliadasis, and S. Y. Vlaskin, 2007b, Phys. Fluids **19**, 114104.
Demekhin, E. A., G. Y. Tokarev, and V. Y. Shkadov, 1991, Physica D **52**, 338.
Derjaguin, B. V., and L. D. Landau, 1941, Acta Physicochim. URSS **14**, 633.
de Souza, E. R., C. Anteneodo, D. Gallez, and P. Bisch, 2001, J. Colloid Interface Sci. **244**, 303.
de Souza, E. R., and D. Gallez, 1998, Phys. Fluids **10**, 1804.
DeWitt, A., D. Gallez, and C. Christov, 1994, Phys. Fluids **6**, 3256.
Diez, J. A., and L. Kondic, 2001, Phys. Rev. Lett. **86**, 632.
Dinh, T. N., M. J. Konovalikhin, and B. R. Sehgal, 2000, Prog. Nucl. Eng. **36**, 405.
Doedel, E., A. Champneys, T. Fairfrieve, Y. Kusnetsov, B. Sandstede, and X. Wang, 1997, *Continuation and Bifurcation Software for Ordinary Differential Equations* (Concordia University, Montreal).
Dong, J., V. D. Almeida, and C. Tsouris, 2001, J. Colloid Interface Sci. **242**, 327.
Dorfman, L. A., 1967, J. Eng. Phys. **12**, 309.
Duffy, B. R., and H. K. Moffatt, 1995, Chem. Eng. J. **60**, 141.
Duffy, B. R., and H. K. Moffatt, 1997, Eur. J. Appl. Math. **8**, 37.
Duffy, B. R., and S. K. Wilson, 2003, Phys. Fluids **15**, 3236.
Duprat, C., C. Ruyer-Quil, S. Kalliadasis, and F. Giorgiutti-Dauphiné, 2007, Phys. Rev. Lett. **98**, 244502.
Dussan V, E. B., and S. H. Davis, 1974, J. Fluid Mech. **65**, 71.
Edmonstone, B. D., R. V. Craster, and O. K. Matar, 2006, J. Fluid Mech. **564**, 105.
Edmonstone, B. D., O. K. Matar, and R. V. Craster, 2004, J. Eng. Math. **50**, 141.
Edmonstone, B. D., O. K. Matar, and R. V. Craster, 2005, J. Colloid Interface Sci. **287**, 261.
Edmonstone, B. D., O. K. Matar, and R. V. Craster, 2006, J. Colloid Interface Sci. **293**, 222.
Edwards, D. A., H. Brenner, and D. T. Wasan, 1991, *Interfacial Transport Processes and Rheology* (Butterworth-Heinemann, New York).
Eggers, J., 1997, Rev. Mod. Phys. **69**, 865.
Eggers, J., and T. F. Dupont, 1994, J. Fluid Mech. **262**, 205.
Eijkel, J. C. T., and A. van den Berg, 2005, Microfluid. Nanofluid. **1**, 249.
Elbaum, M., and S. G. Lipson, 1994, Phys. Rev. Lett. **72**, 3562.
Eliseev, V. I., 1983, J. Appl. Mech. Tech. Phys. **6**, 112.
Emslie, A. G., F. T. Bonner, and L. G. Peck, 1958, J. Appl. Phys. **29**, 858.
Engelund, F., and Z. Wan, 1984, J. Hydraul. Res. **110**, 219.
Eres, M. H., L. W. Schwartz, and R. V. Roy, 2000, Phys. Fluids **12**, 1278.
Eres, M. H., D. E. Weidner, and L. W. Schwartz, 1999, Langmuir **15**, 1859.
Erneux, E., and S. H. Davis, 1993, Phys. Fluids A **5**, 1117.
Espig, H., and R. Hoyle, 1965, J. Fluid Mech. **22**, 671.
Espinosa, F. F., 1991, *Spreading of Surfactant in a Small Pulmonary Airway*, Master's thesis, MIT.
Espinosa, F. F., and R. D. Kamm, 1999, J. Appl. Physiol. **86**, 391.
Espinosa, F. F., A. H. Shapiro, J. J. Fredberg, and R. D. Kamm, 1993, J. Appl. Physiol. **75**, 2028.
Fanton, X., and A. M. Cazabat, 1998, Langmuir **14**, 2554.
Fanton, X., A.-M. Cazabat, and D. Quéré, 1996, Langmuir **12**, 5875.
Fetzer, R., and K. Jacobs, 2007, Langmuir **23**, 11617.
Fetzer, R., K. Jacobs, A. Münch, B. Wagner, and T. P. Witelski, 2005, Phys. Rev. Lett. **95**, 127801.
Fetzer, R., M. Rauscher, R. Seemann, K. Jacobs, and K. Mecke, 2007, Phys. Rev. Lett. **99**, 114503.
Fink, J. H., and R. W. Griffiths, 1990, J. Fluid Mech. **221**, 485.
Fink, J. H., and R. W. Griffiths, 1998, J. Geophys. Res. **103**, 527.
Fischer, B. J., and S. M. Troian, 2003, Phys. Fluids **15**, 3837.
Fisher, L. S., and A. A. Golovin, 2005, J. Colloid Interface Sci. **291**, 515.
Fisher, L. S., and A. A. Golovin, 2007, J. Colloid Interface Sci. **307**, 203.
Forterre, Y., and O. Pouliquen, 2003, J. Fluid Mech. **486**, 21.
Forterre, Y., and O. Pouliquen, 2008, Annu. Rev. Fluid Mech. **40**, 1.
Frank, B., and S. Garoff, 1995, Langmuir **11**, 87.
Fraysse, N., and G. M. Homsy, 1994, Phys. Fluids **6**, 1491.
Frenkel, A. L., 1992, Europhys. Lett. **18**, 583.
Frenkel, A. L., and D. Halpern, 2002, Phys. Fluids **14**, L45.
Fried, E., M. E. Gurtin, and A. Q. Shen, 2006, Phys. Rev. E **73**, 061601.
Frumkin, A. N., 1938, J. Phys. (Moscow) **12**, 337.
Gallez, D., and W. T. Coakley, 1996, Heterog. Chem. Rev. **3**, 443.
Gambaryan-Roisman, T., and P. Stephan, 2007, Microfluid. Nanofluid. **3**, 207.
Gao, P., and X. Y. Lu, 2007, J. Fluid Mech. **591**, 495.
Gaskell, P. H., P. K. Jimack, M. Sellier, H. M. Thompson, and M. C. T. Wilson, 2004, J. Fluid Mech. **509**, 253.
Gaver, D. P., III, and J. B. Grotberg, 1990, J. Fluid Mech. **213**, 127.
Gaver, D. P., III, and J. B. Grotberg, 1992, J. Fluid Mech. **235**, 399.
Geoghegan, M., and G. Krausch, 2003, Prog. Polym. Sci. **28**, 261.
Ghatak, A., M. K. Chaudhury, V. Shenoy, and A. Sharma, 2000, Phys. Rev. Lett. **85**, 4329.
Ghatak, A., R. Khanna, and A. Sharma, 1999, J. Colloid Interface Sci. **212**, 483.
Gjevik, B., 1970, Phys. Fluids **13**, 1918.
Glasner, K. B., and T. P. Witelski, 2003, Phys. Rev. E **67**, 016302.
Golovin, A. A., A. A. Nepomnyashchy, and L. M. Pismen, 1994, Phys. Fluids **6**, 34.
Golovin, A. A., B. Y. Rubinstein, and L. M. Pismen, 2001, Langmuir **17**, 3930.
Gonuguntla, M., and A. Sharma, 2004, Langmuir **20**, 3456.
Gonzalez, A., and A. Castellanos, 1996, Phys. Rev. E **53**, 3573.
Good, R. J., and L. A. Girifalco, 1960, J. Phys. Chem. **64**, 561.
Goodman, J., 1994, Commun. Pure Appl. Math. **47**, 293.
Gotkis, Y., I. Ivanov, N. Murisic, and L. Kondic, 2006, Phys. Rev. Lett. **97**, 186101.
Govor, L. V., J. Parisi, G. H. Bauer, and G. Reiter, 2005, Phys. Rev. E **71**, 051603.
Govor, L. V., G. Reiter, G. H. Bauer, and J. Parisi, 2004, Appl. Phys. Lett. **84**, 4774.
Govor, L. V., G. Reiter, G. H. Bauer, and J. Parisi, 2006, Phys.

Rev. E **74**, 061603.
Govor, L. V., G. Reiter, J. Parisi, and G. H. Bauer, 2004, Phys. Rev. E **69**, 061609.
Greenspan, H. P., 1978, J. Fluid Mech. **84**, 125.
Greve, R., 1997, Philos. Trans. R. Soc. London, Ser. A **355**, 921.
Griffing, E., S. G. Bankoff, M. J. Miksis, and R. Schluter, 2006, Trans. ASME, Ser. C: J. Heat Transfer **128**, 276.
Griffiths, R. W., 2000, Annu. Rev. Fluid Mech. **32**, 477.
Griffiths, R. W., and J. H. Fink, 1993, J. Fluid Mech. **252**, 667.
Griffiths, R. W., and J. H. Fink, 1997, J. Fluid Mech. **347**, 13.
Grigoriev, R., 2005, Physica D **209**, 105.
Grotberg, J. B., 1994, Annu. Rev. Fluid Mech. **26**, 529.
Grotberg, J. B., 2001, Annu. Rev. Biomed. Eng. **3**, 421.
Grotberg, J. B., and D. P. Gaver III, 1996, J. Colloid Interface Sci. **178**, 377.
Grotberg, J. B., D. Halpern, and O. E. Jensen, 1995, J. Appl. Physiol. **78**, 750.
Grotberg, J. B., and O. E. Jensen, 2004, Annu. Rev. Fluid Mech. **36**, 121.
Grün, G., K. Mecke, and M. Rauscher, 2006, J. Stat. Phys. **122**, 1261.
Halpern, D., and A. L. Frenkel, 2003, J. Fluid Mech. **485**, 191.
Halpern, D., and J. B. Grotberg, 1992, J. Fluid Mech. **237**, 1.
Halpern, D., and J. B. Grotberg, 1993, J. Biomech. Eng. **115**, 271.
Halpern, D., O. E. Jensen, and J. B. Grotberg, 1998, J. Appl. Physiol. **85**, 333.
Hammond, P. S., 1983, J. Fluid Mech. **137**, 363.
Hamraoui, A., M. Cachile, C. Poulard, and A. M. Cazabat, 2004, Colloids Surf., A **250**, 215.
Haskett, R. P., T. P. Witelski, and J. Sur, 2005, Physica D **209**, 117.
He, S., and J. Ketterson, 1995, Phys. Fluids **7**, 2640.
Hegseth, J. J., N. Rashidnia, and A. Chai, 1996, Phys. Rev. E **54**, 1640.
Heil, M., and J. P. White, 2002, J. Fluid Mech. **462**, 79.
Herminghaus, S., 1999, Phys. Rev. Lett. **83**, 2359.
Herminghaus, S., K. Jacobs, K. Mecke, J. Bischoff, A. Fery, M. Ibn-Elhaj, and S. Schlagowski, 1998, Science **282**, 916.
Herminghaus, S., K. Jacobs, and R. Seemann, 2001, Eur. Phys. J. E **5**, 531.
Herminghaus, S., K. Jacobs, and R. Seemann, 2003, Eur. Phys. J. E **12**, 101.
Herminghaus, S., R. Seemann, and K. Jacobs, 2002, Phys. Rev. Lett. **89**, 056101.
Hinch, E. J., 1984, J. Fluid Mech. **144**, 463.
Hocking, L. M., W. R. Debler, and K. E. Cook, 1999, Phys. Fluids **11**, 307.
Holman, R. K., M. J. Cima, S. A. Uhland, and E. Sachs, 2002, J. Colloid Interface Sci. **249**, 432.
Homsy, G. M., 1974, Lect. Appl. Math. **15**, 191.
Hooper, A. P., and W. G. C. Boyd, 1983, J. Fluid Mech. **128**, 507.
Hooper, A. P., and R. Grimshaw, 1985, Phys. Fluids **28**, 37.
Hosoi, A. E., and J. W. M. Bush, 2001, J. Fluid Mech. **442**, 217.
Hosoi, A. E., and L. Mahadevan, 2004, Phys. Rev. Lett. **93**, 137802.
Howell, P. D., 2003, J. Eng. Math. **45**, 283.
Hu, H., and R. G. Larson, 2005a, Langmuir **21**, 3972.
Hu, H., and R. G. Larson, 2005b, Langmuir **21**, 3963.
Huang, R., 2005, J. Mech. Phys. Solids **53**, 63.
Huang, R., and Z. Suo, 2002a, Int. J. Solids Struct. **39**, 1791.
Huang, R., and Z. Suo, 2002b, J. Appl. Phys. **91**, 1135.
Huang, X., and M. H. Garcia, 1998, J. Fluid Mech. **374**, 305.
Huck, W. T. S., N. Bowden, P. Onck, T. Pardoen, J. W. Hutchinson, and G. M. Whitesides, 2000, Langmuir **16**, 3497.
Hunter, J. K., Z. Li, and H. Zhao, 2002, J. Comp. Physiol. **183**, 335.
Hunter, R. J., 1991, *Foundations of Colloid Science* (Oxford Science, Oxford).
Huppert, H. E., 1982a, Nature (London) **300**, 427.
Huppert, H. E., 1982b, J. Fluid Mech. **121**, 43.
Huppert, H. E., 2006, J. Fluid Mech. **554**, 299.
Hutter, K., 1983, *Theoretical Glaciology* (Reidel, Dordrecht).
Huynh, H. T., N. Roussel, and P. Coussot, 2005, Phys. Fluids **17**, 033101.
Hyman, J. M., and B. Nikolaenko, 1986, Physica D **18**, 113.
Israelachvili, J. N., 1992, *Intermolecular and Surface Forces with Applications to Colloidal and Biological Systems* (Academic, New York).
Jacobs, K., S. Herminghaus, and K. R. Mecke, 1998, Langmuir **14**, 965.
Jacobs, K., R. Seemann, and S. Herminghaus, 2008, in *Series in Soft Condensed Matter*, edited by O. Tsui and T. Russel (World Scientific, Singapore), Vol. 1, pp. 1–23.
Jacobs, K., R. Seemann, and K. Mecke, 2000, in *Statistical Physics and Spatial Statistics*, edited by K. Mecke, and D. Stoyan (Springer, Heidelberg).
Jacobs, K., R. Seemann, G. Schatz, and S. Herminghaus, 1998, Langmuir **14**, 4961.
Janczuk, B., M. L. Kerkeb, T. Bialopiotrowicz, and F. G. Caballero, 1989, J. Sep. Sci. Technol. **24**, 15.
Jensen, O. E., 1994, Phys. Fluids **6**, 1084.
Jensen, O. E., G. P. Chini, and J. R. King, 2004, J. Eng. Math. **50**, 289.
Jensen, O. E., and J. B. Grotberg, 1992, J. Fluid Mech. **240**, 259.
Jensen, O. E., and J. B. Grotberg, 1993, Phys. Fluids A **5**, 58.
Jensen, O. E., D. Halpern, and J. B. Grotberg, 1993, in *Surface-Tension-Driven Flows*, edited by G. P. Neitzel and M. K. Smith (ASME, New York), Vol. 170, p. 47.
Jensen, O. E., D. Halpern, and J. B. Grotberg, 1994, Chem. Eng. Sci. **49**, 1107.
Jensen, O. E., and S. Naire, 2006, J. Fluid Mech. **554**, 5.
Jerrett, J. M., and J. R. De Bruyn, 1992, Phys. Fluids A **4**, 234.
Jiang, W. Y., B. Helenbrook, and S. P. Lin, 2005, Phys. Fluids **16**, 652.
Jiang, W. Y., B. T. Helenbrook, S. P. Lin, and S. J. Weinstein, 2005, J. Fluid Mech. **539**, 387.
Jiang, W. Y., and S. P. Lin, 2005, Phys. Fluids **17**, 054105.
John, K., M. Bär, and U. Thiele, 2005, Eur. Phys. J. E **18**, 183.
John, K., and U. Thiele, 2007, Appl. Phys. Lett. **90**, 264102.
Johnson, M. F. G., R. A. Schulter, M. J. Miksis, and S. G. Bankoff, 1999, J. Fluid Mech. **394**, 339.
Jolly, M. S., R. Rosa, and R. Temam, 2000, Adv. Differ. Equ. **5**, 31.
Joo, S., S. H. Davis, and S. G. Bankoff, 1991, J. Fluid Mech. **230**, 117.
Joo, S. W., and S. H. Davis, 1992, J. Fluid Mech. **242**, 529.
Joo, S. W., and K.-C. Hsieh, 2000, Fluid Dyn. Res. **26**, 203.
Kabov, O. A., 1998, Thermophys. Aeromech. **5**, 547.
Kabov, O. A., J. Legros, I. V. Marchuk, and B. Scheid, 2000, Izv. Akad. Nauk, Mekh. Zhidk. Gaza **3**, 200.
Kabova, Y. O., A. Alekseev, T. Gambaryan-Roisman, and P. Stephan, 2006, Phys. Fluids **18**, 012104.
Kalliadasis, S., 2000, J. Fluid Mech. **413**, 355.

Kalliadasis, S., C. Bielarz, and G. M. Homsy, 2000, Phys. Fluids **12**, 1889.
Kalliadasis, S., and H.-C. Chang, 1994, J. Fluid Mech. **261**, 135.
Kalliadasis, S., and G. M. Homsy, 2001, J. Fluid Mech. **448**, 387.
Kalliadasis, S., A. Kiyashko, and E. A. Demekhin, 2003a, J. Fluid Mech. **457**, 377.
Kalliadasis, S., A. Kiyashko, and E. A. Demekhin, 2003b, J. Fluid Mech. **475**, 377.
Kalliadasis, S., and U. Thiele, 2007, *Thin Films of Soft Matter* (Springer, New York).
Kapitza, P. L., 1948, J. Exp. Theor. Phys. **18**, 3.
Kapitza, P. L., and S. P. Kapitza, 1949, J. Exp. Theor. Phys. **19**, 105.
Kargupta, K., R. Konnur, and A. Sharma, 2000, Langmuir **16**, 10243.
Kargupta, K., R. Konnur, and A. Sharma, 2001, Langmuir **17**, 1294.
Kargupta, K., and A. Sharma, 2001, Phys. Rev. Lett. **86**, 4536.
Kargupta, K., and A. Sharma, 2002, J. Colloid Interface Sci. **245**, 99.
Kargupta, K., and A. Sharma, 2003, Langmuir **19**, 5153.
Kargupta, K., A. Sharma, and R. Khanna, 2004, Langmuir **20**, 244.
Karim, A., J. F. Douglas, B. P. Lee, S. C. Glotzer, J. A. Rogers, R. J. Jackman, E. J. Amis, and G. M. Whitesides, 1998, Phys. Rev. E **57**, R6273.
Kataoka, D. E., and S. M. Troian, 1997, J. Colloid Interface Sci. **192**, 350.
Kataoka, D. E., and S. M. Troian, 1999, Nature (London) **402**, 794.
Kats-Demyanets, V., A. Oron, and A. A. Nepomnyashchy, 1997, Acta Astron. **40**, 655.
Kavehpour, P., B. Ovryn, and G. H. McKinley, 2002, Colloids Surf., A **206**, 409.
Kerchman, V. I., and A. L. Frenkel, 1994, Theor. Comput. Fluid Dyn. **6**, 235.
Kevrekidis, I. G., B. Nicolaenko, and J. C. Scovel, 1990, SIAM J. Appl. Math. **50**, 760.
Kim, H., S. G. Bankoff, and M. J. Miksis, 1992, Phys. Fluids A **4**, 2117.
Kim, H., S. G. Bankoff, and M. J. Miksis, 1994, Trans. ASME, Ser. C: J. Heat Transfer **116**, 986.
Kim, H. Y., J. H. Kim, and B. H. Kang, 2004, J. Fluid Mech. **498**, 245.
King, J. R., and M. Bowen, 2001, Eur. J. Appl. Math. **12**, 321.
King, J. R., A. Münch, and B. Wagner, 2006, Nonlinearity **19**, 2813.
King, J. R., D. S. Riley, and A. Sansom, 2000, Comp. Assist. Mech. Eng. Sc. **7**, 251.
Kitamura, A., E. Hasegawa, and M. Yoshizawa, 2002, Fluid Dyn. Res. **30**, 107.
Kliakhandler, I. L., 1999, J. Fluid Mech. **391**, 45.
Kliakhandler, I. L., S. H. Davis, and S. G. Bankoff, 2001, J. Fluid Mech. **429**, 381.
Kliakhandler, I. L., A. A. Nepomnyashchy, I. B. Simanovskii, and M. A. Zaks, 1998, Phys. Rev. E **58**, 5765.
Kliakhandler, I. L., and G. I. Sivashinsky, 1997, Phys. Fluids **9**, 23.
Kondic, L., 2003, SIAM Rev. **45**, 95.
Kondic, L., and J. A. Diez, 2001, Phys. Fluids **13**, 3168.
Kondic, L., and J. A. Diez, 2002, Phys. Rev. E **65**, 045301.
Konnur, R., K. Kargupta, and A. Sharma, 2000, Phys. Rev. Lett. **84**, 931.
Krishnamoorthy, S., B. Ramaswamy, and S. W. Joo, 1995, Phys. Fluids **7**, 2291.
Kumar, S., and O. K. Matar, 2004, J. Colloid Interface Sci. **273**, 581.
Kuramoto, Y., 1978, Suppl. Prog. Theor. Phys. **64**, 346.
Kuramoto, Y., and T. Tsuzuki, 1975, Prog. Theor. Phys. **54**, 687.
Kuramoto, Y., and T. Tsuzuki, 1976, Prog. Theor. Phys. **55**, 356.
Lawrence, C. J., 1990, Phys. Fluids A **2**, 453.
Lazar, P., and H. Riegler, 2005, Phys. Rev. Lett. **95**, 136103.
Le Grand-Piteira, N., A. Daerr, and L. Limat, 2006, Phys. Rev. Lett. **96**, 254503.
Lee, C. H., Y. Lu, and A. Q. Shen, 2006, Phys. Fluids **18**, 052105.
Lee, S. W., D. Y. Kwok, and P. E. Laibinis, 2002, Phys. Rev. E **65**, 051602.
Leenaars, A. F., J. A. M. Huethorst, and J. J. van Oekel, 1990, Langmuir **6**, 1701.
Leneweit, G., K. G. Roesner, and R. Koehler, 1999, Exp. Fluids **26**, 75.
Lenz, R. D., and S. Kumar, 2007a, J. Fluid Mech. **571**, 33.
Lenz, R. D., and S. Kumar, 2007b, J. Colloid Interface Sci. **316**, 660.
Lenz, R. D., and S. Kumar, 2007c, Phys. Fluids **19**, 102103.
Lepekhin, G. I., G. V. Ryabchuk, N. V. Tyabin, and E. R. Shulman, 1981, Theor. Found. Chem. Eng. **15**, 391.
Levy, R., and M. Shearer, 2005, Physica D **209**, 145.
Levy, R., and M. Shearer, 2006, SIAM J. Appl. Math. **66**, 1588.
Levy, R., M. Shearer, and T. P. Witelski, 2007, Eur. J. Appl. Math. **18**, 679.
Lin, C. K., C. C. Hwang, and W. Y. Uen, 2000, J. Colloid Interface Sci. **231**, 379.
Lin, S. P., 1969, J. Fluid Mech. **36**, 113.
Lin, Z., T. Kerle, S. M. Baker, D. A. Hoagland, E. Schaffer, U. Steiner, and T. P. Russell, 2001, J. Chem. Phys. **114**, 2377.
Lin, Z. Q., T. Kerle, T. P. Russel, E. Schaffer, and U. Steiner, 2002, Macromolecules **35**, 3971.
Lister, J. R., 1992, J. Fluid Mech. **242**, 631.
Lister, J. R., and R. C. Kerr, 1994, Geology **22**, 93.
Liu, J., and J. P. Gollub, 1993, Phys. Rev. Lett. **70**, 2289.
Liu, J., and J. P. Gollub, 1994, Phys. Fluids **6**, 1702.
Liu, J., J. B. Schneider, and J. P. Gollub, 1995, Phys. Fluids **7**, 55.
Loewenhertz, D. S., and C. J. Lawrence, 1989, Phys. Fluids A **1**, 1686.
Loewenhertz, D. S., C. J. Lawrence, and R. L. Weaver, 1989, J. Glaciol. Geocryol. **35**, 383.
López, P. G., S. G. Bankoff, and M. J. Miksis, 1996, J. Fluid Mech. **324**, 261.
López, P. G., M. J. Miksis, and S. G. Bankoff, 1997, Phys. Fluids **9**, 2177.
Luckham, P. F., 2005, private communication.
Ludviksson, V., and E. N. Lightfoot, 1971, AIChE J. **17**, 1166.
Lyushnin, A. V., A. A. Golovin, and L. M. Pismen, 2002, Phys. Rev. E **65**, 021602.
Malamataris, N. A., M. Vlachogiannis, and V. Bontozoglou, 2002, Phys. Fluids **14**, 1082.
Marangoni, C., 1865, Tipographia dei fratelli Fusi, Pavia.
Marmur, A., and M. D. Lelah, 1981, Chem. Eng. Commun. **13**, 133.
Marra, J., and J. A. M. Huethorst, 1991, Langmuir **7**, 2748.
Martin, A., O. Rossier, A. Buguin, P. Auroy, and F. Brochard-Wyart, 2000, Eur. Phys. J. E **74**, 665.

Matar, O. K., and R. V. Craster, 2001, Phys. Fluids **13**, 1869.
Matar, O. K., and R. V. Craster, 2006, J. Colloid Interface Sci. **303**, 503.
Matar, O. K., R. V. Craster, and S. Kumar, 2007, Phys. Rev. E **76**, 056301.
Matar, O. K., R. V. Craster, and M. R. E. Warner, 2002, J. Fluid Mech. **466**, 85.
Matar, O. K., V. Gkanis, and S. Kumar, 2005, J. Colloid Interface Sci. **286**, 319.
Matar, O. K., and S. Kumar, 2007, J. Eng. Math. **57**, 145.
Matar, O. K., S. Kumar, and R. V. Craster, 2004, J. Fluid Mech. **520**, 243.
Matar, O. K., and C. J. Lawrence, 2006a, Chem. Eng. Sci. **61**, 1074.
Matar, O. K., and C. J. Lawrence, 2006b, Chem. Eng. Sci. **61**, 3838.
Matar, O. K., C. J. Lawrence, and G. M. Sisoev, 2005, Phys. Fluids **17**, 052102.
Matar, O. K., G. M. Sisoev, and C. J. Lawrence, 2004, Phys. Fluids **16**, 1532.
Matar, O. K., G. M. Sisoev, and C. J. Lawrence, 2006, Can. J. Chem. Eng. **84**, 625.
Matar, O. K., and S. M. Troian, 1997, Phys. Fluids **9**, 3645.
Matar, O. K., and S. M. Troian, 1998, Phys. Fluids **10**, 1234.
Matar, O. K., and S. M. Troian, 1999a, Phys. Fluids **11**, 3232.
Matar, O. K., and S. M. Troian, 1999b, Chaos **9**, 141.
Mazouchi, A., and G. M. Homsy, 2001, Phys. Fluids **13**, 2751.
McBirney, A. R., and T. Murase, 1984, Annu. Rev. Earth Planet Sci. **12**, 337.
McKinley, I. S., S. K. Wilson, and B. R. Duffy, 1999, Phys. Fluids **11**, 30.
Mecke, K., and M. Rauscher, 2005, J. Phys.: Condens. Matter **17**, S3515.
Melcher, J. R., and C. V. Smith, 1969, Phys. Fluids **2**, 778.
Melo, F., J. F. Joanny, and S. Fauve, 1989, Phys. Rev. Lett. **63**, 1958.
Merkt, D., A. Pototsky, M. Bestehorn, and U. Thiele, 2005, Phys. Fluids **17**, 064104.
Mertens, K., V. Putkaradze, and P. Vorobieff, 2005, J. Fluid Mech. **531**, 49.
Mestel, A. J., 1994, J. Fluid Mech. **274**, 93.
Miladinova, S., and G. Lebon, 2005, Acta Mech. **174**, 33.
Mitlin, V. S., 1993, J. Colloid Interface Sci. **156**, 491.
Mitlin, V. S., 1994, Colloids Surf., A **89**, 97.
Mitlin, V. S., 1995, J. Colloid Interface Sci. **170**, 65.
Miyasaka, Y., 1974, Bull. Jpn. Soc. Precis. Eng. **17**, 1461.
Moosman, S., and G. M. Homsy, 1980, J. Colloid Interface Sci. **73**, 212.
Morariu, M. D., N. E. Voicua, E. Schaffer, Z. Lin, T. P. Russell, and U. Steiner, 2003, Nature Mater. **2**, 48.
Moriarty, J. A., L. W. Schwartz, and E. O. Tuck, 1991, Phys. Fluids A **3**, 733.
Moyle, D. T., M. S. Chen, and G. M. Homsy, 1999, Int. J. Multiphase Flow **25**, 1243.
Mugele, F., and J.-C. Baret, 2005, J. Phys.: Condens. Matter **17**, R705.
Münch, A., 2000, Nonlinearity **13**, 731.
Münch, A., 2003, Phys. Rev. Lett. **91**, 016105.
Münch, A., and A. Bertozzi, 1999, Phys. Fluids **11**, 2812.
Münch, A., and P. L. Evans, 2005, Physica D **209**, 164.
Münch A. and P. L. Evans, 2006, SIAM J. Appl. Math. **66**, 1610.
Münch, A., and B. Wagner, 2005, Physica D **209**, 178.
Münch, A., B. Wagner, and T. P. Witelski, 2005, J. Eng. Math. **53**, 359.
Münch, A., and B. A. Wagner, 1999, Eur. J. Appl. Math. **10**, 297.
Myers, T., J. Charpin, and S. J. Chapman, 2002, Phys. Fluids **14**, 2788.
Myers, T. G., 1998, SIAM Rev. **40**, 441.
Myers, T. G., and J. P. Charpin, 2001, Int. J. Non-Linear Mech. **36**, 629.
Nagasaki, T., and K. Hijikata, 1989, Proceeding of the ANS National Heat Transfer Conference (unpublished), Vol. 4, p. 23.
Nakaya, C., 1989, Phys. Fluids A **1**, 1143.
Needham, D. J., and J. H. Merkin, 1984, Proc. R. Soc. London, Ser. A **394**, 259.
Needham, D. J., and J. H. Merkin, 1987, J. Fluid Mech. **184**, 357.
Nepomnyashchy, A. A., 1974, Izv. Akad. Nauk SSSR, Mekh. Zhidk. Gaza **3**, 1143.
Nepomnyashchy, A. A., and I. B. Simanovskii, 1997, Q. J. Mech. Appl. Math. **50**, 149.
Neto, C., and K. Jacobs, 2004, Physica A **339**, 66.
Neto, C., K. Jacobs, R. Seemann, R. Blossey, J. Becker, and G. Grün, 2003, J. Phys.: Condens. Matter **15**, 3355.
Nikolov, A. D., D. T. Wasan, A. Chengara, K. Koczo, G. A. Policello, and I. Kolossvary, 2002, Adv. Colloid Interface Sci. **96**, 325.
Nosoko, T., and A. Miyara, 2004, Phys. Fluids **16**, 1118.
Nosoko, T., P. N. Yoshimura, T. Nagata, and L. Okawa, 1996, Chem. Eng. Sci. **51**, 725.
Oddy, M. H., J. G. Santiago, and J. C. Mikkelsen, 2001, Anal. Chem. **73**, 5822.
O'Hara, P. C., and W. M. Gelbart, 1998, Langmuir **14**, 3418.
Oliver, J. M., J. R. King, K. J. McKinlay, P. D. Brown, D. M. Grant, C. A. Scotchford, and J. V. Wood, 2005, IMA J. Math. Appl. Med. Biol. **22**, 53.
Or, A. C., and R. E. Kelly, 1998, J. Fluid Mech. **360**, 21.
Oron, A., 2000a, Phys. Fluids **12**, 1633.
Oron, A., 2000b, Phys. Rev. Lett. **85**, 2108.
Oron, A., and S. G. Bankoff, 1999, J. Colloid Interface Sci. **218**, 152.
Oron, A., and S. G. Bankoff, 2001, Phys. Fluids **13**, 1107.
Oron, A., S. H. Davis, and S. G. Bankoff, 1997, Rev. Mod. Phys. **69**, 931.
Oron, A., and O. Gottlieb, 2004, J. Eng. Math. **50**, 121.
Padmakar, A. S., K. Kargupta, and A. Sharma, 1999, J. Chem. Phys. **110**, 1735.
Panga, M. K. R., and V. Balakotaiah, 2003, Phys. Rev. Lett. **90**, 154501.
Panga, M. K. R., R. R. Mudunuri, and V. Balakotaiah, 2005, Phys. Rev. E **71**, 036310.
Papageorgiou, D. T., 1995a, J. Fluid Mech. **301**, 109.
Papageorgiou, D. T., 1995b, Phys. Fluids **7**, 1529.
Papageorgiou, D. T., C. Maldarelli, and D. S. Rumschitzki, 1990, Phys. Fluids A **2**, 340.
Papageorgiou, D. T., and Y. S. Smyrlis, 1991, Theor. Comput. Fluid Dyn. **3**, 15.
Papageorgiou, D. T., and J.-M. Vanden-Broeck, 2004a, Eur. J. Appl. Math. **15**, 609.
Papageorgiou, D. T., and J.-M. Vanden-Broeck, 2004b, J. Fluid Mech. **508**, 71.
Park, C. D., and T. Nosoko, 2003, AIChE J. **49**, 2715.
Paunov, V. N., K. D. Danov, N. Alleborn, H. Raszillier, and F.

Durst, 1998, Chem. Eng. Sci. **53**, 2839.
Pease, L. F., and W. B. Russel, 2002, J. Non-Newtonian Fluid Mech. **102**, 233.
Pereira, A., P. M. J. Trevelyan, U. Thiele, and S. Kalliadasis, 2007, Phys. Fluids **19**, 112102.
Pinkerton, H., and G. Norton, 1995, J. Volcanol. Geotherm. Res. **68**, 307.
Pismen, L. M., 2001, Phys. Rev. E **64**, 021603.
Pismen, L. M., 2002, Colloids Surf., A **206**, 11.
Pismen, L. M., and Y. Pomeau, 2000, Phys. Rev. E **62**, 2480.
Plesset, M. S., and A. Prosperetti, 1976, J. Fluid Mech. **78**, 433.
Podolny, A., A. A. Nepomnyashchy, and A. Oron, 2007, Phys. Rev. E **76**, 026309.
Podolny, A., A. Oron, and A. A. Nepomnyashchy, 2007, J. Non-Equilib. Thermodyn. **32**, 203.
Pollack, M. G., A. D. Shenderov, and R. B. Fair, 2002, Lab Chip **2**, 96.
Pototsky, A., M. Bestehorn, D. Merkt, and U. Thiele, 2005, J. Chem. Phys. **122**, 224711.
Pototsky, A., M. Bestehorn, D. Merkt, and U. Thiele, 2006, Europhys. Lett. **74**, 665.
Pototsky, A., M. Bestehorn, and U. Thiele, 2004, Physica D **199**, 138.
Poulard, C., O. Benichou, and A. M. Cazabat, 2003, Langmuir **19**, 8828.
Poulard, C., and A. M. Cazabat, 2005, Langmuir **21**, 6270.
Poulard, C., M. Voue, J. D. Coninck, and A. M. Cazabat, 2006, Colloids Surf., A **282**, 240.
Pozrikidis, C., 1988, J. Fluid Mech. **188**, 275.
Pozrikidis, C., 2003, J. Fluid Mech. **496**, 105.
Pozrikidis, C., 2004, Adv. Appl. Mech. **40**, 179.
Prins, M. W. J., W. J. J. Welters, and J. W. Weekamp, 2001, Science **291**, 277.
Pumir, A., P. Manneville, and Y. Pomeau, 1983, J. Fluid Mech. **135**, 27.
Quéré, D., 1990, Europhys. Lett. **13**, 721.
Quéré, D., 1999, Annu. Rev. Fluid Mech. **31**, 347.
Rabani, E., D. R. Reichman, P. L. Geissler, and L. E. Brus, 2003, Nature (London) **426**, 271.
Ramaswamy, B., S. Chippada, and S. W. Joo, 1996, J. Fluid Mech. **325**, 163.
Rauscher, J. W., R. E. Kelly, and J. D. Cole, 1973, J. Appl. Mech. **43**, 43.
Redon, C., F. Brochard-Wyart, and F. Rondelez, 1992, J. Phys. II **2**, 1671.
Redon, C., J. B. Brzoska, and F. Brochard-Wyart, 1994, Macromolecules **27**, 468.
Reisfeld, B., S. G. Bankoff, and S. H. Davis, 1991, J. Appl. Phys. **70**, 5258.
Reiter, G., 1992, Phys. Rev. Lett. **68**, 75.
Reiter, G., 1993, Langmuir **9**, 1344.
Reiter, G., 2001, Phys. Rev. Lett. **87**, 186101.
Reiter, G., 2003, Eur. Phys. J. E **12**, 465.
Reiter, G., and A. Sharma, 2001, Phys. Rev. Lett. **87**, 166103.
Reiter, G., A. Sharma, A. Casoli, M.-O. David, R. Khanna, and P. Auroy, 1999, Langmuir **15**, 2551.
Reynolds, O., 1886, Philos. Trans. R. Soc. London **177**, 157.
Rifert, V. G., P. A. Barabash, and A. A. Muzhilko, 1982, J. Power Eng. **8**, 62.
Rockford, L., P. M. Y. Liu, and T. P. Russell, 1999, Phys. Rev. Lett. **82**, 2602.
Rosenau, P., and A. Oron, 1992, Phys. Fluids A **4**, 117.
Roskes, G. J., 1970, Phys. Fluids **13**, 1440.
Roy, R. V., A. J. Roberts, and M. E. Simpson, 2002, J. Fluid Mech. **454**, 235.
Ruckenstein, E., and R. K. Jain, 1974, J. Chem. Soc., Faraday Trans. 1 **70**, 132.
Ruyer-Quil, C., and P. Manneville, 1998, Eur. Phys. J. B **6**, 277.
Ruyer-Quil, C., and P. Manneville, 2000, Eur. Phys. J. B **15**, 357.
Ruyer-Quil, C., B. Scheid, S. Kalliadasis, M. G. Velarde, and R. K. Zeytounian, 2005, J. Fluid Mech. **538**, 199.
Ruyer-Quil, C., P. Treveleyan, F. Giorgiutti-Dauphiné, C. Duprat, and S. Kalliadasis, 2008, J. Fluid Mech. **603**, 431.
Saffman, P. G., and G. I. Taylor, 1958, Proc. R. Soc. London, Ser. A **245**, 312.
Salamon, T., R. Armstrong, and R. Brown, 1994, Phys. Fluids **6**, 2202.
Samid-Merzel, N., S. G. Lipson, and D. S. Tannhauser, 1998, Phys. Rev. E **57**, 2906.
Saprykin, S., E. A. Demekhin, and S. Kalliadasis, 2005, Phys. Rev. Lett. **94**, 224101.
Saprykin, S., P. M. J. Trevelyan, R. J. Koopmans, and S. Kalliadasis, 2007, Phys. Rev. E **75**, 026306.
Saulnier, F., E. Raphaël, and P. G. deGennes, 2002, Phys. Rev. Lett. **88**, 196101.
Saville, D. A., 1997, Annu. Rev. Fluid Mech. **29**, 27.
Schaffer, E., T. Thurn-Albrecht, T. P. Russell, and U. Steiner, 2000, Nature (London) **403**, 874.
Schaffer, E., T. Thurn-Albrecht, T. P. Russell, and U. Steiner, 2001, Europhys. Lett. **53**, 518.
Scheid, B., C. Ruyer-Quil, S. Kalliadasis, M. G. Velarde, and R. K. Zeytounian, 2005, J. Fluid Mech. **538**, 223.
Scheid, B., C. Ruyer-Quil, and P. Manneville, 2006, J. Fluid Mech. **562**, 183.
Scheid, B., C. Ruyer-Quil, U. Thiele, O. Kabov, J. Legros, and P. Colinet, 2005, J. Fluid Mech. **527**, 303.
Schlagowski, S., K. Jacobs, and S. Herminghaus, 2002, Europhys. Lett. **57**, 519.
Schmid, P. J., and D. S. Henningson, 2001, *Stability and Transition in Shear Flows* (Springer, New York).
Schneemilch, M., and A.-M. Cazabat, 2000a, Langmuir **16**, 9850.
Schneemilch, M., and A.-M. Cazabat, 2000b, Langmuir **16**, 8796.
Schwartz, L. W., 1989, Phys. Fluids A **1**, 443.
Schwartz, L. W., 1998, Langmuir **14**, 3440.
Schwartz, L. W., and R. R. Eley, 1998, J. Colloid Interface Sci. **202**, 173.
Schwartz, L. W., and E. E. Michaelides, 1988, Phys. Fluids **31**, 2739.
Schwartz, L. W., D. Roux, and J. J. Cooper-White, 2005, Physica D **209**, 236.
Schwartz, L. W., and R. V. Roy, 2001, Phys. Fluids **13**, 3089.
Schwartz, L. W., R. V. Roy, R. R. Eley, and H. M. Princen, 2004, J. Eng. Math. **50**, 157.
Seemann, R., S. Herminghaus, and K. Jacobs, 2001a, Phys. Rev. Lett. **86**, 5534.
Seemann, R., S. Herminghaus, and K. Jacobs, 2001b, J. Phys.: Condens. Matter **13**, 4925.
Seemann, R., S. Herminghaus, C. Neto, S. Schlagowski, D. Podzimek, R. Konrad, H. Mantz, and K. Jacobs, 2005, J. Phys.: Condens. Matter **17**, S267.
Sferrazza, M., M. Heppenstall-Butler, R. Cubitt, D. Bucknall, J. Webster, and R. A. L. Jones, 1998, Phys. Rev. Lett. **81**, 5173.

Shahidzadeh-Bonn, N., S. Rafaï, A. Azouni, and D. Bonn, 2006, J. Fluid Mech. **549**, 307.
Shankar, V., and A. Sharma, 2004, J. Colloid Interface Sci. **274**, 294.
Sharma, A., 1993, Langmuir **9**, 861.
Sharma, A., 1998, Langmuir **14**, 4915.
Sharma, A., 2003, Eur. Phys. J. E **12**, 397.
Sharma, A., and A. T. Jameel, 1993, J. Colloid Interface Sci. **161**, 190.
Sharma, A., and R. Khanna, 1998, Phys. Rev. Lett. **81**, 3463.
Sharma, A., and R. Khanna, 1999, J. Chem. Phys. **110**, 4929.
Sharma, A., and G. Reiter, 1996, J. Colloid Interface Sci. **178**, 383.
Sharma, A., and E. Ruckenstein, 1986, J. Colloid Interface Sci. **113**, 456.
Shaw, H. R., 1969, J. Petrol. **10**, 510.
Sheludko, A., 1967, Adv. Colloid Interface Sci. **1**, 391.
Shen, A. Q., B. Gleason, G. H. McKinley, and H. A. Stone, 2002, Phys. Fluids **14**, 4055.
Shenoy, V., and A. Sharma, 2002, Phys. Rev. Lett. **88**, 236101.
Shkadov, V. Y., 1967, Fluid Dyn. Res. **2**, 21.
Shkadov, V. Y., 1973, *Scientific Proceedings 25* (Moscow State University, Moscow), p. 192.
Shkadov, V. Y., 1977, Fluid Dyn. Res. **12**, 63.
Shkadov, V. Y., and G. M. Sisoev, 2004, Fluid Dyn. Res. **35**, 357.
Shklyaev, O. E., and E. Fried, 2007, J. Fluid Mech. **584**, 157.
Shlang, T., and G. I. Sivashinsky, 1982, J. Phys. A **43**, 459.
Shvets, A. F., L. P. Portnov, G. G. Filipov, and A. I. Gorubnov, 1992, Theor. Found. Chem. Eng. **26**, 895.
Shyy, W., M. Francois, H. S. Udaykumar, N. N'dri, and R. Tran-Son-Tay, 2001, Appl. Mech. Rev. **54**, 405.
Silvi, N., and E. B. Dussan V, 1985, Phys. Fluids **28**, 5.
Sisoev, G. M., O. K. Matar, R. V. Craster, and S. V. Gerasimov, 2006, Chem. Eng. Sci. **61**, 7279.
Sisoev, G. M., O. K. Matar, and C. J. Lawrence, 2003a, J. Fluid Mech. **495**, 385.
Sisoev, G. M., O. K. Matar, and C. J. Lawrence, 2003b, J. Chem. Technol. Biotechnol. **78**, 151.
Sisoev, G. M., O. K. Matar, and C. J. Lawrence, 2005, Chem. Eng. Sci. **60**, 2051.
Sisoev, G. M., and V. Y. Shkadov, 1987, J. Eng. Phys. **52**, 671.
Sisoev, G. M., and V. Y. Shkadov, 1990, J. Eng. Phys. **58**, 423.
Sisoev, G. M., and V. Y. Shkadov, 1997a, Fluid Dyn. Res. **32**, 784.
Sisoev, G. M., and V. Y. Shkadov, 1997b, Phys. Dokl. **42**, 683.
Sisoev, G. M., and V. Y. Shkadov, 1999, Dokl. Phys. **44**, 454.
Sisoev, G. M., A. F. Taldrik, and V. Y. Shkadov, 1986, J. Eng. Phys. **51**, 1171.
Sivashinsky, G. I., 1977, Acta Astron. Sin. **4**, 1175.
Sivashinsky, G. I., and D. M. Michelson, 1980, Prog. Theor. Phys. **63**, 2112.
Smith, P. C., 1973, J. Fluid Mech. **58**, 275.
Smolka, L. B., J. North, and B. K. Guerra, 2008, Phys. Rev. E **77**, 036301.
Smyrlis, Y. S., and D. T. Papageorgiou, 1991, Proc. Natl. Acad. Sci. U.S.A. **88**, 11129.
Smyrlis, Y. S., and D. T. Papageorgiou, 1996, ICASE Rep. **96-12**, 1.
Spaid, M. A., and G. M. Homsy, 1996, Phys. Fluids **8**, 460.
Spaid, M. A., and G. M. Homsy, 1997, Phys. Fluids **9**, 823.
Squires, T. M., and S. R. Quake, 2005, Rev. Mod. Phys. **77**, 977.
Sridhar, N., D. J. Srolovitz, and Z. Suo, 2001, Appl. Phys. Lett. **78**, 2482.
Stange, T. G., D. F. Evans, and W. A. Hendrickson, 1997, Langmuir **13**, 4459.
Starov, V. M., S. R. Kostvintsev, V. D. Sobolev, M. G. Velarde, and S. A. Zhdanov, 2002, J. Colloid Interface Sci. **246**, 372.
Starov, V. M., S. R. Kostvintsev, M. G. Velarde, and S. A. Zhdanov, 2002, J. Colloid Interface Sci. **252**, 397.
Starov, V. M., S. A. Zhdanov, and M. G. Velarde, 2002, Langmuir **18**, 9744.
Stasiuk, M. V., C. Jaupart, and R. S. J. Sparks, 1993, Geology **21**, 335.
Stillwagon, L. E., and R. G. Larson, 1988, J. Appl. Phys. **63**, 5251.
Stillwagon, L. E., and R. G. Larson, 1990, Phys. Fluids A **2**, 1937.
Stocker, R., and J. W. M. Bush, 2007, J. Fluid Mech. **583**, 465.
Stocker, R., and A. E. Hosoi, 2005, J. Fluid Mech. **544**, 353.
Stone, H. A., 1990, Phys. Fluids A **2**, 111.
Stone, H. A., A. D. Strook, and A. Ajdari, 2004, Annu. Rev. Fluid Mech. **36**, 381.
Sultan, E., A. Boudaoud, and M. Ben Amar, 2004, J. Eng. Math. **50**, 209.
Sultan, E., A. Boudaoud, and M. Ben Amar, 2005, J. Fluid Mech. **543**, 183.
Suman, B., and S. Kumar, 2006, J. Colloid Interface Sci. **304**, 208.
Sumino, Y., N. Magome, T. Hamada, and K. Yoshikawa, 2005, Phys. Rev. Lett. **94**, 068301.
Sur, J., A. L. Bertozzi, and R. P. Behringer, 2003, Phys. Rev. Lett. **90**, 126105.
Takeshi, O., 1999, Phys. Fluids **11**, 3247.
Tanner, L. H., 1979, J. Phys. D **12**, 1473.
Taylor, G. I., and A. D. McEwan, 1965, J. Fluid Mech. **22**, 1.
Teletzke, G. F., H. T. Davis, and L. E. Scriven, 1988, Rev. Phys. Appl. **23**, 989.
Thiele, U., 2003, Eur. Phys. J. E **12**, 409.
Thiele, U., L. Brusch, M. Bestehorn, and M. Bär, 2003, Eur. Phys. J. E **11**, 255.
Thiele, U., and E. Knobloch, 2003, Phys. Fluids **15**, 892.
Thiele, U., M. Mertig, and W. Pompe, 1998, Phys. Rev. Lett. **80**, 2869.
Thiele, U., M. Velarde, and K. Neuffer, 2001, Phys. Rev. Lett. **87**, 016104.
Thomas, S., A. Faghri, and W. Hankey, 1991, J. Fluids Eng. **113**, 73.
Thomson, J., 1855, Philos. Mag. **10**, 330.
Tilley, B. S., P. G. Petropoulos, and D. T. Papageorgiou, 2001, Phys. Fluids **13**, 3547.
Trefethen, L. N., A. E. Trefethen, S. C. Reddy, and T. A. Driscoll, 1993, Science **261**, 578.
Trevelyan, P. M. J., and S. Kalliadasis, 2004a, Phys. Fluids **16**, 3191.
Trevelyan, P. M. J., and S. Kalliadasis, 2004b, Phys. Fluids **16**, 3209.
Trevelyan, P. M. J., S. Kalliadasis, J. H. Merkin, and S. K. Scott, 2002, Phys. Fluids **14**, 2402.
Trevelyan, P. M. J., B. Scheid, C. Ruyer-Quil, and S. Kalliadasis, 2007, J. Fluid Mech. **592**, 295.
Trifonov, Y. Y., 1992, AIChE J. **38**, 821.
Trifonov, Y. Y., 1998, Int. J. Multiphase Flow **24**, 1139.
Trippa, G., P. Hetherington, and R. J. J. Jachuck, 2002, in Proceedings of the 15th International Symposium on Industrial Crystallization, Sorrento, Italy (unpublished).

Troian, S. M., E. Herbolzheimer, and S. A. Safran, 1990, Phys. Rev. Lett. **65**, 333.
Troian, S. M., E. Herbolzheimer, S. A. Safran, and J. F. Joanny, 1989, Europhys. Lett. **10**, 25.
Troian, S. M., X. L. Wu, and S. A. Safran, 1989, Phys. Rev. Lett. **62**, 1496.
Tseluiko, D., M. G. Blyth, D. T. Papageorgiou, and J.-M. Vanden-Broeck, 2008, J. Fluid Mech. **597**, 449.
Tseluiko, D., and D. T. Papageorgiou, 2006, J. Fluid Mech. **556**, 361.
Tseluiko, D., and D. T. Papageorgiou, 2007, SIAM J. Appl. Math. **67**, 1310.
Tuck, E. O., and L. W. Schwartz, 1990, SIAM Rev. **32**, 453.
Usha, R., R. Ravindran, and B. Uma, 2005, Phys. Fluids **17**, 102103.
Valluri, P., O. K. Matar, G. F. Hewitt, and M. A. Mendes, 2005, Chem. Eng. Sci. **60**, 1965.
Valluri, P., O. K. Matar, M. A. Mendes, and G. F. Hewitt, 2002, Multiphase Sci. Technol. **14**, 303.
VanHook, S. J., M. F. Schatz, W. D. McCormick, J. B. Swift, and H. L. Swinney, 1995, Phys. Rev. Lett. **75**, 4397.
VanHook, S. J., M. F. Schatz, J. B. Swift, W. D. McCormick, and H. L. Swinney, 1997, J. Fluid Mech. **345**, 45.
van Nierop, E. A., A. Ajdari, and H. A. Stone, 2006, Phys. Fluids **18**, 038105.
van Oss, C. J., M. K. Chaudhury, and R. J. Good, 1987, Adv. Colloid Interface Sci. **28**, 35.
Vaynblat, D., J. R. Lister, and T. P. Witelski, 2001, Phys. Fluids **13**, 1130.
Veretennikov, I., A. Indekina, and H.-C. Chang, 1998, J. Fluid Mech. **373**, 81.
Verma, R., and A. Sharma, 2007, Ind. Eng. Chem. Res. **46**, 3108.
Verma, R., A. Sharma, K. Kargupta, and J. Bhaumik, 2005, Langmuir **21**, 3710.
Verwey, E. J., and J. T. G. Overbeck, 1948, *Theory of the Stability of Lyophilic Colloids* (Elsevier, Amsterdam).
Vicevic, M., R. J. J. Jachuck, K. Scott, J. H. Clark, and K. Wilson, 2004, Green Chem. **6**, 533.
Viens, M., D. Drolet, A. Blouin, J. P. Monchalin, and C. Moreau, 1996, in Proceedings of the Ninth Thermal Spray Conference, edited by C. C. Berndt (unpublished), pp. 947–951.
Vlachogiannis, M., and V. Bontozoglou, 2001, J. Fluid Mech. **435**, 191.
Vlachogiannis, M., and V. Bontozoglou, 2002, J. Fluid Mech. **457**, 133.
Vrij, A., 1966, Discuss. Faraday Soc. **42**, 23.
Vrij, A., and J. T. G. Overbeek, 1968, J. Am. Chem. Soc. **90**, 3074.
Warner, M. R. E., R. V. Craster, and O. K. Matar, 2002, Phys. Fluids **14**, 1642.
Warner, M. R. E., R. V. Craster, and O. K. Matar, 2003a, J. Colloid Interface Sci. **268**, 448.
Warner, M. R. E., R. V. Craster, and O. K. Matar, 2003b, J. Colloid Interface Sci. **267**, 92.
Warner, M. R. E., R. V. Craster, and O. K. Matar, 2004a, J. Fluid Mech. **510**, 169.
Warner, M. R. E., R. V. Craster, and O. K. Matar, 2004b, Phys. Fluids **16**, 2933.
Warren, J. A., W. J. Boettinger, and A. R. Roosen, 1998, Acta Mater. **46**, 3247.
Weh, L., 1999, Mater. Sci. Eng., C **8-9**, 463.
Weh, L., 2005, Macromol. Mater. Eng. **290**, 976.
Weh, L., and A. Venthur, 2004, J. Colloid Interface Sci. **271**, 407.
Weibel, E. R., and D. M. Gomez, 1962, Science **137**, 577.
Weinstein, S. J., 1999, Phys. Fluids **11**, 3270.
Weinstein, S. J., and K. J. Ruschak, 2004, Annu. Rev. Fluid Mech. **36**, 29.
Wierschem, A., and N. Aksel, 2003, Physica D **186**, 221.
Wierschem, A., and N. Aksel, 2004a, Phys. Fluids **16**, 3868.
Wierschem, A., and N. Aksel, 2004b, Phys. Fluids **16**, 4566.
Wierschem, A., M. Scholle, and N. Aksel, 2002, Exp. Fluids **33**, 429.
Wierschem, A., M. Scholle, and N. Aksel, 2003, Phys. Fluids **15**, 426.
Williams, M. B., and S. H. Davis, 1982, J. Colloid Interface Sci. **90**, 220.
Wilson, S. K., and B. R. Duffy, 1998, Phys. Fluids **10**, 13.
Wilson, S. K., and B. R. Duffy, 2003, Phys. Fluids **15**, 827.
Wilson, S. K., and B. R. Duffy, 2005a, IMA J. Appl. Math. **70**, 293.
Wilson, S. K., and B. R. Duffy, 2005b, Phys. Fluids **17**, 078104.
Wilson, S. K., B. R. Duffy, and S. H. Davis, 2001, Eur. J. Appl. Math. **12**, 233.
Wilson, S. K., B. R. Duffy, and R. Hunt, 2002, Q. J. Mech. Appl. Math. **55**, 385.
Witelski, T. P., and A. J. Bernoff, 1999, Phys. Fluids **11**, 2443.
Witelski, T. P., M. Shearer, and R. Levy, 2006, Appl. Math. Res. Express **2006**, 1.
Wong, H., D. Rumschitzki, and C. Maldarelli, 1996, Phys. Fluids **8**, 3203.
Woods, B. D., E. T. Hurlburt, and T. J. Hanratty, 2000, Int. J. Multiphase Flow **26**, 977.
Woods, W. P., 1995, *The Hydrodynamics of Thin Liquid Films Flowing Over a Rotating Disc*, Ph.D. thesis, University of Newcastle-upon-Tyne.
Wu, N., L. F. Pease, and W. B. Russel, 2005, Langmuir **21**, 12290.
Xie, R., A. Karim, J. F. Douglas, C. C. Han, and R. A. Weiss, 1998, Phys. Rev. Lett. **81**, 1251.
Ye, Y., and H.-C. Chang, 1999, Phys. Fluids **11**, 2494.
Yeo, L. Y., R. V. Craster, and O. K. Matar, 2003, Phys. Rev. E **67**, 056315.
Yeo, L. Y., R. V. Craster, and O. K. Matar, 2007, J. Colloid Interface Sci. **306**, 368.
Yih, C. S., 1955, *Proceedings of the Second US Congress on Applied Mechanics* (ASME, New York), pp. 623–628.
Yih, C. S., 1963, Phys. Fluids **6**, 321.
Yochelis, A., and L. M. Pismen, 2005, Phys. Rev. E **72**, 025301(R).
Yoo, P. J., and H. H. Lee, 2005, Macromolecules **38**, 2820.
Yoshimura, P. N., T. Nosoko, and T. Nagata, 1996, Chem. Eng. Sci. **51**, 1231.
Young, G. W., and S. H. Davis, 1987, J. Fluid Mech. **176**, 1.
Zadražil, A., F. Stepanek, and O. K. Matar, 2006, J. Fluid Mech. **562**, 1.
Zhang, J., R. P. Behringer, and A. Oron, 2007, Phys. Rev. E **76**, 016306.
Zhang, W. W., and J. R. Lister, 1999, Phys. Fluids **11**, 2454.
Zhang, Y. L., O. K. Matar, and R. V. Craster, 2002, J. Non-Newtonian Fluid Mech. **105**, 53.

Zhang, Y. L., O. K. Matar, and R. V. Craster, 2003a, J. Colloid Interface Sci. **262**, 130.
Zhang, Y. L., O. K. Matar, and R. V. Craster, 2003b, Med. Eng. Phys. **25**, 115.
Zhao, Y., and J. S. Marshall, 2006, J. Fluid Mech. **559**, 355.
Zhou, J. J., B. Dupuy, A. L. Bertozzi, and A. E. Hosoi, 2005, Phys. Rev. Lett. **94**, 117803.
Zope, M., K. Kargupta, and A. Sharma, 2001, J. Chem. Phys. **114**, 7211.